THE NUMERICAL SOLUTION

OF WAVEGUIDE DISCONTINUITY PROBLEMS

by

PAUL HENRY MASTERMAN, B.Sc.

A thesis presented for the
degree of Doctor of Philosophy in
the University of Leeds.

September, 1969

ACKNOWLEDGEMENTS

The work described in this thesis was carried out in the Department of Electrical and Electronic Engineering, University of Leeds, by kind permission of Professor G.W. Carter. Financial assistance was provided as a result of the award of a Science Research Council Research Studentship.

The author particularly wishes to thank Professor P.J.B. Clarricoats, the original supervisor and instigator of this research, for his continued interest and assistance. Thanks are also extended to Dr. C.D. Hannaford and Dr. J.R. Richardson who subsequently supervised the work.

The helpful discussions with Dr. D. Herbison-Evans, formerly of the Signals Research and Development Establishment, Christchurch, and with Dr. P.R. Huckle of Queen Mary College, London, are gratefully acknowledged, as is the assistance of Mr. J. Mark and Mr. B. Claydon of Marconi, Ltd., Chelmsford.

The careful work of Mrs. A.G.Powell in typing the manuscript is greatly appreciated.

ACKNOWLEDGEMENTS

The work described in this thesis was carried out in the Department of Electrical and Electronic Engineering, University of Leeds, by kind permission of Professor G.W. Carter. Financial assistance was provided as a result of the award of a Science Research Council Research Studentship.

The author particularly wishes to thank Professor P.J.B. Clarricoats, the original supervisor and instigator of this research, for his continued interest and assistance. Thanks are also extended to Dr. C.D. Hannaford and Dr. J.R. Richardson who subsequently supervised the work.

The helpful discussions with Dr. D. Herbison-Evans, formerly of the Signals Research and Development Establishment, Christchurch, and with Dr. P.R. Huckle of Queen Mary College, London, are gratefully acknowledged, as is the assistance of Mr. J. Mark and Mr. B. Claydon of Marconi, Ltd., Chelmsford.

The careful work of Mrs. A.G.Powell in typing the manuscript is greatly appreciated.

ABSTRACT

A computational method for solving a wide range of transverse and longitudinal waveguide discontinuity problems is described. Results are obtained by the simultaneous solution of matrix equations, generated by Fourier analysis, which relate the complex amplitudes of orthogonal electric and magnetic field components. In some cases the solution is found to be sensitive to the way in which infinite series of field functions are truncated, and it is shown how the optimum form of truncation can be determined for many configurations of practical importance.

Several examples showing the application of the method are given, and comparison of results with those obtained by experiment, and by other analytical techniques, confirms its accuracy.

The application of the method in the design of discontinuities for higher-mode generation in multimode antennas is considered, particularly in connection with a multimode monopulse feed for a satellite-communication reflector antenna. Primary and secondary characteristics are determined theoretically for various mode-converter configurations, allowing those giving satisfactory all-round performance to be selected. Comparison with conventional feeds shows the multimode feed to be superior in many respects. A prototype multimode feed is constructed, and theoretical primary radiation patterns are compared with those obtained experimentally.

CONTENTS

LIST OF PRINCIPAL SYMBOLS

a, b, c, d	waveguide and/or iris dimensions
a'	feed aperture half-width
a_{im}, a'_{in}	coefficients of modes incident on discontinuity
$a_{rm}, a_p, a'_r, a'_{rn}, a_{mn}, b_{mn}$	coefficients of modes travelling away from discontinuity
A_{MN}, B_{MN}	H_{MN} and E_{MN} mode coefficients at mode-converter
A'_{MN}, B'_{MN}	H_{MN} and E_{MN} mode coefficients in feed aperture
b'	waveguide, iris or slot height
B	equivalent discontinuity susceptance
b_{ki}	electric field function coefficient for transverse aperture
c_{ki}	magnetic field function coefficient for transverse aperture
C_{km}, D_{km}	electric field function coefficients for longitudinal aperture
D	main reflector diameter
$\underline{e}_m, \underline{e}'_n, \underline{e}''_q$	transverse (to z) electric field components for normal modes
$\underline{e}'_{tn}, \underline{e}''_{tn}$	transverse (to x) electric field components for transverse modes
$\underline{E}_{Tw/g}$	transverse electric field in waveguide
$\underline{E}_{Tap}$	transverse electric field in aperture
$E_x, E_y, E_{x'}, E_{y'}, E_\theta, E_\phi$	electric field components in specified co-ordinate directions
E'_r, E'_ϕ	secondary aperture field components

$E_{y\Sigma}, E_{y\Delta AZ}, E_{y\Delta EL}$	normally polarized components of monopulse secondary aperture illuminations
E_{km}, F_{km}	magnetic field function coefficients for longitudinal aperture
F	main reflector focal length
G_{Σ}, $G_{\Delta AZ}$, $G_{\Delta EL}$	monopulse gain factors
h	height of waveguide or septum
$\underline{h}_m$, $\underline{h}'_n$, $\underline{h}''_q$	transverse (to z) magnetic field components for normal modes
$\underline{h}'_{tn}$, $\underline{h}''_{tn}$	transverse (to x) magnetic field components for transverse modes
$\underline{H}_{Tw/g}$	transverse magnetic field in waveguide
$\underline{H}_{Tap}$	transverse magnetic field in aperture
H_x, H_y, H_z	magnetic field components in specified co-ordinate directions
$\hat{\underline{i}}_x, \hat{\underline{i}}_y, \hat{\underline{i}}_z, \hat{\underline{i}}_r, \hat{\underline{i}}_\theta, \hat{\underline{i}}_\phi$	unit vectors in specified co-ordinate directions
$J_n(x)$	Bessel function of the first kind
$J'_n(x)$	$= \frac{d}{dx}\left[J_n(x) \right]$
k_o	free space wavenumber
k_z	longitudinal wavenumber
l, l'	length of intermediate waveguide
l	length of feed uniform section
n, n', n'', p, p'	numbers of modes in waveguides
p_n, p_{1n}, p_{2n}	transverse wavenumbers
q, q_k	number of electric or magnetic aperture field functions
r	radial co-ordinate, cylindrical co-ordinate systems
R	radial co-ordinate, spherical co-ordinate system

R	radius of iris aperture or smaller circular waveguide
R'	radius of larger circular waveguide
S, S', S''	waveguide cross-sectional surfaces
S_k	aperture surface
T_A	effective antenna temperature
u_k, v_k	longitudinal aperture edge locations
x, y, z	cartesian co-ordinates
x', y'	cartesian co-ordinates for feed aperture fields
X	$= 2\pi \frac{D}{F} \frac{a'}{\lambda_o}$
Y_L, Y_R, Y_0, Y'_0	equivalent transmission line characteristic admittances
Z	longitudinal distance from horn apex
α	LSE_{12}/H_{10} mode coefficient ratio
α'	LSE_{22}/H_{20} mode coefficient ratio
β_{MN}	H_{MN} or E_{MN} propagation coefficient at discontinuity
β'_{MN}	H_{MN} or E_{MN} propagation coefficient in feed aperture
Γ'_{MN}	$= \beta'_{MN} / k_o$
$\gamma_{mn}, \gamma_n, \gamma'_n, \Gamma_{MN}$	complex propagation coefficients
$\varepsilon_n, \varepsilon'_n$	complex propagation coefficients for E_{1n} circular waveguide modes
δ_{ij}	Kronecker symbol (=1, i=j, =0, i≠j)
ε_{ij}	Kronecker symbol (=1, i=j, =2, i≠j)
ε_o	free space permittivity
$\varepsilon, \varepsilon_1, \varepsilon_2$	relative permittivities
ζ	half-angle of horn flare

η_o	intrinsic impedance of free space
θ	angular co-ordinate
θ_o	half-angle subtended by reflector at focus
Θ	angular co-ordinate, secondary patterns
λ_o	free space wavelength
λ_g	guide wavelength
μ_o	free space permeability
ξ_n	nth root of $J_1(x)$
ρ	radial co-ordinate, primary patterns
ϕ	angular co-ordinate, primary patterns
Φ	angular co-ordinate, secondary patterns
χ_n	nth root of $J_1'(x)$
ω	angular frequency

CHAPTER I

1.1. Introduction

Determining the nature of the electromagnetic fields in the vicinity of a waveguide discontinuity is a classic microwave engineering problem for which many different methods of solution have been suggested during the past thirty years. In a few specific cases, an exact solution can be found, using, for example, the Integral Transform technique [1], but in general this is not possible and some degree of approximation must be made. Of the approximate techniques, the Variational and Integral Equation methods are applicable to a wide range of problems, and can produce sufficiently accurate results for most purposes. The former method is described by Collin [2], whilst the work of Lewin [3] is well-known in connection with the latter. Both methods are reviewed by Marcuvitz [4]. A serious drawback, particularly with the Variational method, is that the formulation for a given structure may call for considerable mathematical ability on the part of the user. A further restriction is that these methods cannot easily be used in the case of a transverse discontinuity involving waveguides capable of supporting more than one propagating mode.

Many of the conventional techniques aim to produce a formula for a given type of discontinuity from which the solution for a particular set of dimensions may be obtained by hand calculation. Fairly gross approximations must often be made to keep such formulae to manageable proportions. At one time this approach was very valuable, but now that access to high-speed digital computers is generally available, there is much to recommend an accurate technique involving lengthy but

straightforward calculations which can easily be applied to a wide variety of structures. It is the purpose of this thesis to describe such a technique, to investigate its accuracy and limitations, and to consider some of its applications.

The method has been known for some time in a restricted form, particularly applicable to junctions involving a conducting step between waveguides of different cross-sections. In this form it seems to have been developed originally by Slinn [5], and has been subsequently described by Clarricoats and Slinn [6], Wexler [7] and Cole [8]. Wexler's term "Modal Analysis" will be used throughout the thesis to refer to the restricted method. In Modal Analysis the fields on either side of the discontinuity plane are expressed initially as infinite series of waveguide modes. The amplitude of each mode is then equated to a Fourier series of the mode amplitudes on the opposite side of the junction. For the modes on one side this follows from the matching of transverse electric fields, whereas for those on the other side magnetic field matching is considered. Two infinite sets of linear equations are thus generated, which, after truncation, are solved simultaneously to give the amplitude coefficients of the various modes. By taking into account multiplereflections of modes between two adjacent step discontinuities, both Slinn and Wexler were able to extend the method to deal with a thick iris, but found that, as the thickness decreased, progressively more modes had to be included in the calculation for an accurate solution. It was therefore found impossible to use the method to solve an infinitely thin iris.

A method similar to Modal Analysis applicable to thin irises has recently been described by the author [9]. Instead of expressing the fields in the iris aperture in terms of waveguide modes, separate series of orthogonal functions are used for the transverse electric and magnetic components. The aperture magnetic field coefficients are easily found from symmetry considerations, and field matching between the waveguide modes and aperture functions leads, as in Modal Analysis, to two sets of linear equations which can be solved simultaneously to give the required modal amplitudes. This again is a special case of the general computational method, and a study of it forms an important part of the work described in this thesis.

The computational method is primarily concerned with discontinuities whose planes are transverse to the direction of wave propagation, but it can be extended to deal with longitudinal discontinuities, in particular to determine the characteristics of waveguides with longitudinal ridges or slots. Although more limited in application, it is more economical as regards computer time and storage than currently used numerical techniques such as the Finite-Difference [10] and Finite-Element [11] methods. A well-known method which has been used to determine the dispersion characteristics of some ridged and slotted waveguides is known as Transverse-Resonance. Here the fields are reformulated in terms of modes travelling in directions normal to the waveguide axis, and if any such mode is above cut-off its fields are represented by voltage and current distributions on an equivalent transmission line. Waveguide walls and longitudinal discontinuities are represented respectively by short-circuits and lumped admittances.

The dispersion characteristics for various modes of the structure can be found from the resonant frequencies of the equivalent network. The use of lumped susceptance elements implies that multiple reflections of evanescent transverse modes are neglected, which is reasonable for a ridge well away from the waveguide walls. If the separation is small, however, such reflections become significant, and the method gives erroneous results. By applying the computational method to the discontinuity this "proximity effect" can be properly taken into account, because there is no restriction on the number of modes incident on the discontinuity which can be considered. Moreover, structures in which more than one transverse mode can propagate are as easy to deal with using the computational method as single-mode cases. Clarricoats and Slinn [6] have mentioned that Modal Analysis can be applied to some longitudinal discontinuities, and have used it to treat a thick-walled circular waveguide with a longitudinal slot [12]. However, by analogy with their solution of transverse discontinuities, cases involving longitudinal structures of zero width could not be dealt with. This difficulty can be overcome by using an extension of the form of the computational method applicable to thin irises.

An important application of waveguide discontinuities is as mode generators in multimode antennas. By combining several waveguide modes in the radiating aperture of a microwave horn it is possible to obtain a radiation pattern which is superior in terms of gain, sidelobe level or pattern symmetry to that of a conventional single-mode horn. One of the earliest examples of a multimode horn is the rectangular box-

horn described by Silver [13], in which the H_{10} and H_{30} modes are combined in such a way as to produce a nearly uniform aperture field distribution, giving a higher gain than if the H_{10} mode alone were used. A more recent example is the "Potter Horn" [14] - a narrow-angle conical horn in whose aperture the H_{11} and E_{11} circular waveguide modes are combined to give similar field distributions in both principal planes. The radiation pattern can be made very nearly circularly symmetric, with a sidelobe level which does not exceed -25dB in any plane. In both these examples the higher-order mode is excited by a step discontinuity between a guide capable of supporting only the dominant mode and one in which the higher mode can also propagate. It is clearly essential in the design of such horns to be able to calculate accurately the relative amplitude and phase with which the two modes are launched. The computational method to be described in the thesis is ideal for this purpose, since there is no difficulty in applying it to an overmoded case.

Multimode antennas such as the Potter Horn are particularly useful as feeds for paraboloidal reflectors, where low spillover and symmetrical illumination are of paramount importance.

Reflector antennas often use the amplitude - comparison monopulse system to track targets automatically. Monopulse antennas have three separate radiation patterns: the "sum" pattern which has symmetry about the principal axis and which is responsible for the transmission and reception of information and two "difference" patterns, which are antisymmetric about the axis and whose purpose is to determine errors in

alignment of antenna and target as measured in two perpendicular planes. The design of feeds for such antennas presents several problems, one of the more serious of which is the difficulty in producing good reflector illumination with both sum and difference primary patterns simultaneously. For example, the commonly used arrangement of a cluster of four rectangular feed horns has a difference pattern primary beamwidth which is considerably greater than its sum beamwidth, so that an antenna designed for optimum sum performance has poor tracking ability because of excessive spillover. Attempts have been made to overcome this difficulty by using feed horns additional to the basic four which are not used for the sum pattern but which effectively widen the radiating feed aperture for the difference patterns and thus reduce the corresponding primary beamwidths. Such arrangements have been suggested by Hannan [15] and Ricardi and Niro [16] . Their drawbacks are that the associated microwave circuitry is quite complex, and that primary sidelobes are excessively high. The radiation patterns of multi-horn feeds can in some cases be improved by the use of multi-moding in the individual horns. A structure of this type has been described by Drabowitch [17] , and consists of a stack of four rectangular box-horns in which modes additional to the dominant mode are excited by means of step discontinuities. The all-round performance of a reflector antenna using such a feed is excellent, but a serious disadvantage is that only linear polarization can be used.

A rather different approach suitable for designing a circularly polarized monopulse feed is to combine several modes in a single

radiating aperture. For the sum pattern, the multimode field distribution is such as to concentrate the energy in the centre of the aperture, whereas the difference distributions take up its entire width. In this way the requirement for similar sum and difference beamwidths can be satisfied. Such a feed has been described by Keeping [18], but as his design technique was empirical and no attempt was made to analyse the step discontinuity used to excite the various modes, its performance probably falls short of the optimum. The object of the research described in the latter part of this thesis is to use the computational technique to solve a step discontinuity for use in a feed broadly similar to that of Keeping, to design such a feed to give optimum secondary characteristics when used with a front-fed paraboloid or in a Cassegrain system, and then to examine any discrepancies between actual and theoretical performance of the feed using an X-band model.

The research on multimode feed design was prompted originally by reports of improvements in the performance of the SCAT four-horn cluster [19] resulting from the addition of a multimode box structure in front of the horn apertures. The modified SCAT feed will therefore be used as a standard of comparison when investigating the performance of the new multimode horn.

1.2. Development of Thesis

Chapter 1 includes a description of the transverse-discontinuity theory as applied to the general case of a junction between two waveguides involving coupling through several apertures in a thin conducting

diaphragm. A special case of this discontinuity, the thin iris in a waveguide, is discussed in Chapter 2. A particular example, the thin inductive iris in rectangular waveguide, is examined in detail, with emphasis on the effect of the mode/aperture-function ratio on the convergence of the solution. A way of choosing this ratio for optimum convergence is suggested by this investigation, and is applied to other examples. Comparison is made with results by other methods, where these are available. The computing aspect of the problem is also considered.

Chapter 3 deals with the special case of the step discontinuity, where the computational method reduces to conventional Modal Analysis. The formulation given differs from that of some other authors, in that it leads to more economical use of computer-time and storage. It is shown that in some cases this formulation can also be derived using a variational approach. Examples treated include multimode cases, the object being to show that the method can be used successfully in multimode antenna design. The effect on convergence of the ratio of numbers of modes taken into account, which seems to have been overlooked by other workers, is also discussed. Matrix equations are derived for double-step discontinuity examples, including rows of posts and thick irises in waveguides.

Chapter 4 is concerned with the application of the computational method to longitudinal discontinuities. Examples of its use in treating homogeneous ridged waveguides are described. A further application is in determining the characteristics of shielded microstrip transmission lines, and a formulation for this problem is given.

To test the ability of the computational method to predict multi-mode antenna characteristics, it is used in Chapter 5 in calculating the radiation patterns and V.S.W.R. of a simple square box-horn, and comparison is made with experimental results.

In Chapter 6, the computational method is used to analyse a five-waveguide step discontinuity for use as a mode-generator in a multi-mode monopulse feedhorn. Secondary characteristics for various step configurations are calculated, allowing a configuration giving best all-round performance to be selected. Other aspects in the design of the feed, such as correct phasing of the various modes, are also considered. Theoretical performance figures are compared with those for a conventional feed. The possibility of improving performance by using a mode-converting throat having two step discontinuities is investigated.

Chapter 7 describes experimental work on the monopulse feed. Primary radiation patterns obtained with an X-band version of the feed are compared with theoretical predictions.

General conclusions on the work described in the thesis, and suggestions for future work, are contained in Chapter 8.

1.3. The General Case of Two Dissimilar Waveguides Coupled by Several Apertures.

The waveguide junction shown in figure 1.1 is a general case of a waveguide discontinuity whose plane is normal to the direction of propagation. There can be any number of coupling apertures, and it is not necessary for the cross-section of one waveguide to be wholly contained

within the cross-section of the other. The waveguides need not be homogeneous: all that is required is that it must be possible to represent the electric and magnetic fields transverse to the direction of propagation as infinite series of orthogonal modes. In the discontinuity plane, let the transverse electric and magnetic field components of the mth.mode in waveguide 1 be $\underline{e}_m, \underline{h}_m$ respectively, and those of the nth.mode in waveguide 2 be $\underline{e}'_n$, $\underline{h}'_n$ respectively.
The following orthogonality properties apply to H and E modes in homogeneous waveguides and also to LSE and LSM modes in dielectric-filled guides:

$$\int_S \underline{e}_i \times \underline{h}_j \cdot d\underline{s} = 0, \quad i \neq j \qquad 1.1$$

$$\int_{S'} \underline{e}'_i \times \underline{h}'_j \cdot d\underline{s} = 0, \quad i \neq j \qquad 1.2$$

In general there can be an incident field in waveguide 1 consisting of an infinitude of modes with coefficients a_{im}, and an incident field in waveguide 2 with mode coefficients a'_{in} . The coefficients are in general complex. The transverse fields in the discontinuity plane can then be written as:

In waveguide 1:

$$\underline{E}_T = \sum_{m=1}^{\infty} (a_{im} + a_{rm}) \underline{e}_m \qquad 1.3(a)$$

$$\underline{H}_T = \sum_{m=1}^{\infty} (a_{im} - a_{rm}) \underline{h}_m \qquad 1.3(b)$$

In waveguide 2:

$$\underline{E}'_T = \sum_{n=1}^{\infty} (a'_{in} + a'_{rn}) \underline{e}'_n \qquad 1.4(a)$$

$$\underline{H}'_T = \sum_{n=1}^{\infty} (a'_{rn} - a'_{in}) \underline{h}'_n \qquad 1.4(b)$$

The coefficients a_{rm}, a'_{rn} refer to modes travelling away from the junction in waveguides 1 and 2 respectively, and it is these that the

method aims to evaluate.

The diaphragm separating the two waveguides is assumed to be infinitely thin and perfectly conducting. It follows from the latter assumption that the transverse electric field in the discontinuity plane vanishes everywhere except in the apertures, and also that the component of this field parallel to the edge of an aperture must vanish at that edge. In order to apply the method to be described in this section, it is necessary to express the transverse electric field in each aperture as a series of vector functions which satisfy the above boundary condition. The transverse electric field components of the normal modes for a homogeneous waveguide having the same cross-section as the aperture form a convenient set for this purpose. Let $\underline{e}_{ki}$ be the ith. such component for the kth. aperture. The electric field in that aperture is then:

$$\underline{E}_{Tk} = \sum_{i=1}^{\infty} b_{ki} \underline{e}_{ki} \qquad 1.5$$

b_{ki} is the complex amplitude coefficient of the ith. component.

It is now necessary to represent the magnetic field in each aperture in a similar manner, and in such a way that the magnetic and electric aperture field functions have the following orthogonality property:

$$\int_{S_k} \underline{e}_{ki} \times \underline{h}_{kj} \cdot d\underline{\varepsilon} = 0, \quad i \neq j \qquad 1.6$$

This will be the case if the functions $\underline{h}_{kj}$ are derived from the same waveguide modes as the functions $\underline{e}_{ki}$.

The transverse magnetic field in the kth. aperture is then:

$$\underline{H}_{Tk} = \sum_{i=1}^{\infty} c_{ki} \underline{h}_{ki} \qquad 1.7$$

where c_{ki} is the complex amplitude coefficient of the ith. component. By using functions derived from waveguide modes to represent the aperture magnetic field, the condition that the component of $\underline{H}_{Tk}$ normal to the aperture edge should vanish there has been applied. In fact this is not the case, since it can be shown that the magnetic field becomes infinite at an aperture edge. However, by taking a large number of functions to represent the aperture field, very high values of field immediately in front of the edge can be achieved, and in the limit where the number of functions becomes infinite, the singularity is accurately represented.

It should be pointed out that although the vector functions $\underline{e}_{ki}$, $\underline{h}_{ki}$ have properties in common with waveguide modes, they do not form a "mode" in the usual sense of the word. Whereas knowledge of the transverse electric field in a waveguide as a series of modes enables the magnetic field to be calculated using the wave admittances, a series representation for an aperture electric field such as 1.5 gives no information about the magnetic field in that aperture. In a waveguide, longitudinal electric field must vanish at the edge of the cross-section, but this does not hold for an aperture in an infinitely thin conducting sheet. A much wider variety of solutions to Maxwell's equations is therefore possible in the latter case.

The transverse electric and magnetic fields must be continuous across each aperture. Thus, for the kth. aperture,

$$\underline{E}_{Tk} = \sum_{m=1}^{\infty} (a_{im}+a_{rm})\underline{e}_m = \sum_{i=1}^{\infty} b_{ki}\underline{e}_{ki} \qquad 1.8$$

$$= \sum_{n=1}^{\infty} (a'_{in}+a'_{rn})\underline{e}'_n$$

$$\underline{H}_{Tk} = \sum_{m=1}^{\infty} (a_{im}-a_{rm})\underline{h}_m = \sum_{i=1}^{\infty} c_{ki}\underline{h}_{ki}$$

$$= \sum_{n=1}^{\infty} (a'_{rn}-a'_{in})\underline{h}'_n \qquad 1.9$$

Note that 1.8 and 1.9 only hold over the aperture in question. By forming vector products with $\underline{h}_M, \underline{h}'_N$ where M and N can be any positive integers, and integrating over aperture k, 1.8 gives rise to two infinite sets of equations:

$$\sum_{m=1}^{\infty} (a_{im}+a_{rm}) \int_{S_k} \underline{e}_m \times \underline{h}_M \cdot d\underline{s} = \sum_{i=1}^{\infty} b_{ki} \int_{S_k} \underline{e}_{ki} \times \underline{h}_M \cdot d\underline{s} \qquad 1.10$$

$M=1,2,3\ldots\infty$

$$\sum_{n=1}^{\infty} (a'_{in}+a'_{rn}) \int_{S_k} \underline{e}'_n \times \underline{h}'_N \cdot d\underline{s} = \sum_{i=1}^{\infty} b_{ki} \int_{S_k} \underline{e}_{ki} \times \underline{h}'_N \cdot d\underline{s} \qquad 1.11$$

$N=1,2,3\ldots\infty$

Adding together equations of the form 1.10 for all apertures gives:

$$\sum_{m=1}^{\infty} (a_{im}+a_{rm}) \int_{\sum_{k=1}^{N_{ap}} S_k} \underline{e}_m \times \underline{h}_M \cdot d\underline{s} = \sum_{k=1}^{N_{ap}} \sum_{i=1}^{\infty} b_{ki} \int_{S_k} \underline{e}_{ki} \times \underline{h}_M \cdot d\underline{s} \qquad 1.12$$

$M=1,2,3\ldots\infty$

N_{ap} is the total number of apertures. The condition that transverse electric field should vanish over the diaphragm can be expressed as:

$$\sum_{m=1}^{\infty} (a_{im}+a_{rm})\underline{e}_m = 0,$$

over the surface $S_o = S - \sum_{k=1}^{N_{ap}} S_k$

This implies that:

$$\sum_{m=1}^{\infty} (a_{im}+a_{rm}) \int_{S_o} \underline{e}_m \times \underline{h}_M \cdot d\underline{s} = 0 \qquad 1.13$$

for any M. When 1.13 is added to the left-hand side of 1.12, the integral is extended over the whole cross-section S of waveguide 1. Orthogonality condition 1.1 can now be applied, and 1.12 becomes:

$$a_{iM}+a_{rM} = \left[\sum_{k=1}^{N_{ap}}\sum_{i=1}^{\infty} b_{ki}\int_{S_k}\underline{e}_{ki}\times\underline{h}_M\cdot d\underline{s}\right] \Big/ \left[\int_S \underline{e}_M\times\underline{h}_M\cdot d\underline{s}\right] \qquad 1.14$$

$$M=1,2,3\ldots\infty$$

Similarly, from 1.11, using orthogonality property 1.2:

$$a'_{iN}+a'_{rN} = \left[\sum_{k=1}^{N_{ap}}\sum_{i=1}^{\infty} b_{ki}\int_{S_k}\underline{e}_{ki}\times\underline{h}'_N\cdot d\underline{s}\right] \Big/ \left[\int_{S'} \underline{e}'_N\times\underline{h}'_N\cdot d\underline{s}\right] \qquad 1.15$$

$$N=1,2,3\ldots\infty$$

By vector pre-multiplying each term in 1.9 by $\underline{e}_{kI}$, where I is any positive integer, and integrating over aperture k, two further sets of equations result:

$$\sum_{m=1}^{\infty}(a_{im}-a_{rm})\int_{S_k}\underline{e}_{kI}\times\underline{h}_m\cdot d\underline{s} = \sum_{i=1}^{\infty} c_{ki}\int_{S_k}\underline{e}_{kI}\times\underline{h}_{ki}\cdot d\underline{s} \qquad 1.16$$

$$I=1,2,3\ldots\infty$$

$$\sum_{n=1}^{\infty}(a'_{rn}-a'_{in})\int_{S_k}\underline{e}_{kI}\times\underline{h}'_n\cdot d\underline{s} = \sum_{i=1}^{\infty} c_{ki}\int_{S_k}\underline{e}_{kI}\times\underline{h}_{ki}\cdot d\underline{s} \qquad 1.17$$

$$I=1,2,3\ldots\infty$$

Orthogonality condition 1.6 may be applied directly to equations 1.16 and 1.17, which then become:

$$c_{kI} = \left[\sum_{m=1}^{\infty}(a_{im}-a_{rm})\int_{S_k}\underline{e}_{kI}\times\underline{h}_m\cdot d\underline{s}\right] \Big/ \left[\int_{S_k}\underline{e}_{kI}\times\underline{h}_{kI}\cdot d\underline{s}\right] \qquad 1.18$$

$$c_{kI} = \left[\sum_{n=1}^{\infty}(a'_{rn}-a'_{in})\int_{S_k}\underline{e}_{kI}\times\underline{h}'_n\cdot d\underline{s}\right] \Big/ \left[\int_{S_k}\underline{e}_{kI}\times\underline{h}_{kI}\cdot d\underline{s}\right] \qquad 1.19$$

$$I=1,2,3\ldots\infty$$

$$k=1,2,3\ldots N_{ap}$$

In order to solve equations 1.14, 1.15, 1.18 and 1.19 for the unknown modal amplitudes a_{rm}, a'_{rn}, it is first necessary to truncate the infinite series involved so that the equations can be conveniently handled by a computer. If the numbers of modes taken into account in waveguides 1 and 2 are p,p' respectively, and the number of functions taken into account in aperture k is q_k, then $m \leqslant p, M \leqslant p, n \leqslant p', N \leqslant p'$ and, for aperture k, $i < q_k$ and $I \leqslant q_k$. It is then possible to write 1.14 as a matrix equation:

$$\begin{Bmatrix} a_{i1} \\ \vdots \\ a_{ip} \end{Bmatrix} + \begin{Bmatrix} a_{r1} \\ \vdots \\ a_{rp} \end{Bmatrix} = \left[\begin{array}{ccc|c|ccc} R_1(1,1) & \cdots & R_1(1,q_1) & & R_{N_{ap}}(1,1) & \cdots & R_{N_{ap}}(1,q_{N_{ap}}) \\ \vdots & & \vdots & \cdots & \vdots & & \vdots \\ R_1(p,1) & \cdots & R_1(p,q_1) & & R_{N_{ap}}(p,1) & \cdots & R_{N_{ap}}(p,q_{N_{ap}}) \end{array}\right] \left\{\begin{array}{c} b_{11} \\ \vdots \\ b_{1q_1} \\ \hline \vdots \\ b_{N_{ap}1} \\ \vdots \\ b_{N_{ap}q_{N_{ap}}} \end{array}\right\} \qquad 1.20$$

In this equation

$$R_k(i,j) = \int_{S_k} \underline{e}_{kj} \times \underline{h}_i \cdot d\underline{s} \Big/ \int_S \underline{e}_i \times \underline{h}_i \cdot d\underline{s} \qquad 1.21$$

For convenience, 1.20 will be written as:

$$\{a_i\} + \{a_r\} = [R]\{b\} \qquad 1.22$$

If q_T is defined as $\sum_{k=1}^{N_{ap}} q_k$, then $[R]$ has dimensions p x q_T and $\{b\}$ has q_T elements.

The following matrix equation results from 1.15:

$$\{a'_i\} + \{a'_r\} = [R']\{b\} \qquad 1.23$$

The column vectors $\{a'_i\}$, $\{a'_r\}$ have p' elements, and $[R']$ has dimensions p' x q_T. The elements of $[R']$ are defined in a similar manner

to those of $[R]$, i.e.:

$$R'_k(i,j) = \int_{S_k} \underline{e}_{kj} \times \underline{h}'_i \cdot d\underline{s} \Big/ \int_{S'} \underline{e}'_i \times \underline{h}'_i \cdot d\underline{s} \qquad 1.24$$

The N_{ap} sets of equations represented by 1.18 can be lumped together to give a single matrix equation:

$$\begin{Bmatrix} c_{11} \\ \vdots \\ c_{1q_1} \\ \hline \vdots \\ \hline c_{N_{ap}1} \\ \vdots \\ c_{N_{ap}q_{N_{ap}}} \end{Bmatrix} = \begin{bmatrix} S_1(1,1) & \cdots & S_1(1,p) \\ \vdots & & \vdots \\ S_1(q_1,1) & \cdots & S_1(q_1,p) \\ \hline & \vdots & \\ \hline S_{N_{ap}}(1,1) & \cdots & S_{N_{ap}}(1,p) \\ \vdots & & \vdots \\ S_{N_{ap}}(q_{N_{ap}},1) & \cdots & S_{N_{ap}}(q_{N_{ap}},p) \end{bmatrix} \begin{Bmatrix} a_{il} - a_{rl} \\ \vdots \\ a_{ip} - a_{rp} \end{Bmatrix} \qquad 1.25$$

In this equation:

$$S_k(i,j) = \int_{S_k} \underline{e}_{ki} \times \underline{h}_j \cdot d\underline{s} \Big/ \int_{S_k} \underline{e}_{ki} \times \underline{h}_{ki} \cdot d\underline{s} \qquad 1.26$$

Writing 1.25 in a more convenient form:

$$\{c\} = [S]\{a_i\} - [S]\{a_r\} \qquad 1.27$$

where $\{c\}$ has q_T elements, and $[S]$ has dimensions q_T x p. Similarly, from 1.19:

$$\{c\} = [S']\{a'_r\} - [S']\{a'_i\} \qquad 1.28$$

where the q_T x p' matrix $[S']$ has elements of the form

$$S'_k(i,j) = \int_{S_k} \underline{e}_{ki} \times \underline{h}'_j \cdot d\underline{s} \Big/ \int_{S_k} \underline{e}_{ki} \times \underline{h}_{ki} \cdot d\underline{s} \qquad 1.29$$

By multiplying 1.22 through by $[S]$, $\{a_r\}$ can be eliminated from 1.27,

to give:

$$\{c\} = 2[S]\{a_i\} - [S][R]\{b\} \qquad 1.30$$

Similarly, eliminating $\{a'_r\}$ from 1.23 and 1.28:

$$\{c\} = [S'][R']\{b\} - 2[S']\{a'_i\} \qquad 1.31$$

Equating 1.30 and 1.31

$$[[S][R] + [S'][R']]\{b\} = 2[S]\{a_i\} + 2[S']\{a'_i\} \qquad 1.32$$

The column vectors $\{a_i\}$ and $\{a'_i\}$ are known, so 1.32 represents a set of q_T simultaneous equations in q_T unknowns b_{ki}. Having solved these equations, the values for the elements of $\{b\}$ can be substituted in equations 1.22 and 1.23 to give the required modal amplitude vectors $\{a_r\}$ and $\{a'_r\}$.

Figure 1.2 shows the variation with q, the number of aperture functions, of the transmission-line equivalent circuit parameters for an H-plane junction between two rectangular waveguides with a thin single-aperture inductive iris in the discontinuity plane, for various values of p/p'. The equivalent circuit relates to the H_{10} mode, which, for the dimensions in question (see inset), is the only propagating mode in either guide since the structure has symmetry about the plane x=0. Details of the calculation will not be given here: the purpose of this example is merely to illustrate the way in which the choice of the ratios of modes and aperture functions affects the solution of discontinuity problems. It is clear that for a given ratio p/p', even small changes in q can cause very large variations in the equivalent shunt susceptance, so that in order for the method to be of practical value some criteria for choosing the ratios must be

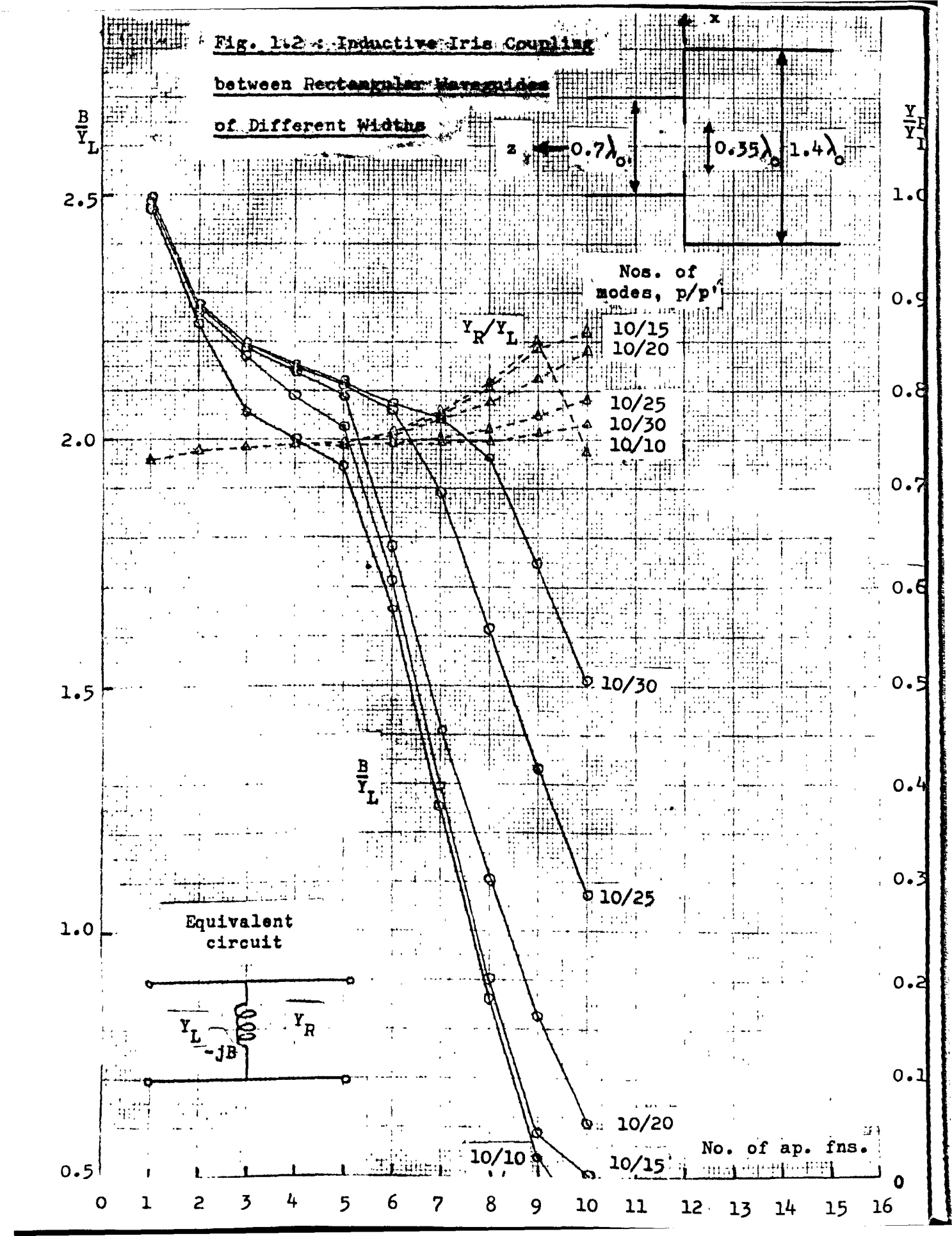
Fig. 1.2 : Inductive Iris Coupling between Rectangular Waveguides of Different Widths
x
z
0.7λo
0.35λo
1.4λo
B/YL
YR/YL
Nos. of modes, p/p'
10/15
10/20
10/25
10/30
10/10
Equivalent circuit
YL
-jB
YR
No. of ap. fns.
2.5
2.0
1.5
1.0
0.5
1.0
0.9
0.8
0.7
0.6
0.5
0.4
0.3
0.2
0.1
0
0 1 2 3 4 5 6 7 8 9 10 11 12 13 14 15 16

determined. This problem will be approached by considering, in the following two chapters, two simpler structures in which only one ratio is involved, namely a thin iris in a waveguide and a step discontinuity in which the smaller guide's cross-section is entirely contained within that of the larger at the discontinuity plane.

CHAPTER II THE SPECIAL CASE OF A THIN IRIS IN A WAVEGUIDE

2.1. Theory.

A particular case of the general discontinuity described in Chapter 1, and one which has important applications in the design of matching devices for microwave circuitry, is that of a thin, conducting iris in a waveguide, transverse to the direction of wave propagation. Here again there can be any number of apertures, but in this case the waveguides on either side of the discontinuity have identical properties, and there is no step between them. Thus the matrices $[R]$ and $[R']$ in the general analysis become identical, as do $[S]$ and $[S']$. It has, of course, been necessary to put $p=p'$. Equation 1.32 therefore becomes:

$$[S][R]\{b\} = [S]\{a_i\} + [S]\{a'_i\} \qquad 2.1$$

In the more usual case where incidence is from one side only, one of the terms on the right-hand side of 2.1 vanishes. The above result can then be arrived at by a slightly different argument, and one which throws some light on the problem of choosing the ratios of numbers of modes and aperture functions. If incidence is from the left-hand side only, the transverse electric field in the discontinuity plane is:

$$\underline{E}_T = \sum_{m=1}^{\infty} (a_{im} + a_{rm})\underline{e}_m = \sum_{n=1}^{\infty} a'_{rn}\underline{e}_n \qquad 2.2$$

The equality holds for the entire cross-section of the guide, because $\underline{E}_T$ is zero except in the apertures. Thus the relationship

$$a_{im} + a_{rm} = a'_{rm} \qquad 2.3$$

must hold for all m. Matching the magnetic fields in one of the apertures gives

$$\underline{H}_T = \sum_{m=1}^{\infty} (a_{im} - a_{rm})\underline{h}_m = \sum_{n=1}^{\infty} a'_{rn}\underline{h}_n \qquad 2.4$$

By substituting 2.3 in 2.4 it is found that $\sum_{m=1}^{\infty} a_{rm}\underline{h}_m = 0$, which leads to the result that

$$\underline{H}_T = \sum_{m=1}^{\infty} a_{im}\underline{h}_m \qquad 2.5$$

The outcome of this argument may be stated in the following way: In any aperture, the transverse magnetic field is that of the incident field alone. By using series representations for the magnetic fields in the various apertures, and matching these fields to the incident field, the following matrix equation can be obtained:

$$\{c\} = [S]\{a_i\} \qquad 2.6$$

$\{a_i\}$ is known, so the elements of $\{c\}$ can be found. When this result is substituted in 1.27, it is found that:

$$[S]\{a_r\} = 0 \qquad 2.7$$

It might at first be thought that this set of equations could be solved to give the unknown coefficients a_{rm}. However, a unique solution is only possible if there are at least as many linearly independent equations as there are unknowns, and it is clear that if this is the case the solution will be $a_{rm}=0$ for all m, which implies that no iris is present. In order to obtain the correct solution the problem must be under-specified in 2.7, in which case $q_T<p$. Equation 1.22 can then be used to impose the condition for electric field matching

on the solution. If this equation is multiplied through by $[S]$, 2.7 can be used to eliminate $\{a_r\}$, the resulting equation being 2.1.

It is not sufficient merely to set $q_T < p$ in order to obtain optimum convergence; the ratios q_k/p are critical and their values depend on the dimensions of the structure in question. So as to illustrate this point and to demonstrate the use of the method a particular case will now be considered, namely that of a thin single-aperture inductive iris in a rectangular waveguide.

2.2. The Thin Inductive Iris in Rectangular Waveguide.

2.2.1. Formulation of Problem.

This case is shown in figure 2.1(a). If the dimensions are chosen so that only the dominant H_{10} mode can propagate in the waveguide, the discontinuity can be represented by the simple equivalent circuit of figure 2.1(b). Y_0 is the characteristic admittance of the equivalent transmission line for the H_{10} mode, and the discontinuity is represented by a shunt inductive susceptance $-jB$ across the line. This susceptance is a consequence of magnetic energy storage by evanescent modes excited at the discontinuity. The incident field is assumed to consist only of the dominant mode, and this can be taken to have unit amplitude without loss of generality. Thus:

$$a_{im} = 1, \quad m=1 \qquad 2.8$$

$$a_{im} = 0, \quad m \neq 1$$

The susceptance of the iris can be deduced from the complex reflection coefficient a_{r1} from the expression:

$$\frac{1-a_{r1}}{1+a_{r1}} = 1 + j\frac{B}{Y_0} \qquad 2.9$$

Fig. 2.1(a) : Thin Inductive Iris in Rectangular Waveguide

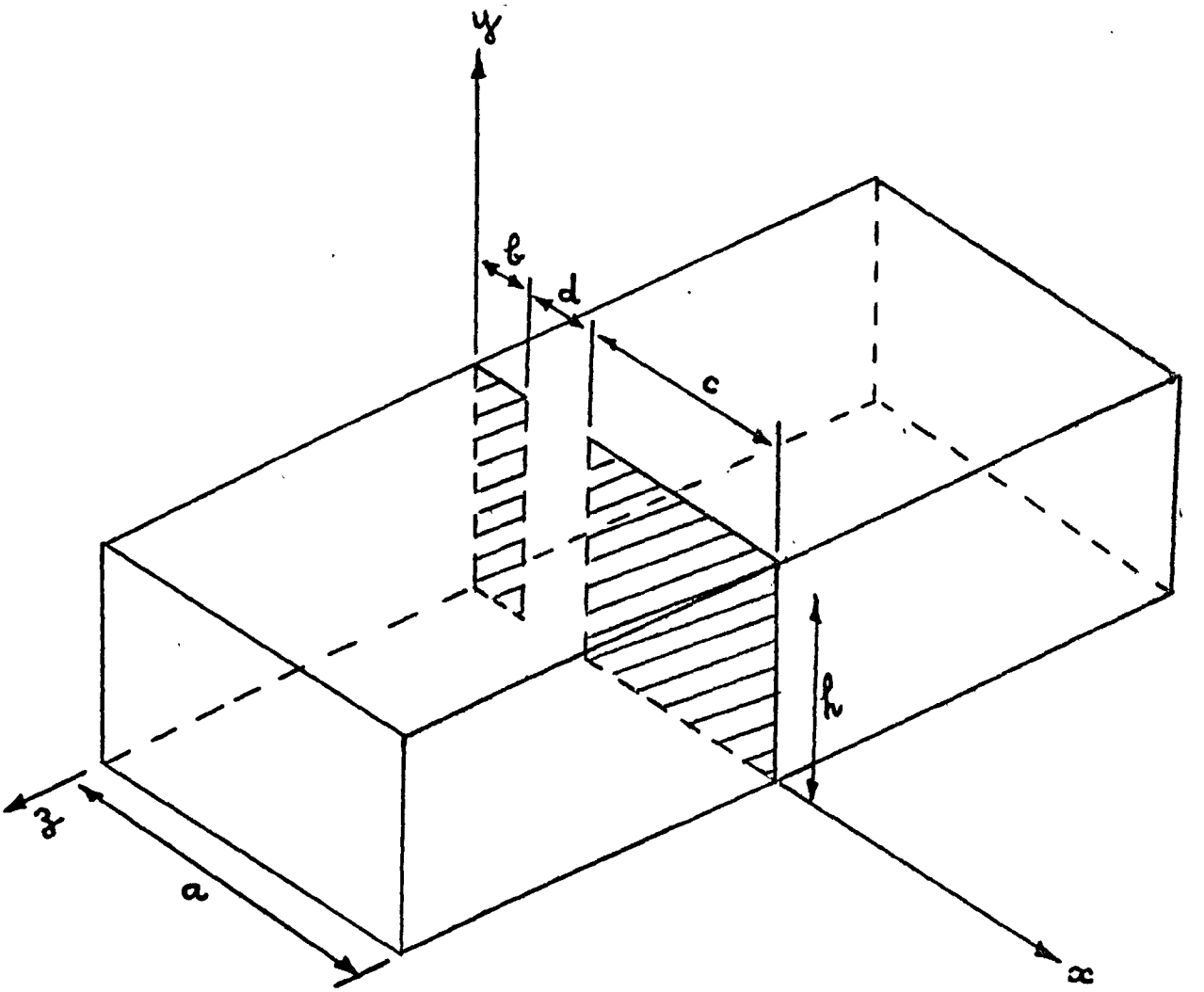

Fig. 2.1(b) : Transmission Line Equivalent Circuit

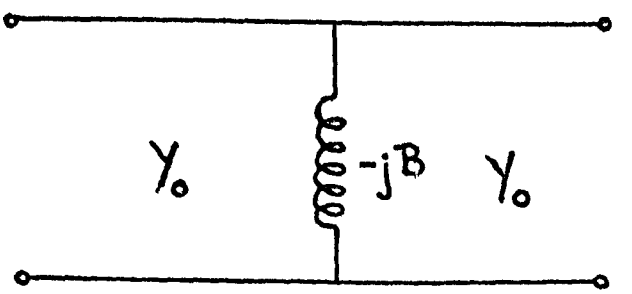

Both the discontinuity and the incident field are uniform in the y - direction: it follows that modes excited by the discontinuity must also have this uniformity, and are therefore of type H_{nO} , where n can be any positive integer. Notice, however, that if b=c only modes for which n is odd will be excited, because of the symmetry of the structure.

The derivation of expressions for the field components of modes in a rectangular waveguide is given in many standard textbooks, and so it is sufficient merely to state expressions for the transverse fields of the H_{nO} mode in the plane z=0:

$$\underline{e}_n = \sin \frac{n\pi x}{a} \hat{\underline{i}}_y \qquad 2.10(a$$

$$\underline{h}_n = j\sqrt{\frac{\varepsilon_o}{\mu_o}}\bar{\gamma}_n \sin \frac{n\pi x}{a} \hat{\underline{i}}_x \qquad 2.10(b$$

where $$\bar{\gamma}_n = \sqrt{\frac{n^2}{4(a/\lambda_o)^2} - 1}$$

Suitable expressions for the aperture field components are:

$$\underline{e}_{1m} = \sin \frac{m\pi}{a-b-c} (x-b) \hat{\underline{i}}_y \qquad 2.11(a$$

$$\underline{h}_{1m} = \sin \frac{m\pi}{a-b-c} (x-b) \hat{\underline{i}}_x \qquad 2.11(b$$

When the electric field expressions are substituted into 1.21, it is found that:

$$R_{nm} = \frac{2}{a} \int_b^{a-c} \sin \frac{n\pi x}{a} \sin \frac{m\pi}{a-b-c} (x-b)\, dx \qquad 2.12$$

Using 1.26, the elements of $[S]$ are found to be related to those of $[R]$ through the equation:

$$S_{mn} = j \frac{a}{a-b-c}\sqrt{\frac{\varepsilon_o}{\mu_o}}\,\gamma_n R_{nm} \qquad 2.13$$

It is possible to drop the constant multiplier $j \frac{a}{a-b-c}\sqrt{\frac{\varepsilon_o}{\mu_o}}$ from the above equation, in which case it becomes incorporated in the vector $\{c\}$, which does not need to be evaluated. 2.13 then becomes:

$$S_{mn} = \gamma_n R_{nm} \qquad 2.13(a$$

The evaluation of the integral in 2.12 is straight-forward, and leads to the result:

$$R_{nm} = \frac{2m}{\pi}\frac{a-b-c}{a}\,\frac{\sin n\pi\frac{b}{a} - (-1)^m \sin n\pi\frac{a-c}{a}}{m^2 - \left[\frac{a-b-c}{a}\right]^2 n^2}, \qquad am\neq(a-b-c)n \qquad 2.14(a)$$

$$R_{nm} = \frac{a-b-c}{a}\cos\frac{n\pi b}{a}, \qquad am=(a-b-c)n. \qquad 2.14(b)$$

The flow diagram shown in figure 2.2 illustrates the way in which results can be obtained for this case using a digital computer. The basic operation is the solution of the matrix equation obtained by substituting 2.8 into 2.1, i.e.

$$[S][R]\{b\} = \{S_1\} \qquad 2.15$$

where $\{S_1\}$ is the first column of $[S]$.

A difficulty arises in that the elements of $\{b\}$ are complex, and

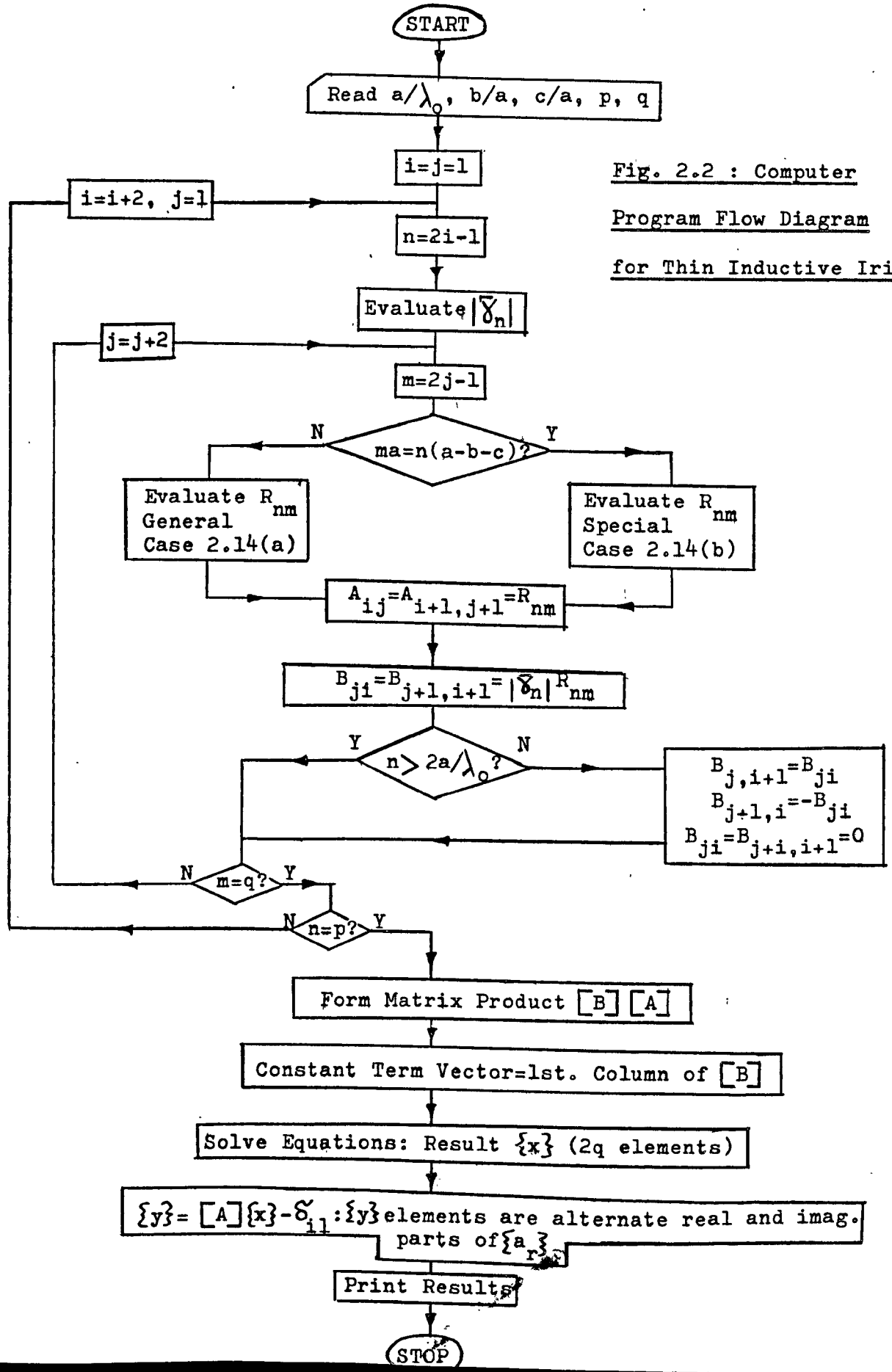

Fig. 2.2 : Computer Program Flow Diagram for Thin Inductive Iris

those of $[S]$ are imaginary if the suffix m in 2.13(a) refers to a propagating waveguide mode. Since the computer used (KDF9) cannot deal directly with complex numbers, each equation in the set represented by 2.15 must be separated into its real and imaginary parts, yielding a set of 2q equations in 2q real unknowns, which form the vector $\{x\}$ in figure 2.2. The matrices $[R]$ and $[S]$ are replaced by $[A]$ and $[B]$ respectively, where $[A]$ has dimensions 2p x 2q and $[B]$ has dimensions 2q x 2p. The elements of $[R]$ are real, and consequently values are assigned only to alternate elements of $[A]$. Values are assigned to the elements of $[B]$ simultaneously with those of $[A]$, to avoid unnecessary duplication of calculations. When an element of $[S]$ is evaluated, it is initially assumed real, and its value is copied to the two appropriate elements of $[B]$. A test is then made to see if the corresponding waveguide mode is above cut-off, and if this is so the values just assigned to $[B]$ are transfered to new locations, in one case with a sign change. The exact manner in which these operations are carried out can be seen in the flow diagram. The simultaneous equations were solved in practice by the method of elimination and back-substitution, although an iterative method could be used as an alternative, possibly with some saving of computing time. However, by writing the appropriate subroutine, and also that for matrix multiplication, in "Usercode", a low-level programming language suitable for use with the KDF9 computer, it was found possible for example to obtain a solution for the case p=30, q=15 in about 16 seconds, and further attempts to reduce computing time were thought unnecessary. Moreover, the use

of an iterative method would introduce small errors into the solution which would complicate an investigation of the convergence properties of this type of analysis.

2.2.2. Computed Results for the Thin Inductive Iris.

The first investigation which was carried out using the computer program described above was concerned with the dependence of the solution for a particular iris configuration on the number of functions taken into account in the iris aperture, the number of waveguide modes being held constant. As indicated in the previous section, the choice of q/p can be expected to have a considerable effect on the computed results. The configuration chosen for investigation has an aperture width equal to one half of the waveguide width a, which is such that $a=0.8\lambda_c$. Note that for single-mode propagation $\lambda_0/2<a<\lambda_0$. In figure 2.3, results are given for three positions of the iris aperture; the symmetric case b=c (see fig. 2.1 for definition of dimensions), the case b=0 in which the waveguide wall forms one edge of the aperture, and an intermediate case b=0.1a. These cases are designated (A), (B) and (C) respectively. Twenty waveguide modes were taken into account, and in case (A) these were such that n was odd in expressions 2.10. Because of symmetry, the even modes cannot be excited, and a step was included in the program to exclude them from the calculation in this case, and thus economise on time and storage.

In cases (A) and (B) there is uniform convergence of the values of normalized susceptance, calculated from 2.9, for q increasing from

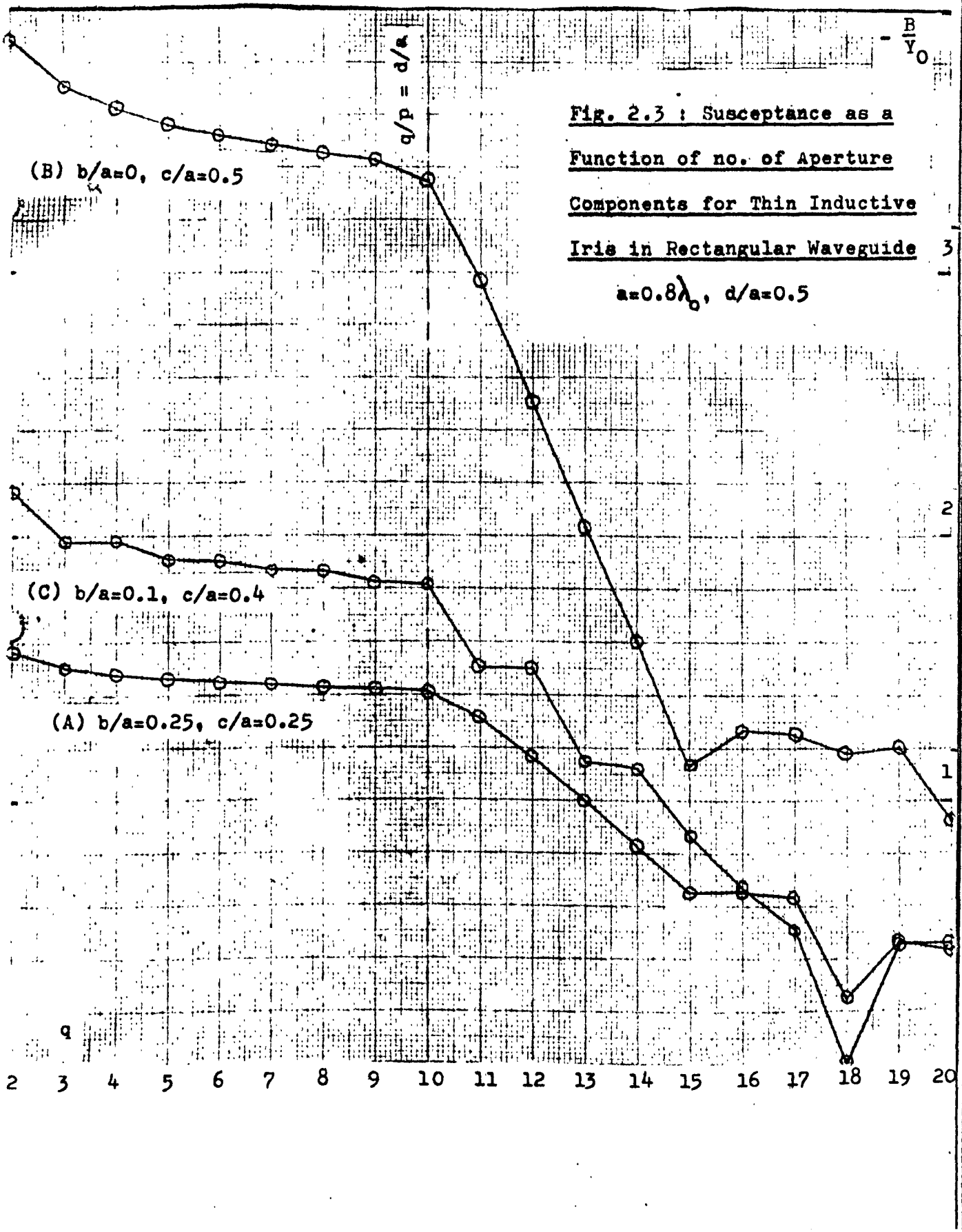

Fig. 2.3 : Susceptance as a Function of no. of Aperture Components for Thin Inductive Iris in Rectangular Waveguide

$a=0.8\lambda_0$, d/a=0.5

2 to 9. Between q=9 and q=10 the slopes increase slightly, and for q greater than 10 the value of $|B/Y_0|$ falls away rapidly, at first almost linearly, but with erratic behaviour as the situation q=p is approached. In the previous section, consideration of equation 2.7 showed that a_{r1}, and consequently B/Y_0, should be zero when p and q are equal, but this is not borne out by the results in figure 2.3. However, solutions obtained using fewer waveguide modes have behaved in the expected manner, and it seems likely that the irregular variations when q lies between 15 and 20 are the result of computational errors associated with the generation of very large numbers, and therefore have no real significance. The variation with q of the susceptance in case (C) follows the same general pattern as in the other two cases, but is not as regular. This is because additional aperture functions taken into account have alternate odd and even dependence. The odd functions are more strongly excited, and therefore have a greater effect on the calculated susceptance value.
A feature that the three graphs have in common is the abrupt change in slope at the point q/p=d/a. Results have been obtained for other aperture widths, and in every case a distinct change of slope occurs at this point. The phenomenon is not restricted to the inductive iris, as will be seen when other cases are dealt with later in this chapter. The reason for the change of slope can be explained as follows: The amplitudes of the aperture magnetic field functions are obtained from the theoretical aperture magnetic field (that of the incident waveguide mode) by Fourier analysis (equation 2.6) and are thus fixed before the main body of the program is entered. Each of

these field functions is matched across the aperture by a series of waveguide modes. If the highest-order aperture function has a field variation sin $\frac{m\pi}{d}$ (x-b) across the aperture, the predominant term in the mode series will be that for which n=ma/d, since this has the same order of field variation across the aperture. If the series of modes is truncated before this term is reached, as is the case when $q/p > d/a$, magnetic field matching for this function will therefore be poor. Similarly the highest order electric field function cannot be correctly matched to the waveguide field, and has been found to acquire an excessively large amplitude. The more q/p exceeds d/a, the greater the number of badly matched aperture functions, and the less accurate does the solution become. A similar effect occurs when there are insufficient aperture functions for good field matching of the highest-order waveguide modes, i.e. when $q/p < d/a$, but this is not as serious because the excessively high order modes' amplitudes are determined by the calculations rather than by being fixed beforehand, as was the case with the aperture magnetic field functions. These tend to be small and thus the excess modes have a comparatively minor effect on the solution. The change of slope, or "breakpoint", represents the transition from the above situation to one in which the highest order aperture functions are incorrectly matched. The value of susceptance at this point can be taken to be the most accurate, since field matching is good for all modes and aperture functions.

It does not always happen that the ratio of aperture width to waveguide width can be expressed as a ratio of integers, and in this

case it is not possible to selectp and q to give a solution at the "breakpoint". It can be seen from fig. 2.3 that if q/p is slightly less than d/a, the error is much smaller than if q/p were greater by the same amount, for the reasons explained above. Thus if q/p is chosen to be as near d/a as possible without exceeding it, the best solution will generally be obtained, and results indicate that the error caused by this discrepancy is unlikely to be serious unless p and q are very small.

Having determined the optimum value of q/p for a particular configuration, it is interesting to investigate the convergence of the solution as q and p increase with this ratio held constant, at the same time comparing the results with an accepted value of known accuracy. Formulae are given in the "Waveguide Handbook" [4] from which normalized susceptance values can be found for the symmetric case b=c, and for the single-obstacle case b=0. These are derived by the "equivalent static" method, which is essentially different from the one used here and therefore suitable for comparison purposes. The formulae are stated to be in error by less than 1% in the former case, and by about one per cent in the latter, for the range $\lambda_o/2 < a < \lambda_o$. Results for both the above cases are given in table 2.1, the dimensions having been chosen such that $a=0.8\lambda_o$ and $d=0.667a$. p and q are taken in the ratio 3:2, which corresponds to the condition for optimum field matching derived above. There is uniform convergence in both cases, and this has enabled Aitken's δ^2 process to be used to estimate the final values as p and q tend to infinity. The percentage

p	q	b=c	Error (%)	b=0	Error (%)
6	4	0.48382	1.13	0.83586	2.92
12	8	0.48060	0.45	0.85289	0.95
18	12	0.47958	0.24	0.85708	0.46
24	16	0.47911	0.14	0.85881	0.26
30	20	0.47885	0.09	0.85971	0.16
36	24	0.47869	0.05	0.86025	0.09

Extrapolated Converged Value	0.47843	0.86106
From "Waveguide Handbook" Formula	0.4782	0.8485

Table 2.1 : Convergence of Normalised Susceptance Values for Thin Inductive Iris in Rectangular W/G

$a = 0.8\lambda_o$, $d = 0.667a$

p	q	b=c	Error (%)	b=0	Error (%)
6	4	0.48382	1.13	0.83586	2.92
12	8	0.48060	0.45	0.85289	0.95
18	12	0.47958	0.24	0.85708	0.46
24	16	0.47911	0.14	0.85881	0.26
30	20	0.47885	0.09	0.85971	0.16
36	24	0.47869	0.05	0.86025	0.09

Extrapolated Converged Value	0.47843	0.86106
From "Waveguide Handbook" Formula	0.4782	0.8485

Table 2.1 : Convergence of Normalised Susceptance Values for Thin Inductive Iris in Rectangular W/G

$a = 0.8\,\lambda_o$, $d = 0.667a$

error caused by truncating the series of modes and aperture functions could therefore be found, and this is given in the table for each value of p. It is clear that p need not be very large in order to give an accurate solution: an error of 1% is generally acceptable, and this is not exceeded in either case when p=12. In fact the error when p=6 in the symmetric case is only slightly greater than this. The accuracy for a given value of p is greater in the case b=c than in the case b=0, because only odd modes and aperture functions are considered, so the order of approximation to the true fields is double that in the asymmetric case. Notice that in the symmetric case the result for any value of p is an upper bound to the solution, whereas in the asymmetric case it is a lower bound. It seems that the only way to determine the sense in which convergence occurs is to find results for various values of p.

The agreement between the estimated converged value and the result derived from the "Waveguide Handbook" formula for the symmetric case is excellent, the discrepancy being less than 0.1%. For the asymmetric case, the solutions agree to within 1.5%, a sufficiently small discrepancy to confirm the correctness of the method, bearing in mind the tolerance quoted for the standard value.

With the object of verifying that the theoretically-predicted characteristics of the fields in the vicinity of the iris are well represented when $q/p = d/a$, it was decided to examine the form of the field distributions in the aperture and in the waveguide, as calculated from the complex amplitude coefficients generated by the program.

Of particular importance are the variations of the distributions as p and q increase, the degree of accuracy with which the aperture and waveguide fields match one another, and the degree of accuracy with which they match the theoretical distributions, when these are known.

Figures 2.4(a) and 2.4(b) show respectively the electric and magnetic field distributions in the discontinuity plane, for an iris with an aperture of width d=0.5a, offset from centre, whose dimensions correspond to case (C) in figure 2.3. In the case of the electric field there is no need to show both real and imaginary parts, since the components of the aperture and waveguide fields are all excited with the same phase, and so the parts are identical except in amplitude. Theory predicts that the electric field should vanish over the iris, and that the imaginary part of the magnetic field should vanish in the aperture, because the aperture magnetic field is just that of the incident mode, and therefore purely real. It can be seen from figure 2.4 that in both cases the field oscillates about zero, the amplitude of oscillation increasing towards the aperture edges. Also, the magnetic field should theoretically become infinite at the edges. This does not happen when a finite number of modes is considered, but the field does become large at the edges compared with the field elsewhere. The aperture magnetic field shown in figure 2.4(b), is the approximation to the theoretical distribution - a truncated sinusoid - given by a Fourier series of the aperture functions, in this case containing fifteen terms. Here again the

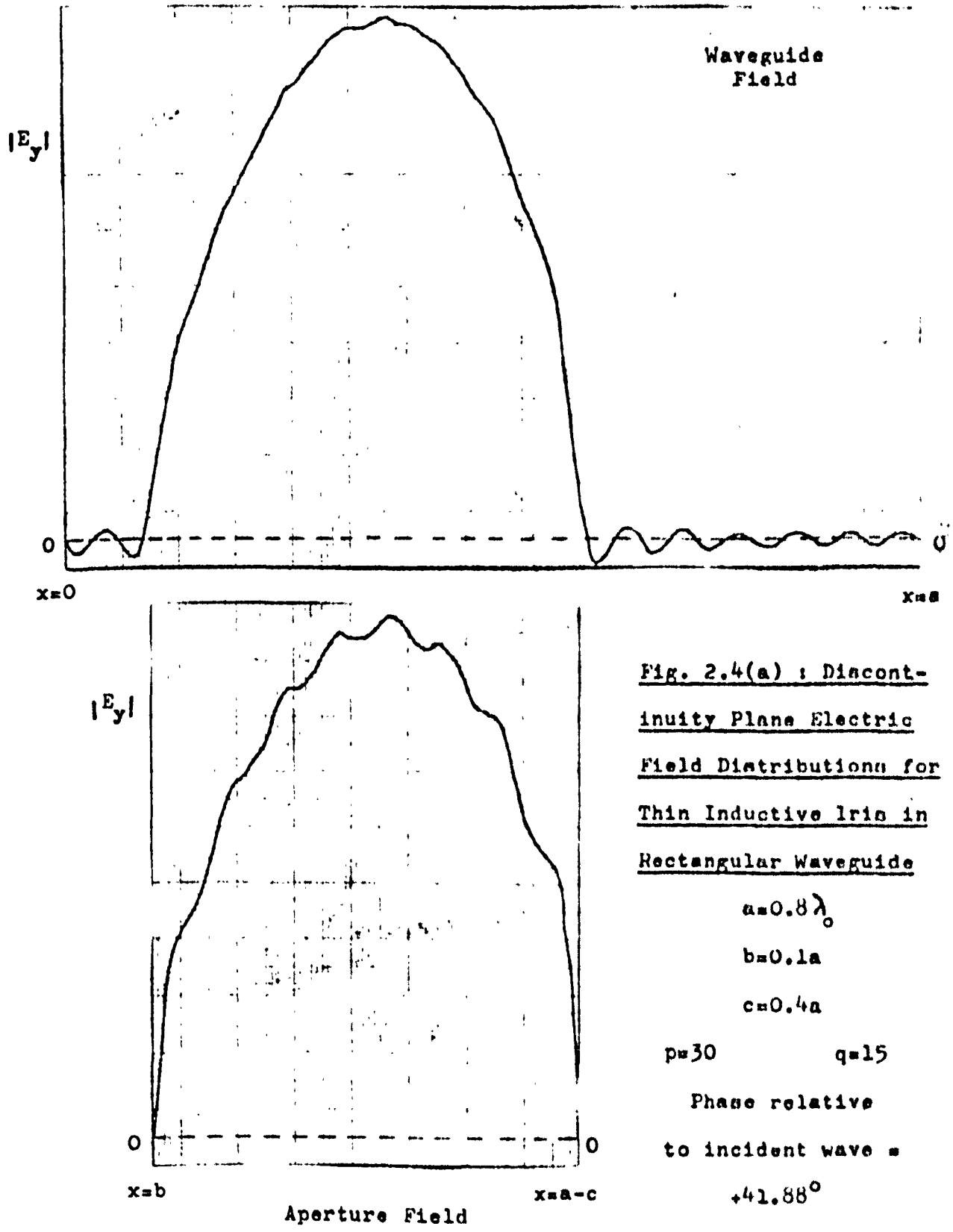

Fig. 2.4(a) : Discontinuity Plane Electric Field Distributions for Thin Inductive Iris in Rectangular Waveguide

$a=0.8\lambda_o$

$b=0.1a$

$c=0.4a$

$p=30$ $q=15$

Phase relative to incident wave = $+41.88^{\circ}$

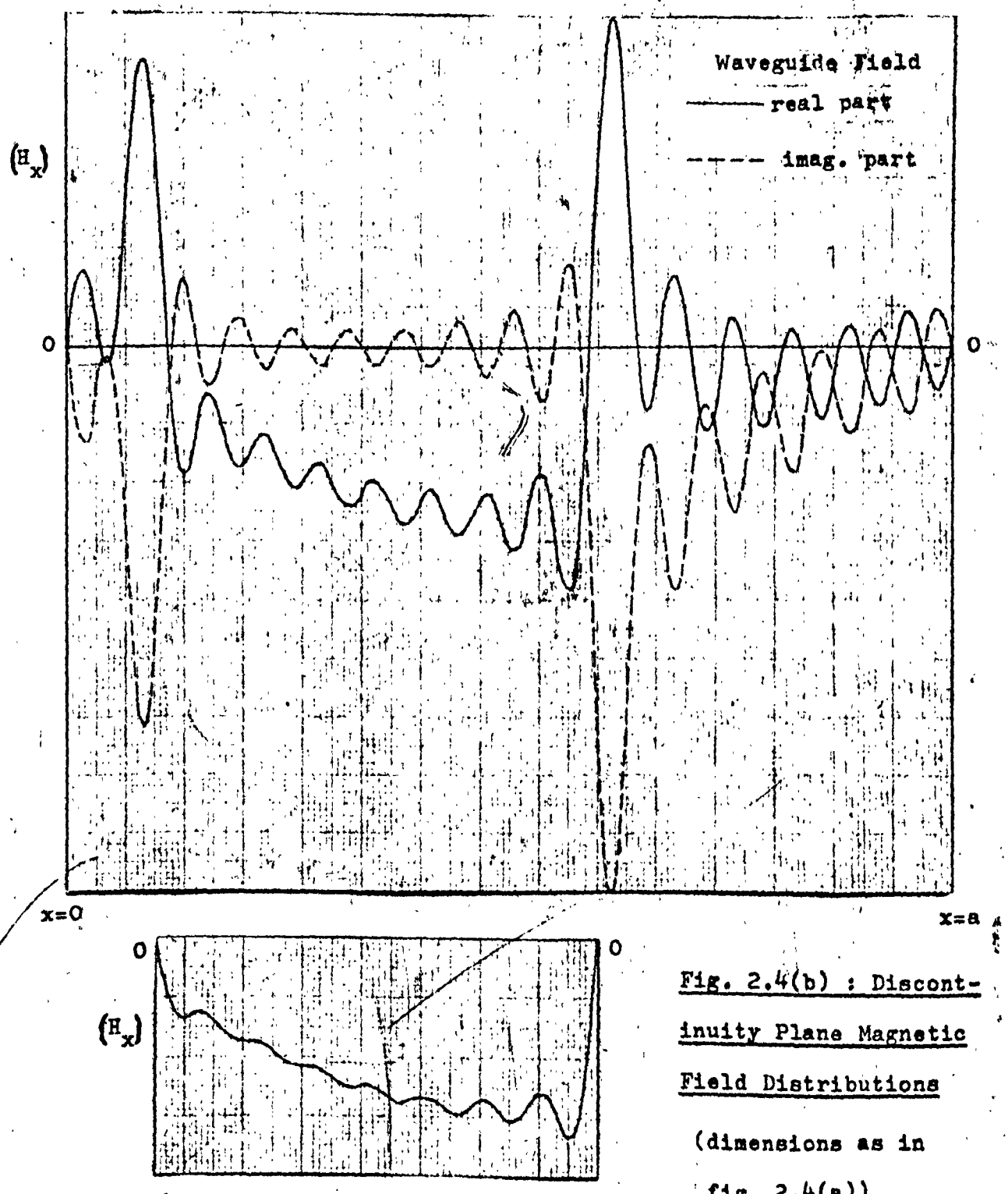

Fig. 2.4(b) : Discontinuity Plane Magnetic Field Distributions

(dimensions as in fig. 2.4(a))

ripple is most pronounced near the aperture edges. It is not surprising that the ripple in the waveguide magnetic field across the aperture has greater amplitude, because this field attempts to match the ripple in the approximate aperture field and also adds its own contribution owing to the fact that only a finite number of modes is taken into account. The same effect can be seen in the electric field, except that series of aperture functions are now used to match the waveguide modes - the reverse process to the magnetic field case - and so the ripple is worse in the aperture than in the waveguide. The effect on the field distributions of increasing p and q in the correct ratio has been investigated, and it is found that whereas the frequency of the ripple increases, its amplitude decreases, except near the aperture edges. This overshoot is known as Gibb's phenomenon, and occurs whenever a Fourier series is used to represent a discontinuous function. In the limit as p and q tend to infinity, such overshoots will become spikes of zero width, which do not affect field matching as assessed by integrating the squared deviation of the two distributions. The waveguide magnetic field at the aperture edges is found to increase as p and q increase, and it seems likely that the theoretical infinite amplitude will be achieved in the limit.

A necessary, though probably not sufficient, condition for the solution in the limit as p and q tend to infinity to be exact is that discrepancies in field matching across the aperture should tend to zero. As this cannot be adequately confirmed by merely examining the field distributions, it is necessary to make a quantitative determination of such discrepancies. The matching of the magnetic

fields to the theoretical aperture magnetic field distribution, as well as the matching of the waveguide fields to those represented by the series of aperture functions, will be considered.

By analogy with Cole's treatment of the step [8] , an error parameter is determined for each pair of fields whose matching is to be investigated, being defined as the mean square deviation between the two distributions integrated over a surface s'. In general this surface will be that of the aperture, but it is sometimes also of interest to investigate field matching over a more limited range. The electric field error parameter $\mathcal{E}_E$ is expressed as:

$$\mathcal{E}_E = \frac{\int_{s'} |(\underline{E}_{Tw/g} - \underline{E}_{Tap})|^2 ds}{\int_{s'} |\underline{E}_{Tinc}|^2 ds} \qquad 2.16$$

Similarly, for the magnetic field error parameter:

$$\mathcal{E}_H = \frac{\int_{s'} |(\underline{H}_{Tw/g} - \underline{H}_{Tap})|^2 ds}{\int_{s'} |\underline{H}_{Tinc}|^2 ds} \qquad 2.17$$

For convenience the above quantities are normalized using the incident field components $\underline{E}_{Tinc}$ and $\underline{H}_{Tinc}$. The remaining parameter concerns the matching of the waveguide magnetic field to the theoretical field, and is expressed as:

$$\mathcal{E}_{DH} = \frac{\int_{s'} |(\underline{H}_{Tw/g} - \underline{H}_{Tinc})|^2 ds}{\int_{s'} |\underline{H}_{Tinc}|^2 ds} \qquad 2.18$$

The error parameters may be evaluated by substituting the series representations for the waveguide and aperture fields. For example, in the general thin iris case 2.16 becomes:

$$\mathcal{E}_E = \frac{\int_{s'} \left| \sum_{n=1}^{p} (\delta_{n1} + a_{rn})\underline{e}_n - \sum_{m=1}^{q} b_m \underline{e}_{1m} \right|^2 ds}{\int_{s'} \underline{e}_1 \cdot \underline{e}_1 \, ds} \qquad 2.19$$

The numerator is now expressed as the sum of the squares of real and imaginary parts, the coefficients being written as $a_{rn}=a_{rn}^{(r)}+ja_{rn}^{(i)}$ and $b_m=b_m^{(r)}+jb_m^{(i)}$. After expanding the squared terms, 2.19 becomes:

$$\mathcal{E}_E = \left\{ \sum_{n=1}^{p} ([\delta_{n1} + a_{rn}^{(r)}]^2 + a_{rn}^{(i)2}) \int_{s'} \underline{e}_n \cdot \underline{e}_n \, ds + 2 \sum_{n=1}^{p-1} \sum_{j=n+1}^{p} ([\delta_{n1} + a_{rn}^{(r)}]a_{rj}^{(r)} + a_{rn}^{(i)} a_{rj}^{(i)}) \int_{s'} \underline{e}_n \cdot \underline{e}_j \, ds - 2 \sum_{n=1}^{p} \sum_{m=1}^{q} ([\delta_{n1} + a_{rn}^{(r)}]b_m^{(r)} + a_{rn}^{(i)} b_m^{(i)}) \int_{s'} \underline{e}_n \cdot \underline{e}_{1m} \, ds + \sum_{m=1}^{q} (b_m^{(r)2} + b_m^{(i)2}) \int_{s'} \underline{e}_{1m} \cdot \underline{e}_{1m} \, ds + 2 \sum_{m=1}^{q-1} \sum_{j=m+1}^{q} (b_m^{(r)} b_j^{(r)} + b_m^{(i)} b_j^{(i)}) \int_{s'} \underline{e}_{1m} \cdot \underline{e}_{1j} \, ds \right\} \Bigg/ \left\{ \int_{s'} \underline{e}_1 \cdot \underline{e}_1 \, ds \right\} \qquad 2.20$$

The mode and aperture functions are assumed to have been defined so that $\underline{e}_n$ and $\underline{e}_{1m}$ are real. Notice that if s' extends over the whole aperture, the last term in the numerator vanishes because of orthogonality. The expanded form of 2.17 for evaluating $\mathcal{E}_H$ is similar, except that the magnetic field functions $\underline{h}_n$ and $\underline{h}_{1m}$ can be imaginary. Account is taken of this by interchanging real and imaginary parts of the coefficients where necessary. The expression

for $\mathcal{E}_{DH}$ does not involve the aperture field, and consequently only terms equivalent to the first two in 2.20 appear in the numerator. In the case of the inductive iris, analytic expressions can easily be obtained for the integrals in 2.20, and the error parameters can be rapidly evaluated using the computer.

Figure 2.5 shows the variation with p of the error parameters in the case of a thin inductive iris whose dimensions are those of case (C) in figure 2.3. Three values of the ratio q:p are considered: the optimum value 1:2 and two values on either side of the "break-point" - 2:5 and 3:5.

Considering first of all the error integrated over the whole aperture area, it is clear that with the optimum ratio $\mathcal{E}_E$ decreases fairly rapidly as p increases, although convergence is not uniform because additional modes taken into account have varying effects on the solution. The magnetic field parameters, on the other hand, do not vary appreciably with p, and are several orders of magnitude higher than $\mathcal{E}_E$. This result does not, however, mean that the method is incorrect, because the range of integration includes the aperture edges, and in the limit as p tends to infinity the magnetic field distribution has singularities there. The infinite spikes which develop at the ends of the integration range, although having zero width in the limit, can have finite area, and thus the error parameters can have finite values even though magnetic field matching across the aperture is exact. To confirm this, field-matching errors were evaluated over a reduced area, so as to exclude the aperture

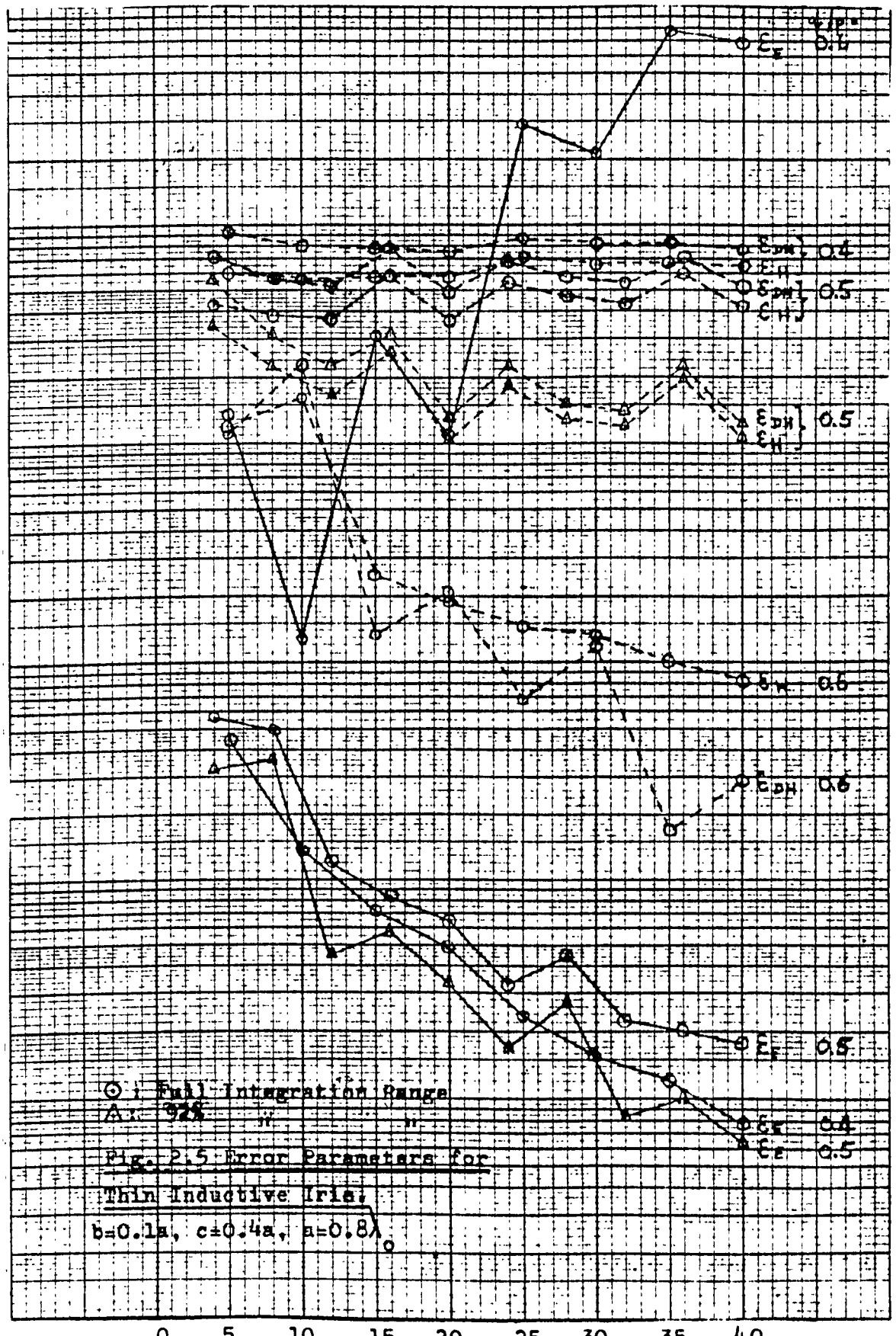

Fig. 2.5 Error Parameters for Thin Inductive Iris; b=0.1a, c=0.4a, a=0.8λ

edges from the range of integration. Figure 2.5 includes graphs for a 92% range, and the general downward trend of $\mathcal{E}_H$ and $\mathcal{E}_{DH}$ can be clearly seen. It is not clear from this diagram, however, that convergence is to zero rather than to some constant value, so to check this the symmetric case b=c was investigated, because here the variation of error parameters is more regular, and higher order functions can be considered since the even modes are omitted. The results are shown in figure 2.6, and it seems likely that the relevant curves will tend to zero, although this is again not obvious because of their oscillatory nature. Values of p greater than 50 could not be considered because of limitations on computer storage.

When q=0.4p, figure 2.5 shows that $\mathcal{E}_E$ tends to zero as p increases, and is somewhat lower than when q=0.5p, but that magnetic field errors are significantly higher. In the symmetric case (fig.2.6) the convergence of magnetic field matching over the reduced range when q=0.4p can be clearly seen, suggesting that with this ratio also correct field matching will be obtained in the limit, although convergence will be slower than when q=0.5p.

Notice that with both the ratios considered so far, there is mutual convergence of the curves for $\mathcal{E}_H$ and $\mathcal{E}_{DH}$, confirming that the aperture field will give an exact mean-square fit to the theoretical field in the limit as p tends to infinity.

In the case q=0.6p, i.e. to the right of the "breakpoint", figure 2.5 shows that although $\mathcal{E}_H$ and $\mathcal{E}_{DH}$ tend to zero as p increases, electric field matching becomes progressively worse. This confirms

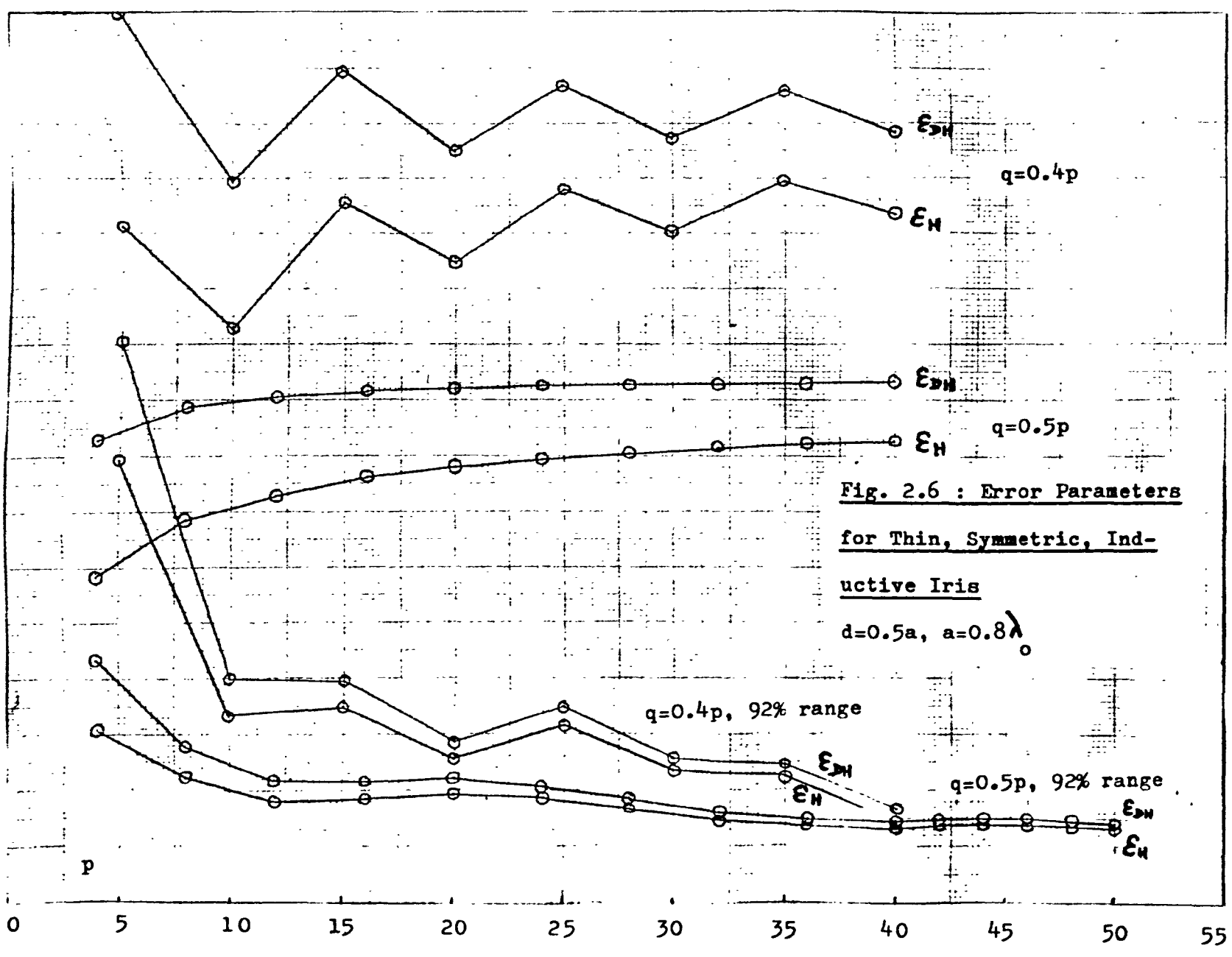

Fig. 2.6 : Error Parameters for Thin, Symmetric, Inductive Iris

d=0.5a, a=0.8λ_o

earlier remarks that $q/p > d/a$ leads to an incorrect solution and emphasises the critical nature of the ratio.

To conclude the treatment of the thin inductive iris, susceptance values of practical significance have been calculated, and these are given in figure 2.7. The curves show the variation of B/Y_0 with aperture displacement, for various values of aperture and waveguide width. In every case 30 modes were taken into account, and q/p was taken equal to d/a. The accuracy of the results, determined from convergence tests, is estimated to range from about 10% for the case $d=0.1a$ to less than 1% when $d=0.7a$. For the single-obstacle and symmetric cases, denoted by $2b/(a-d)$ equal to 0 and 1 respectively, the results could be compared with those from the "Waveguide Handbook", and agreement was found to be satisfactory when the estimated accuracies of both methods of solution were taken into account.

The behaviour of the curves for $a=\lambda_0$, $d/a=0.5$ and 0.7 is unusual, because the susceptance is greater for the symmetric case than for the single-obstacle case, whereas the reverse is generally true. This effect is confirmed by the "Waveguide Handbook" results, and seems to be connected with the excitation of the H_{20} mode, here at cut-off, which is not excited in the symmetric case but which has a considerable effect on the solution when $b=0$.

2.3. Further Thin Iris Examples - I. Capacitive Iris in Rectangular Waveguide.

The general configuration for a thin capacitive iris is shown in figure 2.8(a). When only the dominant mode can propagate, the equivalent circuit of figure 2.8(b) applies. Note that in this

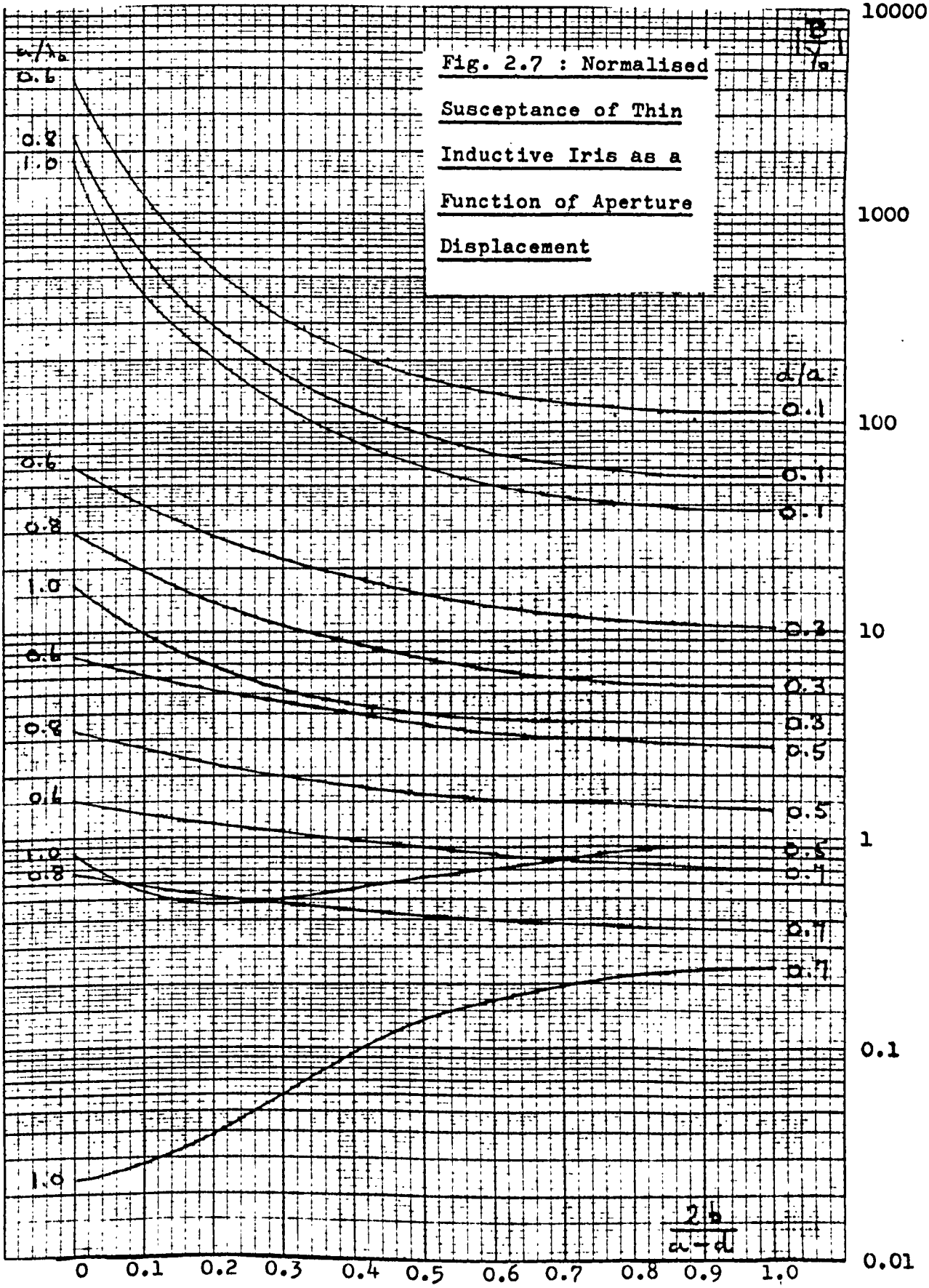
Fig. 2.7 : Normalised Susceptance of Thin Inductive Iris as a Function of Aperture Displacement
B/Y0
10000
1000
100
10
1
0.1
0.01
λ/λb
0.6
0.8
1.0
d/a
0.1
0.2
0.3
0.5
0.7
0
0.1
0.2
0.3
0.4
0.5
0.6
0.7
0.8
0.9
1.0
2b/a-d

Fig. 2.8(a) : Thin Capacitive Iris in Rectangular Waveguide

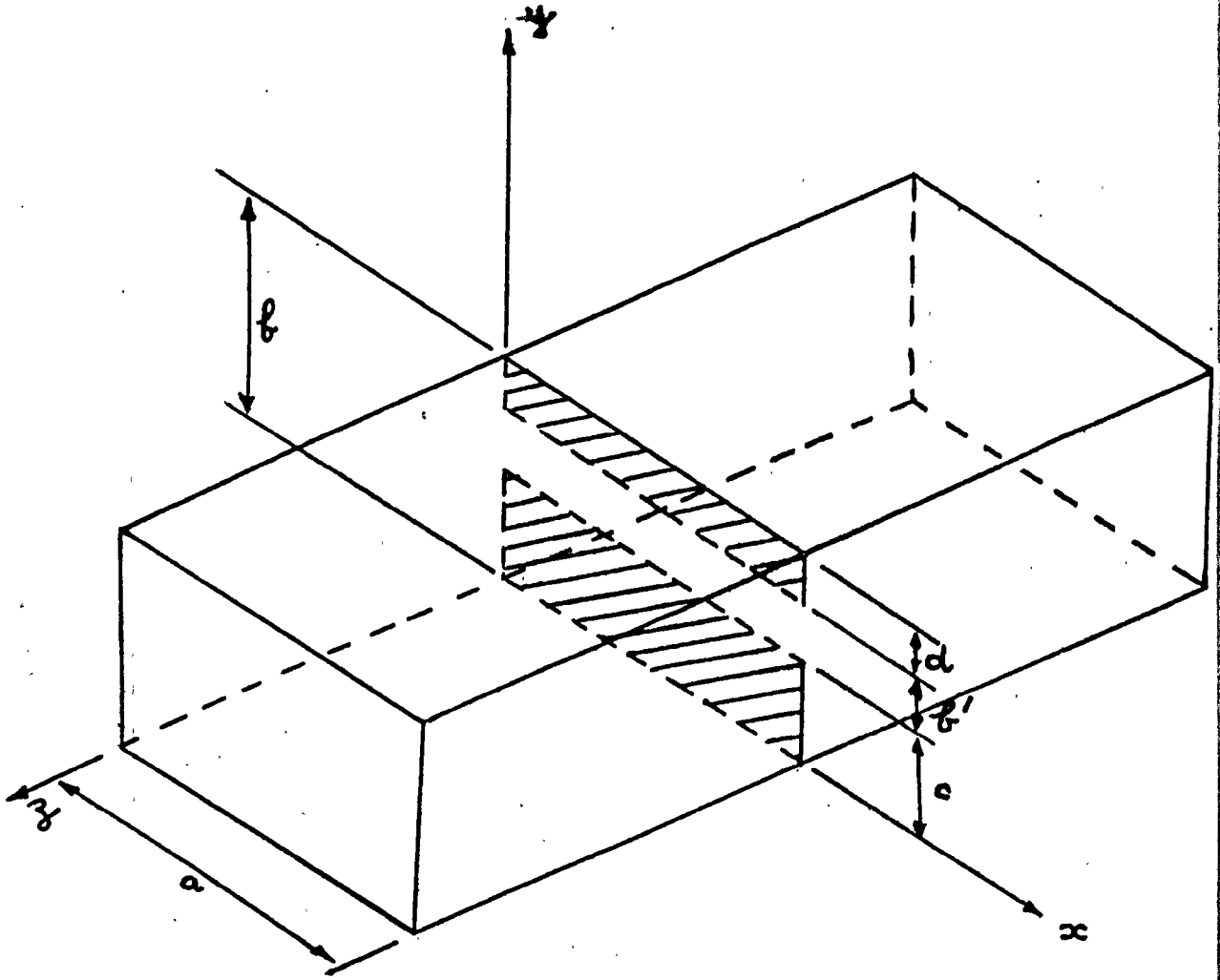

Fig. 2.8(b) : Transmission Line Equivalent Circuit

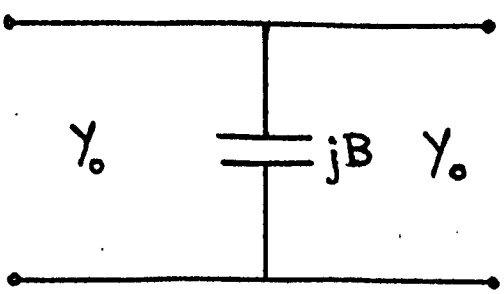

example the condition for single-mode propagation is that $\frac{\lambda_o}{2} < a < \frac{\lambda_o}{2}\sqrt{1+\frac{a^2}{b^2}}$, provided that c≠d. The method of analysis is similar to that for the inductive iris, but the expressions for the modes and aperture functions are slightly more involved, because an incident dominant mode can excite evanescent modes with field variations in both x and y directions, and these can be E-modes, whereas only H-modes were involved in the previous example. Since the iris is uniform in the x-direction, however, these modes must have the same field variation with x as the incident mode, and are therefore of type E_{1n} and H_{1n}. In general n can be any positive integer, but when c=d only modes for which n is even are excited.

The incident electric field is polarized entirely in the y-direction, and such fields satisfy the boundary condition at the aperture edges. The solution can therefore be simplified if the problem can be formulated in terms of modes having no x-component of electric field. By combining the modes H_{1n} and E_{1n} in the correct amplitude ratio this component can be eliminated, creating a hybrid mode designated LSE_{1n}. If modes of this type are used in the analysis rather than individual H and E modes, there is a considerable saving of computer time and storage for a solution of given accuracy.

The transverse field components in the plane z=0 for the LSE_{1n} mode can be written as follows:

$$\underline{e}_n = \sin\frac{\pi x}{a} \cos\frac{n\pi y}{b}\,\hat{\underline{i}}_y \qquad 2.21(a)$$

$$\underline{h}_n = j\sqrt{\frac{\varepsilon_o}{\mu_o}}\frac{1}{\gamma_{1n}}\left\{\left(\frac{\lambda_o^2}{4a^2} - 1\right)\sin\frac{\pi x}{a}\cos\frac{n\pi y}{b}\,\hat{\underline{i}}_x + \frac{n\lambda_o^2}{4ab}\cos\frac{\pi x}{a}\sin\frac{n\pi y}{b}\,\hat{\underline{i}}_y\right\} \qquad 2.21(b)$$

where $\bar{\gamma}_{1n} = \sqrt{\left(\frac{\lambda_o^2}{4}\left[\frac{1}{a^2} + \frac{n^2}{b^2}\right] - 1\right)}$

Notice that if n=0 the expressions reduce to those for the H_{10} mode, so the incident field can also be thought of as that of the lowest-order LSE mode. Suitable functions for expanding the aperture fields are derived from the LSE modes for a waveguide with the same cross-section as the aperture, i.e.:

$$\underline{e}_{1m} = \sin\frac{\pi x}{a}\cos\frac{m\pi}{b'}(y-c)\,\hat{\underline{i}}_y \qquad 2.22(a)$$

$$\underline{h}_{1m} = \left(\frac{\lambda_o^2}{4a^2} - 1\right)\sin\frac{\pi x}{a}\cos\frac{m\pi}{b'}(y-c)\,\hat{\underline{i}}_x + \frac{m\lambda_o^2}{4ab'}\cos\frac{\pi x}{a}\sin\frac{m\pi}{b'}(y-c)\,\hat{\underline{i}}_y \qquad 2.22(b)$$

It can easily be shown that the important orthogonality properties

$$\int_{y=0}^{b}\int_{x=0}^{a}\underline{e}_i \times \underline{h}_j \cdot \hat{\underline{i}}_z\,dxdy = 0,\ i\neq j \quad \text{and} \quad \int_{y=c}^{c+b'}\int_{x=0}^{a}\underline{e}_{1i} \times \underline{h}_{1j} \cdot \hat{\underline{i}}_z\,dxdy = 0,\ i\neq j$$

hold for the above functions. The elements of matrix $[R]$, defined by 1.21, become:

$$R_{nm} = \frac{2\varepsilon_{n0}}{ab}\int_{y=c}^{c+b'}\int_{x=0}^{a}\sin^2\frac{\pi x}{a}\cos\frac{n\pi y}{b}\cos\frac{m\pi}{b'}(y-c)\,dxdy \qquad 2.23$$

When the integral is evaluated this becomes:

$$R_{nm} = \frac{2n}{\pi}\left(\frac{b'}{b}\right)^2 \frac{\sin\frac{n\pi c}{b} + (-1)^{m+1}\sin\frac{n\pi(c+b')}{b}}{m^2 - n^2\left(\frac{b'}{b}\right)^2}, \quad bm \neq b'n \qquad 2.24(a)$$

$$R_{nm} = \frac{b'}{b}\cos\frac{m\pi c}{b'}, \quad bm = b'n \qquad 2.24(b)$$

The elements of matrix $[S]$ are related to those of $[R]$ through the expression:

$$S_{mn} = j\sqrt{\frac{\varepsilon_0}{\mu_0}}\frac{1}{\delta_{1n}}\frac{b}{b'}\frac{\varepsilon_{m0}}{\varepsilon_{n0}}R_{nm} \qquad 2.25$$

In these equations ε_{ij} is defined as:

$$\varepsilon_{ij} = 1, \; i=j \qquad \varepsilon_{ij} = 2, \; i \neq j$$

Notice the similarity between the above expressions and those for the inductive iris (2.13 and 2.14). The method of solution on the computer is entirely analogous to that for the inductive iris, and only minor modifications to the flow diagram in figure 2.2 are required, to account for the special case m=0, n≠0, and the new location of the propagation coefficient.

Figure 2.9 shows the dependence of the computed susceptance on the number of aperture functions, q, when 18 waveguide modes are taken into account. Various values of b'/b are considered, and results are presented for both the symmetric case c=d and the single-obstacle case c=0. Distinct "breakpoints" can be seen where q/p = b'/b, and these can be accounted for in the same way as in the inductive iris case. The susceptance values at the "breakpoints"

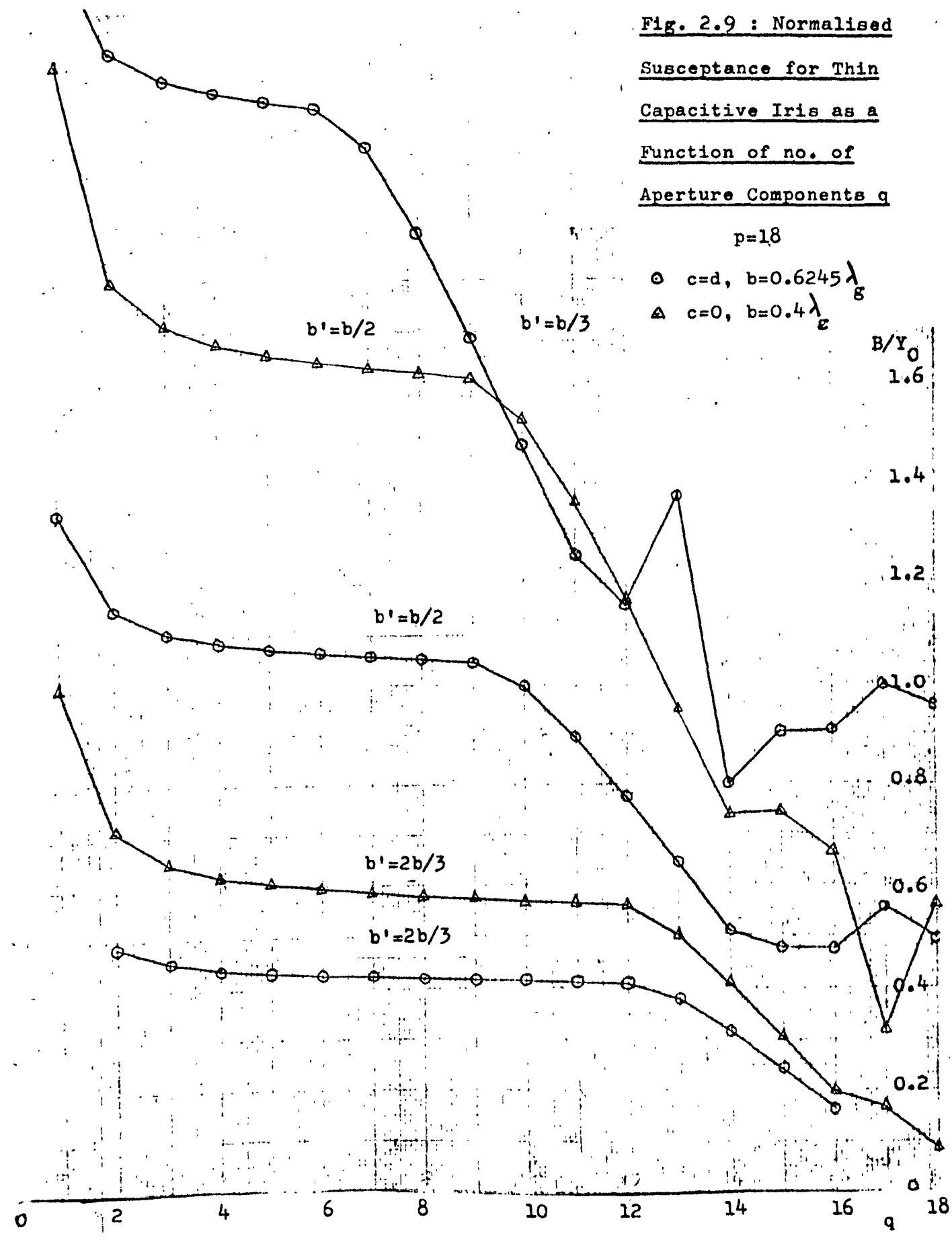

Fig. 2.9 : Normalised Susceptance for Thin Capacitive Iris as a Function of no. of Aperture Components q

p=18

⊙ c=d, b=0.6245 λ_g

△ c=0, b=0.4 λ_g

should, by analogy with the inductive iris treatment, be the most accurate. Here again, the erratic behaviour near q=p, where there is also a deviation of the admittance ratio from unity, is a result of computational errors. Note that before this region is reached the solution appears to tend to zero, as predicted by theory.

By specifying the dimensions in terms of the guide wavelength λ_g for the dominant mode, where $\lambda_g = \lambda_o/(1-\lambda_o^2/4a^2)^{\frac{1}{2}}$, the waveguide width 'a' does not come into the calculation. In figure 2.9, the height of the guide for the symmetric case is such that $b=0.6245\,\lambda_g$, which corresponds to the case $a=b=0.8\,\lambda_o$.

Table 2.2 shows the convergence of the solution in the case q/p=b'/b=2/3 for both symmetric and single-obstacle cases. This is not as rapid as in the inductive iris example, and there is less difference between the convergence rates for symmetric and single-obstacle cases. About 20 modes would need to be taken into account for one per cent accuracy. The estimated converged values differ from those of Marcuvitz [4] by about 4% in the case c=d, $b=0.6245\lambda_g$, and by about 3.2% in the case c=0, $b=0.4\,\lambda_g$. As the accuracy for Marcuvitz's results is given as less than 5%, the agreement is satisfactory.

Figure 2.10 shows the normalized susceptance of a symmetric capacitive iris as a function of b'/b, with b/λ_g as parameter. In the range $0.1 \leqslant b'/b \leqslant 0.7$, 40 waveguide modes were taken into account, and the accuracy of the results in this range is thought to be better than one per cent.

p	q	Case 1	Error (%)	Case 2	Error (%)
6	4	0.4112	6.09	0.5889	6.83
12	8	0.3960	2.16	0.5641	2.32
18	12	0.3921	1.16	0.5578	1.18
24	16	0.3903	0.70	0.5551	0.69
30	20	0.3894	0.46	0.5536	0.42
36	24	0.3888	0.31	0.5527	0.25

Extrapolated Converged Value	0.3876	0.5513
From "Waveguide Handbook" Formula	0.4031	0.5697

Table 2.2 : Convergence of Normalised Susceptance Values for Thin Capacitive Iris in Rectangular W/G

Case 1: c=d, $b=0.6245\lambda_g$, $b'/b=0.667$

Case 2: c=0, $b=0.4\lambda_g$, $b'/b=0.667$

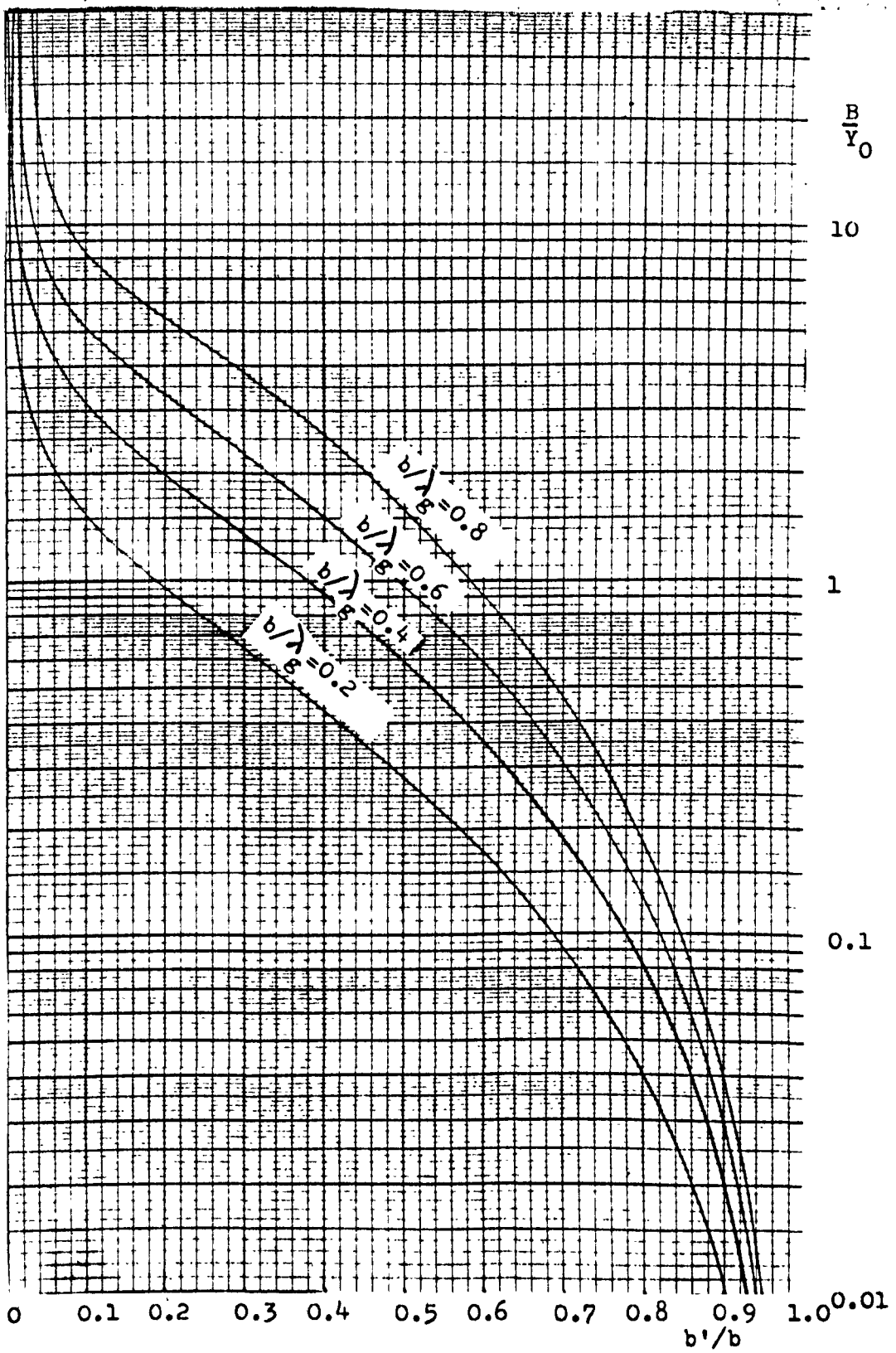

Fig. 2.10 : Normalised Susceptance of Thin, Symmetric Capacitive Iris in Rectangular Waveguide

2.4 Further Thin Iris Examples - II

Circular Iris in Circular Waveguide - H_{11} mode incident

An example of a thin iris problem with cylindrical geometry is shown in figure 2.11(a). By taking the incident field to be a unit-amplitude H_{11} mode, the problem becomes more complex than the previous examples, since both H and E modes are excited at the discontinuity, in this case with unknown relative amplitudes. The susceptance in the transmission-line equivalent circuit for single-mode propagation (Fig.2.11(b)) can be either inductive or capacitive, depending on the dimensions of the structure. It follows that certain configurations will give a resonant condition, where the iris has no effect on the H_{11} mode. The condition for single-mode propagation is $0.293\lambda_o < R' < 0.610\lambda_o$. Because the structure has circular symmetry, the only modes excited at the iris will be those with the same azimuthal field variation as the incident mode, which will therefore be of type H_{1n} and E_{1n}. The transverse fields of these modes in the plane z=0 are written as follows:

$\underline{H_{1n}}$

$$\underline{e}_n^{(H)} = J_1'(k_n'r)\cos\theta\,\hat{\underline{i}}_\theta + \frac{1}{k_n'r}J_1(k_n'r)\sin\theta\,\hat{\underline{i}}_r \qquad 2.26(a)$$

$$\underline{h}_n^{(H)} = -j\frac{\gamma_n}{\omega\mu_o}\left[\frac{1}{k_n'r}J_1(k_n'r)\sin\theta\,\hat{\underline{i}}_\theta - J_1'(k_n'r)\cos\theta\,\hat{\underline{i}}_r\right] \qquad 2.26(b)$$

where $k_n' R' = \chi_n'$, the nth. root of $J_1'(x)$
and $\gamma_n = \sqrt{(k_n'^2 - k_o^2)}$.

Fig. 2.11(a) : Circular Iris in Circular Waveguide

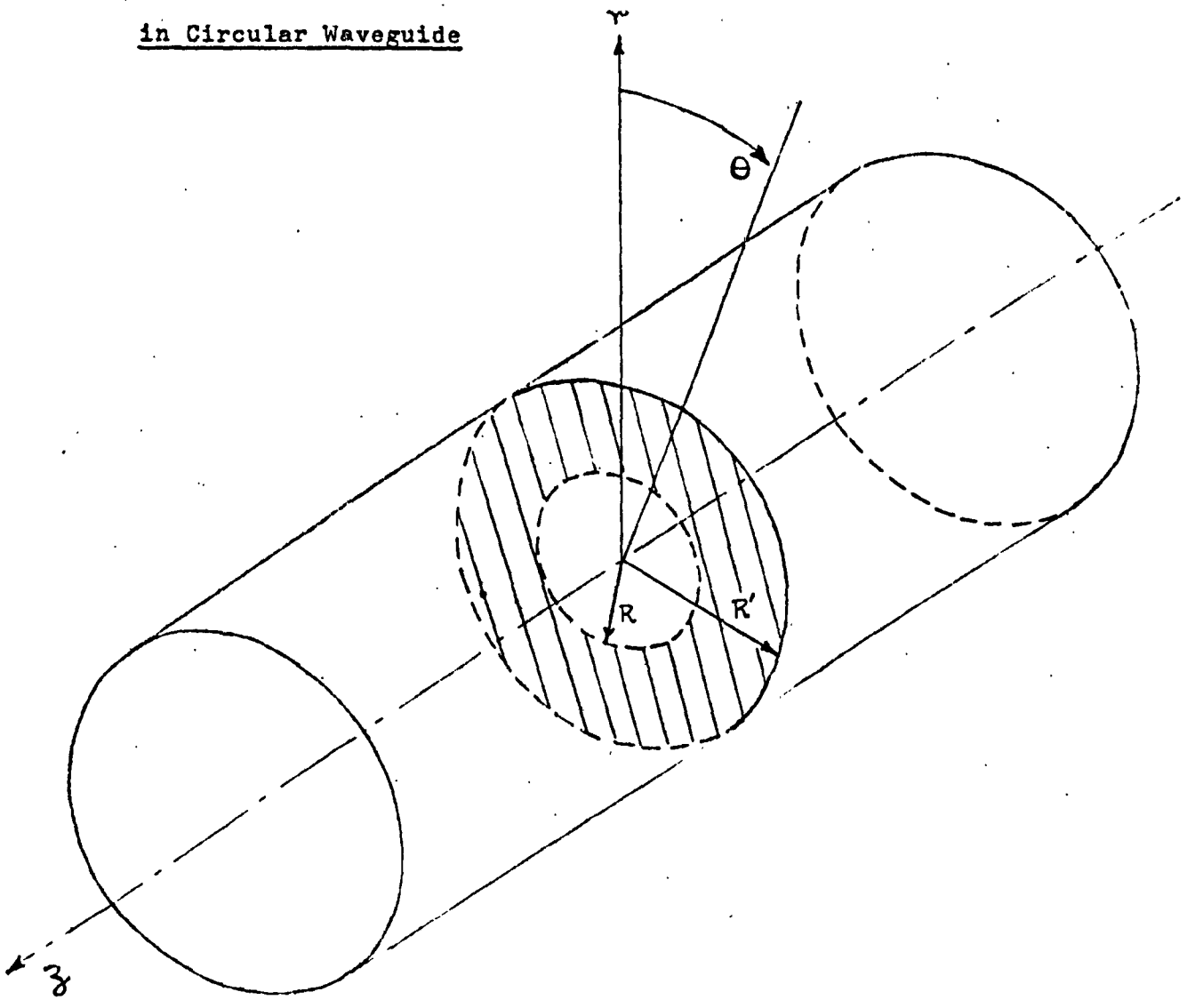

Fig. 2.11(b) : Transmission Line Equivalent Circuit

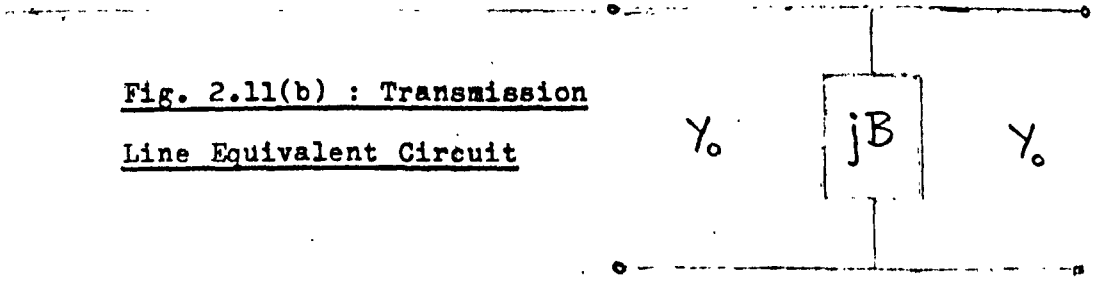

$\underline{F_{1n}}$

$$\underline{e}_n^{(E)} = \frac{1}{l'_n r} J_1(l'_n r) \cos\theta \hat{\underline{i}}_\theta + J'_1(l'_n r) \sin\theta \hat{\underline{i}}_r \qquad 2.27(a)$$

$$\underline{h}_n^{(E)} = j \frac{\omega\varepsilon_o}{\delta_n}\left[J'_1(l'_n r) \sin\theta \hat{\underline{i}}_\theta - \frac{1}{l'_n r} J_1(l'_n r) \cos\theta \hat{\underline{i}}_r\right] \qquad 2.27(b)$$

where $l'_n R' = \chi_n$, the nth. root of $J_1(x)$
and $\delta_n = \sqrt{(l'^2_n - k_o^2)}$.

The relevant orthogonality properties of the electric field functions are:

$$\int_{r=0}^{R'} \int_{\theta=0}^{2\pi} \underline{e}_i^{(H)} \times \underline{h}_j^{(H)} \cdot \hat{\underline{i}}_z \; r \, d\theta \, dr = 0, \quad i \neq j \qquad 2.28$$

$$= -j \frac{\gamma_i}{\omega\mu_o} \pi \frac{R'^2}{2} \left[1 - \frac{1}{\chi_i^2}\right] J_1^2(\chi_i) \;, \quad i=j$$

$$\int_{r=0}^{R'} \int_{\theta=0}^{2\pi} \underline{e}_i^{(E)} \times \underline{h}_j^{(E)} \cdot \hat{\underline{i}}_z \; r \, d\theta \, dr = 0, \quad i \neq j \qquad 2.29$$

$$= j \frac{\omega\varepsilon}{\delta_i} \pi \frac{R'^2}{2} J_0^2(\chi_i) \;, \quad i=j$$

The surface integral of the vector product of $\underline{e}_i^{(H)}$ and $\underline{h}_j^{(E)}$ or of $\underline{e}_i^{(E)}$ and $\underline{h}_j^{(H)}$ over the waveguide cross-section vanishes for all i and j.

As in previous examples, the aperture field functions are derived from modes for a waveguide with the same cross-section.

Suitable functions for this case are:

mth. "H-type" functions

$$\underline{e}_{1m}^{(H)} = J_1'(k_m r)\cos\theta\,\hat{\underline{i}}_\theta + \frac{1}{k_m r} J_1(k_m r)\sin\theta\,\hat{\underline{i}}_r \qquad 2.30(a)$$

$$\underline{h}_{1m}^{(H)} = -\frac{1}{k_m r} J_1(k_m r)\sin\theta\,\hat{\underline{i}}_\theta + J_1'(k_m r)\cos\theta\,\hat{\underline{i}}_r \qquad 2.30(b)$$

mth. "E-type" functions.

$$\underline{e}_{1m}^{(E)} = \frac{1}{l_m r} J_1(l_m r)\cos\theta\,\hat{\underline{i}}_\theta + J_1'(l_m r)\sin\theta\,\hat{\underline{i}}_r \qquad 2.31(a)$$

$$\underline{h}_{1m}^{(E)} = J_1'(l_m r)\sin\theta\,\hat{\underline{i}}_\theta - \frac{1}{l_m r} J_1(l_m r)\cos\theta\,\hat{\underline{i}}_r \qquad 2.31(b)$$

In these expressions $k_m R = \chi_m$ and $l_m R = \xi_m$. The aperture magnetic field functions have the following orthogonality properties:

$$\int_{r=0}^{R}\int_{\theta=0}^{2\pi} \underline{e}_{1i}^{(H)} \times \underline{h}_{1j}^{(H)} \cdot \hat{\underline{i}}_z \, r\, d\theta dr = 0, \quad i \neq j \qquad 2.32$$

$$= \frac{\pi R^2}{2}\left[1 - \frac{1}{\chi_i^2}\right] J_1^2(\chi_i), \quad i=j$$

$$\int_{r=0}^{R}\int_{\theta=0}^{2\pi} \underline{e}_{1i}^{(E)} \times \underline{h}_{1j}^{(E)} \cdot \hat{\underline{i}}_z \, r\, d\theta dr = 0, \quad i \neq j \qquad 2.33$$

$$= \frac{\pi R^2}{2} J_0^2(\xi_i), \quad i=j$$

The vector product of $\underline{e}_{1i}^{(H)}$ and $\underline{h}_{1j}^{(E)}$ or of $\underline{e}_{1i}^{(E)}$ and $\underline{h}_{1j}^{(H)}$ integrated over the aperture cross-section, vanishes for all i and j.

If waveguide modes and aperture functions of types "H" and "E" are taken into account alternately, the elements of matrix [R] will have the following forms:

$$R_{2n-1,2m-1} = \frac{\int_{r=0}^{R}\int_{\theta=0}^{2\pi} \underline{e}_{1m}^{(H)} \times \underline{h}_{n}^{(H)} \cdot \hat{\underline{i}}_z \; r \, d\theta dr}{\int_{r=0}^{R'}\int_{\theta=0}^{2\pi} \underline{e}_{n}^{(H)} \times \underline{h}_{n}^{(H)} \cdot \hat{\underline{i}}_z \; r \, d\theta dr}$$

$$= \frac{2\chi_m J_1(\chi_m) \, J_1'(\chi_n R/R')}{(\chi_m^2 \, \frac{R'^2}{R^2} - \chi_n^2)(1 - 1/\chi_n^2) \, J_1^2(\chi_n)} \qquad 2.34$$

$$R_{2n-1,2m} = \frac{\int_{r=0}^{R}\int_{\theta=0}^{2\pi} \underline{e}_{1m}^{(E)} \times \underline{h}_{n}^{(H)} \cdot \hat{\underline{i}}_z \; r \, d\theta dr}{\int_{r=0}^{R'}\int_{\theta=0}^{2\pi} \underline{e}_{n}^{(H)} \times \underline{h}_{n}^{(H)} \cdot \hat{\underline{i}}_z \; r \, d\theta dr} = 0 \qquad 2.35$$

$$R_{2n,2m-1} = \frac{\int_{r=0}^{R}\int_{\theta=0}^{2\pi} \underline{e}_{1m}^{(H)} \times \underline{h}_{n}^{(E)} \cdot \hat{\underline{i}}_z \; r \, d\theta dr}{\int_{r=0}^{R'}\int_{\theta=0}^{2\pi} \underline{e}_{n}^{(E)} \times \underline{h}_{n}^{(E)} \cdot \hat{\underline{i}}_z \; r \, d\theta dr} \qquad 2.36$$

$$= \frac{2R\, J_1(\chi_m)\, J_1(\xi_n R/R')}{\xi_n \chi_m R'\, J_0^2(\xi_n)}$$

$$R_{2n,2m} = \frac{\int_{r=0}^{R}\int_{\theta=0}^{2\pi} \underline{e}_{1m}^{(E)} \times \underline{h}_n^{(E)} \cdot \hat{\underline{i}}_z \; r\, d\theta dr}{\int_{r=0}^{R'}\int_{\theta=0}^{2\pi} \underline{e}_n^{(E)} \times \underline{h}_n^{(E)} \cdot \hat{\underline{i}}_z \; r\, d\theta dr} \qquad 2.37$$

$$= \frac{2(\xi_n R/R')\, J_1'(\xi_m)\, J_1(\xi_n R/R')}{\left[\xi_n^2 - (\xi_m R'/R)^2\right] J_0^2(\xi_n)}$$

The elements of matrix $[S]$ have the forms:

$$S_{2m-1,2n-1} = \frac{\int_{r=0}^{R}\int_{\theta=0}^{2\pi} \underline{e}_{1m}^{(H)} \times \underline{h}_n^{(H)} \cdot \hat{\underline{i}}_z \; r\, d\theta dr}{\int_{r=0}^{R}\int_{\theta=0}^{2\pi} \underline{e}_{1m}^{(H)} \times \underline{h}_{1m}^{(H)} \cdot \hat{\underline{i}}_z \; r\, d\theta dr} \qquad 2.38$$

$$= j\frac{\gamma_n}{\omega\mu_0} \; \frac{2\chi_m\, J_1'(\chi_n R/R')}{(\chi_m^2 - \chi_n^2 \frac{R^2}{R'^2})\,(1 - 1/\chi_m^2)\, J_1(\chi_m)}$$

$$S_{2m,2n-1} = \frac{\int_{r=0}^{R}\int_{\theta=0}^{2\pi} \underline{e}_{1m}^{(E)} \times \underline{h}_{n}^{(H)} \cdot \hat{\underline{i}}_z \; r \, d\theta dr}{\int_{r=0}^{R}\int_{\theta=0}^{2\pi} \underline{e}_{1m}^{(E)} \times \underline{h}_{1m}^{(E)} \cdot \hat{\underline{i}}_z \; r \, d\theta dr} = 0 \qquad 2.39$$

$$S_{2m-1,2n} = \frac{\int_{r=0}^{R}\int_{\theta=0}^{2\pi} \underline{e}_{1m}^{(H)} \times \underline{h}_{n}^{(E)} \cdot \hat{\underline{i}}_z \; r \, d\theta dr}{\int_{r=0}^{R}\int_{\theta=0}^{2\pi} \underline{e}_{1m}^{(H)} \times \underline{h}_{1m}^{(H)} \cdot \hat{\underline{i}}_z \; r \, d\theta dr}$$

$$= -\frac{j\omega\varepsilon_0}{\delta_n} \frac{2 J_1(\xi_n R/R')}{\chi_m(\xi_n R/R')\,(1 - 1/\chi_m^2)\, J_1(\chi_m)} \qquad 2.40$$

$$S_{2m,2n} = \frac{\int_{r=0}^{R}\int_{\theta=0}^{2\pi} \underline{e}_{1m}^{(E)} \times \underline{h}_{n}^{(E)} \cdot \hat{\underline{i}}_z \; r \, d\theta dr}{\int_{r=0}^{R}\int_{\theta=0}^{2\pi} \underline{e}_{1m}^{(E)} \times \underline{h}_{1m}^{(E)} \cdot \hat{\underline{i}}_z \; r \, d\theta dr}$$

$$= \frac{j\omega\varepsilon_0}{\tilde{\delta}_n} \frac{2(\xi_n R/R')\, J_1'(\xi_m)\, J_1(\xi_n R/R')}{(\xi_m^2 - \xi_n^2 \frac{R^2}{R'^2})\, J_0^2(\xi_m)} \qquad 2.41$$

Having assigned values to the elements of matrices [R] and [S], the method of solution is almost identical to that for the rectangular waveguide examples.

The application to this problem of the "breakpoint" technique for determining the optimum value of p/q is illustrated in figure 2.12, from which it is clear that p/q=R'/R is the required relationship. Table 2.4 shows how the solution converges in the case R'/R=3/2, R'=0.3 λ_o, when p/q corresponds to the "breakpoint" value. Convergence is rapid, and compares favourably with that for the inductive iris in rectangular waveguide. For example, in both cases only 12 modes are required to give better than one percent accuracy. It should be noted that in both figure 2.12 and table 2.4 only even values of p and q have been considered. This is to ensure that the correct ratio of modes to aperture functions holds independently for both "E" and "H" modes and functions. If, for example, p and q were taken as 9 and 6 respectively in the case R'/R=3/2, the numbers of "E" modes and functions would be in the ratio 4:3, the corresponding "H" ratio being 5:3. Neither ratio corresponds to the "breakpoint", and consequently the solution would be much less accurate than if p and q had both been even.

In order to check the correctness of susceptance values computed for this case, a comparison was made with values calculated from the simple formula:

$$\frac{B}{Y_0} = - \frac{\lambda_g}{4R'} \left[\frac{(2R')^3}{8.40} \cdot \frac{6}{(2R)^3} - 2.344 \right] \qquad 2.42$$

where $\lambda_g = \lambda_o \left\{ 1 - \left(\frac{\lambda_o}{3.412R'} \right)^2 \right\}^{-\frac{1}{2}}$

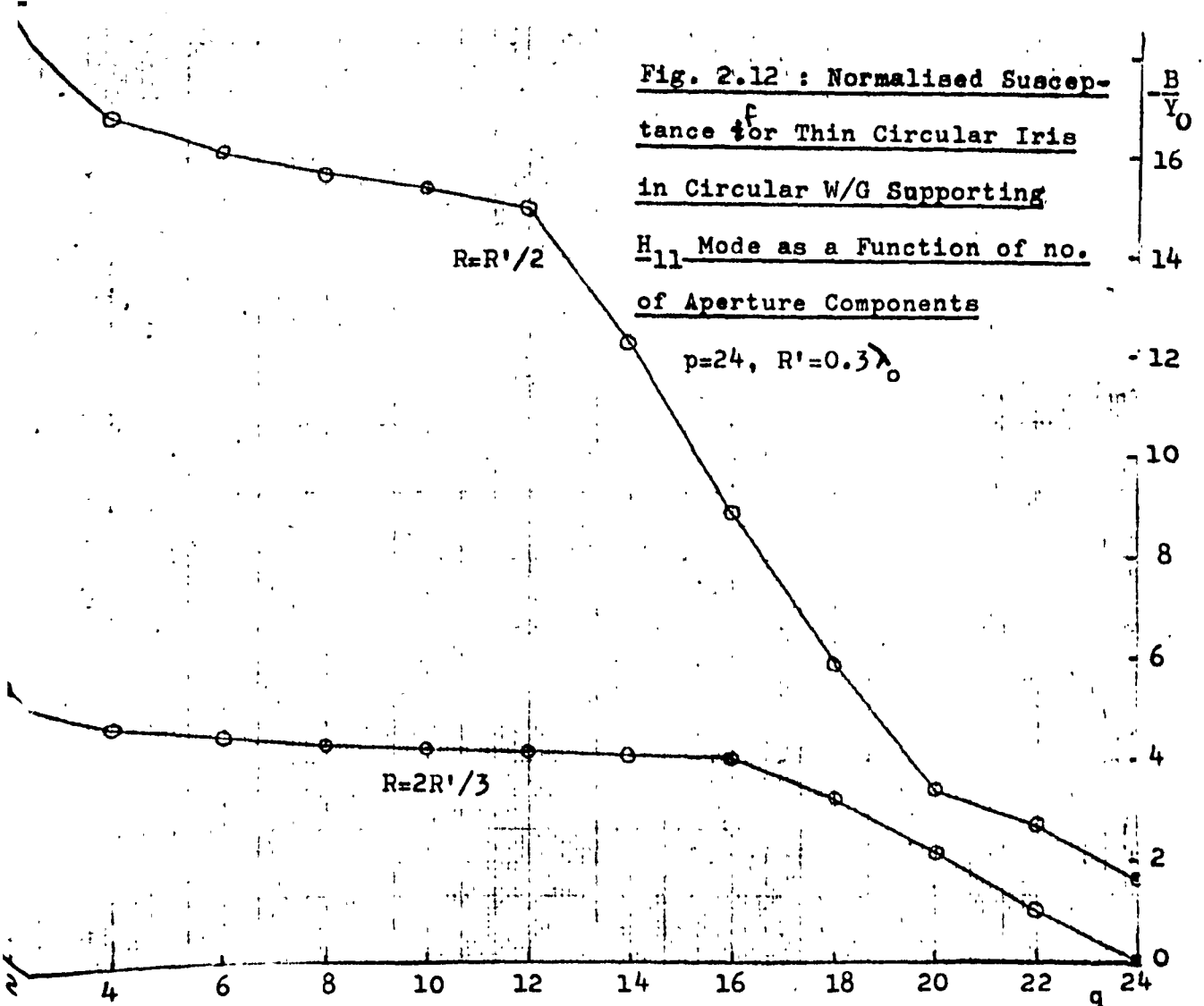

Fig. 2.12 : Normalised Susceptance for Thin Circular Iris in Circular W/G Supporting H_{11} Mode as a Function of no. of Aperture Components

p=24, $R'=0.3\lambda_0$

$\frac{R'}{\lambda_0}$	$\frac{R}{R'}$	B/Y_0 (comp.)	B/Y_0 (ref.8)	Discrepancy (%)
0.3	0.1	-2632	-2780	5.6
0.3	0.3	-90.50	-94.13	4.0
0.3	0.5	-14.96	-13.16	12.0
0.4	0.1	-612.8	-653.9	6.7
0.4	0.3	-19.03	-22.14	16.4
0.4	0.5	-2.678	-3.095	15.5
0.5	0.1	-403.3	-439.4	9.0
0.5	0.3	-10.08	-14.88	47.6
0.5	0.5	-0.799	-2.080	160.1

Table 2.3 : Computed Susceptances for Circular Iris Compared with "Waveguide Handbook" values

p	q	B/Y_0	Error (%)
6	4	-4.111	1.91
12	8	-4.066	0.79
18	12	-4.051	0.42
24	16	-4.044	0.25
30	20	-4.040	0.15
36	24	-4.037	0.07

Estimated converged value = -4.034

Table 2.4 : Convergence of Circular Iris Solution

$R=2R'/3$, $R'=0.3\lambda_0$

This formula is given by Marcuvitz [4], who derived it by an integral - equation method. It is subject to the limitations that R should be small compared with R' and λ_o/π, and that the second mode should be well below cut-off. No estimates of accuracy are given. The results of the comparison are shown in table 2.3. In general, the smaller R/R' and R'/λ_o become, the better the agreement between the two solutions. This is to be expected in view of the above limitations, and tends to confirm the correctness of the computational method.

Figure 2.13 shows the normalised susceptance of a thin circular iris as a function of R/R', with R'/λ_o as parameter. Forty waveguide modes were taken into account for $R/R'<0.7$, and the accuracy is estimated to be less than one percent for R/R' greater than about 0.25. The susceptance is inductive except where otherwise stated. Notice the resonant condition on the $R/\lambda_o=0.6$ curve, which cannot be adequately predicted using expression 2.42.

This example clearly shows the advantage of the computational method over a conventional technique in which the need to make approximations severely limits the range of applicability.

2.5. Discussion.

The three above examples clearly illustrate the value of the computational technique for solving thin iris problems, and show that the location of a "breakpoint" is a reliable way of determining the optimum mode-aperture function ratio.

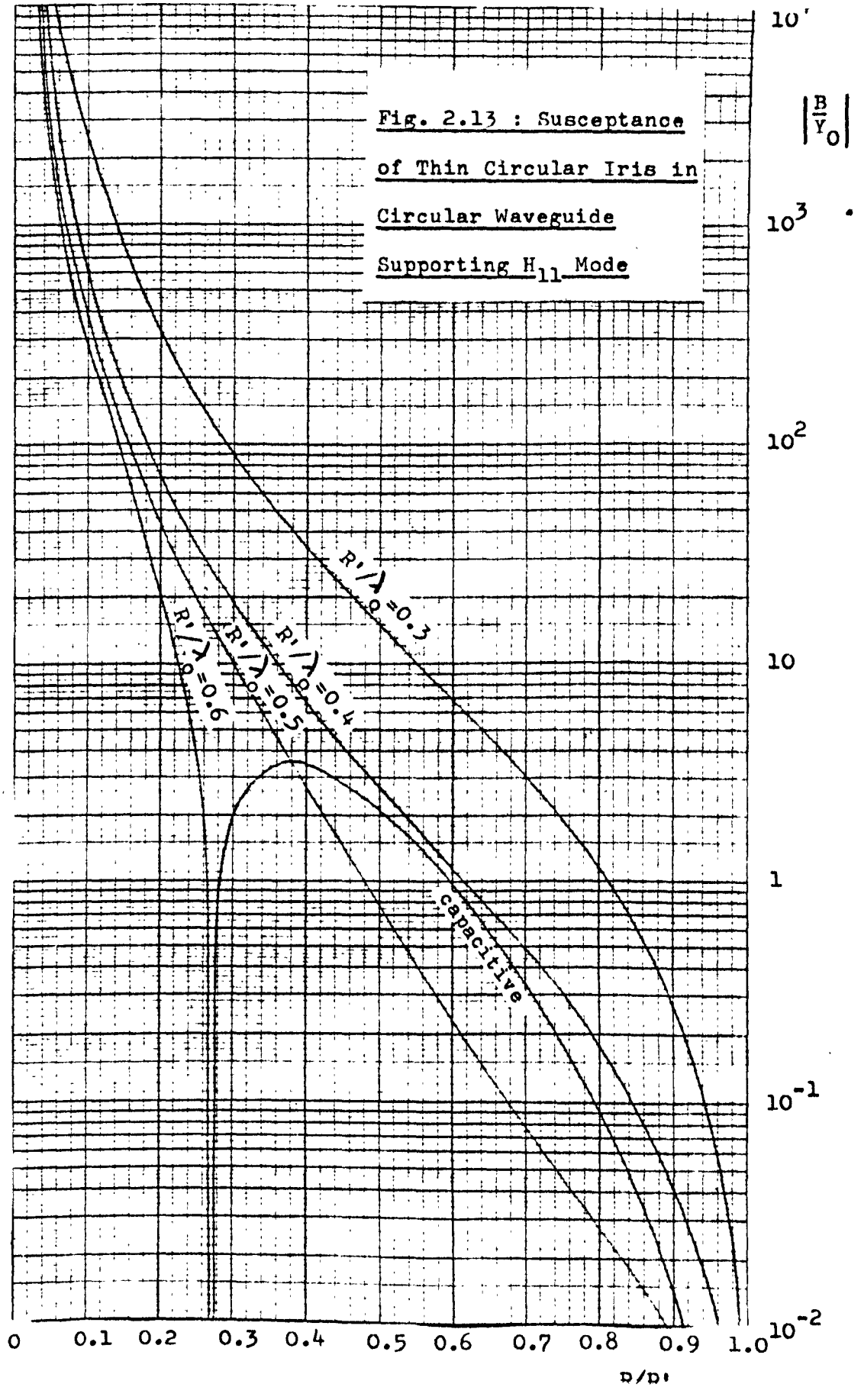
Fig. 2.13 : Susceptance of Thin Circular Iris in Circular Waveguide Supporting H_{11} Mode
$\left|\frac{B}{Y_0}\right|$
10^{1}
10^{3}
10^{2}
10
1
10^{-1}
10^{-2}
R'/λ0 =0.3
R'/λ0 =0.4
R'/λ0 =0.5
R'/λ0 =0.6
capacitive
0
0.1
0.2
0.3
0.4
0.5
0.6
0.7
0.8
0.9
1.0
R/R'

The application of the technique to multi-aperture problems such as inductive or capacitive strips in rectangular guide or annular irises in circular guide is also straightforward. The general thin iris theory of section 2.1 applies, using the forms for matrices $[R]$ and $[S]$ given by 1.20 and 1.25. Here again, the "breakpoint" technique can be used to confirm the optimum values for the ratios q_k/p.

In all the examples considered so far, the aperture and waveguide cross-sections have had similar geometries. If this is not the case the argument put forward in section 2.2 for the existence of the "breakpoint" does not apply. Consider the case of an iris in rectangular waveguide having a circular aperture: the waveguide fields are expressed in terms of sines and cosines whereas those in the aperture involve Bessel Functions. It is difficult to see how any particular ratio q/p could correspond to optimum field matching, since, after conversion to Cartesian co-ordinates, the spatial frequency of a given aperture component varies with x and y, whereas that of a waveguide mode does not. A plot of B/Y_0 as a function of q with p held constant would probably give no indication of the optimum ratio.

The results of the field-matching investigation in section 2.2 showed that correct matching could be obtained with a less than optimum value of q/p, although convergence was slower. Whether the final value of B/Y_0 is the same under these circumstances as with the "breakpoint" ratio is questionable, but results indicate that if there is a discrepancy it will be very small. For example, in the symmetrical inductive iris case where $d/a = 0.5$, $a=0.8\,\lambda_o$ solutions for $q/p=0.4$ and $q/p = 0.5$ agree to within 0.6% when $q=20$. Applying these

findings to the mixed - geometry example, a fairly accurate solution should be obtained with an arbitrarily chosen value of q/p, provided this is small enough to avoid a divergent situation. Some experimentation would reveal the value which gave most rapid convergence. A drawback in the solution of this type of problem is that the surface integrals involved in the expressions for the elements of matrices [R] and [S] must be evaluated numerically. This is a rather time-consuming process, and one which introduces further inaccuracies. For these reasons the solution of a problem of this type was not attempted. However, it is suggested that future work on thin irises should include a study of the mixed - geometry case. It might, for example, be possible to speed up the solution in such cases by modifying the method to include the use of Fast Fourier Transforms.

An aspect of the thin iris problem which has not been investigated is the way in which the magnetic field goes to infinity near the aperture edges in the limit as p becomes infinite, and how this depends on q/p. There seems to be an analogy here with Mittra's investigation of a method for treating a thin bifurcation in rectangular waveguide [20], in which he shows that there is a unique choice of the ratios of numbers of modes for which the condition that the field goes to infinity as $r^{-\frac{1}{2}}$ at the edge of the septum is satisfied, and that only with this choice does convergence to the correct solution occur. (r is here the radial distance from the edge). A study of the magnetic field's behaviour near an iris edge might therefore show whether values of q/p less than the "breakpoint" value could give an exact solution.

CHAPTER III THE SPECIAL CASE OF A WAVEGUIDE STEP DISCONTINUITY

3.1. Description of Problem and Method of Solution.

The type of discontinuity which will be considered in this chapter consists of a junction between two waveguides of different cross-sections, such that at the discontinuity plane the cross-section of the smaller guide is entirely contained within the cross-section of the larger. The two guides are joined by means of a perfectly conducting step. Since the large waveguide may support more propagating modes than the smaller, the junction is useful as a launcher of higher order modes. The treatment can be extended to bifurcations, or to junctions of several parallel waveguides. A further development is the analysis of double step discontinuities, for example a thick iris.

In the general two-waveguide junction of figure 1.1, consider now that the thin diaphragm in the discontinuity plane is removed, and that, in cross-section AA', surface S lies entirely within surface S'. The coupling aperture now has the same cross-section as waveguide 1, so the aperture functions $\underline{e}_{1m}, \underline{h}_{1m}$ become identical to the field components $\underline{e}_m, \underline{h}_m$ in waveguide 1. It follows from 1.1, 1.5 and 1.7 that

$$a_{im} + a_{rm} = b_{1m}$$

and

$$a_{im} - a_{rm} = c_{1m} \qquad 3.1$$

for all m.

Having set q=p, it is clear from 1.21 and 1.26 that $[R]$ and $[S]$ will now be unit matrices. Substituting for $\{b\}$ and $\{c\}$ in 1.31 using 3.1, the equation becomes

$$\{a_i\} - \{a_r\} = [S'][R']\{a_i\} + [S'][R']\{a_r\} - 2[S']\{a'_i\} \qquad 3.2$$

The elements of the two matrices are now such that:

$$R'_{ij} = \frac{\int_S \underline{e}_j \times \underline{h}'_i \cdot d\underline{s}}{\int_{S'} \underline{e}'_i \times \underline{h}'_i \cdot d\underline{s}} \quad , \quad S'_{ij} = \frac{\int_S \underline{e}_i \times \underline{h}'_j \cdot d\underline{s}}{\int_S \underline{e}_i \times \underline{h}_i \cdot d\underline{s}} \qquad 3.3$$

In equation 3.2, $\{a_i\}$ and $\{a'_i\}$ are known, so 3.2 represents a set of p linear equations in p complex unknowns a_{rm}, which may be solved as in the thin iris case. A matrix equation similar to 3.2 but involving the vector $\{a'_r\}$ instead of $\{a_r\}$ could have been derived, but as p is generally smaller than p', 3.2 gives the least number of simultaneous equations to be solved. Two special cases of 3.2 are of particular interest; that in which incidence is in the form of a unit-amplitude dominant mode in the smaller guide, i.e. $\{a_i\} = \{\Delta\}, \{a'_i\} = 0$, and the converse situation $\{a'_i\} = \{\Delta'\}$, $\{a_i\} = 0$ for incidence from the larger guide. The vectors $\{\Delta\}$ and $\{\Delta'\}$ are here defined so that $\Delta_1 = \Delta'_1 = 1, \Delta_i = \Delta'_i = 0$, $i \neq 1$. The vectors have p and p' elements respectively. For incidence from the small guide, 3.2 becomes:

$$([T'] + [I])\{a_r\} = \{\Delta\} - \{T_1\} \qquad 3.4$$

where $[T'] = [S'][R']$ and $[I]$ is a pxp unit matrix. $\{T_1\}$ is the first column of $[T']$. The equation for incidence from the large guide is:

$$([T'] + [I])\{a_r\} = 2\{S'_1\} \qquad 3.5$$

where $\{S'_1\}$ is the first column of $[S']$.

Except for the inclusion of the unit matrix and the different constant terms, 3.4 and 3.5 are similar to the thin iris equation 2.15, and a single computer program can be used to solve either a step or an iris problem. Details of the modifications involved will be given later.

Having obtained the small-waveguide coefficients a_{rm}, these for the large waveguide may be obtained from 1.23, having substituted for $\{b\}$ using 3.1. The version of 1.23 corresponding to 3.4 is

$$\{a'_r\} = [R'] \{a_r\} + \{R'_1\} \qquad 3.6$$

where $\{R'_1\}$ is the first column of $[R']$, and that corresponding to 3.5 is

$$\{a'_r\} = [R'] \{a_r\} - \{\Delta'\} \qquad 3.7$$

As mentioned in chapter 1, the use of the above approach to solve step problems is not new, although the formulation given here differs in some respects from that of other workers. For example, an improvement which has been made on the work of Clarricoats and Slinn [6] is the elimination of one unknown column vector to give an equation such as 3.1. In their treatment, $\{a_r\}$ and $\{a'_r\}$ were obtained simultaneously by solving a set of p+p' equations in p+p' unknowns. Unnecessarily large amounts of computer time and storage were therefore required. The advantage of eliminating one vector has also been recognised by Cole [8], who derives an equation very similar to 3.4, but solves it by an iterative method as opposed to the direct technique of elimination and back-substitution used here. There seems little advantage in this, since solutions have been obtained with quite adequate speed using the direct method. (Run time is comparable to that for the thin iris solution - see section 2.21). Moreover, Cole seems to have had some difficulty in obtaining reliable convergence with the iterative technique. The approach described in Cole's paper also differs in that the expressions for the elements of matrices $[R']$ and $[S']$ involve scalar products of two electric or magnetic field components rather than the vector products as shown in 3.3. If the waveguides are homogeneous, the two

methods give rise to identical sets of equations, but if scalar products are used junctions involving dielectric-filled guides cannot in general be treated, because the transverse electric or magnetic field components of any two modes may no longer be orthogonal.

Wexler [7] has formulated the solution in a similar way to that described here, but does not use matrix notation. Although not essential for the solution of a single step, matrix notation is almost indispensable when treating double discontinuities such as the thick iris, as will be seen later in this chapter.

It should be pointed out that although in some instances it parallels the work of Cole and Wexler, the research described in this chapter was largely carried out before the publication of these papers.

3.2. The Equivalence of Modal Analysis and Variational Methods in the Case of a single-mode Step Discontinuity.

In the particular case of a step discontinuity where incidence is in the form of a dominant-mode wave from one side, other modes being below cut-off, a variational approach based on that given by Collin and Brown [21] can lead to the generation of a set of linear equations identical to that obtained by Modal Analysis, as represented by 3.4 or 3.5.

The coefficients of modes on both sides of the junction are expressed in terms of the transverse electric field, $\underline{E}_T$, in the discontinuity plane, using Fourier analysis:

$$\delta_{M1} + a_{rM} = \frac{\left[\underline{E}_T, \underline{h}_M \right]_S}{\left[\underline{e}_M, \underline{h}_M \right]_S} \qquad 3.8$$

$$a'_{rN} = \frac{[\,\underline{E}_T,\ \underline{h}'_N\,]_S}{[\,\underline{e}'_N,\ \underline{h}'_N\,]_S}, \qquad 3.9$$

$$M,N = 1,2,3\ldots\infty$$

Dashed quantities refer to the larger guide, incidence is from the smaller guide, and the notation

$$[\,\underline{u},\underline{v}\,]_S \equiv \int_S \underline{u} \times \underline{v}.d\underline{s}$$

has been used. In equation 3.9, the vanishing of the electric field over the step has been incorporated to enable orthogonality of modes in the larger guide to be used. The coefficient in the magnetic field matching equation

$$\underline{h}_1 - \sum_{m=1}^{\infty} a_{rm}\,\underline{h}_m = \sum_{n=1}^{\infty} a'_{rn}\,\underline{h}'_n \qquad 3.10$$

are now replaced by the expressions in 3.8 and 3.9, with the exception of a_{r1}. The following equation can be obtained:

$$\frac{1-a_{r1}}{1+a_{r1}}\frac{[\,\underline{E}_T,\underline{h}_1\,]_S}{[\,\underline{e}_1,\underline{h}_1\,]_S}\underline{h}_1 = \sum_{m=2}^{\infty}\frac{[\,\underline{E}_T,\underline{h}_m\,]_S}{[\,\underline{e}_m,\underline{h}_m\,]_S}\underline{h}_m + \sum_{n=1}^{\infty}\frac{[\,\underline{E}_T,\underline{h}'_n\,]_S}{[\,\underline{e}'_n,\underline{h}'_n\,]_S}, \qquad 3.11$$

The term $\frac{1-a_{r1}}{1+a_{r1}}$ will be written as Y_{in}, the complex input admittance for the transmission line equivalent circuit. Each term in 3.11 is vector pre-multiplied by $\underline{\mathcal{E}}_T$, an arbitrary transverse vector function which exists over surface S, and then integrated over S. The result is:

$$Y_{in} = \frac{\displaystyle\sum_{m=2}^{\infty}\frac{[\,\underline{E}_T,\underline{h}_m\,]_S\,[\,\underline{\mathcal{E}}_T,\underline{h}_m\,]_S}{[\,\underline{e}_m,\underline{h}_m\,]_S} + \sum_{n=1}^{\infty}\frac{[\,\underline{E}_T,\underline{h}'_n\,]_S\,[\,\underline{\mathcal{E}}_T,\underline{h}'_n\,]_S}{[\,\underline{e}'_n,\underline{h}'_n\,]_S}}{\dfrac{[\,\underline{E}_T,\underline{h}_1\,]_S\,[\,\underline{\mathcal{E}}_T,\underline{h}_1\,]_S}{[\,\underline{e}_1,\underline{h}_1\,]_S}}, \qquad 3.12$$

It can easily be shown that Y_{in} is stationary for small changes in $\underline{\mathcal{E}}_T$. To make it also stationary for small changes in $\underline{E}_T$, it is necessary to put $\underline{E}_T = \underline{\mathcal{E}}_T$. The variational expression for Y_{in} is therefore:

$$Y_{in} = \frac{\sum_{m=2}^{\infty} \frac{[\underline{E}_T, \underline{h}_m]_S^2}{[\underline{e}_m, \underline{h}_m]_S} + \sum_{n=1}^{\infty} \frac{[\underline{E}_T, \underline{h}'_n]_S^2}{[\underline{e}'_n, \underline{h}'_n]_S}}{\frac{[\underline{E}_T, \underline{h}_1]_S^2}{[\underline{e}_1, \underline{h}_1]_S}} \qquad 3.13$$

$\underline{E}_T$ must now be chosen so that the above expression is satisfied. If it is written as an infinite series of the electric fields of modes in the smaller guide, i.e.

$$\underline{E}_T = \underline{e}_1 + \sum_{M=1}^{\infty} a_{rM} \underline{e}_M ,$$

Y_{in} will have the required property if

$$\frac{\partial Y_{in}}{\partial a_{rM}} = 0 \text{ for all } M.$$

After substituting for $\underline{E}_T$ in 3.13 and using the fact that orthogonality holds for modes in the smaller guide, the equation becomes:

$$Y_{in} = \sum_{m=2}^{\infty} a_{rm}^2 \frac{[\underline{e}_m, \underline{h}_m]_S}{(1+a_{r1})^2 [\underline{e}_1, \underline{h}_1]_S} + \sum_{n=1}^{\infty} \frac{\left\{ \sum_{p=1}^{\infty} (\delta_{p1} + a_{rp}) [\underline{e}_p, \underline{h}'_n]_S \right\}^2}{(1+a_{r1})^2 [\underline{e}_1, \underline{h}_1]_S [\underline{e}'_n, \underline{h}'_n]_S} \qquad 3.14$$

For M>1, the application of the condition for Y_{in} to be stationary for small changes in a_{rM} is straightforward, the result being:

$$a_{rM} + \sum_{n=1}^{\infty} \left\{ \frac{[\underline{e}_M, \underline{h}'_n]_S}{[\underline{e}_M, \underline{h}_M]_S} \sum_{p=1}^{\infty} (\delta_{p1} + a_{rp}) \frac{[\underline{e}_p, \underline{h}'_n]_S}{[\underline{e}'_n, \underline{h}'_n]_S} \right\} = 0 \qquad 3.15$$

When M=1, differentiation of 3.14 gives:

$$\frac{\partial Y_{in}}{\partial a_{r1}} = \frac{2}{(1+a_{r1})^2} \sum_{n=1}^{\infty} \left\{ \frac{[\underline{e}_1, \underline{h}'_n]_S}{[\underline{e}_1, \underline{h}_1]_S} \sum_{p=1}^{\infty} (\delta_{p1}+a_{rp}) \frac{[\underline{e}_p, \underline{h}'_n]_S}{[\underline{e}'_n, \underline{h}'_n]_S} \right\}$$

$$- 2 \frac{(1+a_{r1})^2}{(1+a_{r1})^3} Y_{in} \qquad 3.16$$

Writing $Y_{in} = \frac{1-a_{r1}}{1+a_{r1}}$ in the second part of 3.16 and setting $\frac{\partial Y_{in}}{\partial a_{r1}} = 0$ leads to the result:

$$a_{r1} + \sum_{n=1}^{\infty} \left\{ \frac{[\underline{e}_1, \underline{h}'_n]_S}{[\underline{e}_1, \underline{h}_1]_S} \sum_{p=1}^{\infty} (\delta_{p1}+a_{rp}) \frac{[\underline{e}_p, \underline{h}'_n]_S}{[\underline{e}'_n, \underline{h}'_n]_S} \right\} = 1 \qquad 3.17$$

If the integrals in 3.15 and 3.17 are now expressed using the notation given by 3.3, these equations can be written in the general form:

$$a_{rM} + \sum_{p=1}^{\infty} \sum_{n=1}^{\infty} S'_{Mn} R'_{np} (\delta_{p1}+a_{rp}) = \delta_{M1} \qquad 3.18$$

$$M = 1,2,3 \ldots \infty$$

It can be seen by comparing 3.18 and 3.4 that apart from the replacement of infinite by truncated series the two expressions are identical. Similarly, if incidence from the larger waveguide is considered, an expression equivalent to 3.5 can be obtained.

Although leading to the same result, the variational formulation is not nearly as straightforward as Model Analysis. It is also more restricted in application, since the above approach is not valid if several modes are simultaneously incident on the junction.

This illustration of a parallel between the computational and variational methods in a particular case is valuable in that it tends to confirm the correctness of the new method, at the same time showing its advantages in terms of generality and simplicity over a well-established technique.

3.3 Choosing the Ratio of the Numbers of Modes.

By analogy with the thin iris, the choice of the mode ratio p/p' can be expæted to have a significant effect on the convergence of a step discontinuity's solution as p and p' increase, and a similar argument regarding correct matching of field components in the aperture can be applied. For junctions of waveguides with similar geometries, it is easy to see what ratios will equate the spatial frequencies of the highest order modes on either side of the discontinuity plane. For example, the ratios for the junctions shown in figure 3.1 should be $p/p'=d/a$ for case (a), the H-plane step, and $p/p'=b'/b$ for case (b), the E-plane step. To confirm that such ratios also give optimum convergence, the equivalent normalised susceptance for a symmetric E-plane step discontinuity in which $b'/b=0.5$ has been calculated as a function of p, for various mode ratios p/p'. The results are shown in figure 3.2. In all cases convergence is to very similar, if not identical, values. Any discrepancy there may be between the final values is less than 0.3%. The choice of p/p' is therefore not nearly so critical as the choice of q/p for the thin iris, and it is clear how other workers succeeded in obtaining accurate results with arbitrarily chosen ratios. It can be seen, however, that with the ratio for optimum field matching, $p/p'=0.5$,

Fig. 3.1 : Rectangular Waveguide Step Discontinuities with Equivalent Circuits for Single-Mode Propagation

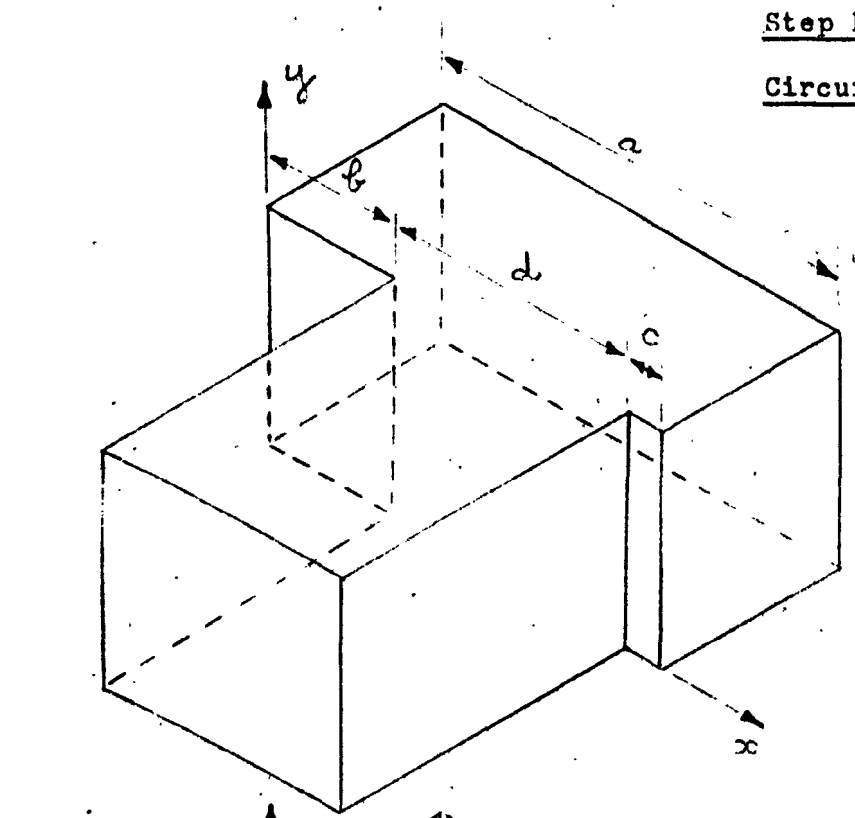

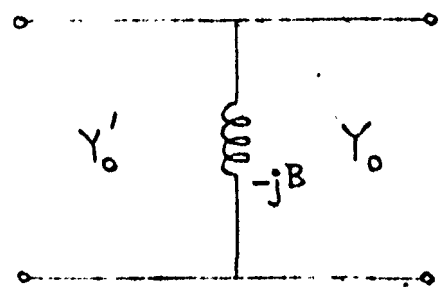

(a) H-Plane Step

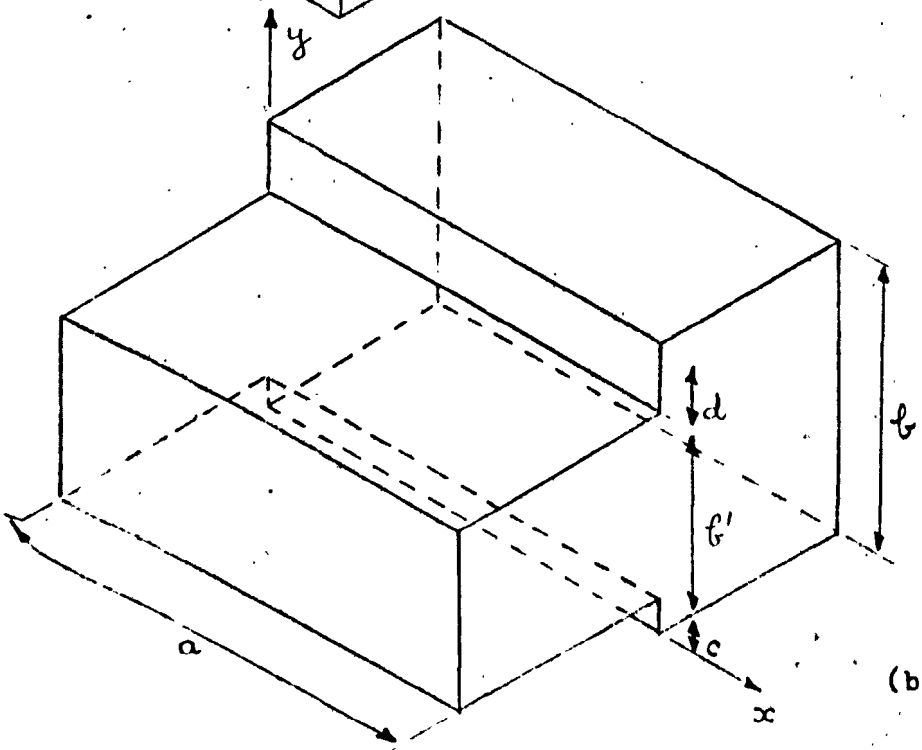

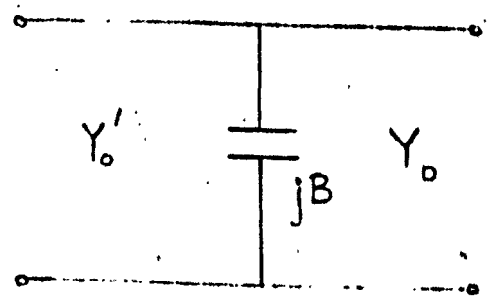

(b) E-Plane Step

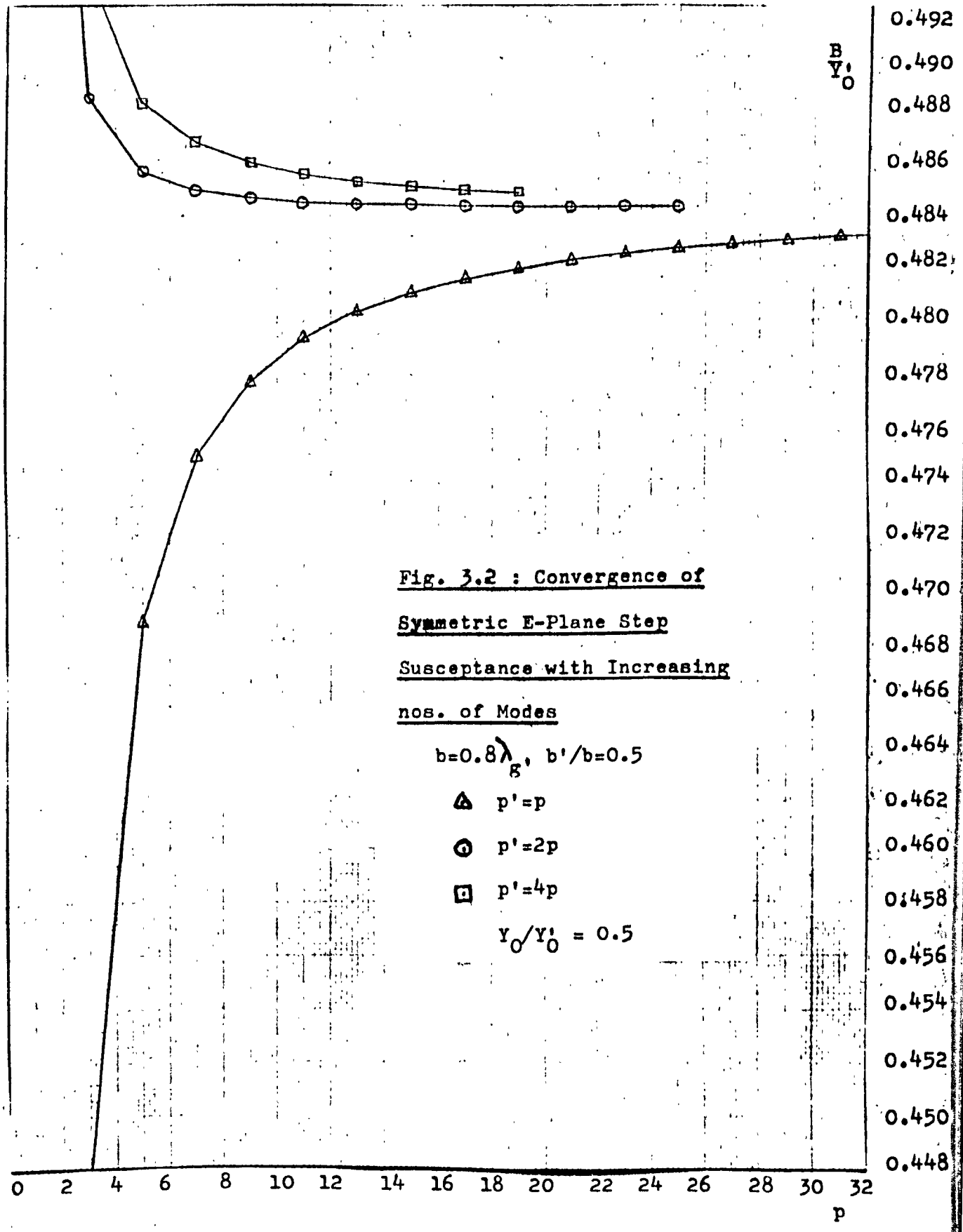

Fig. 3.2 : Convergence of Symmetric E-Plane Step Susceptance with Increasing nos. of Modes

convergence is considerably faster than in the other cases. For example, an error of less than one percent can be achieved with only three modes in the small waveguide whereas five modes are required in the case $p/p'=0.25$, and twelve when p and p' are equal. Since the value of p governs the number of simultaneous equations to be solved, it is clear that for a solution of given accuracy there will be a considerable saving of computer time and storage if p/p' is correctly chosen.

Referring back to the combined step and iris for which results were given in figure 1.2, it is now possible to apply the condition of spatial-frequency matching for the highest order modes and aperture functions to obtain the correct values of the ratios q/p and p/p'. Clearly, the most accurate solution for B/Y_L will lie on the 10:20 characteristic at the point q=5. Note that this value corresponds to a well-defined "breakpoint". If the ratio q/p is held constant at 1/2, an increase in p' from 20 to 30 changes the value of B/Y_L by less than 1½%. If p' is reduced to 10 the change is about 7½%. Similarly, if q/p' is kept as near as possible to 1/4, and p/p' is varied, no change greater than 10% occurs even though q may be as small as 2. Y_R/Y_L does not vary by more than 1% in any of these cases. When these figures are viewed in the light of the gross variations which may occur if other values of p,p' and q are selected, it is clear that provided there is correct spatial-frequency matching between the aperture functions and one set of waveguide modes, errors in the choice of the number in the other set will not drastically affect the solution. This is always the case with the type of step discontinuity treated in

this chapter, since the modes in the smaller guide also serve as aperture functions, and this explains why mode ratio is a comparatively minor consideration in the step case.

3.4 H-Plane Step in Rectangular Waveguide

An H-plane step discontinuity in rectangular waveguide is illustrated in figure 3.1(a). If incidence is in the form of the dominant H_{10} mode in either guide, only modes of type H_{n0} will be excited, because of the structure's uniformity in the y-direction. The modal fields in the discontinuity plane may then be expressed as follows:

Small Waveguide

$$\underline{e}_m = \sin \frac{m\pi}{d}(x-b)\hat{\underline{i}}_y \qquad 3.19(a)$$

$$\underline{h}_m = j\sqrt{\frac{\varepsilon_o}{\mu_o}}\,\bar{\gamma}_m \sin \frac{m\pi}{d}(x-b)\,\hat{\underline{i}}_x \qquad 3.19(b)$$

where $\bar{\gamma}_m = \sqrt{\frac{m^2}{4(d/\lambda_o)^2} - 1}$

Large Waveguide

$$\underline{e}'_n = \sin \frac{n\pi x}{a}\,\hat{\underline{i}}_y \qquad 3.20(a)$$

$$\underline{h}'_n = j\sqrt{\frac{\varepsilon_o}{\mu_o}}\,\bar{\gamma}'_n \sin \frac{n\pi x}{a}\,\hat{\underline{i}}_x \qquad 3.20(b)$$

where $\bar{\gamma}'_n = \sqrt{\frac{n^2}{4(a/\lambda_o)^2} - 1}$

The expression for an element of $[R']$, defined by 3.3, is identical to that for an element of $[R]$ in the iris case, as given by expressions 2.14(a) and (b). The elements of $[S']$ are related to those of $[R']$ through the equation:

$$S'_{mn} = \frac{a}{d} \frac{\bar{\gamma}'_n}{\bar{\gamma}_m} R'_{nm} \qquad 3.21$$

Because two propagation coefficients, which can be real or imaginary, are involved in the above expression, the procedure for assigning values to the real matrices $[A]$ and $[B]$ corresponding to the complex matrices $[R']$ and $[S']$ is slightly more complicated than in the case of the thin iris. However, the details of this operation should be clear from the flow diagram of figure 3.3. Comparison of this diagram with figure 2.2 shows that, with only minor modifications, a program for solving the H-plane step could be made to solve the thin inductive iris as well.

The conditions for single-mode propagation, when only the H_{10} mode is above cut-off in either waveguide, are:

$0.5 < a/\lambda_0 < 1.5, \quad 0.5 < d/\lambda_0 < 1.5$ when c=b

$0.5 < a/\lambda_0 < 1.0, \quad 0.5 < d/\lambda_0 < 1.0$ when c≠b

It is possible in this case to represent the junction by the transmission line equivalent circuit included in figure 3.1(a). When incidence is from the smaller guide, the circuit parameters are derived from the reflection coefficient a_{r1} using the equation:

$$\frac{1 - a_{r1}}{1 + a_{r1}} = \frac{Y_0}{Y'_0} + \frac{jB}{Y'_0} \qquad 3.22$$

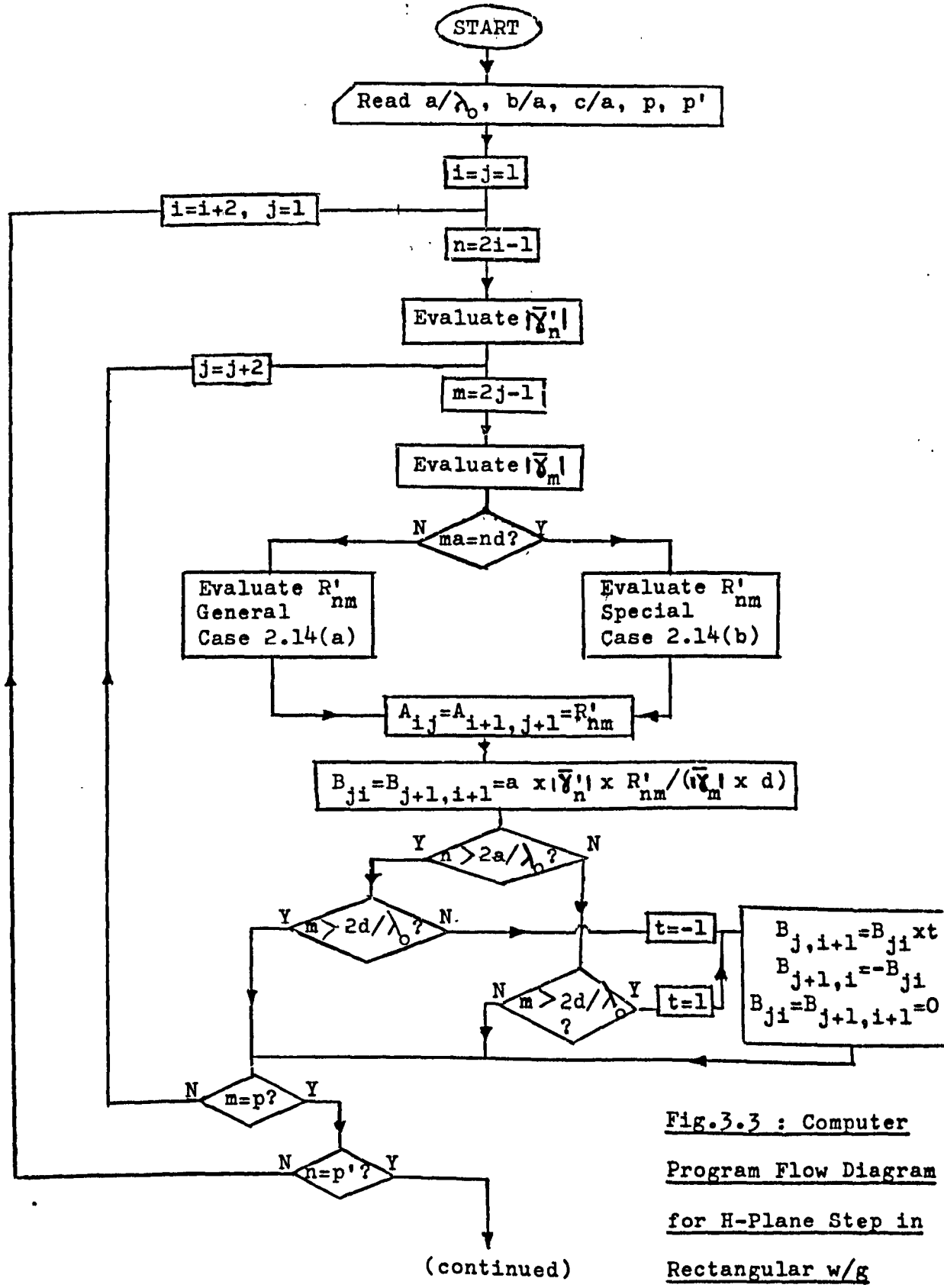

Fig.3.3 : Computer Program Flow Diagram for H-Plane Step in Rectangular w/g

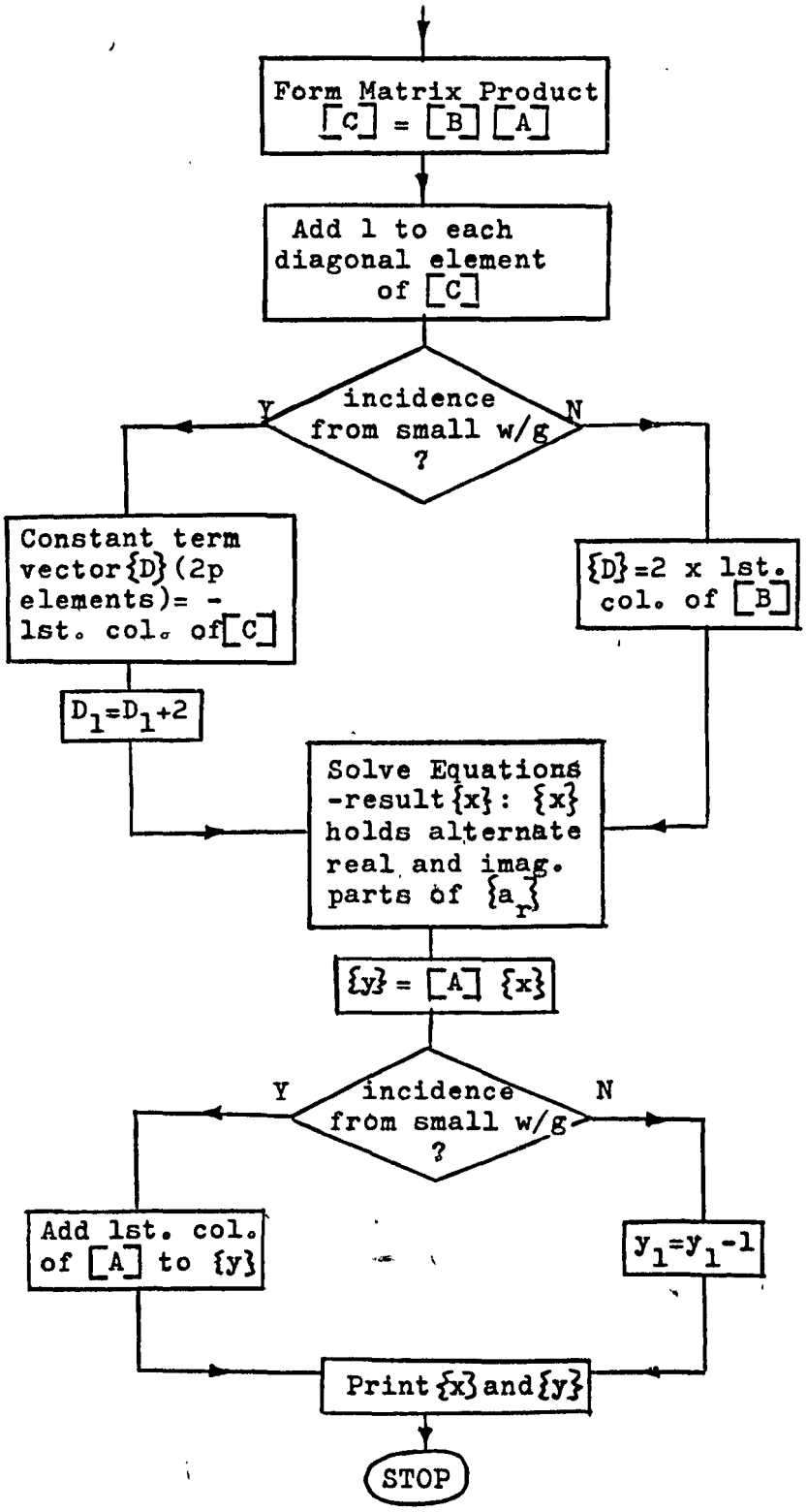

Fig.3.3 (continued)

Note, however, that if incidence is from the larger guide the parameters will not be exactly the same as those given by 3.22.

Results for the single-mode case will not be given here, as its solution by modal analysis has already been investigated by other workers. Clarricoats and Slinn [6] have obtained values of the equivalent circuit parameters which agree with those given by Marcuvitz [4] to within the accuracy specified for the latter results. As they arbitrarily set the mode ratio equal to unity, and took only seven modes into account, their work confirms the non-critical nature of the mode ratio and rapid convergence of the solution when the computational method is applied to step discontinuities.

An H-plane junction of rectangular waveguides capable of supporting more than one propagating mode has been solved by Felsen [22] using a quasi-optical technique. Comparison has been made between his results and those derived by the computational method in both symmetric and asymmetric cases, and for incidence of the dominant mode from either waveguide. Agreement was found to be satisfactory in all cases. The results presented here (figures 3.4 and 3.5) are for a symmetric step in which the dominant mode is incident in the smaller guide, the guide widths being in the ratio 2:1. 24 modes were taken into account in the larger guide and 12 in the smaller. The amplitudes of H_{10}, H_{30} and H_{50} modes reflected from the junction are shown in figure 3.4 as functions of frequency, whilst figure 3.5 gives their phases relative to that of the incident H_{10} mode. Whereas Felsen's curves are smooth, those derived by the computational method have several "breakpoints"

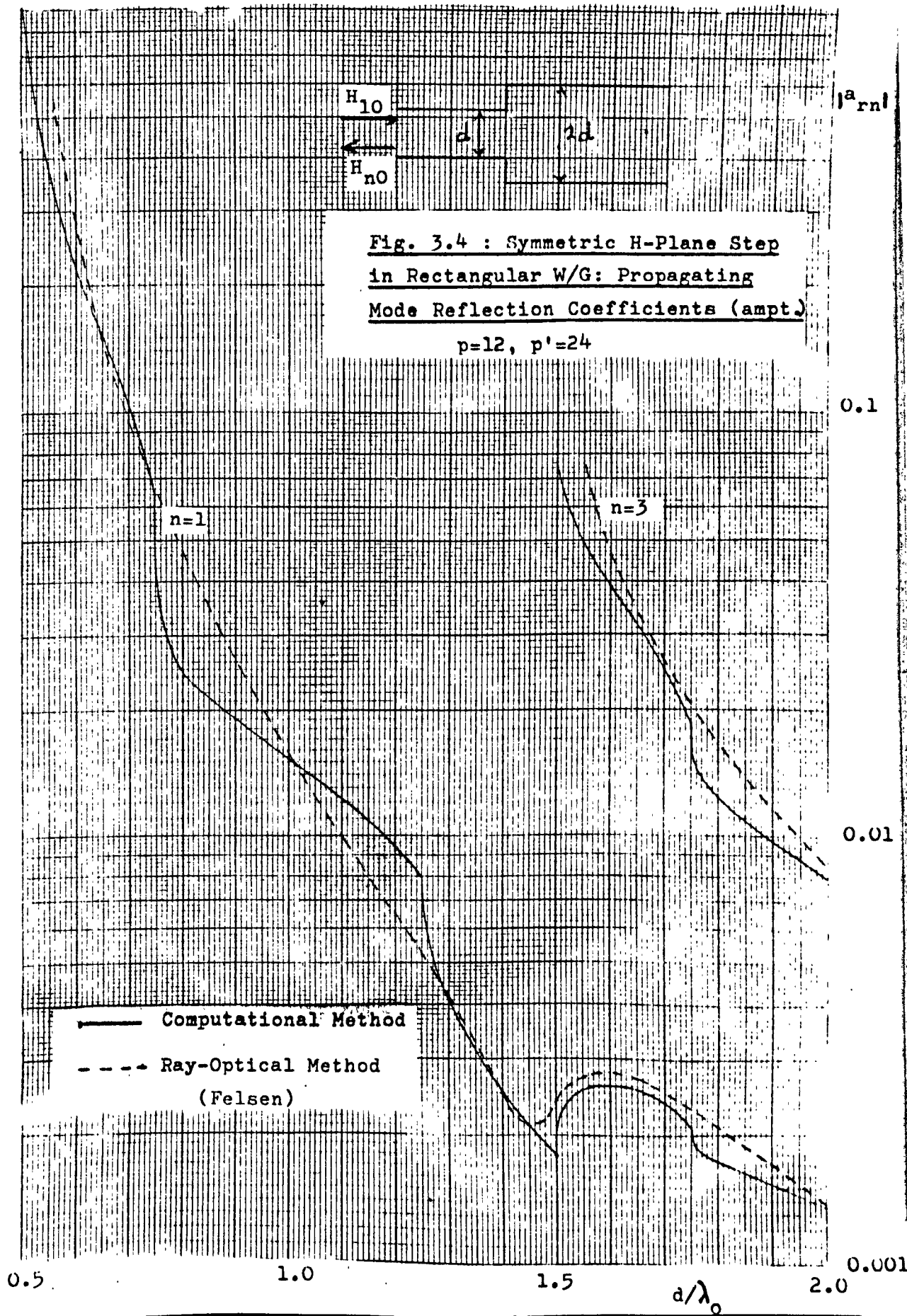

Fig. 3.4 : Symmetric H-Plane Step in Rectangular W/G: Propagating Mode Reflection Coefficients (ampt.)

p=12, p'=24

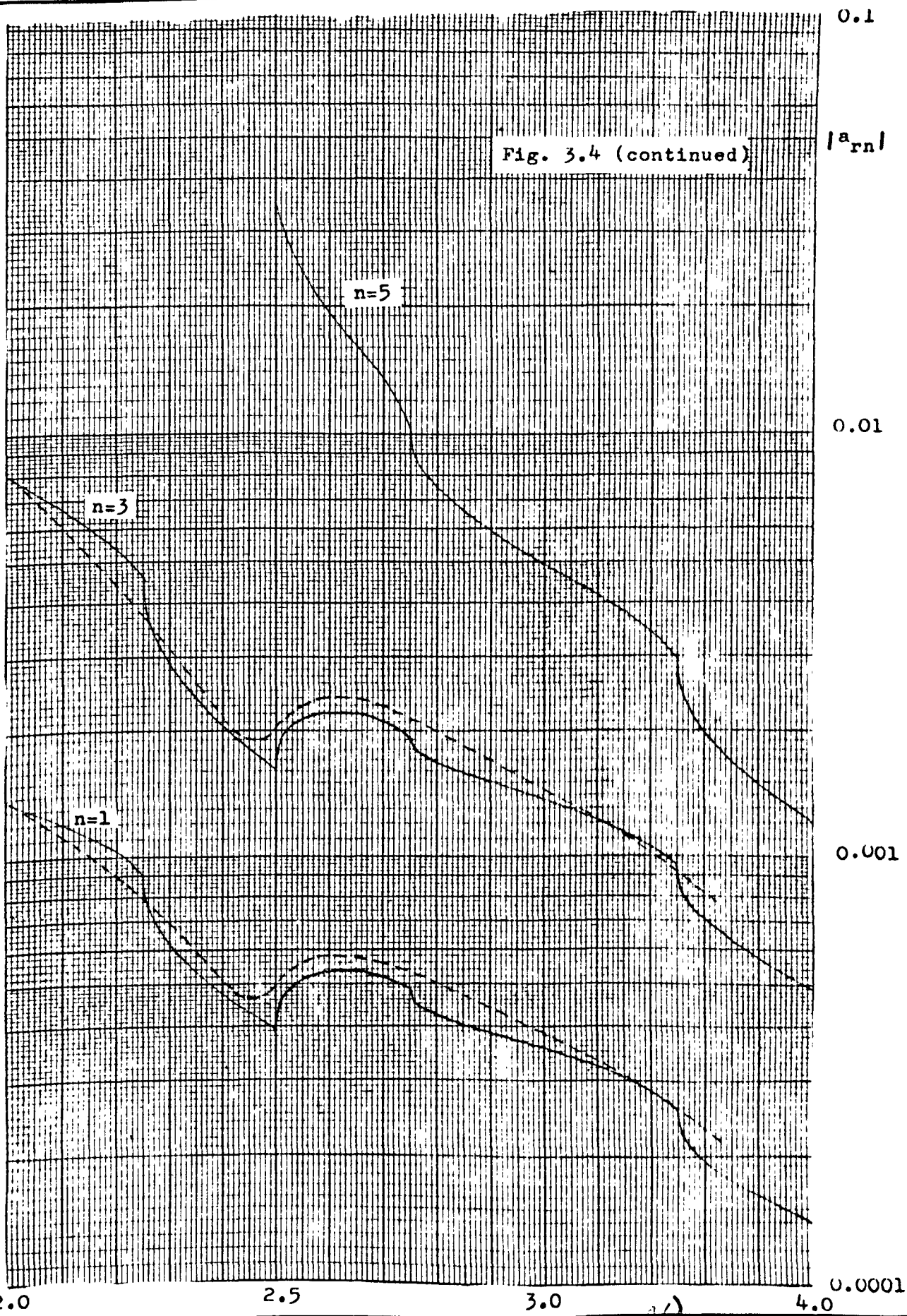
Fig. 3.4 (continued)
$|a_{rn}|$
0.1
0.01
0.001
0.0001
n=5
n=3
n=1
2.0
2.5
3.0
4.0

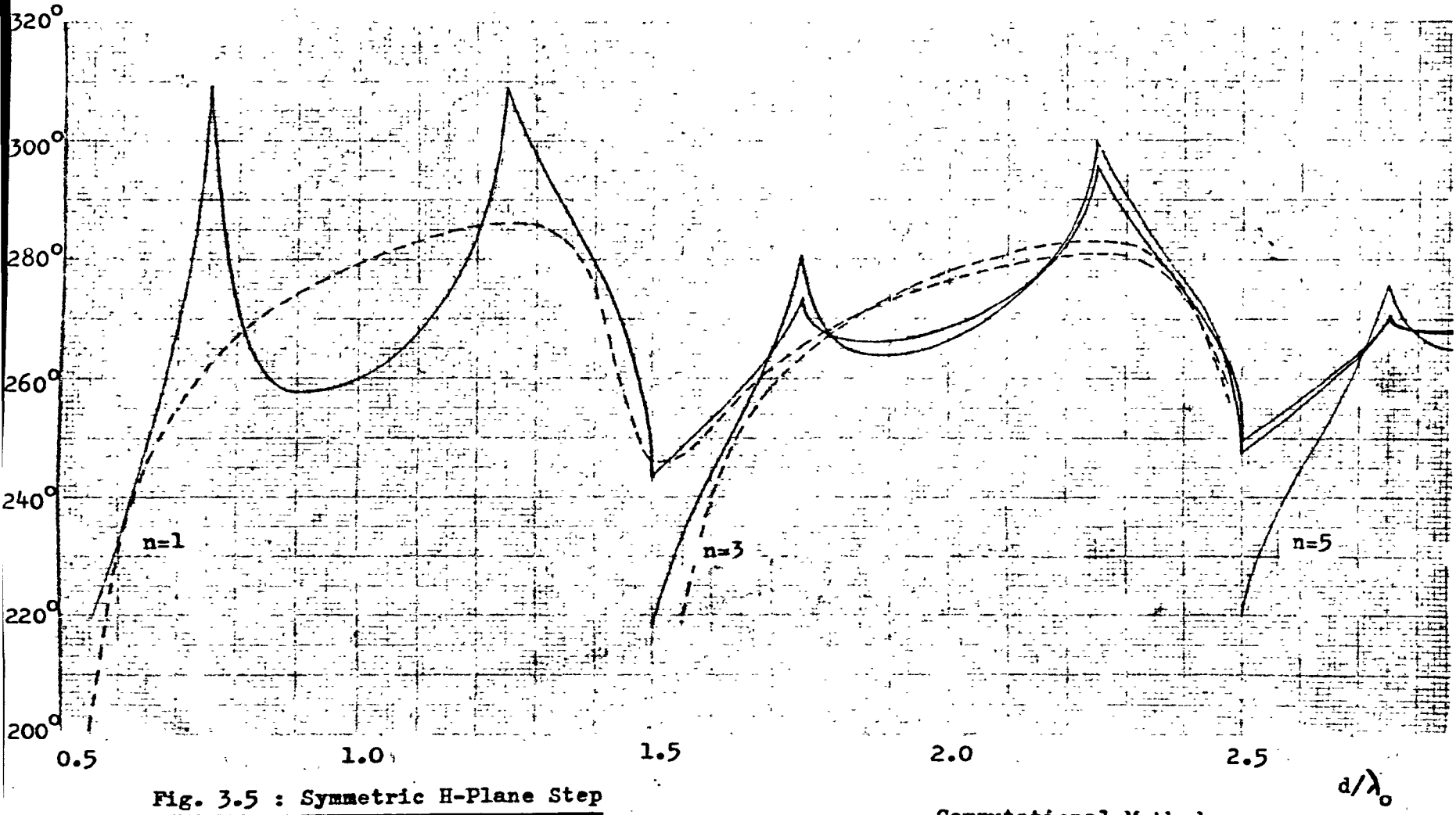

Fig. 3.5 : Symmetric H-Plane Step in Rectangular Waveguide - Propagating Mode Reflection Coefficients (phase)

corresponding to higher-mode cut-off frequencies. It would seem that Felsen's method is too approximate to bring out the fine structure of the curves. Since the discrepancy between the solutions in the vicinity of a "breakpoint" can be as much as 90% in amplitude and 50° in phase, the computational method is particularly valuable if operation near a cut-off point is of interest.

3.5 E-plane Step Discontinuity in Rectangular Waveguide.

The E-plane step, illustrated in figure 3.1(b), has already been mentioned in section 3.3. As in the case of the capacitive iris (section 2.3), the solution can be formulated in terms of modes of type LSE_{1n}, n being odd for a symmetrical junction, i.e. c=d. These modes have transverse fields in the discontinuity plane given by:

In the large waveguide

$$\underline{e}'_n = \sin\frac{\pi x}{a}\cos\frac{n\pi y}{b}\,\hat{\underline{i}}_y \qquad 3.23(a)$$

$$\underline{h}'_n = j\sqrt{\frac{\varepsilon_o}{\mu_o}}\,\frac{1}{\underline{\gamma}'_n}\left\{\left(\lambda_o^2/4a^2 - 1\right)\sin\frac{\pi x}{a}\cos\frac{n\pi y}{b}\,\hat{\underline{i}}_x + \frac{n\lambda_o^2}{4ab}\cos\frac{\pi x}{a}\sin\frac{n\pi y}{b}\,\hat{\underline{i}}_y\right\} \qquad 3.23(b)$$

In the small waveguide

$$\underline{e}_m = \sin\frac{\pi x}{a}\cos\frac{m\pi y}{b'}\,\hat{\underline{i}}_y \qquad 3.24(a)$$

$$\underline{h}_m = j\sqrt{\frac{\varepsilon_o}{\mu_o}}\,\frac{1}{\underline{\gamma}_m}\left\{\left(\lambda_o^2/4a^2 - 1\right)\sin\frac{\pi x}{a}\cos\frac{m\pi y}{b'}\,\hat{\underline{i}}_x + \frac{m\lambda_o^2}{4ab'}\cos\frac{\pi x}{a}\sin\frac{m\pi y}{b'}\,\hat{\underline{i}}_y\right\} \qquad 3.24(b)$$

where $\underline{\gamma}'_n = \sqrt{\left\{\frac{\lambda_o^2}{4}\left[\frac{1}{a}^2 + \frac{n}{b}^2\right] - 1\right\}}$ & $\underline{\gamma}_m = \sqrt{\left\{\frac{\lambda_o^2}{4}\left[\frac{1}{a}^2 + \frac{m}{b'}^2\right] - 1\right\}}$

The elements of $[R']$ are then identical to those of $[R]$ in the capacitive iris formulation, and may be evaluated using 2.24. The relation between the elements of $[S']$ and $[R']$ is:

$$S'_{mn} = \frac{\bar{\gamma}_m}{\bar{\gamma}'_n} \frac{b}{b'} \frac{\varepsilon_{mO}}{\varepsilon_{nO}} R'_{nm} \qquad 3.25$$

Having assigned values to the elements of these matrices, the method of solution is then identical to that for the H-plane step.

In the case of single-mode propagation, i.e.

$$b/\lambda_g < 0.5, \quad b'/\lambda_g < 0.5 \quad \text{when } c \neq d$$
$$b/\lambda_g < 1, \quad b'/\lambda_g < 1 \quad \text{when } c = d$$

where $\lambda_g = \lambda_o/\sqrt{(1-\lambda_o^2/4a^2)}$, the transmission line equivalent circuit included in figure 3.1(b) can be used, the parameters being derived from the complex reflection coefficient through 3.22. In this particular case the circuit parameters are the same whichever side incidence is from. The computed results show that, for any set of dimensions or ratio of modes, the admittance ratio is exactly that of the heights of the guides, i.e.

$$\frac{Y_O}{Y'_O} = \frac{b'}{b} \qquad 3.26$$

This is in agreement with the findings of Marcuvitz [4].

In figure 3.6, computed values of normalised equivalent susceptance for a symmetrical junction are shown superimposed on curves from the "Waveguide Handbook" [4]. 20 modes were taken into account in the larger waveguide, and the mode ratio was taken as $p'/p = b/b'$. It can

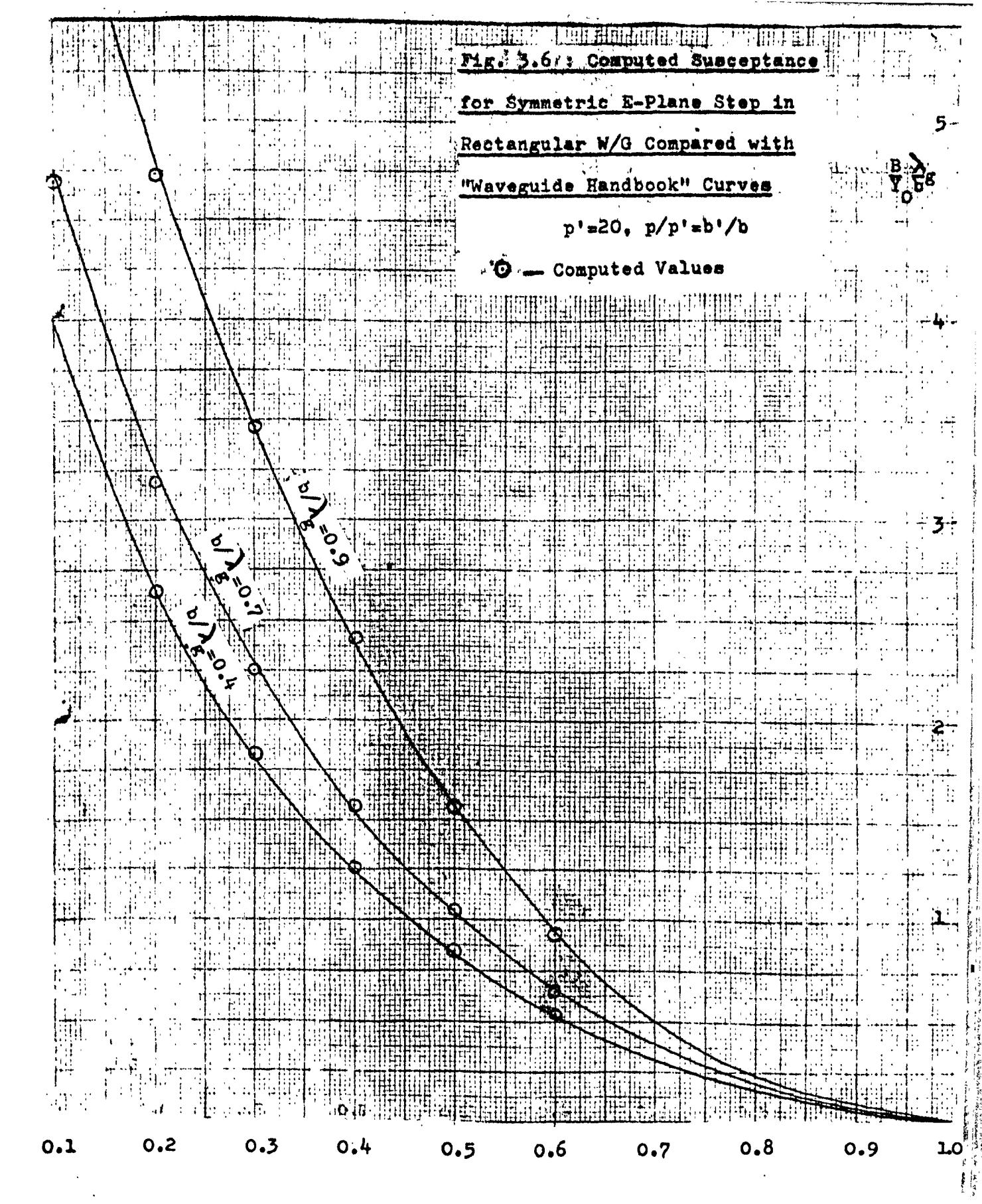
Fig. 3.6 : Computed Susceptance for Symmetric E-Plane Step in Rectangular W/G Compared with "Waveguide Handbook" Curves
p'=20, p/p'=b'/b
— Computed Values
B/Y0 λg/b
λg/b=0.9
λg/b=0.7
λg/b=0.4
5
4
3
2
1
0.1
0.2
0.3
0.4
0.5
0.6
0.7
0.8
0.9
1.0

be seen that agreement is very good, even for small values of b'/b, where accuracy can be expected to be lower because only a few modes in the small waveguide are included in the solution.

3.6 Junction of Circular Waveguides - H_{11} Mode Incident.

A circularly symmetric junction of homogeneous circular waveguides is shown in figure 3.7. If the H_{11} mode is incident from either side, modes of type H_{1n} and E_{1n} will be excited in both waveguides. In the large waveguide, expressions for the transverse fields $\underline{e}'^{(H)}_n$, $\underline{h}'^{(H)}_n$ and $\underline{e}'^{(E)}_n$, $\underline{h}'^{(E)}_n$ are identical to 2.26 and 2.27, except that the propagation coefficients must now be written as γ'_n and δ'_n to distinguish them from those of the small waveguide. The field expressions for the small waveguide are:

$\underline{H}_{1m}$ mode

$$\underline{e}_m^{(H)} = J_1'(k_m r)\cos\theta\,\hat{\underline{i}}_\theta + \frac{1}{k_m r} J_1(k_m r)\sin\theta\,\hat{\underline{i}}_r \qquad 3.27(a)$$

$$\underline{h}_m^{(H)} = -j\frac{\gamma_m}{\omega\mu_o}\left\{\frac{1}{k_m r} J_1(k_m r)\sin\theta\,\hat{\underline{i}}_\theta - J_1'(k_m r)\cos\theta\,\hat{\underline{i}}_r\right\} \qquad 3.27(b)$$

where $k_m R = \chi_m$ and $\gamma_m = \sqrt{(k_m^2 - k_o^2)}$

$\underline{E}_{1m}$ mode

$$\underline{e}_m^{(E)} = \frac{1}{l_m r} J_1(l_m r)\cos\theta\,\hat{\underline{i}}_\theta + J_1'(l_m r)\sin\theta\,\hat{\underline{i}}_r \qquad 3.28(a)$$

$$\underline{h}_m^{(E)} = \frac{j\omega\varepsilon_o}{\delta_m}\left\{J_1'(l_m r)\sin\theta\,\hat{\underline{i}}_\theta - \frac{1}{l_m r} J_1(l_m r)\cos\theta\,\hat{\underline{i}}_r\right\} \qquad 3.28(b)$$

where $l_m R = \xi_m$ and $\delta_m = \sqrt{(l_m^2 - k_o^2)}$

Fig. 3.7 : Junction of

Circular Waveguides

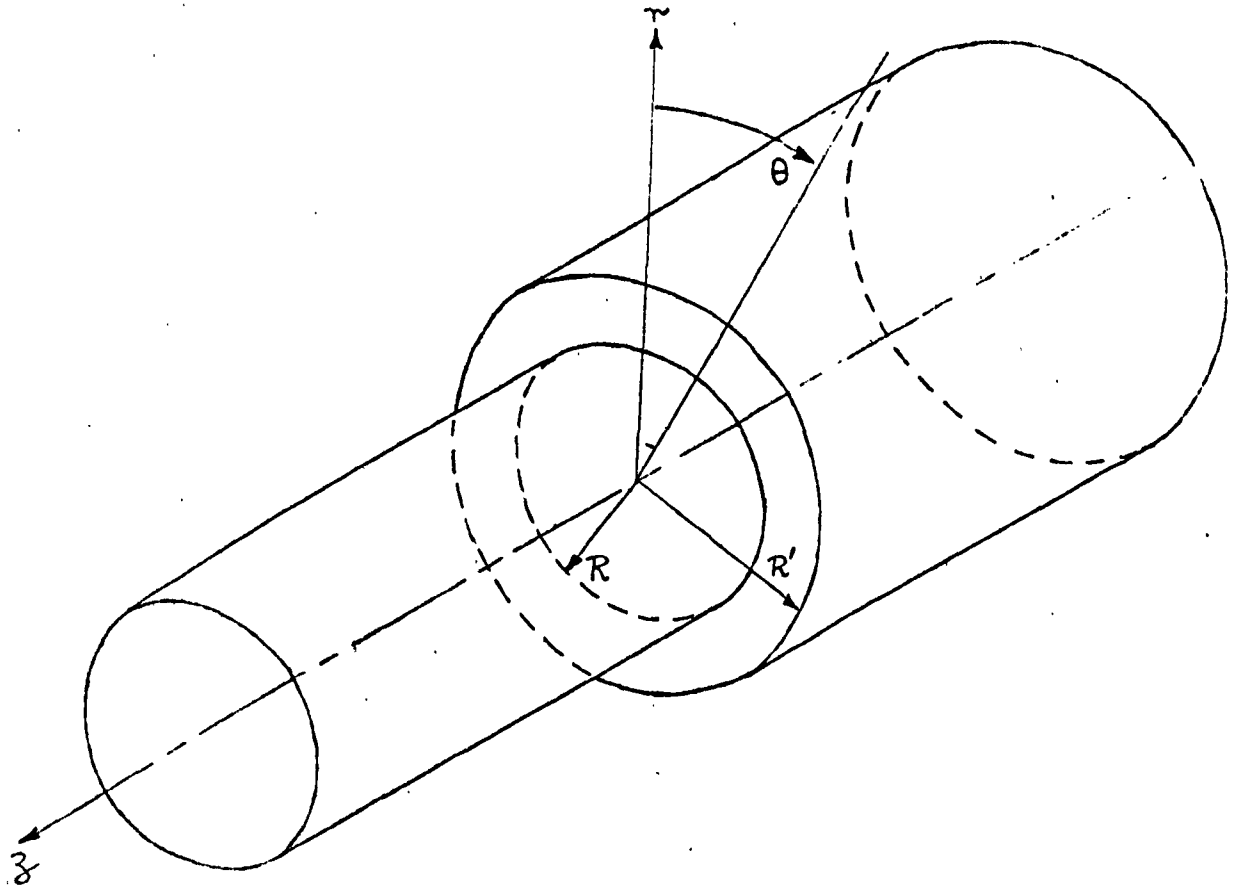

Transmitted Mode

Field Patterns

——— Electric

– – – Magnetic

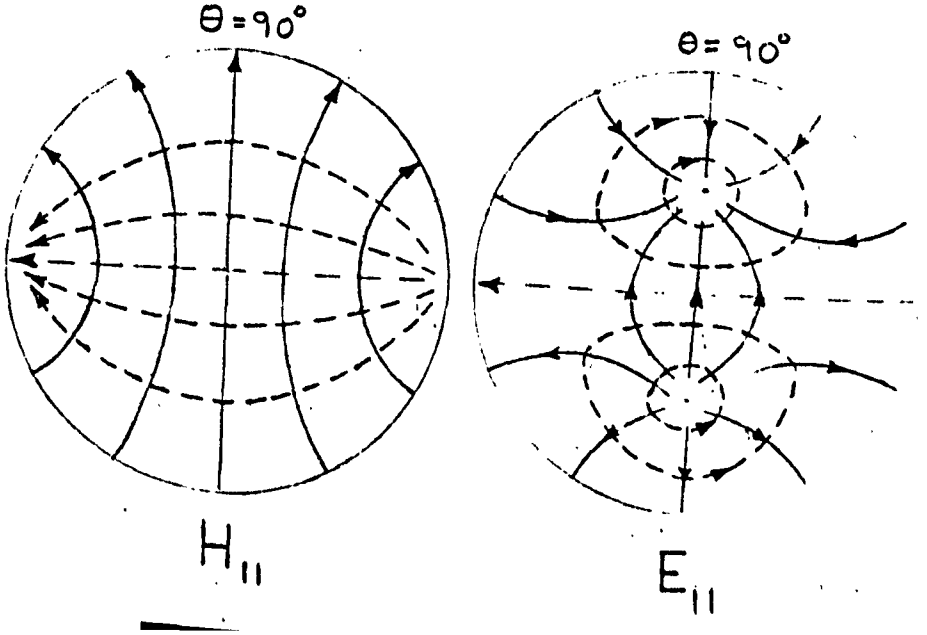

Values can now be assigned to the elements of $[R']$ using expressions 2.34 to 2.37. The elements of $[S']$ are given as follows:

H-modes in both guides:

$$S'_{2m-1,2n-1} = \frac{\gamma'_n}{\gamma_m} \frac{2\chi_m J'_1(\chi_n R/R')}{(\chi_m^2 - \chi_n^2 R^2/R'^2)(1 - 1/\chi_m^2) J_1(\chi_m)} \qquad 3.29$$

H- large guide, E - small guide:

$$S'_{2m,2n-1} = 0 \qquad 3.30$$

E - large guide, H - small guide:

$$S'_{2m-1,2n} = -\frac{k_o^2}{\xi'_n \gamma_m} \frac{2 J_1(\xi_n R/R')}{\chi_m(\xi_n R/R')(1 - 1/\chi_m^2) J_1(\chi_m)} \qquad 3.31$$

E - modes in both guides:

$$S'_{2m,2n} = \frac{\delta_m}{\delta'_n} \frac{2(\xi_n R/R') J'_1(\xi_m) J_1(\xi_m R/R')}{(\xi_m^2 - \xi_n^2 R^2/R'^2) J_0^2(\xi_m)} \qquad 3.32$$

Here again, the treatment for the rectangular waveguide H- plane step, as set out in figure 3.3, applies once matrices $[R']$ and $[S']$ have been generated.

An important application of the circular waveguide junction is as a mode-converter in the "Potter Horn" multimode antenna [14], where an H_{11} mode incident in the small guide excites both H_{11} and E_{11} propagating modes in the large guide. The transverse field patters of these modes are included in figure 3.7. If other modes are to be evanescent, the dimensions must be chosen such that:

$$0.293 < R/\lambda_o < 0.610, \quad 0.610 < R'/\lambda_o < 0.847$$

The amplitude ratio with which the H_{11} and E_{11} modes are excited in the larger guide has been determined experimentally by Nagelberg and Shefer [23], who express it in terms of a "mode conversion factor", being the ratio of the radial electric field amplitude of the E_{11} mode to that of the H_{11} mode, measured at the waveguide wall. In terms of decibels, this is written as:

$$M = 20 \log_{10} \left| \frac{a'_{r2}\, \underline{e}_1'^{(E)}}{a'_{r1}\, \underline{e}_1'^{(H)}} \right|_{r=R'} \quad \text{dB} \qquad 3.33$$

a'_{r2} and a'_{r1} being the complex transmission coefficients of the E_{11} and H_{11} modes respectively.

Computed values of M are compared with Nagelberg's experimental results in figure 3.8. Sixteen H and sixteen E modes were taken into account in the larger waveguide, and the mode ratio was taken as $p'/p \approx R'/R$. The agreement between theory and experiment is clearly good, especially for the smaller values of R/R'. When 2R=2.5", there is a discrepancy of about 1dB, but one would expect experimentally determined values to disagree with theory here, because the E_{11} mode is only very weakly excited, and any imperfections in the manufacture of the junction will have significant effects on its amplitude.

The "breakpoints" observable on the 2R=2.3" and 2R=2.5" curves correspond to E_{11} cut-off in the small waveguide.

Values of V.S.W.R. for the case 2R=2.5" are included in figure 3.9, with experimental points for comparison. Although there is good agreement in magnitude, the computed values show no sign of the oscillatory behaviour observed by Nagelberg.

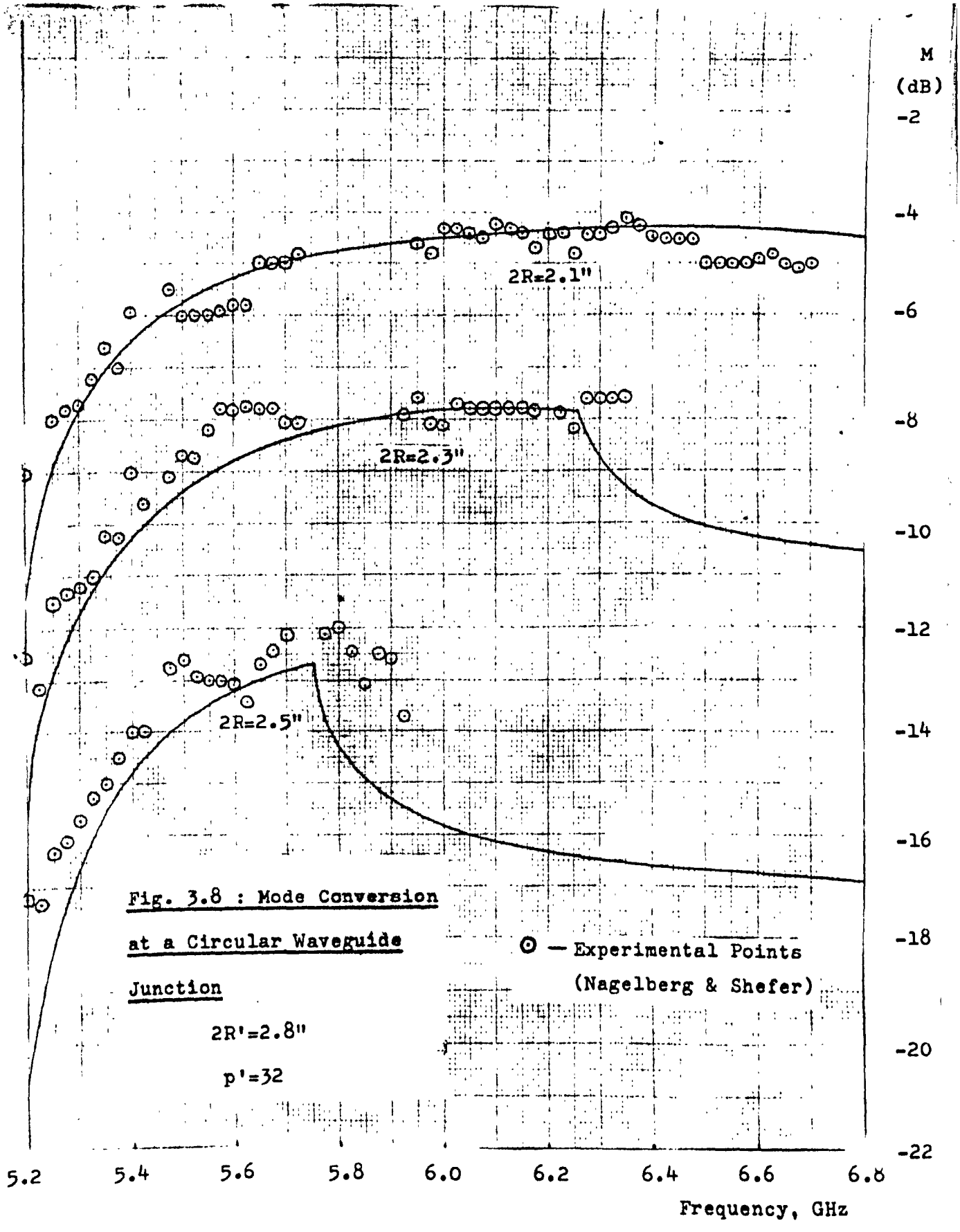

Fig. 3.8 : Mode Conversion at a Circular Waveguide Junction

2R'=2.8"

p'=32

⊙ — Experimental Points (Nagelberg & Shefer)

Fig. 3.9 : Properties of Circular Waveguide Junction

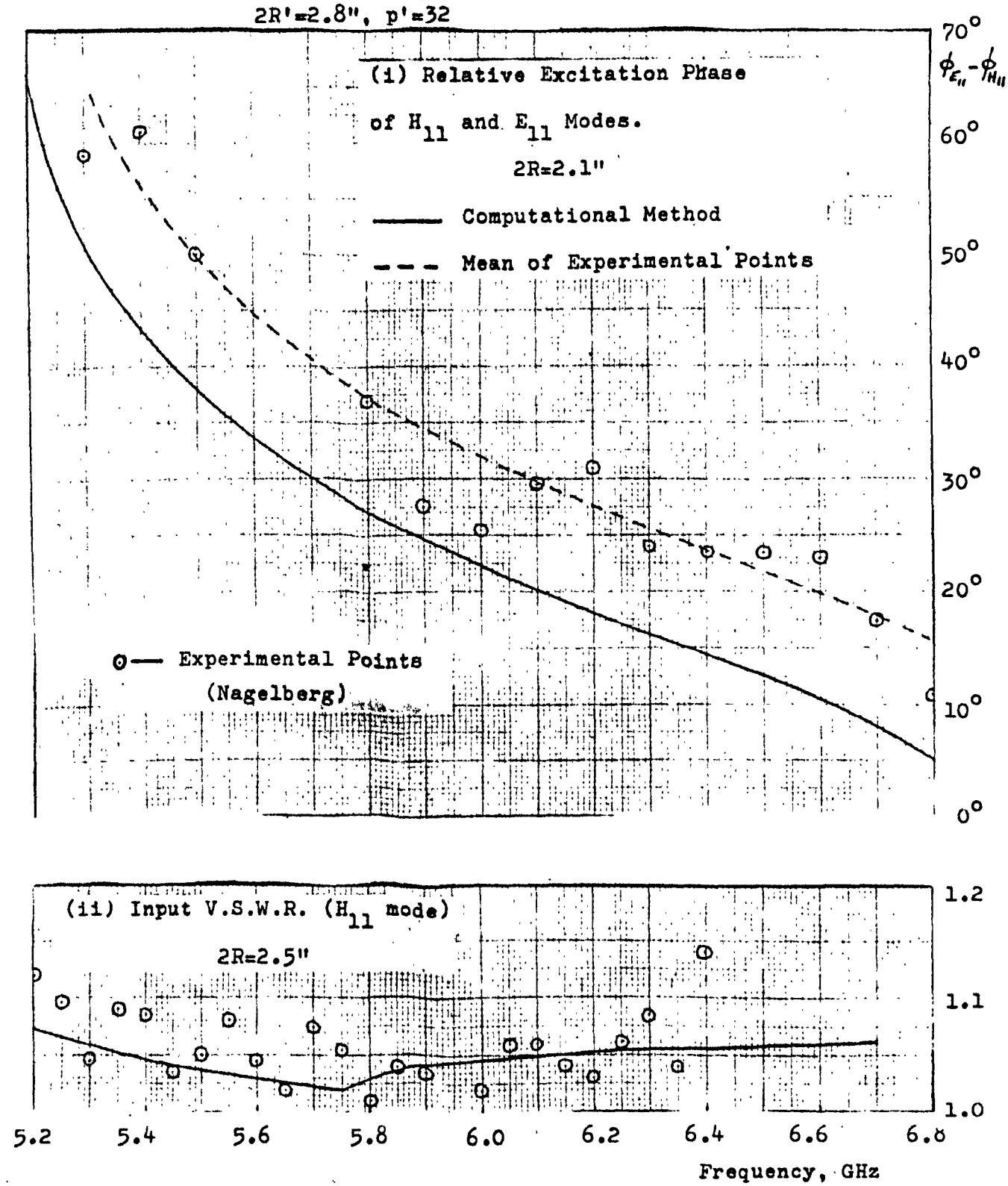

There seems to be no physical reason why such behaviour should occur, so it may well be a spurious effect connected with Nagelberg's particular set-up.

Nagelberg has also measured the relative phase with which the H_{11} and E_{11} modes are launched in the case 2R=2.1"[24]. This is shown in figure 3.9, together with a graph of computed results. It can be seen that on average the experimental values differ from the computed ones by about 10^{o}, a satisfactory figure in view of the scatter on the experimental points.

The modal analysis technique has also been applied to this problem by Cole [8], who gives values of M for the case R'=2.8", R=2.1". These values do not differ appreciably from the ones presented here.

3.7 The Treatment of a Junction involving More than Two Waveguides.

Figure 3.10 shows a junction between a single waveguide on one side of the discontinuity plane, and several smaller waveguides on the other, such that the axes of all guides are parallel and the cross-sections of all the small guides lie within that of the large guide. The guides are joined by a perfectly conducting step. The method of solution is an extension of that for a simple junction described in section 3.1: equation 3.2 applies when $[R']$ and $[S']$ are expressed in partitioned forms similar to those in 1.20 and 1.25. The elements of the sub-matrices resulting from field matching in aperture k are given by 1.24 and 1.26, where $\underline{e}_{kj}$ and $\underline{h}_{kj}$ are now the transverse field components in the discontinuity plane of the jth. mode in the kth. small waveguide, whose cross-section is S_k. Each of the column vectors $\{a_r\}$ and $\{a_i\}$ in

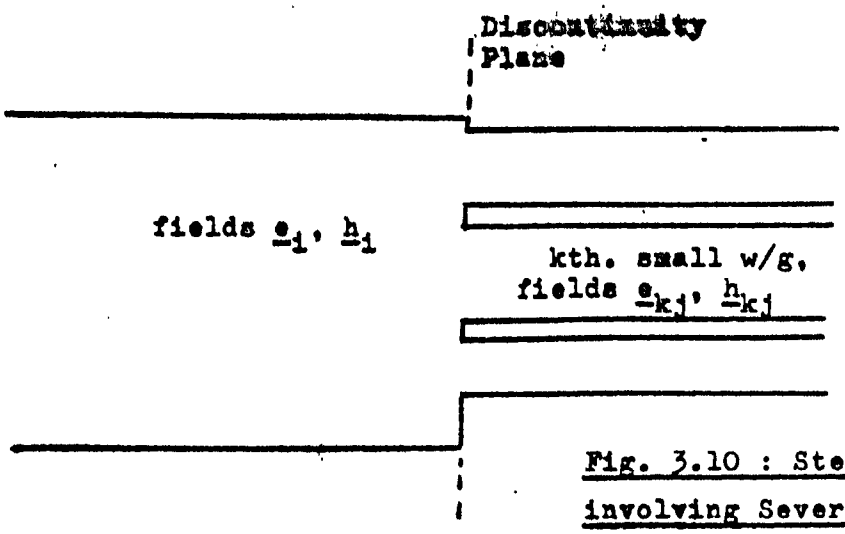

Fig. 3.10 : Step Junction involving Several Waveguides

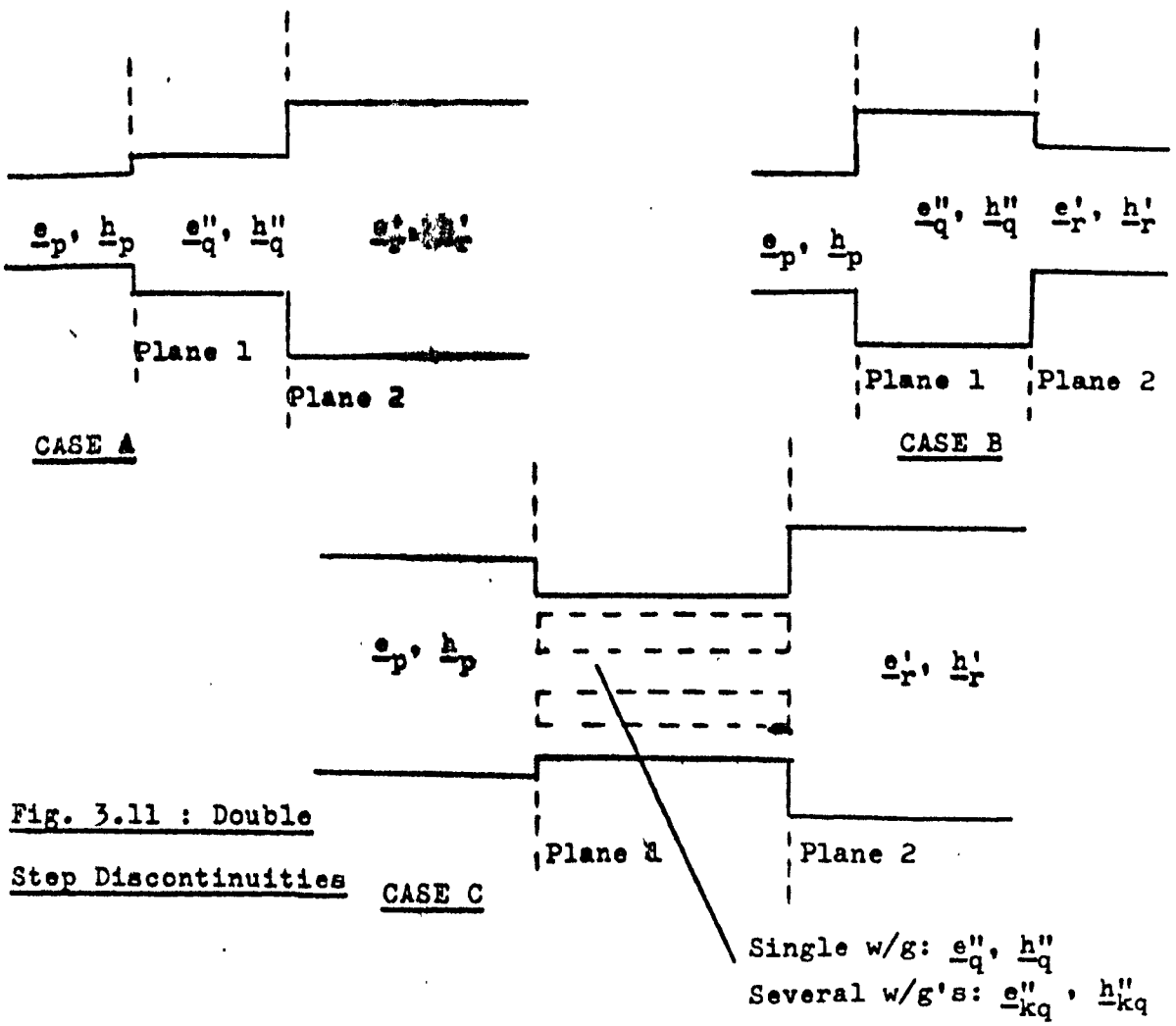

Fig. 3.11 : Double Step Discontinuities

equation 3.2 now contains series of modal amplitudes for all the small waveguides. In the usual case, where the dominant mode is incident from the large waveguide, equation 3.5 can be used to give the amplitude coefficients for the modes in all the small guides. The large guide's mode coefficients are then obtained using 3.7.

For most rapid convergence, the numbers of modes taken into account in the various guides should be chosen for best matching of the highest-order modes' spatial frequencies across the apertures.

Some simplifications can be made in the case of a structure with symmetry about a centre line, such as a symmetrical H-plane bifurcation in rectangular waveguide. A dominant mode incident from the large guide excites in that guide only H_{n0} modes for which n is odd. A magnetic wall along the axis can be inserted without affecting the fields, and because the orthogonality of the odd modes holds over half the cross-section, the problem reduces to a simple step junction between two rectangular guides, one of which has a magnetic wall. This type of simplification is applied in chapter 6 when treating a junction with four-fold symmetry used in multimode antenna design.

The symmetric H-plane bifurcation has been solved by Wexler [7] using modal analysis. In the case where the two small guides are separated by an infinitely thin septum, his results are in excellent agreement with exact values obtained by a transform technique.

3.8 The Treatment of Double Step Discontinuities.

In this section, a pair of interconnected step discontinuities between waveguides with parallel axes is considered. Some examples

are shown in figure 3.11. In case A, there is boundary enlargement in both planes 1 and 2 if incidence is from the left, or boundary reduction at both planes for incidence from the right: such configurations have applications as waveguide impedance transformers. Figure 3.11 B shows the case of enlargement at the first plane followed by reduction at the second. An example of this arrangement is given in chapter 6, where its use as a mode generator for a multimode antenna is discussed. In case C, a boundary reduction at plane 1 is followed by enlargement at plane 2. A particular case of this junction is the thick iris in a waveguide. Since the method of treatment for type C junctions applies also when there is more than one interconnecting guide, it is possible to tackle such problems as a row of posts across a guide.

For a general 3-waveguide junction of the above type, with a unit-amplitude dominant mode incident from the left, field matching at plane 1 gives:

$$\underline{e}_1 + \sum_{p=1}^{\infty} a_p \underline{e}_p = \sum_{q=1}^{\infty} (\vec{\tau}_q + \overleftarrow{\tau}_q)\, \underline{e}''_q \qquad 3.34$$

$$\underline{h}_1 - \sum_{p=1}^{\infty} a_p \underline{h}_p = \sum_{q=1}^{\infty} (\vec{\tau}_q - \overleftarrow{\tau}_q)\, \underline{h}''_q \qquad 3.35$$

where the amplitude of the qth mode in the intermediate guide at plane 1 is expressed in terms of components travelling away from and towards the junction, denoted by $\vec{\tau}_q$ and $\overleftarrow{\tau}_q$ respectively. The fields of this mode at plane 2 can be expressed in terms of those at plane 1 using the propagation coefficient γ''_q and the length l of the intermediate section. Field matching at plane 2 then gives:

$$\sum_{q=1}^{\infty} \left(\vec{\tau}_q e^{-\gamma''_q l} + \overleftarrow{\tau}_q e^{\gamma''_q l} \right) \underline{e}''_q = \sum_{r=1}^{\infty} a'_r \underline{e}'_r \qquad 3.36$$

$$\sum_{q=1}^{\infty} \left(\vec{\tau}_q e^{-\gamma''_q l} - \overleftarrow{\tau}_q e^{\gamma''_q l} \right) \underline{h}''_q = \sum_{r=1}^{\infty} a'_r \underline{h}'_r \qquad 3.37$$

Matrix Equations for Junction 1

Equation 3.34 is vector post-multiplied by each of the magnetic field functions in the larger guide taken in turn, and each term is integrated over the smaller guide's cross-section. The range of integration on one side of each equation is extended over the larger waveguide's cross-section to take account of the vanishing electric field over the step, and the orthogonality of the modes in this guide is used to reduce the relevant series to a single term. By restricting the numbers of modes in the input and intermediate guides to n and n" respectively, the equations can be expressed in matrix form:

For boundary enlargement:

$$\{b\} = [R_1] \{a\} + \{R_{11}\} \qquad 3.38(a)$$

For boundary reduction:

$$\{\Delta\} + \{a\} = [R'_1] \{b\} \qquad 3.38(b)$$

In these expressions:

$$R_1(i,j) = \int_S \underline{e}_j \times \underline{h}''_i \cdot d\underline{s} \Big/ \int_{S''} \underline{e}''_i \times \underline{h}''_i \cdot d\underline{s}, \quad R'_1(i,j) = \int_{S''} \underline{e}''_j \times \underline{h}_i \cdot d\underline{s} \Big/ \int_S \underline{e}_i \times \underline{h}_i \cdot d\underline{s}$$

Matrices $[R_1]$ and $[R'_1]$ have dimensions n"xn and nxn" respectively.

Vector $\{b\}$ has elements $b_i = \vec{\tau}_i + \overleftarrow{\tau}_i$, and $\{R_{11}\}$ is the first column of $[R_1]$.

The magnetic field matching equation, 3.35, is vector pre-multiplied in turn by each of the smaller guide's electric field functions, the various terms then being integrated over that guide's cross-section. The orthogonality of the smaller guide's modes is used directly. Eventually the following matrix equations are obtained:

For boundary enlargement:

$$\{\Delta\} - \{a\} = [S_1]\{c\} \qquad 3.39(a)$$

For boundary reduction:

$$\{S'_{11}\} - [S'_1]\{a\} = \{c\} \qquad 3.39(b)$$

where $[S_1]$ and $[S'_1]$ have elements:

$$S_1(i,j) = \frac{\int_S \underline{e}_i \times \underline{h}''_j \cdot d\underline{s}}{\int_S \underline{e}_i \times \underline{h}_i \cdot d\underline{s}} \quad , \quad S'_1(i,j) = \frac{\int_{S''} \underline{e}''_i \times \underline{h}_j \cdot d\underline{s}}{\int_{S''} \underline{e}''_i \times \underline{h}''_i \cdot d\underline{s}}$$

the dimensions being n x n" and n" x n respectively. $\{S'_{11}\}$ is the first column of $[S'_1]$ and $c_i = \vec{\tau}_i - \overleftarrow{\tau}_i$, $i \leqslant n''$.

Matrix Equations for Junction 2

The coefficients of the intermediate waveguide modes at junction 2 can be written in terms of b_i and c_i. 3.36 and 3.37 then become:

$$\sum_{q=1}^{\infty} \left[b_q \cosh(\gamma''_q l) - c_q \sinh(\gamma''_q l) \right] \underline{e}''_q = \sum_{r=1}^{\infty} a'_r \underline{e}'_r \qquad 3.40$$

$$\sum_{q=1}^{\infty} \left[-b_q \sinh(\gamma''_q l) + c_q \cosh(\gamma''_q l) \right] \underline{h}''_q = \sum_{r=1}^{\infty} a'_r \underline{h}'_r \qquad 3.41$$

Vector multiplication and integration are carried out as for junction 1, and after restricting the number of modes in the right-hand guide to n', the matrix equations resulting from electric field matching are as follows:

For boundary enlargement:

$$[R_2][ch]\{b\} - [R_2][sh]\{c\} = \{a'\} \qquad 3.42(a)$$

For boundary reduction:

$$[ch]\{b\} - [sh]\{c\} = [R_2']\{a'\} \qquad 3.42(b)$$

where $R_2(i,j) = \dfrac{\int_{S''} \underline{e}_j'' \times \underline{h}_i' \cdot d\underline{s}}{\int_{S'} \underline{e}_i' \times \underline{h}_i' \cdot d\underline{s}}$, $R_2'(i,j) = \dfrac{\int_{S'} \underline{e}_j' \times \underline{h}_i'' \cdot d\underline{s}}{\int_{S''} \underline{e}_i'' \times \underline{h}_i'' \cdot d\underline{s}}$,

$[R_2]$ and $[R_2']$ having dimensions n' x n'' and n'' x n' respectively. $[sh]$ and $[ch]$ are n'' x n'' diagonal matrices having elements $sh_{ii} = \sinh(\gamma_i'' l)$ and $ch = \cosh(\gamma_i'' l)$.

Again following the method for junction 1, the matrix equations obtained by matching magnetic fields at junction 2 are:

For boundary enlargement:

$$-[sh]\{b\} + [ch]\{c\} = [S_2]\{a'\} \qquad 3.43(a)$$

For boundary reduction:

$$\{a'\} = -[S_2'][sh]\{b\} + [S_2'][ch]\{c\} \qquad 3.43(b)$$

Matrices $[S_2]$ and $[S_2']$ are n'' x n' and n' x n'' respectively, with elements: $S_2(i,j) = \dfrac{\int_{S''} e_i'' \times \underline{h}_j' \cdot d\underline{s}}{\int_{S''} \underline{e}_i'' \times \underline{h}_i'' \cdot d\underline{s}}$, $S_2'(i,j) = \dfrac{\int_{S'} \underline{e}_i' \times \underline{h}_j'' \cdot d\underline{s}}{\int_{S'} \underline{e}_i' \times \underline{h}_i' \cdot d\underline{s}}$

Simultaneous Solution of the Equations

Having generated, for a given double step junction, a set of four matrix equations involving four unknown column vectors, one method of solution is to lump all these unknowns together into a single vector, and produce a single matrix equation which can be solved to give all the coefficients simultaneously. Clarricoats and Slinn [6] have successfully used this method to treat a thick inductive iris in rectangular waveguide. A serious disadvantage, however, is that $2n + 4n'' + 2n'$ linear equations in the same number of real unknowns have to be solved, and for average-sized computers storage limitations severely restrict the numbers of modes which can be taken into account - about 12 modes in any one waveguide is the maximum if n, n'' and n' are approximately equal. This restriction can be overcome by combining the matrix equations to give an equation involving only one of the original column vectors. Once this equation has been solved, the other unknowns can be found by back-substitution. In this way the number of linear equations to be solved is reduced by a factor of four when $n = n'' = n'$, and it is found that, for a given store limit, at least twice as many modes can be taken into account.

The elimination of $\{a\}$ from 3.38 and 3.39 gives:

$$[R_1][S_1]\{c\} + \{b\} = 2\{R_{11}\} \qquad 3.44(a)$$

$$[S'_1][R'_1]\{b\} + \{c\} = 2\{S'_{11}\} \qquad 3.44(b)$$

The equations apply for boundary enlargement and reduction respectively.

Similarly, $\{a'\}$ can be eliminated from 3.42 and 3.43 to give:

$$([S_2][R_2][ch]+[sh])\{b\} = ([S_2][R_2][sh]+[ch])\{c\} \qquad 3.45(a)$$

$$([R_2'][S_2'][sh]+[ch])\{b\} = ([R_2'][S_2'][ch]+[sh])\{c\} \qquad 3.45(b)$$

If there is boundary enlargement at the first junction, 3.44(a) should be combined with either 3.45(a) or 3.45(b) to give an equation involving only the vector $\{c\}$. For boundary reduction at junction 1, elimination of $\{c\}$ from 3.44(b) and 3.45(a) or (b) gives an equation in $\{b\}$ only. Writing the matrices on the left and right hand sides of 3.45(a) as $[U]$ and $[V]$ respectively, and those in 3.45(b) as $[U']$ and $[V']$, the final equations to be solved are:

Enlargement at both junctions:

$$([U][R_1][S_1]+[V])\{c\} = 2[U]\{R_{11}\} \qquad 3.46$$

Reduction at both junctions:

$$([U'][S_1'][R_1']+[V'])\{b\} = 2[U']\{S_{11}'\} \qquad 3.47$$

Enlargement at junction 1, reduction at junction 2:

$$([V'][R_1][S_1]+[U'])\{c\} = 2[V']\{R_{11}\} \qquad 3.48$$

Reduction at junction 1, enlargement at junction 2:

$$([V][S_1'][R_1']+[U])\{b\} = 2[V]\{S_{11}'\} \qquad 3.49$$

Back-substitution to obtain the other unknowns is most easily done as follows: For enlargement at junction 1, $\{a\}$ is found from 3.39(a) and substituted in 3.38(a) to give $\{b\}$. For reduction at junction 1, $\{a\}$ is found from 33.8(b) and substituted in 3.39(b) to give $\{c\}$. Knowing $\{b\}$ and $\{c\}$, $\{a'\}$ can be evaluated using 3.42(a) or 3.43(b).

For configurations of type C in figure 3.11 where there is more than one interconnecting waveguide, matrices $[R_1']$, $[R_2]$, $[S_1']$, $[S_2]$, $[sh]$ and $[ch]$ should be written in partitioned form following the technique outlined in section 3.7.

In the case of a thick iris or row of rectangular posts in a waveguide, junctions 1 and 2 are identical. $[R_1']$ and $[R_2]$ are then equal, as are $[S_1']$ and $[S_2]$. Recognition of this leads to some simplifications in programming.

If the numbers of modes in the various waveguides are chosen using the field-matching criterion for the highest order modes, n" will be less than n or n' for type C junctions. Thus the smallest column vectors, in this case $\{b\}$ and $\{c\}$, are determined first - the most economical arrangement as regards computer time and storage.

As mentioned in chapter 1, Slinn [5] and Wexler [7] have found that when modal analysis is applied to a double step junction the rate of convergence decreases with the length of the intermediate section. However, Slinn [5] has obtained an accurate solution for a rectangular waveguide inductive iris of thickness $0.03\lambda_0$ with n"=7, so it appears that the effect is only troublesome when l is very small, in which case a fairly good solution can be obtained by putting l=0 and treating the junction as a simple thin iris, step, or a combination of the two.

A junction of type B in figure 3.11 has been treated using the above method (see chapter 6), and it was found that results were unreliable for l greater than about $2\lambda_0$. This seems to be because terms of the form $e^{\gamma_q'' l}$ become very large for the highest-order modes,

so that rounding errors occurring during the solution of the simultaneous equations have a serious effect on the values of the unknown coefficients. In cases such as this multiple reflections of evanescent modes could be neglected, and a solution obtained by considering a transmission line equivalent circuit whose parameters were calculated by treating each junction separately.

3.9 Discussion and Conclusions.

In this chapter the Modal Analysis technique for step discontinuities has been developed as a special case of the general computational method of chapter 1. Matrix equations applicable to a wide range of both single and double discontinuity problems have been derived. It has been shown that although the choice of the ratios of numbers of modes considered is not nearly as critical as for the thin iris, ratios selected by field-matching considerations give most rapid convergence. Results obtained using Modal Analysis have been shown to agree well with values found by experiment and by other theoretical methods, for both single mode and multimode cases. The technique can therefore be used with confidence in the design of mode-generators for multimode antennas.

As with the thin iris, solution of junctions involving mixed geometries may be lengthy because of the need to use numerical integration. However, since no divergent situation can occur in the step case, the choice of mode ratio can be quite arbitrary.

Although the treatment in section 3.8 applies only to two adjacent steps, there is no reason why it should not be extended to

any number of successive junctions. Manipulation of the matrix equations for the various junctions would lead to the elimination of all but one of the unknown column vectors, giving a set of simultaneous equations to be solved in the usual way. This final set of equations would require no more storage than in the double step case, but additional storage would be needed for the matrices generated by field matching at the new junctions, and in practice this would limit the complexity of structures that could be treated.

A restriction which has applied to all the configurations dealt with in this chapter is that every aperture in a discontinuity plane has the same cross-section as one of the waveguides. If this is not the case, separate series of functions must be used to describe the aperture fields, and the general method of chapter 1 should be used. Note that such junctions can still be true "steps", i.e. transverse discontinuities where no thin diaphragm is involved.

CHAPTER IV. THE APPLICATION OF THE COMPUTATIONAL METHOD TO LONGITUDINAL WAVEGUIDE DISCONTINUITIES

4.1. Introduction.

So far the computational method has been applied only to discontinuities whose planes are transverse to the direction of wave propagation. It is the purpose of this chapter to show how the method can be extended to determine the properties of some waveguides which are uniform in the direction of propagation, but which have discontinuity surfaces parallel to the longitudinal axis. This development depends on the re-formulation of the fields within the waveguide in terms of modes travelling in directions normal to both the axis and the discontinuity surfaces, so that a field-matching technique similar to that for transverse discontinuities can be used to determine relationships between their coefficients. Field expressions for such "transverse" modes applicable to cartesian and cylindrical geometries have been given by Goldstone and Oliner [25], [26]. Figure 4.1 shows the types of discontinuity which are amenable to treatment. With the cartesian co-ordinate system, the transverse modes travel in the x - direction, and the types of discontinuity which can be considered are those whose planes lie parallel to the x = 0 plane. Similarly in the cylindrical case the transverse modes travel radially and discontinuity surfaces must correspond to cylinders for which r is constant.

As with conventional modes, it is possible to represent the fields of a propagating transverse mode by voltage and current distributions on an equivalent transmission line. The cross-section of a waveguide

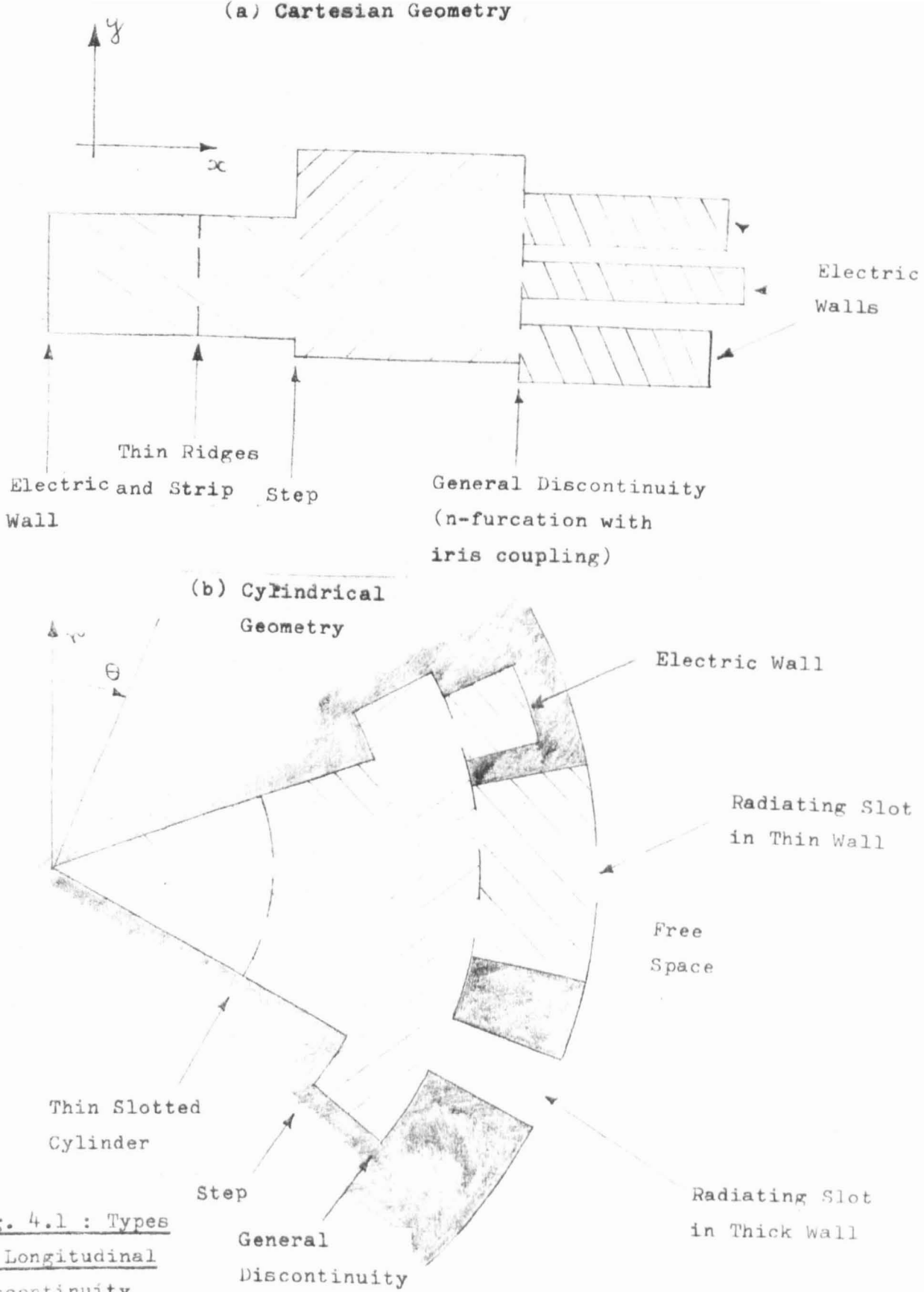

Fig. 4.1 : Types of Longitudinal Discontinuity

containing longitudinal discontinuities can therefore be represented by an equivalent transverse network, in which transmission lines for the various propagating transverse modes are coupled by transformers at the discontinuities and have lumped susceptance elements to account for stored energy. Perfectly conducting walls are represented by short circuits and radiating slots by complex admittances. It is usually the dispersion characteristics for different modes of the structure which are required, and these are found by specifying values, in general complex, for the longitudinal propagation coefficient, γ, which is involved in the determination of the equivalent network parameters, and then finding the corresponding resonant frequencies of the network by solving a transcendental equation. In the case of a lossless homogeneous structure, the γ/ω characteristics may be found from a knowledge of the cut-off frequencies alone, in which case γ may be set equal to zero. This Transverse-Resonance* method has been used by Marcuvitz [4] to treat simple structures with a single propagating transverse mode in any region, where either no discontinuity susceptances are involved or where general formulae are available for calculating the susceptances. In a homogeneous rectangular waveguide at cut-off, for example, the transverse modes reduce to conventional modes for a parallel-plate waveguide, and equivalent susceptances for longi-

---

* Although the computational method for longitudinal discontinuities is, in a sense, a transverse-resonance technique, the expression will be used in this chapter to refer to the method using an equivalent-network formulation.

tudinal ridges can be determined from formulae applicable to irises in parallel-plate guide. It is only in a few cases, however, that suitable formulae for calculating discontinuity susceptance are available, and in general it is necessary to derive formulae for the equivalent circuit parameters before the Transverse-Resonance method can be applied. This can present considerable difficulty, particularly if several propagating modes are involved. A further drawback resulting from the use of lumped elements is that evanescent transverse modes excited at a discontinuity are assumed to have negligible amplitudes by the time they have reached an adjacent one. In a case such as that of a ridge close to a waveguide wall multiple reflections of evanescent modes can be significant, and Transverse-Resonance gives inaccurate results because this "proximity effect" is not taken into account.

The disadvantages of the Transverse-Resonance method can be overcome by treating the determination of dispersion characteristics, as a field problem rather than a network problem. The calculations are more lengthy, but solutions are obtained rapidly using a computer. With reference to figure 4.1, it can be seen that, provided the discontinuity surfaces are those of constant x or r, analogies can be drawn between the interaction of transverse modes with longitudinal discontinuities and that of conventional modes with the transverse discontinuities whose solutions have already been described in this thesis. The generation of matrix equations to relate the coefficients of modes in different regions proceeds in exactly the same way as in the transverse case. For example, a thin longitudinal ridge or strip in rectangular

waveguide would be treated as a thin iris, with suitable functions being introduced to represent the transverse (to x) fields in the aperture(s). Care would need to be taken in choosing the ratios of numbers of modes and aperture functions, making the same considerations as in chapter 2. As multiple reflections are involved, the mode coefficients are composed of two components, referring to parts of the wave travelling in positive and negative x or r directions. At a perfectly conducting wall the relationship between the components is such that the transverse (to x or r) electric field for the mode vanishes. Having applied the field-matching technique to all the discontinuities in the structure, sufficient matrix equations will have been generated to allow their reduction to a single matrix equation involving only one set of coefficients. As there is no "incident" field in the transverse-mode case, one solution will always be that for which these coefficients are all zero. However, the situation of interest is that where other values are possible, and for this to be the case the determinant of the matrix must vanish. Each element of the matrix is a function of frequency, and those frequencies at which, for a particular γ, the determinant vanishes, correspond to points on the dispersion curves for various modes of the structure. The most convenient way of finding such frequencies is first to supply an approximate value and then to use an iterative technique to improve the solution.

As multiple reflections of evanescent modes are taken into account, the restrictions caused by the proximity effect do not apply with this computational technique.

In the case of cartesian geometry, structures amenable to treatment include rectangular waveguides with longitudinal ridges which can be infinitely thin or of finite width. There are many commonly-occurring examples of waveguides of this type in which the cross-section is symmetrical about a vertical or horizontal plane, and in such cases the treatment can be simplified because the field distribution for any mode will be such that either an electric or a magnetic wall can be introduced in the plane of symmetry. Only half the structure need then be treated, and, in the case of a vertical plane of symmetry, the number of boundaries at which field matching must be considered is correspondingly reduced.

Suitable cases for treatment which involve cylindrical geometry include circular or coaxial waveguides with longitudinal corrugations, partial dielectric filling, or radiating longitudinal slots. The latter type of problem can be considered because radially propagating modes can be used to represent the fields in free space surrounding the waveguide, so the slot can be viewed as a discontinuity between two radial guides in the same way as any of the other discontinuities shown in figure 4.1(b). Clarricoats and Slinn [12] have used a method similar to the one described here in the case of a slot in a thick-walled circular guide, and have obtained satisfactory agreement with experimental results. It would now be possible to solve this problem if the wall were infinitely thin, because of the extension of the computational technique to include thin irises. Moreover, the solution for a thin wall would be less complicated, because only one discontinuity surface is involved.

4.2 Rectangular Waveguide with Thin Longitudinal Strips, having Different Permittivities on Either Side of the Discontinuity Plane.

In this section the technique outlined above is applied to the determination of dispersion characteristics for a rectangular waveguide containing a number of infinitely thin strips, uniform in the z - direction, which lie in the x = 0 plane (see Fig. 4.2). The relative permittivity ε_1 for the region $x>0$ is in general different from ε_2, that for the region $x<0$. It is assumed that the waveguide walls and the strips are perfectly conducting, and that the dielectric is lossless. This structure has important applications, since if l_1 is small compared with l_2 and $\varepsilon_2=1$, it can be viewed as a number of coupled microstrip transmission lines surrounded by a conducting shield. Although microstrip lines are generally regarded as open structures for the purpose of analysis, a treatment of the shielded case is also valuable as this arrangement commonly occurs in practice. The dispersion curve for the quasi - TEM mode is of particular interest, and the rigorous nature of the method should allow the deviations from linearity of this characteristic to be investigated.

Although only the theory for the general case $\varepsilon_1 \neq \varepsilon_2$ is given here, computed results have been obtained for the special case $\varepsilon_1 = \varepsilon_2$, and these are presented in section 4.3.

Using the formulation of Goldstone and Oliner [25], the transverse modes for representing the fields in either region of the structure can be either E-type, for which $\underline{h}_z=0$, or H-type, for which $\underline{e}_z=0$. Any given

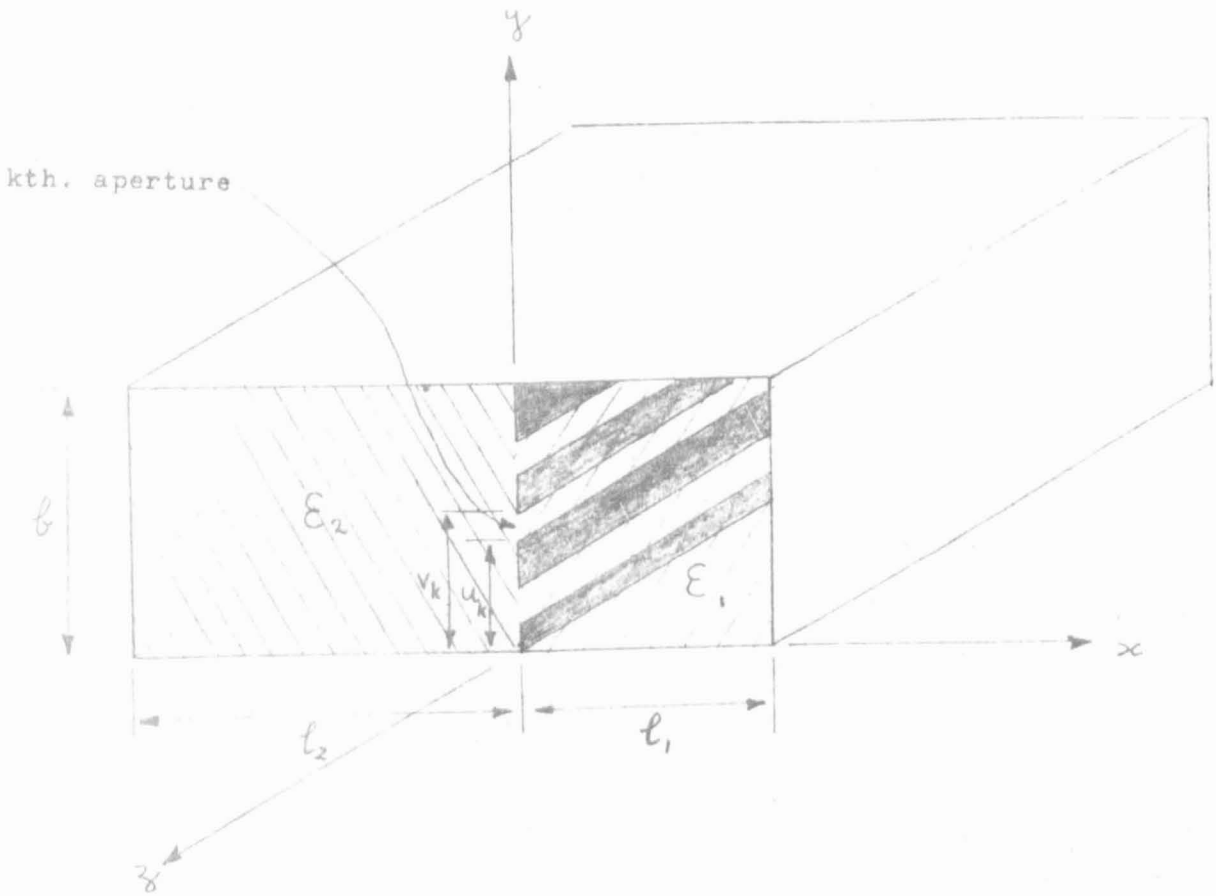

Fig. 4.2 : Rectangular Waveguide with Thin Longitudinal Strips

field distribution can be represented by an infinite series involving both types of modes. For a region with relative permittivity ε, the transverse (to x) fields for the E-type mode of order n are:

$$\underline{e}'_{tn} = \sin \frac{n\pi y}{b} \hat{\underline{i}}_z - j \frac{n\pi}{b} \frac{k_z}{\varepsilon k_o^2 - k_z^2} \cos \frac{n\pi y}{b} \hat{\underline{i}}_y \qquad 4.1$$

$$\underline{h}'_{tn} = \frac{\omega \varepsilon_o \varepsilon p_n}{\varepsilon k_o^2 - k_z^2} \sin \frac{n\pi y}{b} \hat{\underline{i}}_y \qquad 4.2$$

For the H-type mode of order n:

$$\underline{e}''_{tn} = - \cos \frac{n\pi y}{b} \hat{\underline{i}}_y \qquad 4.3$$

$$\underline{h}''_{tn} = \frac{\varepsilon k_o^2 - k_z^2}{\omega \mu_o p_n} \cos \frac{n\pi y}{b} \hat{\underline{i}}_z + j \frac{n\pi}{b} \frac{k_z}{\omega \mu_o p_n} \sin \frac{n\pi y}{b} \hat{\underline{i}}_y \qquad 4.4$$

The factor $e^{-j(k_z z + p_n x)}$ has been suppressed, and the wavenumbers are related through the expression:

$$\varepsilon k_o^2 = \omega^2 \mu_o \varepsilon \varepsilon_o = p_n^2 + \frac{n^2 \pi^2}{b^2} + k_z^2 \qquad 4.5$$

Coefficients $\vec{A}'_n$, $\vec{A}''_n$ will be used to represent the amplitudes of nth order E-type and H-type modes respectively, immediately to the right of the x=0 plane and travelling in the positive x direction. Similarly, $\overleftarrow{A}'_n$, $\overleftarrow{A}''_n$ refer to the components of these modes travelling in the negative x direction. On the left of the x=0 plane the corresponding coefficients are $\vec{B}'_n$, $\vec{B}''_n$, $\overleftarrow{B}'_n$ and $\overleftarrow{B}''_n$. The transverse (to x) electric fields on either side of the x=0 plane must match in

the apertures and vanish on the strips. They are therefore identical over the entire longitudinal cross-section at x=0, i.e.

$$\underline{E}_T = \sum_{n=1}^{\infty} (\vec{A}'_n + \overleftarrow{A}'_n)\, \underline{e}'_{tn}(\varepsilon_1) + \sum_{n=0}^{\infty} (\vec{A}''_n + \overleftarrow{A}''_n)\, \underline{e}''_{tn}$$

$$= \sum_{n=1}^{\infty} (\vec{B}'_n + \overleftarrow{B}'_n)\, \underline{e}'_{tn}(\varepsilon_2) + \sum_{n=0}^{\infty} (\vec{B}''_n + \overleftarrow{B}''_n)\, \underline{e}''_{tn} \qquad 4.6$$

The notation $\underline{e}'_{tn}(\varepsilon_1)$ implies that ε is replaced by ε_1 in 4.1. Similarly with $\underline{e}'_{tn}(\varepsilon_2)$, etc.

On equating the z - components it is found that:

$$\vec{A}'_n + \overleftarrow{A}'_n = \vec{B}'_n + \overleftarrow{B}'_n \quad \text{for all n} \qquad 4.7$$

Equating y - components, and substituting for $\vec{B}'_n + \overleftarrow{B}'_n$:

$$\vec{B}''_n + \overleftarrow{B}''_n = \vec{A}''_n + \overleftarrow{A}''_n + j\frac{n\pi}{b}(\vec{A}'_n + \overleftarrow{A}'_n)\left\{\frac{k_z}{\varepsilon_1 k_o^2 - k_z^2} - \frac{k_z}{\varepsilon_2 k_o^2 - k_z^2}\right\} \qquad 4.8$$

The transverse (to x) electric field must vanish at $x=l_1$ and $x=-l_2$. For the right-hand wall this gives:

$$\vec{A}'_n e^{-jp_{1n}l_1} + \overleftarrow{A}'_n e^{jp_{1n}l_1} = 0 \qquad 4.9$$

$$\vec{A}''_n e^{-jp_{1n}l_1} + \overleftarrow{A}''_n e^{jp_{1n}l_1} = 0 \qquad 4.10$$

If, therefore, $\bar{A}'_n$ is defined as $\vec{A}'_n + \overleftarrow{A}'_n$ and $\bar{A}''_n$ as $\vec{A}''_n + \overleftarrow{A}''_n$,

$$\vec{A}'_n - \overleftarrow{A}'_n = -j\bar{A}'_n \cot(p_{1n}l_1) \qquad 4.11$$

$$\vec{A}''_n - \overleftarrow{A}''_n = -j\bar{A}''_n \cot(p_{1n}l_1) \qquad 4.12$$

Allowing for vanishing transverse electric field at the left-hand wall, and using 4.7 and 4.8,

$$\vec{B}'_n - \overleftarrow{B}'_n = j\bar{A}'_n \cot(p_{2n}l_2) \qquad 4.13$$

$$\vec{B}''_n - \overleftarrow{B}''_n = j\cot(p_{2n}l_2)\left\{\bar{A}''_n + j\frac{n\pi}{b}\bar{A}'_n\left(\frac{k_z}{\varepsilon_1 k_o^2 - k_z^2} - \frac{k_z}{\varepsilon_2 k_o^2 - k_z^2}\right)\right\} \qquad 4.14$$

The magnetic field transverse to x in the plane x=0 can then be written as:

On the right of the strips:

$$\underline{H}_{TR} = -j\sum_{n=1}^{\infty}\cot(p_{1n}l_1)\bar{A}'_n\underline{h}'_{tn}(\varepsilon_1,p_{1n}) - j\sum_{n=0}^{\infty}\cot(p_{1n}l_1)\bar{A}''_n\underline{h}''_{tn}(\varepsilon_1,p_{1n}) \qquad 4.15$$

On the left of the strips:

$$\underline{H}_{TL} = j\sum_{n=1}^{\infty}\cot(p_{2n}l_2)\,\bar{A}'_n\underline{h}'_{tn}(\varepsilon_2,p_{2n})$$

$$+j\sum_{n=0}^{\infty}\cot(p_{2n}l_2)\left\{\bar{A}''_n + j\frac{n\pi}{b}\bar{A}'_n\left(\frac{k_z}{\varepsilon_1 k_o^2 - k_z^2} - \frac{k_z}{\varepsilon_2 k_o^2 - k_z^2}\right)\right\}\underline{h}''_{tn}(\varepsilon_2,p_{2n}) \qquad 4.16$$

A suitable representation for the fields in the kth aperture is:

$$\underline{E}_{Tk} = \sum_{m=0}^{\infty}\left(C_{km}\sin m\pi\frac{y-u_k}{v_k-u_k}\,\hat{\underline{i}}_z + D_{km}\cos m\pi\frac{y-u_k}{v_k-u_k}\,\hat{\underline{i}}_y\right) \qquad 4.17$$

$$\underline{H}_{Tk} = \sum_{m=0}^{\infty}\left(E_{km}\cos m\pi\frac{y-u_k}{v_k-u_k}\,\hat{\underline{i}}_z + F_{km}\sin m\pi\frac{y-u_k}{v_k-u_k}\,\hat{\underline{i}}_y\right) \qquad 4.18$$

The electric fields must match in each aperture. Therefore, for the kth aperture, matching of z and y components separately gives,

from 4.6, 4.1, 4.3 and 4.17:

$$\sum_{n=1}^{\infty} \bar{A}'_n \sin \frac{n\pi y}{b} = \sum_{m=1}^{\infty} C_{km} \sin m\pi \frac{y-u_k}{v_k-u_k} \qquad 4.19$$

$$-\sum_{n=0}^{\infty} \left(j\bar{A}'_n \frac{n\pi}{b} \frac{k_z}{\varepsilon_1 k_o^2 - k_z^2} + \bar{A}''_n\right) \cos \frac{n\pi y}{b} = \sum_{m=0}^{\infty} D_{km} \cos m\pi \frac{y-u_k}{v_k-u_k} \qquad 4.20$$

As for a transverse discontinuity, each of the modal amplitudes $\bar{A}'_n$ is expressed in terms of the electric field function coefficients C_{km} for all N_{ap} apertures, using Fourier analysis and taking into account the vanishing of the field over the strips.

$$\bar{A}'_N = \frac{2}{b} \sum_{k=1}^{N_{ap}} \sum_{m=1}^{\infty} C_{km} \int_{u_k}^{v_k} \sin m\pi \frac{y-u_k}{v_k-u_k} \sin \frac{N\pi}{b} y \, dy \qquad 4.21$$

$$N = 1,2,3\ldots\infty$$

Having truncated the infinite series, bearing in mind the requirement for matching the spatial frequencies of the highest order functions, this can be written in matrix form:

$$\{\bar{A}'\} = \frac{2}{b} [R_1] \{C\} \qquad 4.22$$

Similarly, from 4.20:

$$\bar{A}''_N + j\frac{N\pi}{b} \frac{k_z}{\varepsilon_1 k_o^2 - k_z^2} \bar{A}'_N = -\frac{\varepsilon_{NO}}{b} \sum_{k=1}^{N_{ap}} \sum_{m=1}^{\infty} D_{km} \int_{u_k}^{v_k} \cos m\pi \frac{y-u_k}{v_k-u_k} \cos \frac{N\pi y}{b} \, dy \qquad 4.23$$

$$N = 0,1,2\ldots\infty$$

After truncation this can be written as:

$$\{\bar{A}''\} + j \frac{k_z}{\varepsilon_1 k_o^2 - k_z^2} [d] \{\bar{A}'\} = -\frac{1}{b} [\varepsilon] [\bar{R}_2] \{D\} \qquad 4.24$$

Matrices $[R_1]$, $[R_2]$ and vectors $\{C\}$, $\{D\}$ have partitioned forms as

in 1.20. $[d]$ is a diagonal matrix with elements $d_{ii} = \frac{i-1}{b}\pi$. $[\varepsilon]$ is a diagonal matrix with elements $\varepsilon_{ii} = 1, i=1, \varepsilon_{ii} = 2, i \neq 1$. A dummy coefficient $\bar{A}'_0$ is included for convenience in equations 4.22 and 4.24, although the value of this is irrelevant as all fields for the E-type mode vanish when n=0.

The coefficient of each magnetic aperture field component can be expressed as a series of modes on either side of the strips, using the orthogonality of such components in the aperture in question. Here again, y and z components can be considered separately. Thus, using 4.15 and 4.18:

Matching z-components:

$$E_{kM} = -j\frac{\mathcal{E}_{MO}}{v_k-u_k}\frac{\varepsilon_1 k_o^2 - k_z^2}{\omega\mu_o}\sum_{n=0}^{\infty}\bar{A}''_n\frac{\cot(p_{1n}l_1)}{p_{1n}}\int_{u_k}^{v_k}\cos M\pi\frac{y-u_k}{v_k-u_k}\cos\frac{n\pi y}{b}\,dy \qquad 4.25$$

$M = 0,1,2\ldots\infty$

Matching y-components:

$$F_{kM} = \frac{2}{v_k-u_k}\sum_{n=1}^{\infty}\left\{\frac{n\pi}{b}\frac{k_z}{\omega\mu_o p_{1n}}\bar{A}''_n - j\frac{\omega\varepsilon_o\varepsilon_1 p_{1n}}{\varepsilon_1 k_o^2 - k_z^2}\bar{A}'_n\right\}\cot(p_{1n}l_1)\int_{u_k}^{v_k}\sin M\pi\frac{y-u_k}{v_k-u_k}\sin\frac{n\pi y}{b}\,dy \qquad 4.26$$

$M = 1,2,3\ldots\infty$

Using 4.16 and 4.18, and matching z-components:

$$E_{kM} = \frac{\mathcal{E}_{MO}}{v_k-u_k}\frac{\varepsilon_2 k_o^2 - k_z^2}{\omega\mu_o}\sum_{n=0}^{\infty}\left\{j\bar{A}''_n - \frac{n\pi}{b}\bar{A}'_n\left(\frac{k_z}{\varepsilon_1 k_o^2 - k_z^2} - \frac{k_z}{\varepsilon_2 k_o^2 - k_z^2}\right)\right\}\frac{\cot(p_{2n}l_2)}{p_{2n}} \qquad 4.27$$

$$\int_{u_k}^{v_k}\cos M\pi\frac{y-u_k}{v_k-u_k}\cos\frac{n\pi}{b}y\,dy$$

$M = 0,1,2\ldots\infty$

Matching y-components:

$$F_{kM} = \frac{2}{v_k-u_k}\sum_{n=1}^{\infty}\left\{-\frac{n\pi}{b}\frac{k_z}{\omega\mu_o p_{2n}}\bar{A}''_n + j\bar{A}'_n\left[\frac{\omega\varepsilon_o\varepsilon_2 p_{2n}}{\varepsilon_2 k_o^2 - k_z^2} - \frac{n^2\pi^2}{b^2}\frac{k_z}{\omega\mu_o p_{2n}}\left(\frac{k_z}{\varepsilon_1 k_o^2 - k_z^2} - \frac{k_z}{\varepsilon_2 k_o^2 - k_z^2}\right)\right]\right\}\cot(p_{2n}l_2)\int_{u_k}^{v_k}\sin M\pi\frac{y-u_k}{v_k-u_k}\sin\frac{n\pi y}{b}\,dy \qquad 4.28$$

$M = 1,2,3\ldots\infty$

Combining expressions of the form of 4.25 and 4.27 for all apertures and expressing the result in matrix form, then eliminating the coefficients E_{kM}:

$$- j \frac{1}{\omega\mu_o} [R_2]^T \left[(\varepsilon_1 k_o^2 - k_z^2)[p_1] + (\varepsilon_2 k_o^2 - k_z^2)[p_2] \right] \{\bar{A}''\}$$
$$+ \omega\varepsilon_o k_z \frac{\varepsilon_2 - \varepsilon_1}{\varepsilon_1 k_o^2 - k_z^2} [R_2]^T [p_2] [d] \{\bar{A}'\} = 0 \qquad 4.29$$

where $p_{1ii} = \dfrac{\cot(p_{1,i-1} l_1)}{p_{1,i-1}}$, $p_{2ii} = \dfrac{\cot(p_{2,i-1} l_2)}{p_{2,i-1}}$

Similarly, eliminating F_{kM} from 4.26 and 4.28:

$$\frac{k_z}{\omega\mu_o} [R_1]^T \left[[p_1] + [p_2] \right] [d] \{\bar{A}''\} - j [R_1]^T \left[\frac{\omega\varepsilon_o\varepsilon_1}{\varepsilon_1 k_o^2 - k_z^2} ([p_1'] - \frac{k_z^2}{\varepsilon_1 k_o^2} [p_2] [d] [d]) + \frac{\omega\varepsilon_o\varepsilon_2}{\varepsilon_2 k_o^2 - k_z^2} ([p_2'] + \frac{k_z^2}{\varepsilon_2 k_o^2} [p_2] [d] [d]) \right] \{\bar{A}'\} = 0 \qquad 4.30$$

where

$$p'_{1ii} = p_{1,i-1} \cot(p_{1,i-1} l_1) \ , \ p'_{2ii} = p_{2,i-1} \cot(p_{2,i-1} l_2)$$

If the choice of ratios of modes and aperture functions has been made as suggested in chapter 2, the total number of aperture functions will be less than the number of modes. Thus there will be insufficient equations in the sets represented by 4.29 and 4.30 to allow the elimination of one unknown column vector. If, however, $\{\bar{A}'\}$ and $\{\bar{A}''\}$ are replaced by expressions involving $\{C\}$ and $\{D\}$, using 4.22 and 4.24, either $\{C\}$ or $\{D\}$ can be eliminated by combining the resulting equations, which are given below:

$$- \frac{j}{2} [R_2]^T \left[(\varepsilon_1 k_o^2 - k_z^2) [p_1] + (\varepsilon_2 k_o^2 - k_z^2) [p_2] \right] [\varepsilon] [R_2] \{D\} + k_z [R_2]^T$$
$$\left[[p_1] + [p_2] \right] [d] [R_1] \{C\} = 0 \qquad 4.31$$

$$\frac{k_z}{2}[R_1]^T\left[[p_1]+[p_2]\right][d][\varepsilon][R_2]\{D\}+j[R_1]^T\left[\frac{\varepsilon_1 k_o^2}{\varepsilon_1 k_o^2-k_z^2}([p_1']+\frac{k_z^2}{\varepsilon_1 k_o^2}[p_1][d][d])+\frac{\varepsilon_1 k_o^2}{\varepsilon_2 k_o^2-k_z^2}([p_2']-\frac{k_z^2}{\varepsilon_1 k_o^2}[p_2][d][d])\right][R_1]\{C\}=0 \quad 4.32$$

These can be written in more convenient form as:

$$-j[T_1]\{D\}+k_z[T_2]\{C\}=0 \quad 4.31(a)$$

$$k_z[T_3]\{D\}+j[T_4]\{C\}=0 \quad 4.32(a)$$

$\{D\}$ can be eliminated by multiplying 4.31(a) through by $[T_1]^{-1}$ and substituting for $\{D\}$ in 4.32(a). It is preferable to invert $[T_1]$ or $[T_4]$ rather than $[T_2]$or $[T_3]$, since the former are symmetric, and rapid iterative methods dependent on this property can be used. The final equation is:

$$[-k_z^2[T_3][T_1]^{-1}[T_2]-[T_4]]\{C\}=0 \quad 4.33$$

Notice that all the matrix elements are real.

Having specified k_z, the values of k_o for which the determinant of the matrix in 4.33 vanishes are required. As $[p_1]$, $[p_2]$, $[p_1']$ and $[p_2']$ are functions of k_o, it is necessary to generate new matrices $[T_1]$, $[T_2]$, $[T_3]$ and $[T_4]$, using 4.31 and 4.32, for each trial value of this parameter.

An alternative way of formulating this problem would be to define sets of E-type and H-type aperture functions and then expand each set of modal amplitudes in terms of both sets of aperture components using the orthogonality properties:

$$\int_0^b \underline{e}'_{tn} \times \underline{h}'^{*}_{tm}\cdot d\underline{s} = \int_0^b \underline{e}''_{tn} \times \underline{h}''^{*}_{tm}\cdot d\underline{s} = \int_0^b \underline{e}'_{tn} \times \underline{h}''^{*}_{tn}\cdot d\underline{s} = \int_0^b \underline{e}''_{tn} \times \underline{h}'^{*}_{tn}\cdot d\underline{s} = 0 \quad , \quad m\neq n$$

Similar properties would apply to the aperture field components, and would be used when matching the magnetic fields. It is doubtful, however, whether there would be any advantage in this, since the derivation of equations relating the sets of coefficients would be more involved, and each would contain three sets of unknowns whereas 4.21 and 4.25 contain only two. Moreover, the need to invert a matrix would not be avoided.

4.3 Homogeneous Rectangular Waveguide with Thin Longitudinal Ridges.

The special case of the structure described above which will be analysed in this section is an otherwise empty rectangular waveguide fitted with an infinitely thin longitudinal ridge, or a pair of ridges in the same longitudinal plane such that there is a single coupling slit. By introducing thin ridges in a rectangular guide, it is possible to reduce significantly the cut-off frequency of the dominant mode, because of the effective increase in length of the guide boundary. Also, if the ridges are centrally positioned, the H_{20} mode's cut-off frequency is unaffected since it has no y-component of electric field in the plane of symmetry. As the H_{20} is the next higher-order mode for usual aspect ratios, the useful bandwidth of the guide can therefore be increased.

As the ridged guide is a homogeneous structure, the cut-off wavenumber k_c for a given mode is related to k_z and k_o through the equation:

$$k_z^2 = k_o^2 - k_c^2 \qquad 4.34$$

Thus if k_c is determined by setting $k_z = 0$, the value of k_o corresponding to any other value of k_z may easily be found.

If the values $\varepsilon=1$, $k_z=0$ are substituted in the transverse mode expressions 4.1-4.4, it is found that the E-type and H-type mode fields become identical to those for conventional E and H modes in parallel-plate waveguide. The second term on the right-hand side of 4.8 vanishes, which implies that the two types of transverse mode no longer couple together at the slit, so solutions may be found using one type of mode alone. Solutions using transverse E-modes give H-mode cut-off frequencies for the ridged guide, since their fields are such that $h_z = 0$, whilst E-mode cut-off frequencies are obtained using transverse H-modes. Solutions for the transverse E-mode case are found by using 4.22 and putting $k_z = 0$, $\varepsilon_1 = \varepsilon_2 = \varepsilon$ in 4.30. The latter equation becomes:

$$[R_1]^T \left[[p_1'] + [p_2'] \right] \{\bar{A}'\} = 0 \qquad 4.35$$

Imposing the electric field matching condition using 4.22:

$$[R_1]^T \left[[p_1'] + [p_2'] \right] [R_1] \{C\} = 0 \qquad 4.36$$

This now involves the required square matrix whose determinant must vanish for a non-trivial solution.

Matrix equations for the transverse H-mode case are found by substituting for k_z, ε_1 and ε_2 in 4.24 and 4.29:

$$\{\bar{A}''\} = -\frac{1}{b} [\varepsilon] [R_2] \{D\} \qquad 4.37$$

$$[R_2]^T \left[[p_1] + [p_2] \right] \{\bar{A}''\} = 0 \qquad 4.38$$

Upon elimination of $\{\bar{A}''\}$, the final equation for this case is:

$$[R_2]^T \left[[p_1] + [p_2] \right] [\varepsilon] [R_2] \{D\} = 0 \qquad 4.39$$

A computer program has been written which determines values of k_o for which the determinant of the matrix in either 4.36 or 4.39 vanishes, using the method of False Position. The method requires initial values of k_o on either sides of the zero, and where necessary, these are obtained by stepping k_o by small increments over a suitable range and watching for sign changes in the value of the determinant. Iteration then proceeds until two successive estimates of k_c agree to within a prescribed criterion. As the elements of $[R_1]$ and $[R_2]$ are independent of k_o, these matrices may be generated before iteration begins, and stored by the computer. However, the generation of the diagonal matrix and the formation of the matrix product must be performed for each estimate of k_c .

Computed values of cut-off wavelength for a rectangular waveguide of aspect ratio 2:1, fitted with a pair of identical centrally-positioned ridges, are given in tables 4.1-4.3 and figure 4.3. Because of symmetry, transverse modes with odd and even y - dependences are not coupled by the slit in this case, and a solution may therefore be found using only one of these types. Table 4.1 shows the convergence of the solution for the perturbed H_{10} mode in the case $b'/b=0.25$, as more modes and aperture functions are taken into account. The ratio of these is 4:1, equal to that of the heights of guide and slit. Convergence is clearly rapid, and the solution using 20 transverse modes differs by less than 0.1% from the estimated converged value. By analogy with the thin iris problem, the 4:1 mode/aperture-function ratio should give the most accurate solution, and this is supported by the results displayed in table 4.2. Here the effect of changing the

Table 4.1 (H_{10} mode, b'/b=0.25)

No. of transverse modes	No. of ap. fns.	λ_c/a
4	1	2.6413
8	2	2.6093
12	3	2.6020
16	4	2.5990
20	5	2.5975

Estimated converged value
= 2.5960

Table 4.2 (H_{10} mode, b'/b=0.25)

No. of transverse modes	No. of ap. fns.	λ_c/a
10	5	2.4064
15	5	2.5582
20	5	2.5975
25	5	2.5994
30	5	2.6005
35	5	2.6012
40	5	2.6015

Table 4.3(a) (H_{10} mode)

b'/b	No. of transverse modes	No. of ap. fns.	λ_c/a	"Waveguide Handbook" value
0.10	20	2	3.084	3.062
0.15	20	3	2.873	2.925
0.20	20	4	2.719	2.747
0.25	20	5	2.598	2.636
0.30	20	6	2.498	2.536
0.35	20	7	2.413	2.505
0.40	10	4	2.344	2.374
0.50	10	5	2.226	2.268

Tables refer to symmetric thin-ridged w/g for which a=2b (see inset to fig.4.3)

Table 4.3(b) (H_{30} mode)

0.10	20	2	0.888	0.880
0.20	20	4	0.851	0.867
0.25	20	5	0.834	0.858

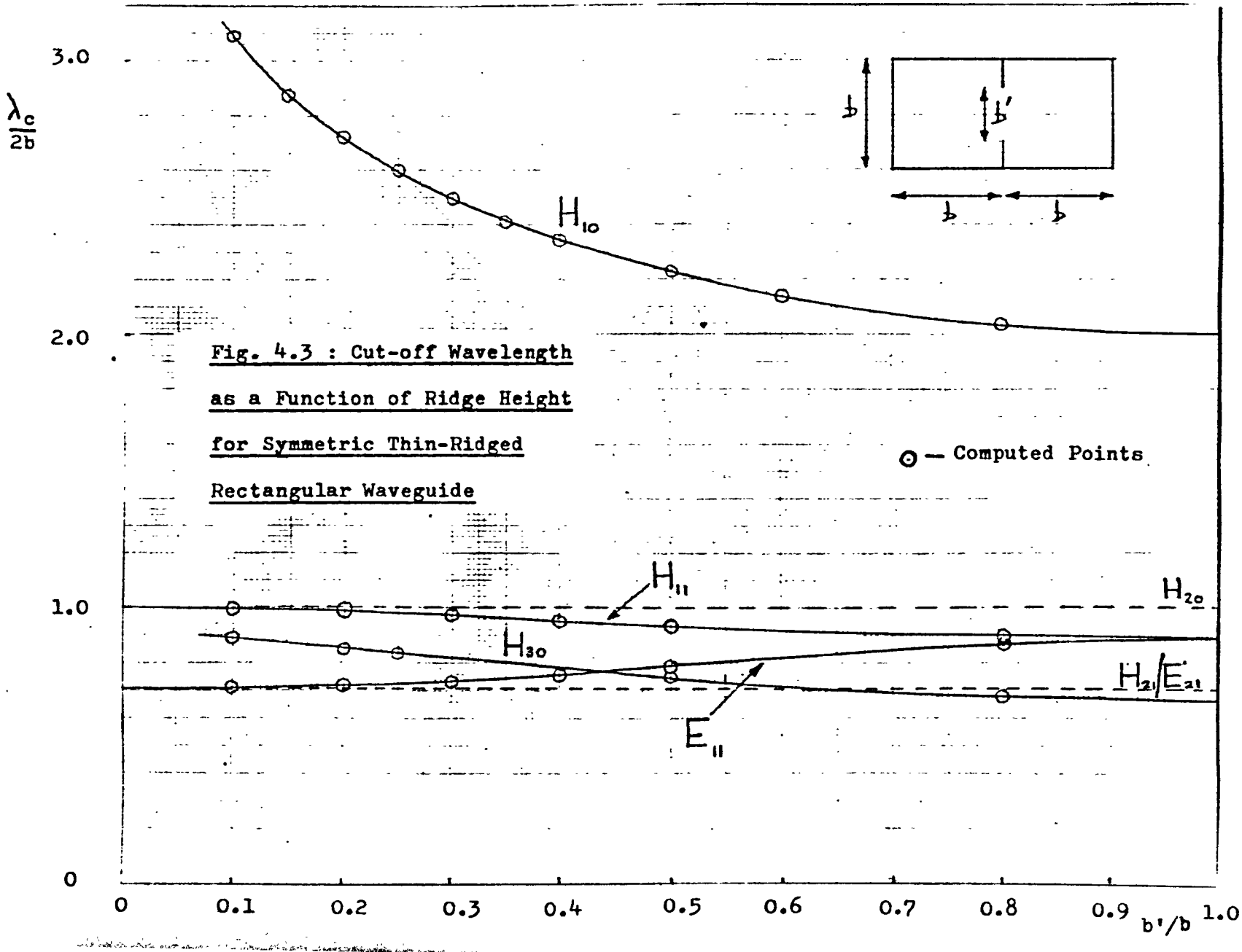

Fig. 4.3 : Cut-off Wavelength as a Function of Ridge Height for Symmetric Thin-Ridged Rectangular Waveguide

number of transverse modes while keeping the number of aperture functions constant is investigated, and it can be seen, for example, that whereas increasing the ratio from 4:1 to 8:1 alters the solution by less than 0.2%, reducing it to 2:1 produces a change of over 7%. The ratio 4:1 corresponds to a "breakpoint" in the characteristic, and it therefore seems that the argument of section 2.2.2 regarding the choice of this ratio applies equally to both transverse and longitudinal discontinuities.

In table 4.3, computed values of H_{10} and H_{30} cut-off wavelength for various slit heights are compared with those given in the Waveguide Handbook [4]. The mode/aperture-function ratio was set equal to b/b'. The results in reference 4 were obtained by conventional Transverse-Resonance, and can be expected to be less accurate than the computed ones, particularly as the latter lie on a smooth curve (see fig. 4.3) whereas the former do not. The agreement is quite good in most cases, however, the maximum discrepancy being about 4%. For the case b'/b=0.5, Ahmed [27] has obtained a solution $\lambda_c/a = 2.140$ using the Finite-Element method. As this is known to be a lower bound to the true value and was obtained using a very coarse mesh, the agreement is felt to be satisfactory.

Figure 4.3 shows the computed variation of cut-off wavelength with slit height for the H_{10}, H_{30}, H_{11} and E_{11} modes. Twenty transverse modes were taken into account for $b'/b \leqslant 0.35$, otherwise ten were considered. Cut-off wavelengths for the H_{20}, H_{21} and E_{21} modes, which are unaffected by the ridges, are shown dashed. It can be seen

that by inserting thin ridges such that b'/b is about 0.1, the useful bandwidth of the guide can be increased by a factor of two.

As the height of the slit is decreased, the field pattern of the H_{11} mode is transformed into that of two individual H_{01} modes in the two separate square guides formed when b'/b=0. Similarly, the E_{11} mode transforms into two individual E_{11} modes. When b'/b=0, the H_{11} and E_{11} modes have the same cut-off wavelengths as the H_{20} and E_{21} modes respectively. Care had therefore to be taken when determining H_{11} and E_{11} cut-off's for small values of b'/b, in view of the proximity of the two solutions, particularly as the antisymmetric mode solutions in this case correspond to poles of the determinant, and the inclusion of such a pole in the iteration range causes divergence of the False Position method.

4.4 T - Septate Waveguide.

A structure whose analysis is similar to that of the thin-ridged waveguide is a rectangular guide fitted with a thin T - shaped septum such that there is symmetry about a horizontal plane halfway up the guide. (See figure 4.4). With the correct choice of dimensions, this guide can support two modes which propagate with the same phase velocity, and it can then form the basis for a slotted line-source antenna with arbitrary polarization.

Approximate electric field distributions for the two modes, referred to as "sum" and "difference", are included in figure 4.4. Because of symmetry, there is no x-component of electric field, in the plane $y = b, x > 0$ for the sum mode, nor is there an x-component of

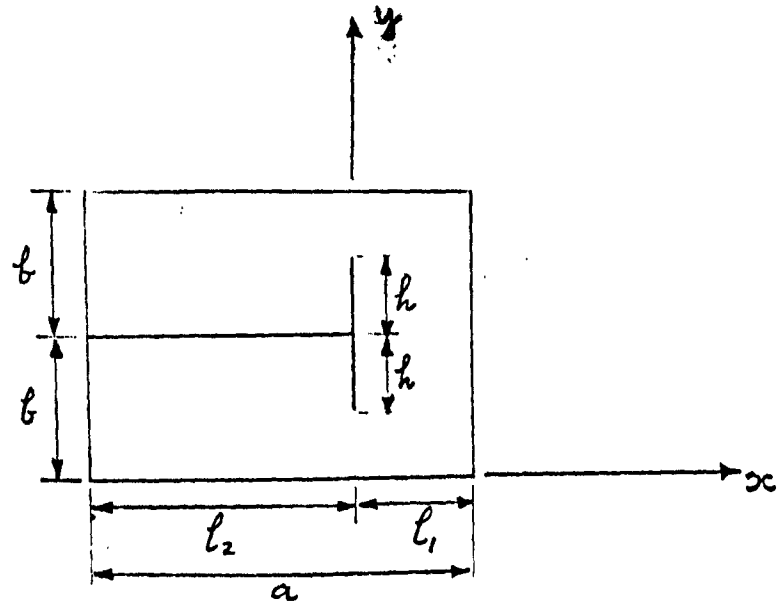

"Sum" Mode

"Difference" Mode

Transverse Electric Field Distribution

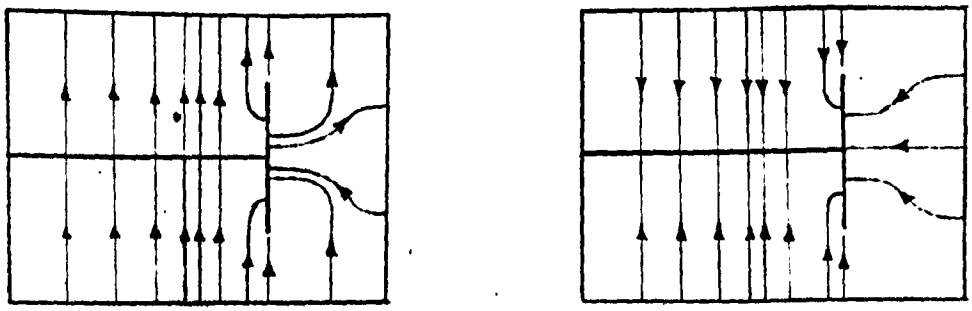

Magnetic Wall

Equivalent Single-Ridged Waveguide

Fig. 4.4 : The T-Septate Waveguide

magnetic field in this plane for the difference mode. It is therefore permissible to insert an electric wall in this plane for the former case and a magnetic wall for the latter, and then consider only the lower half of the structure. This gives two single-ridged guides, also shown in figure 4.4, for which the perturbed H_{10} mode cut-off wavelengths are identical to those for the sum and difference modes in the T - septate guide. The equivalent single-ridged guide for the sum mode may be analysed as in the previous section, but a slight modification is needed for the equivalent difference structure because of the magnetic wall - n must be replaced by $(2n+1)/2$ in the expressions for the transverse E-type and H-type mode fields on the right of the ridge.

A check on the correctness of the difference mode solution was made by comparing the cut-off wavelength for the case h=0 with that found by rotating the guide through 90° and treating it as a rectangular guide with a centrally located thin ridge. There was found to be excellent agreement between the two solutions.

The T - septate waveguide has been analysed by Elliott [28], who uses a variational method to determine the effect of the ridge in the equivalent single-ridged guide. This author also gives experimentally derived guide wavelengths for both principal modes for a T - septate guide in which a=1.372", 2b=0.622", operated at a frequency of 6 GHz. These are shown in figure 4.5 as functions of the parameters l_2 and h, together with curves derived by the computational method using twenty transverse modes in both regions and 20 $\frac{b-h}{b}$, or the nearest lower integer, functions in the aperture. It can be seen that the experi-

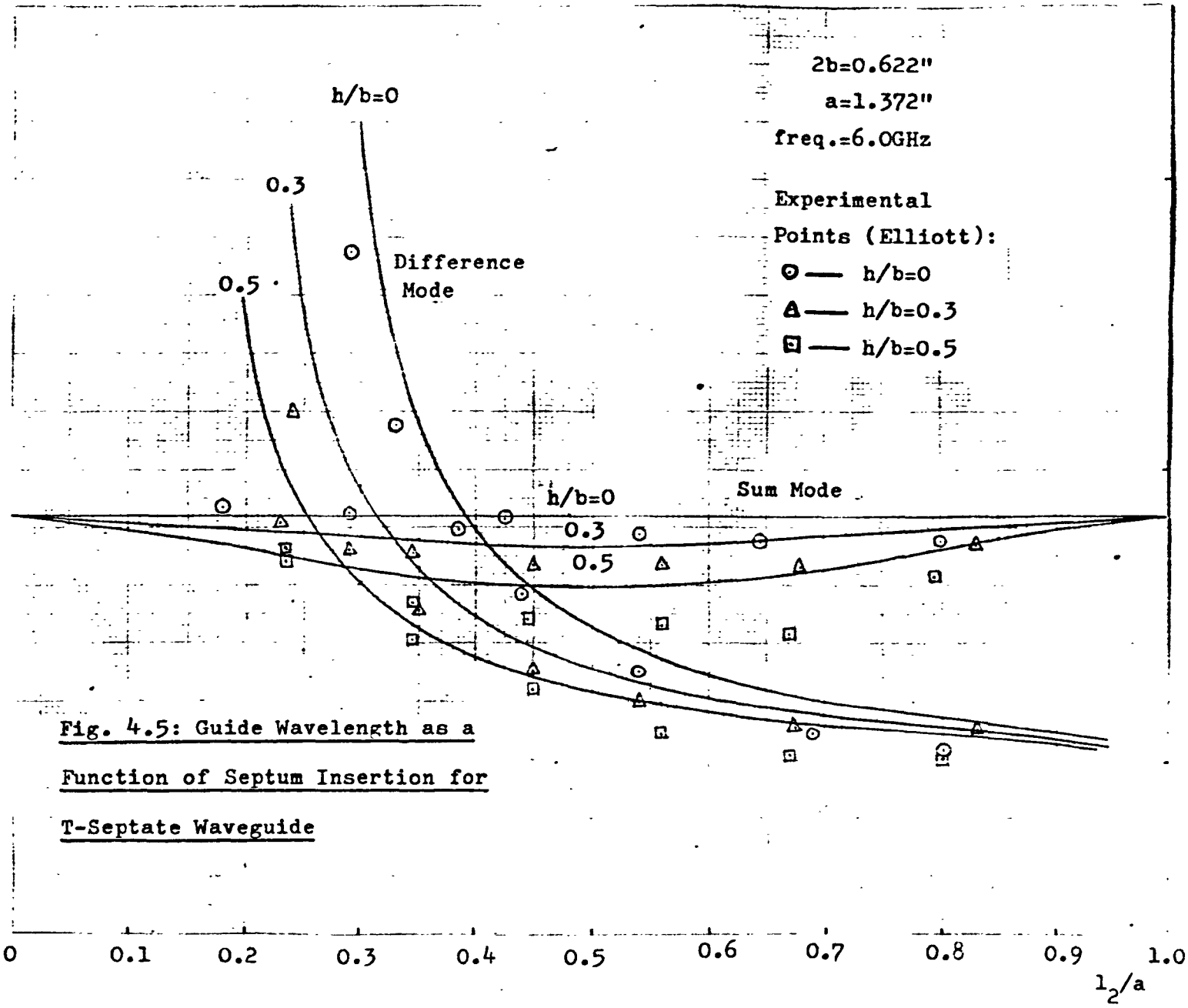

Fig. 4.5: Guide Wavelength as a Function of Septum Insertion for T-Septate Waveguide

mental values are generally less than the theoretical ones, but this can be accounted for by the finite thickness (0.063") of the septum in the experimental case. Elliott's theoretical results agree well with those in figure 4.5 for the sum mode, but the discrepancy for the difference mode is very considerable, and the agreement between theory and experiment in this case is far better using the computational method. For example, the septum insertion required for equal guide wavelengths can be predicted to within about 15% using the computational method, despite the thickness of the septum, whereas that given by Elliott's theory can be almost 100% in error.

4.5 Discussion

In this chapter the application of the computational method to longitudinal discontinuities has been described, and examples involving thin conducting strips and septa in rectangular waveguide have been given. It has been shown that for homogeneous structures of the latter type the formulation is quite straightforward, particularly if use can be made of symmetry, and that very accurate results can be obtained with no more than twenty transverse modes. In fact, it seems that with this method the dispersion characteristics of such waveguides can be determined to an accuracy which was not previously possible except by using numerical techniques such as the Finite-Difference and Finite-Element methods.

Although these numerical methods are invaluable for treating waveguides with irregular boundaries to which the method described here

is inapplicable, they are uneconomical by comparison in cases where both types of method can be used. For example, Davies and Muilwyk [10] have stated that up to four minutes of computing time are required for 0.1% accuracy using the Finite-Difference method, and in the case of ridged rectangular waveguide they needed to store field values for some 8,000 mesh points. With the computational method, on the other hand, results of similar accuracy were obtained in under ten seconds, and with a corresponding storage requirement (for the various matrix elements) of only two or three hundred words. Another advantage is that whereas, for homogeneous structures, the Finite-Difference method in the form described by Davies and Muilwyk determines only the lowest-order H and E mode cut-off wavelengths, a programme using the method described here can find cut-off's for higher-order modes without modification.

The Finite-Element method [11] appears to require less time and storage for a given accuracy than Finite-Difference, but still compares unfavourably in this respect with the computational method.

In conclusion, the computational method seems to be the most economical way of obtaining very accurate solutions to a wide range of longitudinal waveguide discontinuity problems of practical importance.

CHAPTER V ANALYSIS OF A SQUARE MULTIMODE BOX-HORN

5.1 Introduction.

The ability of step discontinuities in waveguides to excite higher-order propagating modes can be made use of in the design of box-horn antennas such as that described by Silver [13]. As well as the increase in gain which can be achieved under certain circumstances, box-horns have the advantage of short physical length when compared with conventional flared horns, and this makes them particularly suitable for use in compact airborne radar installations involving solid-state circuitry. This chapter is concerned with the determination, using the computational method of chapter 3, of the performance of X-band box-horns for such applications.

The horn structure is shown in figure 5.1(a), it being specified that the aperture width a should be about 3". Both the box section and the input waveguide are of square cross-section, allowing the horn to be circularly polarized. It is required that the gain should be at least 10dB relative to an isotropic source, and should if possible compare favourably with that of a flared horn of the same aperture size. The length of the box section should preferably be about 1".

The step discontinuity analysis provides an opportunity for testing a computer program intended eventually for use in monopulse feed design. As box-horn radiations patterns are determined both theoretically and experimentally, the accuracy of the computational method as applied to multimode step discontinuities can be verified.

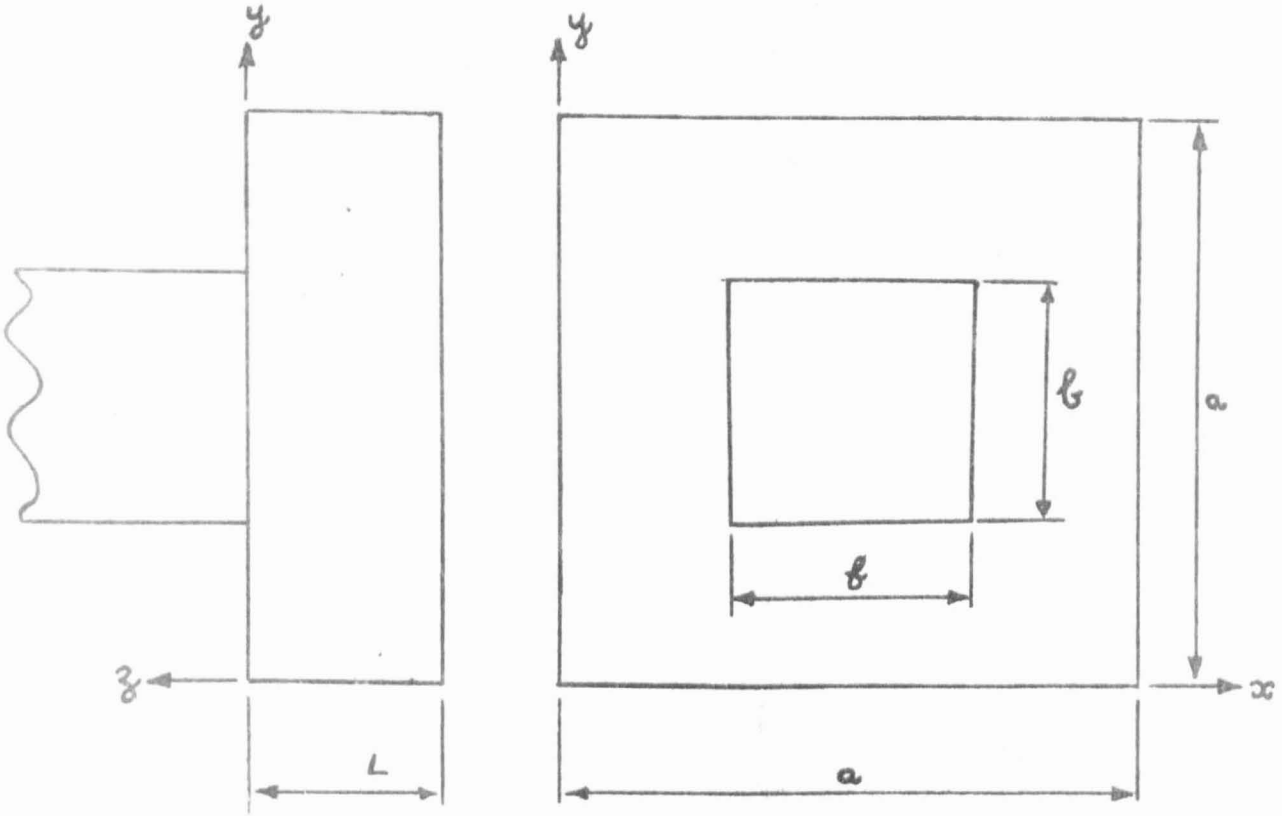

Fig. 5.1(a) Box Horn Structure

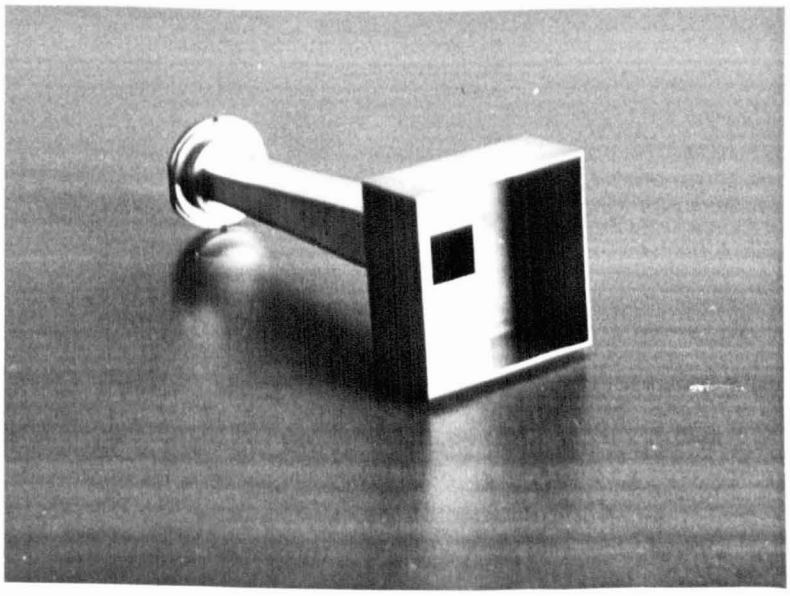

Fig. 5.1(b) Experimental Box Horn & Input Taper

5.2 Design Considerations.

The symmetry of the junction is such that only modes having an odd horizontal field dependence and an even vertical field dependence are excited in the box section by an H_{10} mode incident in the input waveguide. Thus the propagating modes in the box section for the specified aperture width of about 2.4 free space wavelengths are H_{10}, H_{12}, E_{12}, H_{30}, H_{32}, E_{32}, H_{14} and E_{14}, the range of a/λ_o for which only these modes can propagate being given by:

$$2.06 < a/\lambda_o < 2.5 \qquad 5.1$$

Of these modes, only the H_{10} and H_{30} contribute to the on-axis component of the horn's far-field radiation pattern, and they should therefore be excited as strongly as possible relative to the other modes for maximum gain. The choice of the length L of the box section governs the relative phase of the H_{10} and H_{30} modes in the aperture, because of their different phase velocities. If the transverse aperture electric fields due to these modes are written as:

$$\underline{E}_{T(1,0)} = A'_{10} \sin \frac{\pi}{a} x \, \hat{\underline{i}}_y \qquad 5.2(a)$$

and

$$\underline{E}_{T(3,0)} = A'_{30} \sin \frac{3\pi x}{a} \hat{\underline{i}}_y \qquad 5.2(b)$$

the complex coefficients A'_{10} and A'_{30} need to have the same phase for maximum gain, since the two-mode illumination law then most nearly approximates the optimum uniform distribution.

The width b of the input waveguide should be large enough for the H_{10} mode to propagate, but not so large that over-moding occurs. As

the restrictions imposed by symmetry on the mode-orders in the box section also apply to the input waveguide, the next higher-order modes that can be excited are the H_{12} and E_{12}, with a cut-off wavelength of $2b/\sqrt{5}$. The range of b/λ_o is therefore:

$$0.5 < b/\lambda_o < 1.12 \qquad 5.3$$

To avoid excessive attenuation, the input waveguide should not be operated too close to cut-off.

5.3 Step Solution.

The step discontinuity was analysed using the method of section 3.1, it being assumed that reflections of modes from the aperture and source were negligible. As the box-horn step discontinuity is a special case of the more general junction treated in section 6.5.1, mathematical details will not be given here. In the small waveguide, eleven modes were taken into account, being chosen in order of increasing cut-off frequency up to the Hand E_{34}. In the box section, twenty modes were considered, the H_{70} having the highest cut-off frequency. The choice of the highest-order x and y dependences was somewhat arbitrary, but for some of the configurations considered it corresponded well to the condition for matching the highest-order spatial frequencies of modes on either side of the discontinuity plane, shown in section 3.3 to be the optimum. Four values of a/λ_o in the range given by 5.1 were considered, namely 2.1, 2.2, 2.3 and 2.4. Values of b/a were taken in the range 0.28 to 0.43, in steps of 0.05.

The computed distribution of power among the propagating modes excited at the step is shown in figure 5.2, from which it is clear that

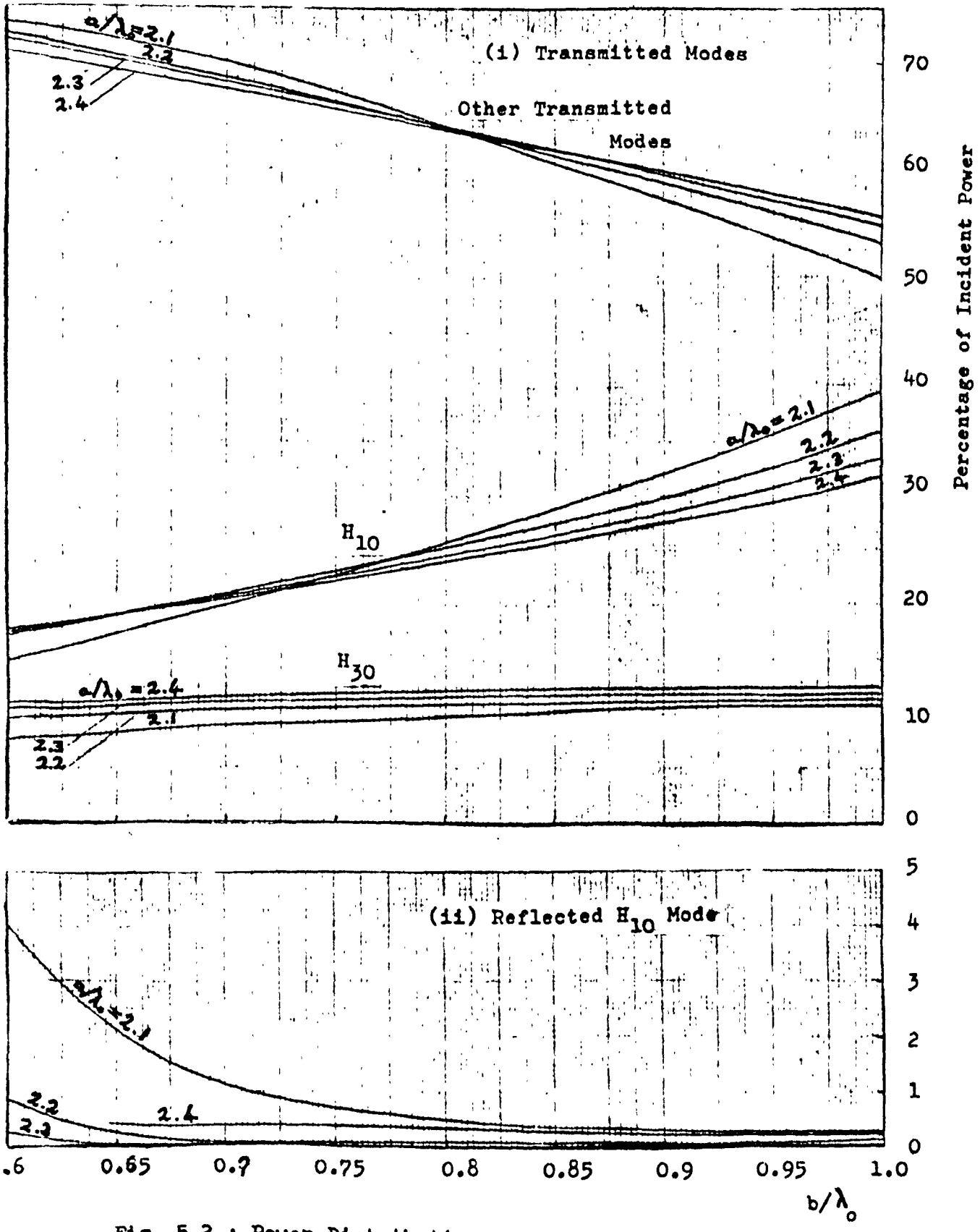

Fig. 5.2 : Power Distribution among Propagating Modes at Square Box-Horn Step Discontinuity

b/λ_o should be as large as possible for maximum power transfer to the transmitted H_{10} mode, and minimum reflected power. The proportion of power transferred to the H_{30} mode, on the other hand, is largely independent of a and b. Other transmitted modes convey at least 50% of the power throughout the range considered. The level of reflected power is generally very low, particularly with the $a/\lambda_o = 2.2$ and 2.3 configurations, where it in no case exceeds 1% of the incident power. Propagating E and H modes of the same order were found, for small values of b/λ_o, to be excited with very nearly the relative amplitude and phase needed for them to form the corresponding LSE hybrid mode with no associated cross-polarized field. The relative phase of excitation of the H_{10} and H_{30} modes was calculated as $178^\circ \pm 1^\circ$ for all the values of a and b considered.

5.4 Theoretical Performance

As mentioned in section 5.2, maximum gain for a particular choice of step dimensions occurs when A'_{10} and A'_{30} have the same phase. As the phase difference between the H_{10} and H_{30} modes at the step has been shown to be almost exactly 180°, a relative phase shift of $(2n+1)\pi$ radians is required, n being any positive or zero integer. This can be produced by choosing L such that:

$$L = (2n+1)\pi/(\beta'_{10} - \beta'_{30}) \qquad 5.4$$

where β'_{10} and β'_{30} are the propagation coefficients of the H_{10} and H_{30} modes respectively. Unfortunately, the values of L for n=0 vary from about $1.8\lambda_o$ when $a=2.1\lambda_o$ to about $2.5\lambda_o$ when $a=2.4\lambda_o$, giving a box length at least twice that specified. To assess the effect of

reducing the box length, the gain of the horn was calculated as follows:

The electric far-field component at a distance R along the horn axis, due to the multimode aperture illumination, is given by:

$$\underline{E}_0 = j \frac{k_o a^2}{2\pi^2 R} \left\{ A'_{10}(1+\bar{\beta}'_{10}) + A'_{30}(1+\bar{\beta}'_{30}) \right\} e^{-jk_o R} \hat{\underline{i}}_y \qquad 5.5$$

The power on axis per unit solid angle is:

$$P_0 = \frac{1}{2\eta_o} |E_0|^2 R^2 \qquad 5.6$$

and the input power to the horn due to the unit-amplitude H_{10} mode is:

$$P_i = \frac{1}{4} \frac{\beta_{10}}{\omega\mu_o} b^2 \qquad 5.7$$

where β_{10} is the H_{10} propagation coefficient for the input waveguide. The gain relative to an isotropic source is defined as:

$$G = 4\pi P_0 / P_i \qquad 5.8$$

Substituting for P_0 and P_i using 5.5, 5.6 and 5.7:

$$G = \frac{8a^4}{b^2 \pi \lambda_o^2 \bar{\beta}_{10}} \left| \left\{ A'_{10}(1+\bar{\beta}'_{10}) + A'_{30}(1+\bar{\beta}'_{30}) \right\} \right|^2 \qquad 5.9$$

For comparison purposes, the gain of a dominant-mode horn of narrow flare angle with a square aperture of side a is given by:

$$G_{DM} = \frac{8a^2}{\pi \lambda_o^2 \bar{\beta}'_{10}} (1+\bar{\beta}'_{10})^2 \qquad 5.10$$

Figure 5.3 shows how G and G_{DM} vary with the parameters a and b. For the box-horn, values of L for optimum phasing (see equation 5.4), and equal to $0.804\lambda_o$ (1" at 9.5GHz) are considered. The results

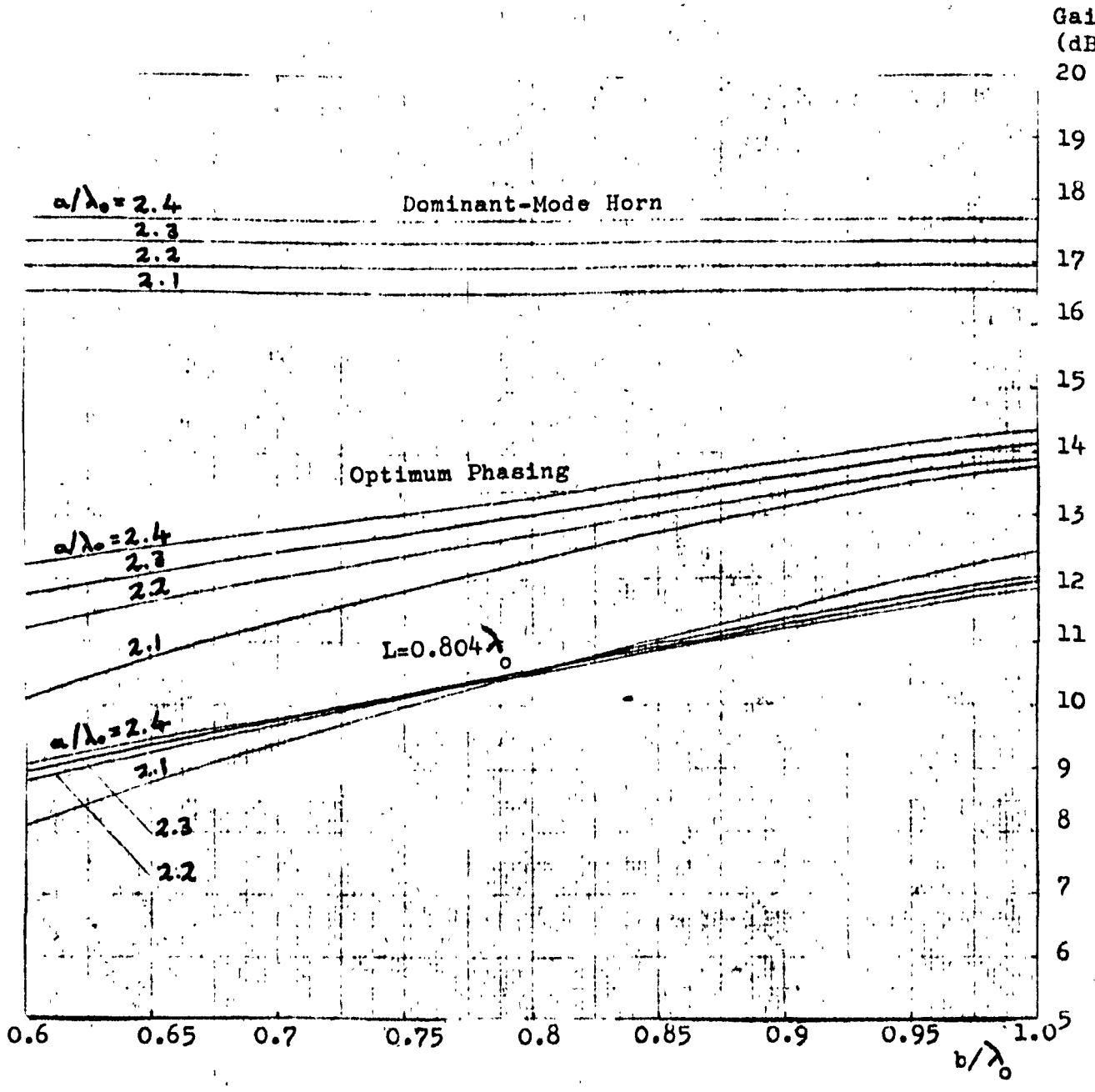

Fig. 5.3 : Gain of Square Box-Horns and Dominant-Mode Horns

confirm that the increase with b/λ_o in power transfer to the H_{10} mode brings about an increase in gain, and show that a reduction in box length from that for in-phase H_{10} and H_{30} modes at the aperture to the specified 1" causes a loss in gain of about 2dB. The gain of the single-mode horn is always greater than that for the box-horn, but the difference can be as small as 3dB for a correctly phased box-horn in which b/λ_o is about 1.0. The specified minimum gain of 10dB is exceeded throughout the considered range of a and b if L is chosen for correct phasing, but if a 1" box is used b/λ_o must exceed about 0.75.

Principal-plane far-field radiation patterns for a square box-horn in which $a=2.3\lambda_o$, $b=0.28a$, have been calculated for various values of box-length L, and are shown in figure 5.4. These were obtained by summing the patterns due to individual modes in the aperture, derived from formulae given by Silver [29]. Only the H_{10} and H_{30} modes contribute to the H-plane pattern, where the 49° main lobe and 7½ dB sidelobe level obtained with in-phase modes will clearly lead to a higher value of gain than the very broad beam associated with short box-lengths. In the E-plane, where all the propagating modes affect the pattern, the beam tends to be broader and more flat-topped than that of the dominant-mode horn. The modes other than H_{10} and H_{30}, which have no on-axis radiated field, are responsible for this effect. The pattern for $L = \lambda_o$ is interesting because of the near-null at around $\theta=43^\circ$, a feature which is clearly sensitive to the relative phases of the modes, and whose experimental verification would therefore tend to confirm the accuracy of the step solution.

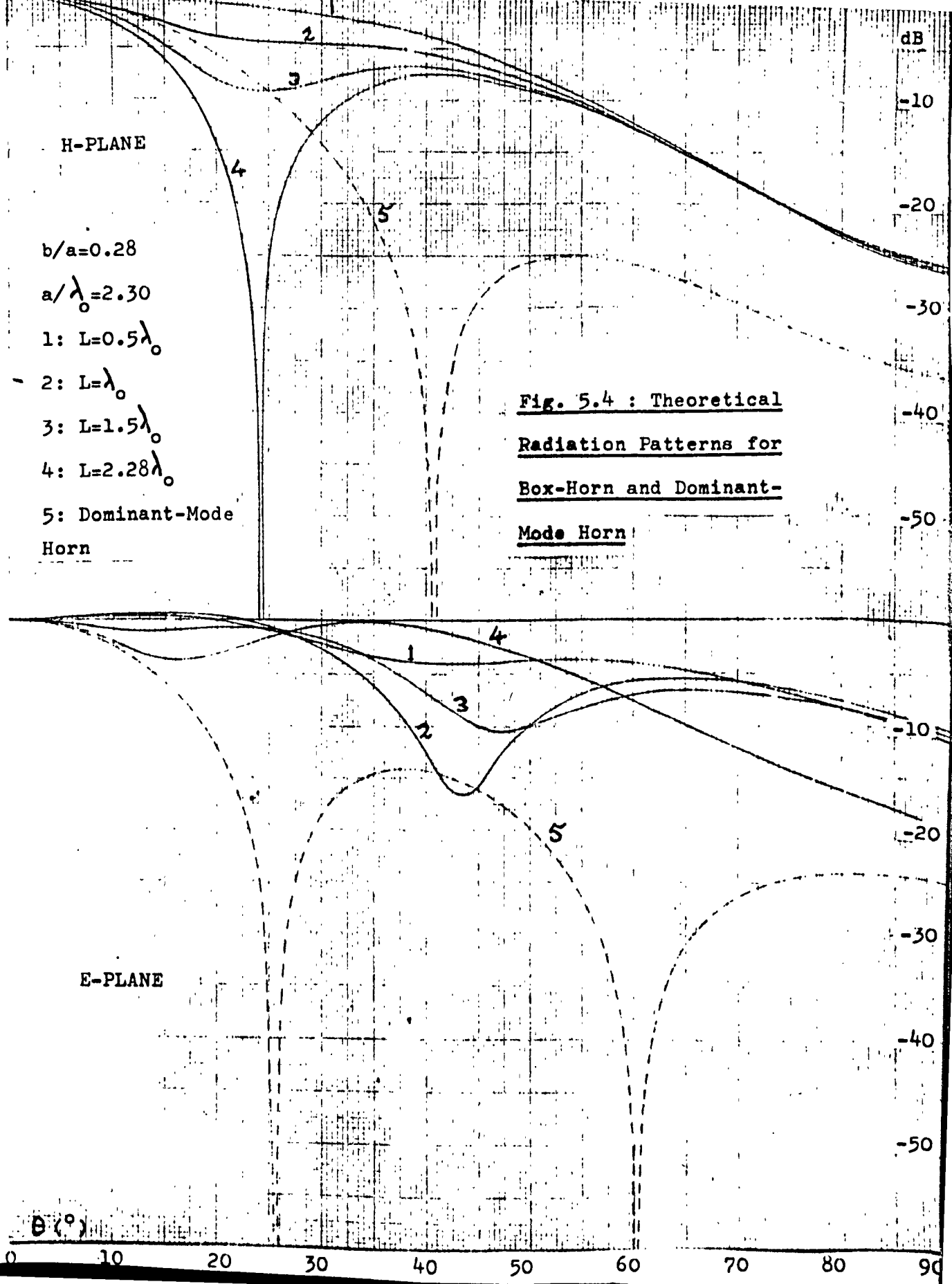

Fig. 5.4 : Theoretical Radiation Patterns for Box-Horn and Dominant-Mode Horn

5.5. Measured Characteristics.

A box-horn for which $a=2.3\lambda_o$, $b=0.28a$, $L=\lambda_o$, for operation at 9.5 GHz was manufactured out of 0.055" brass sheet. The horn was fed from no. 16 waveguide via a section of guide linearly tapered in both planes. The behaviour of such tapers has been determined by Johnson [30], who has shown that their input V.S.W.R. when correctly terminated oscillates about a gradually falling value as the taper length increases. For the guide dimensions in question, minima of oscillation occur when the length is a multiple of 0.915", and a value of 3.66" was found to be convenient. The theoretical V.S.W.R. for this taper is 1.010. The combined box-horn and input taper is shown in figure 5.1(b).

For pattern measurement, the antenna test range which will be described in chapter 7 was used. The box-horn was mounted on the turntable and used as the transmitting antenna, the receiving horn being at a distance of about 12'. This is an entirely adequate separation, since the minimum distance to ensure that the far-field pattern predominates at the receiving horn is $2a^2/\lambda_o$, in this case only about 14".

Principal-plane radiation patterns were measured at 9.5GHz, and these are shown in figure 5.5. The patterns were calibrated individually because of the non-linearity of the detector. In the H-plane, there are no major discrepancies between theory and experiment. The most prominent feature, namely the 4½dB "shoulder" for θ in the region of 30°, can be clearly seen in both theoretical and experimental patterns.

In the E-plane, the experimental pattern shows the expected flat-

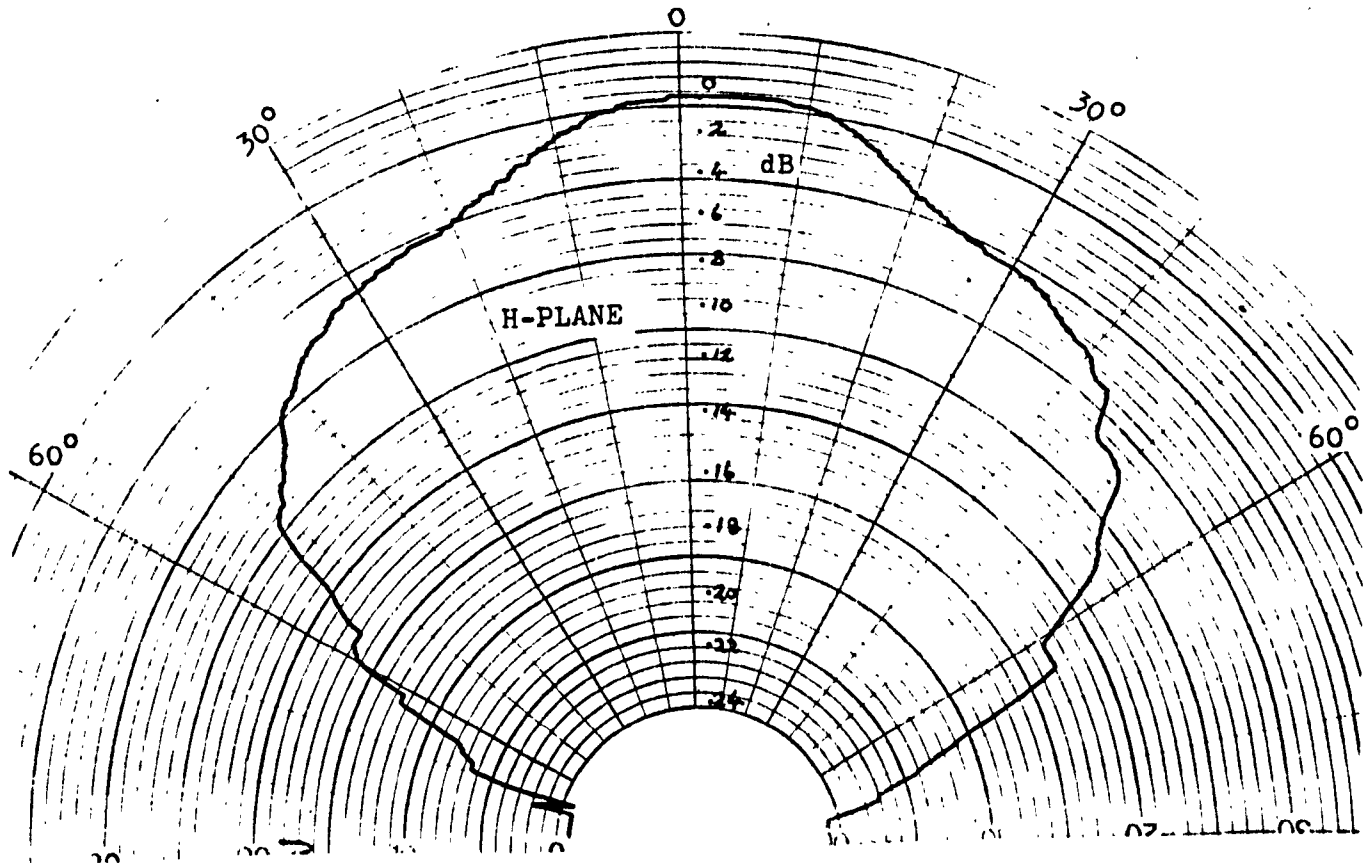

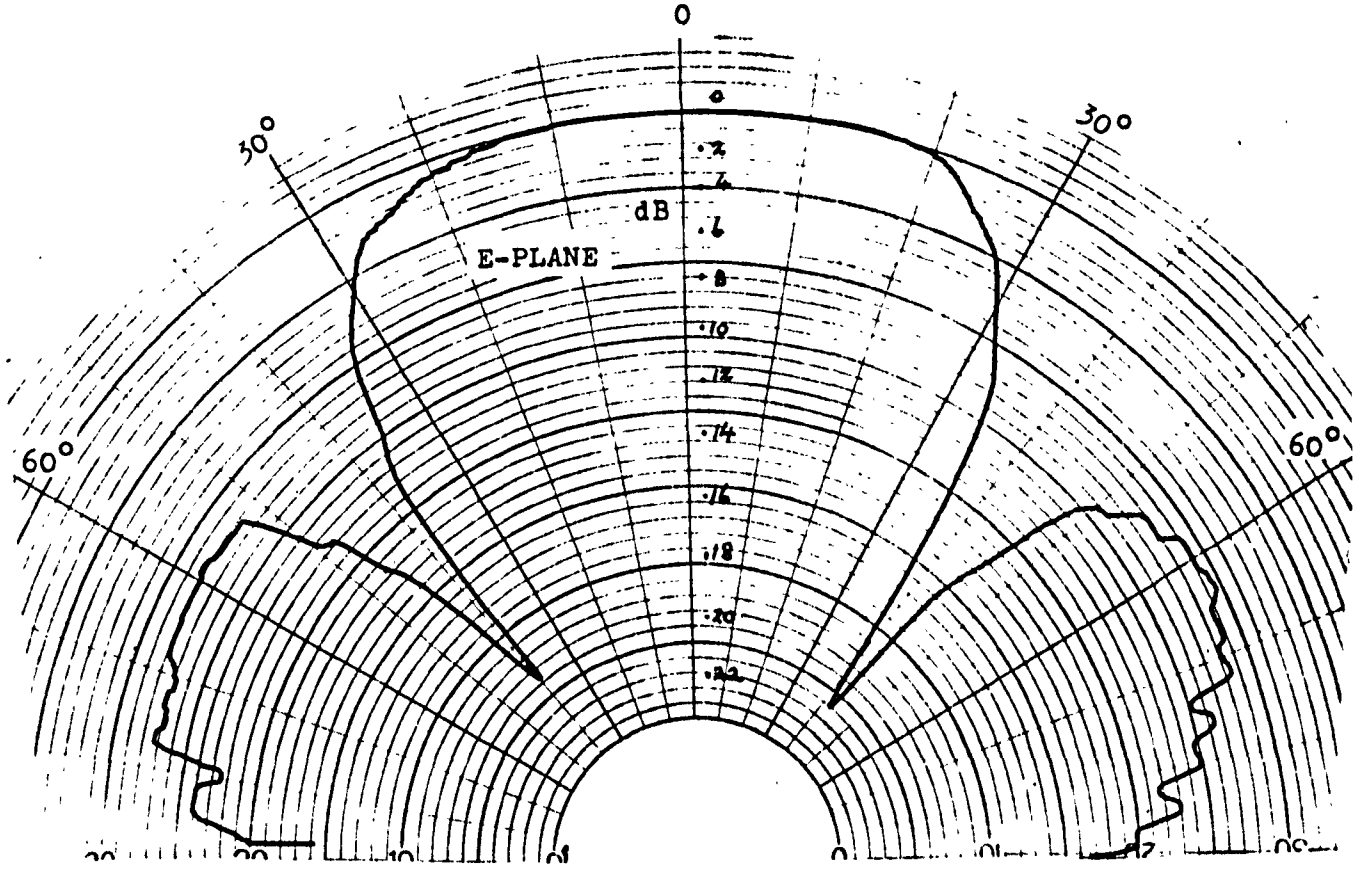

Fig. 5.5 : Measured Box-Horn Radiation Patterns ($a=2.3\lambda_o$, $b=0.28a$, $L=\lambda_o$)

topped beam and near-null at around 43°. There are some small discrepancies, however, particularly in the sidelobe level which was predicted as -6dB but measured as -8dB. The predicted ½dB increase in field strength at about 17° is not apparent, and the "null" is deeper by about 5dB in the experimental case.

The V.S.W.R. of the combined horn and input taper was measured over the frequency range 8.8-10.2GHz at intervals of about 0.1GHz, using an Elliott type 1637 slotted line and Hewlett-Packard type 415D S.W.R. meter, the average of about three measurements being taken at each frequency. The results are displayed in figure 5.6, together with a theoretical curve derived from the step analysis results. Agreement is considered satisfactory in view of the fact that the effects of the taper, whose V.S.W.R. is particularly frequency-sensitive, and of reflections of modes at the radiating aperture were neglected in the theoretical case.

Notice that in both theoretical and practical cases minimum V.S.W.R. occurs at the design frequency, where a value as low as 1.11 can be realised.

5.6. Discussion

It has been shown that, for the preferred horn dimensions given in section 5.1, the required minimum gain can be achieved by making the input waveguide sufficiently large. If b exceeds $\lambda_o/\sqrt{2}$, however, care must be taken to ensure that the H_{11} and E_{11} modes are suppressed. Although symmetry precludes the generation of these modes at the step, they may be generated together with the H_{10} mode in the input waveguide if, for example, this is excited by a probe.

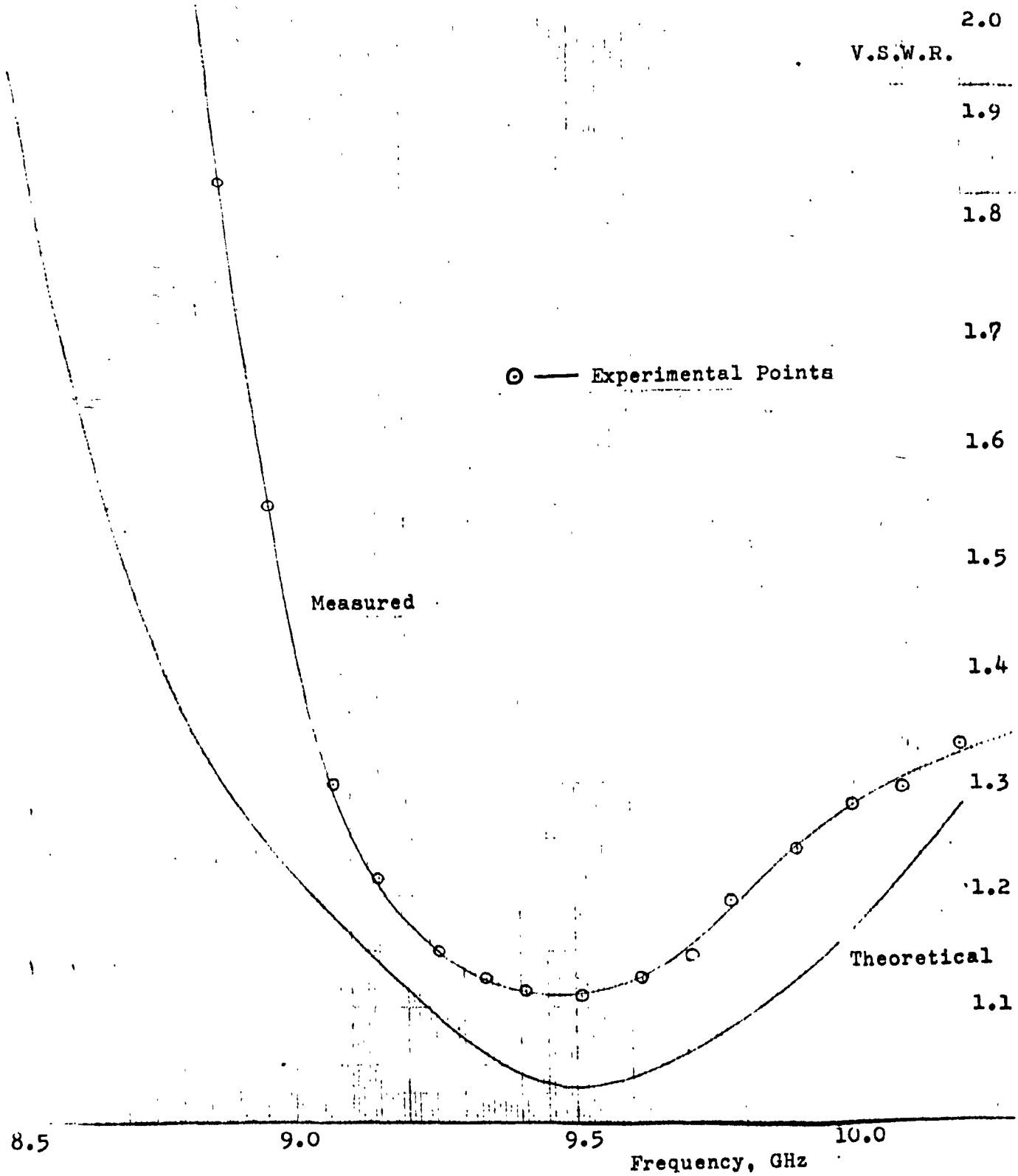

Fig. 5.6 : Square Box-Horn V.S.W.R.

($a=2.3\lambda_o$, $b=0.28a$, $L=\lambda_o$ at 9.5 GHz)

The dominant-mode flared horn has been shown to be superior to the box-horn in terms of gain, by at least 5dB for the preferred box-length. About 3dB of gain have been sacrificed by making the horn square, because of the modes having no axial radiation which are then generated, but this loss is offset by the advantage of circular polarizability.

A desirable feature of the square box-horn is the very low V.S.W.R. obtainable with certain dimensions, which has been shown both theoretically and experimentally. Comparison of computed results for a symmetric square-waveguide junction with those for E and H-plane steps of similar dimensions indicates that although the H-plane discontinuity predominates at low frequencies, the solution tends towards that of the E-plane step as frequency increases. Thus a resonant frequency may exist where the effects of the E and H-plane discontinuities are almost mutually cancelling, giving a very low reflection coefficient. The results of figure 5.6 clearly support this hypothesis.

The discrepancies between theory and experiment do not necessarily cast doubt on the accuracy of the step solution, since they can be attributed to effects neglected in the calculation of radiation patterns and V.S.W.R. The reflection of modes at the aperture, with subsequent re-reflection from the step, is an important source of error, high-order propagating modes such as the H_{14} and E_{14} being particularly affected since their propagation coefficients are much smaller than that of free space. Since such modes carry an appreciable proportion of the total power, the radiation characteristics may be significantly modified. Currents on the outer surface of the horn may also affect the patterns, especially in regions of low signal strength where most of the discrepancy occurs.

CHAPTER VI THE DESIGN OF A MULTIMODE MONOPULSE FEED FOR A SATELLITE-TRACKING ANTENNA.

6.1. Introduction.

As mentioned in section 1.1, the use of multi-moding in a square aperture seems an attractive proposition in the design of monopulse feeds for front-fed paraboloid or Cassegrain reflector systems. The use of higher modes, particularly the H_{12}, E_{12} and H_{30}, in addition to the basic H_{10} for sum-channel operation can result in a feed aperture field distribution with nearly equal tapers in both principal planes, whose far-field radiation pattern is almost circularly symmetric and has a low sidelobe level. Thus the reflector is efficiently illuminated and spillover is low, giving a considerable increase in gain and signal-to-noise ratio over a system with a conventional feed. Also, sum and difference primary beamwidths are more compatible, since the sum feed aperture illumination is now concentrated in the centre.

A circularly polarized wave can be viewed as a combination of two components of equal magnitude, at right angles to one another and differing in phase by 90°. A feed with four-fold symmetry can radiate such a wave, since propagation conditions for modes corresponding to each component are the same. Thus a square-aperture feed can be circularly polarized, an important consideration for satellite tracking applications where the satellite's antenna may be randomly orientated.

Several designs have been published for multimode feeds of the type described above: these differ mainly in the way in which the various propagating modes are excited. In the usual configuration, there is a transition from four input waveguides of square cross-sectior

to a single square guide large enough to allow the required modes to propagate. In some cases, for example in the design of Jensen [31] or in that of Galindo and Pon [32] , the four input guides share common walls, and the transition is merely the point at which these walls terminate, the other walls continuing to form the output waveguide. If, as in the latter case, there are no further discontinuities, only the H_{10} propagating mode is excited for the sum channel (unless overmoding of the input guides is allowed) and the desired central concentration of the sum-channel aperture illumination cannot be achieved. Alternatively, the transition may incorporate a conducting step, in which case there is more scope for optimisation of feed performance in the design of the transition itself, since the relative sizes of the input and output waveguides and the diagonal displacement of the input guides from the centre of the output guide's cross-section all have a significant effect on the amplitudes and phases with which higher-order propagating modes are excited. A feed design involving such a step transition is that of Keeping [18] , in which the input guides are clustered together at the centre of the output guide's cross-section. This configuration, together with an appropriate choice of waveguide dimensions, brings about the suppresion of the H_{30} mode, whose presence can be detrimental if sum-channel bandwidth is an important consideration. However, this is not necessarily the best arrangement as far as the other modes' amplitudes and phases are concerned. In the feed to be described, the output guide is not large enough for the H_{30} mode to propagate, thus allowing more freedom in the step transition design. The computational method for treating step discontinuities, as described in chapter 3, enables the amplitudes and

phases of propagating modes excited at this transition to be accurately determined, and such an analysis forms the basis of the feed design described in this chapter.

6.2 Structure and Excitation of the Multimode Feed

The structure of the multimode monopulse feed is shown in figure 6.1. The four input waveguides, of width b, terminate in a step transition to a single waveguide of width 2a, where $a \geqslant b$, and of length l. This is followed by a pyramidal flared section whose flare angle is 2ζ. The open end of this section, whose width is 2a', forms the radiating aperture of the feed.

The use of a section of waveguide of uniform cross-section in addition to the flare enables two pairs of propagating modes to be given their correct relative phases at the aperture. This is achieved by adjusting l and ζ, and will be explained in section 6.6.3.

The flare angle is considered small, so that the modes in the aperture can be taken as those in a square waveguide of side 2a'. It is assumed that no mode conversion occurs within the flared section, so that the power associated with a particular propagating mode remains constant during its transit from step to aperture.

The size of the radiating aperture determines, to a large extent, the beamwidths of the feed's radiation patterns. Since the feed is intended for use with a front-fed paraboloid having a large F/D ratio, or with a Cassegrain system in which the angle subtended by the sub-reflector at the feed centre is small, these beamwidths need to be fairly narrow. In a typical case, the 15 dB sum-channel beamwidth might need to be 30°, requiring a feed aperture approximately five

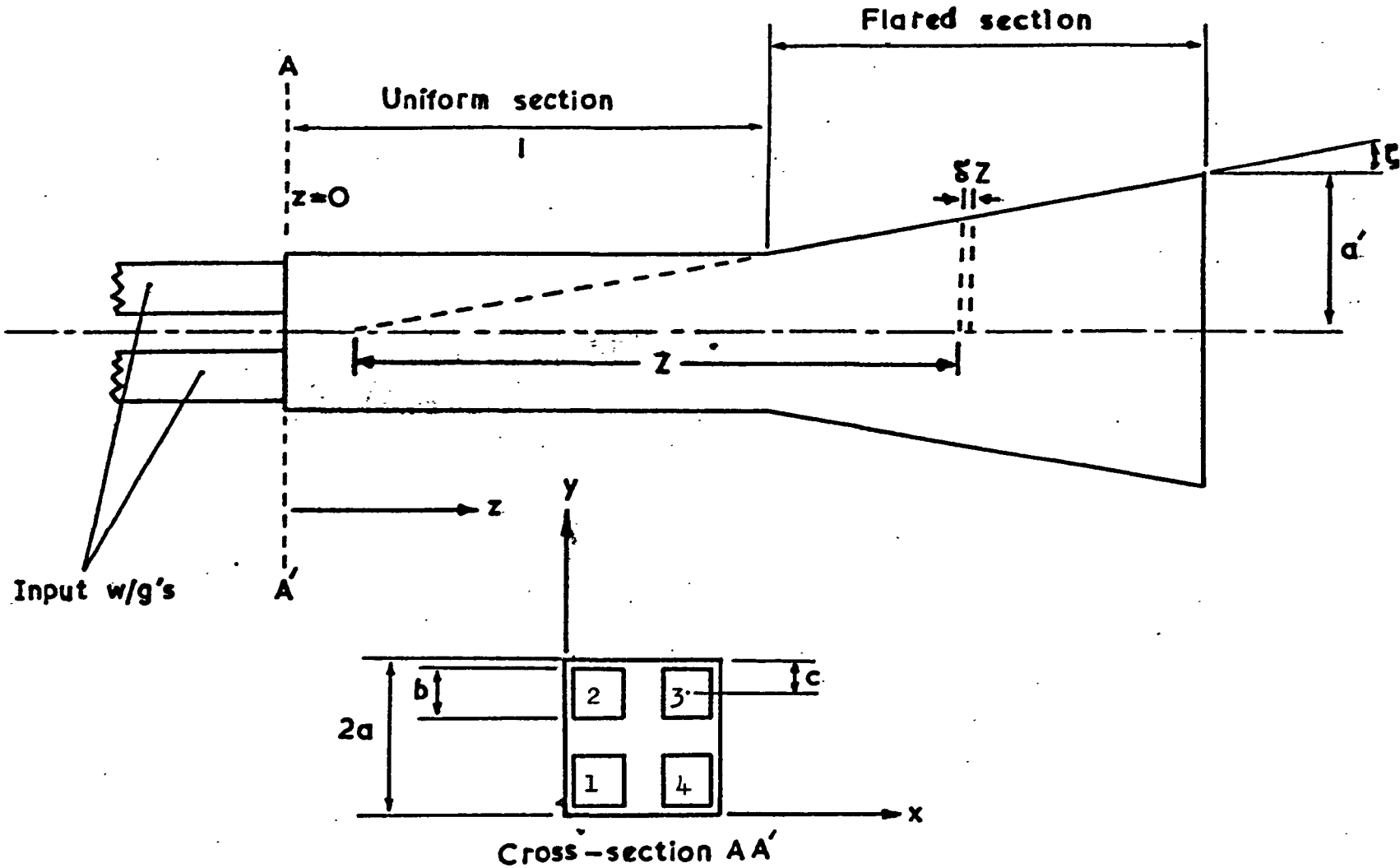

Fig. 6.1 Structure of Multimode Monopulse Feed

wavelengths across. Such an aperture is large enough for all the propagating modes excited by the step to have propagation coefficients in the aperture that are approximately equal to that of free space. The mismatch at the aperture is therefore small, and reflections of modes will be considered negligible. Any reflections from the transition from uniform to flared guide will also be neglected.

In the treatment which follows, the feed is assumed to be linearly polarized. Because the feed has four-fold symmetry the sum-channel performance is unaffected when this is changed to circular polarization, but certain design restrictions arise in the difference-channel case, and these will be discussed in Section 6.6.2.

The following table gives the relative phases with which the H_{10} modes in the four input waveguides are excited to produce radiation patterns corresponding to the three monopulse channels and to the redundant "double difference" channel. The table also shows whether the corresponding modes excited in the larger square guide have odd or even x and y dependences.

TABLE 6.1

Channel	Phase, Guide 1.	Phase, Guide 2.	Phase, Guide 3.	Phase, Guide 4.	Modal x-dependence.	Modal y-dependence.
Sum	+	+	+	+	ODD	EVEN
Azimuth Difference	+	+	-	-	EVEN	EVEN
Elevation Difference	+	-	-	+	ODD	ODD
Double Difference	+	-	+	-	EVEN	ODD

(Phases denoted by "+" and "-" differ by 180°).

The four guides are excited in practice by a network of hybrid-tees known as a comparator. This has four inputs, each of which corresponds to one of the four channels.

The radiation patterns for sum-channel modes are symmetric about the axis in both principal planes: those for azimuth-difference modes are anti-symmetric in the H (y= 0) plane, and those for elevation-difference modes are anti-symmetric in the E (x = 0) plane.

6.3 Multimode Primary Radiation Patterns

6.3.1. Sum Channel

The lowest order propagating mode that can be excited in this case is the H_{10}, which gives rise to the feed aperture illumination shown in figure 6.2 (a). The illumination law has a sinusoidal taper in the H-plane, and is uniform in the E-plane. The electric field in the aperture may be written as:

$$E_{x'} = 0, \quad E_{y'} = A'_{10} \sin\frac{\pi x'}{2a'} \qquad 6.1$$

The resulting principal-plane far-field radiation patterns are then:

H- Plane:

$$E_\theta = 0,$$

$$E_\phi = -j\, A'_{10} \frac{k_o a'^2}{2\rho} \left(\cos\theta + \bar{\beta}'_{10} \right) \frac{\cos(k_o a' \sin\theta)}{(k_o a' \sin\theta)^2 - (\pi/2)^2} e^{-jk_o\rho} \qquad 6.2(a)$$

E- Plane:

$$E_\theta = j\, A'_{10} \frac{k_o a'^2}{2\rho} \left(1 + \bar{\beta}'_{10} \cos\theta \right) \frac{4}{\pi^2} \frac{\sin(k_o a' \sin\theta)}{k_o a' \sin\theta} e^{-jk_o\rho} \qquad 6.2(b)$$

$$E_\phi = 0.$$

The primary pattern co-ordinate system is included in figure 6.7. Expressions 6.2 are derived from formulae given by Silver [29] and are shown graphically in figures 6.3(a) and (b) (solid curves) for the case $a'/\lambda_o = 2.29$, when the 15dB H-plane beamwidth is 30°. The level

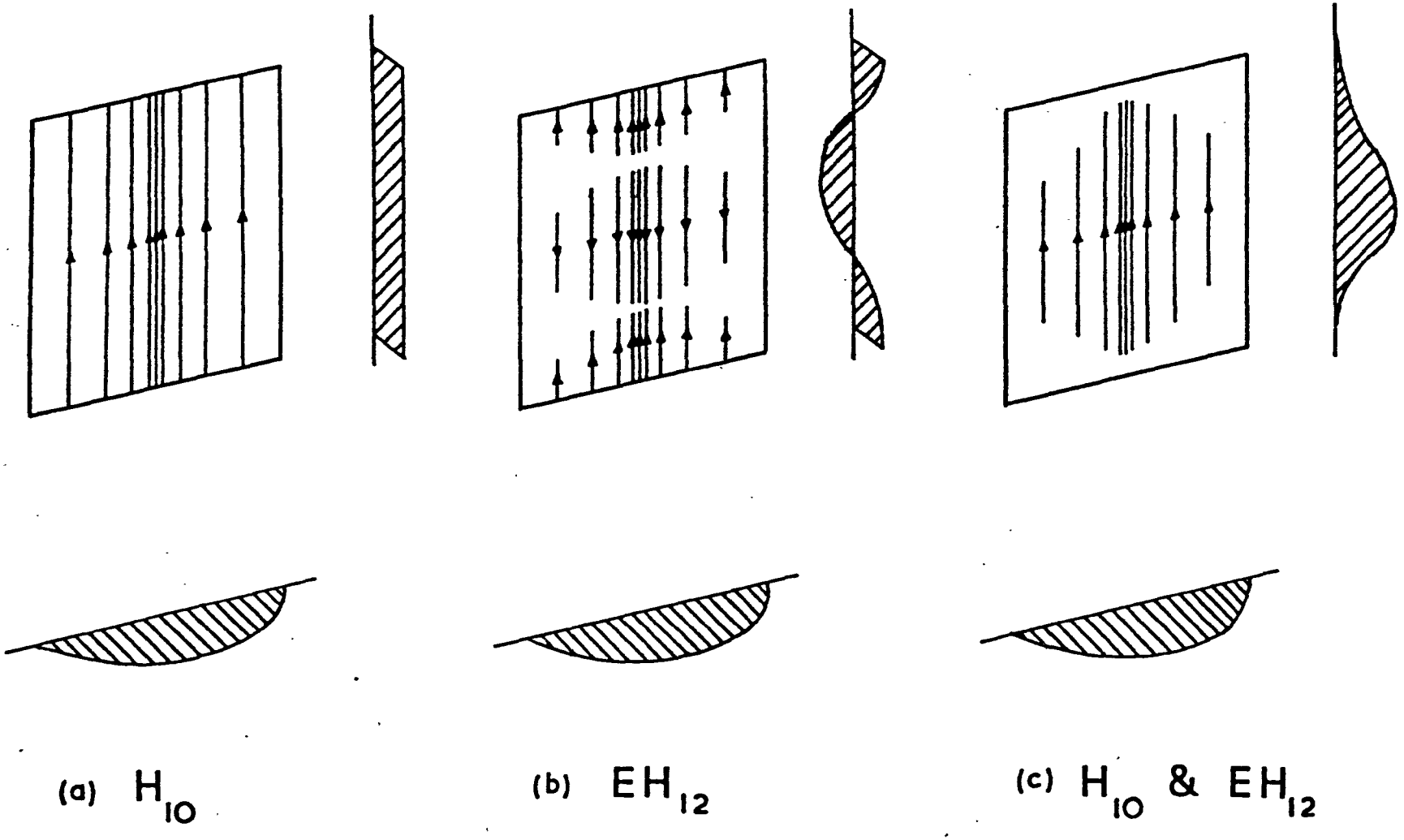

Fig.6.2 Feed Aperture Electric Field Distributions for Sum Channel Modes

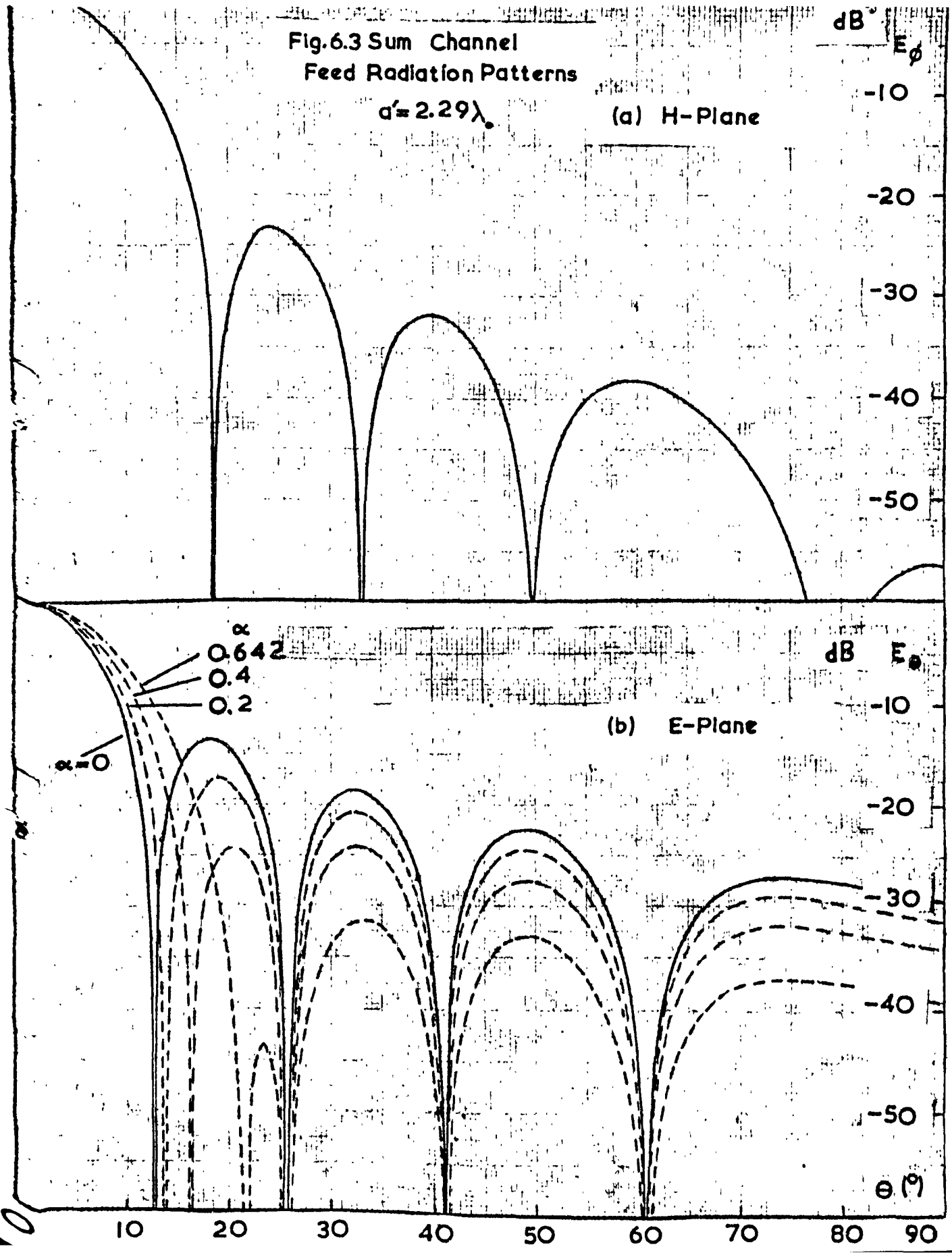
Fig. 6.3 Sum Channel
Feed Radiation Patterns
a'= 2.29λ
(a) H-Plane
dB
Eφ
-10
-20
-30
-40
-50
α
0.642
0.4
0.2
α=0
dB Eθ
(b) E-Plane
-10
-20
-30
-40
-50
θ (°)
0
10
20
30
40
50
60
70
80
90

of the first sidelobe in this plane is -23dB, an acceptable figure for most applications. In the E-plane, however, the main lobe is much narrower than in the H-plane, and the level of the first sidelobe is only -13.5dB. Thus the use of the H_{10} mode alone leads to a reflector illumination with very unequal principal-plane edge tapers and considerable spillover loss. In fact, it will be shown that the gain of a reflector illuminated in this way cannot exceed about 72% of that which would be obtained with ideal illumination.

The poor E-plane pattern is a result of the uniform E-plane feed aperture field distribution, from which it is derived by Fourier transformation. The high sidelobes are a consequence of the abrupt discontinuities in the distribution at the aperture edges, so it is clear that in order to improve the pattern this distribution must be tapered in some way. This can be done by using the two permitted modes next in order of increasing cut-off frequency, namely the H_{12} and E_{12}. These modes have the same cut-off frequency, and propagate with the same phase velocity in the uniform waveguide, and also, with the assumptions embodied in the "quasi-uniform" approximation (see Section 6.6), at any cross-section of the horn flare. The transverse electric field in the feed aperture due to these two modes may be written as:

$$E_{x'} = (B'_{12}-2A'_{12}) \cos \frac{\pi x'}{2a'} \sin \frac{\pi y'}{a'}$$

$$E_{y'} = (2B'_{12}+A'_{12}) \sin \frac{\pi x'}{2a'} \cos \frac{\pi y'}{a'} \qquad 6.3$$

Since the transverse electric field in all four input waveguides is linearly polarized in the y-direction, the component $E_{x'}$ is generally small compared with $E_{y'}$. As a first approximation it can be assumed

that $B'_{12} = 2A'_{12}$ so that $E_x' = 0$. The resulting hybrid mode is the LSE_{12} (or "EH_{12}") whose electric field structure is shown in figure 6.2 (b). If this mode is shifted in phase by 180^o, and superimposed on the H_{10}, the aperture field distribution is then of the form shown in figure 6.2 (c). The effect of introducing the LSE_{12} mode is to reduce the intensity of E_y' at the upper and lower edges of the aperture, and to increase it in the centre: the resulting E-plane illumination law is then tapered so as to produce an E-plane radiation pattern with a wider main lobe and lower sidelobes than obtained previously. The ratio of LSE_{12} to H_{10} modes in the aperture is denoted by α, where:

$$\alpha = \left|\frac{A'_{12} + 2B'_{12}}{A'_{10}}\right| = 5\left|\frac{A'_{12}}{A'_{10}}\right| = \frac{5}{2}\left|\frac{B'_{12}}{A'_{10}}\right| \qquad 6.4$$

The aperture transverse electric field is then:

$$E_x' = 0$$

$$E_{y'} = A'_{10}\sin\frac{\pi x'}{2a'}\left(1 - \alpha\cos\frac{\pi y'}{a'}\right) \qquad 6.5$$

Since the H-plane illumination law is unaffected by the introduction of the LSE_{12}mode, the H-plane radiation pattern remains that of the H_{10} mode alone. The E-plane pattern is now:

$$E_\theta = jA'_{10}\frac{2k_o^2 a'^3}{\pi^2\rho}\sin\theta(1+\cos\theta)\sin(k_o a'\sin\theta)\left\{\frac{1}{(k_o a'\sin\theta)^2} - \frac{\alpha}{(k_o a'\sin\theta)^2 - \pi^2}\right\} e^{-jk_o\rho}/\rho, \quad E_\phi = 0 \qquad 6.6$$

This expression has been simplified by putting $\bar{\beta}'_{10} = \bar{\beta}'_{12} = 1$, which is very nearly so when the aperture is several free-space wavelengths across. E-plane radiation patterns have been calculated for

various values of α , and these are shown in figure 6.3 (b).

It is often desired to equate the principal-plane edge tapers of the reflector illumination, and the value of α that makes them equal when the angle subtended by the reflector at the feed centre is $\pm\theta_o$ is given by:

$$\alpha = \frac{u^2 - \pi^2}{u} \left\{ \frac{\pi^2 \cot(u)}{4u^2 - \pi^2} + \frac{1}{u} \right\} \qquad 6.7$$

in which $u = k_o a' \sin\theta_o$

For example, for equal 15dB edge tapers when $\theta_o = 15^\circ$ which, as mentioned above , requires that $a'/\lambda_o = 2.29$, α is found to be 0.642. The E-plane pattern for this case, which is included in figure 6.3 (b), clearly shows the effect of the LSE_{12} mode on the sidelobes, in that the first sidelobe is almost completely suppressed and the level of the other sidelobes does not now exceed -30dB.

In order to show that the use of the LSE_{12} mode does not adversely affect the radiation patterns in other planes, 45°-plane patterns are also given (fig. 6.3 (c)). It can be seen that the level of sidelobes for this plane is extremely low, even when $\alpha = 0$. When $\alpha = 0.642$, in which case the sidelobes are all below -60dB, the 15dB beamwidth is slightly greater than in the principal planes, but the resulting deviation from a circularly symmetric reflector illumination is too small to be serious in practice.

It will be shown that the gain of a reflector illuminated by a feed in which the H_{10} and LSE_{12} modes are combined can attain about 83% of the maximum possible value.

The next higher mode available for sum-channel beam shaping is the H_{30}, which, when superimposed on the H_{10} can taper the H-plane aperture

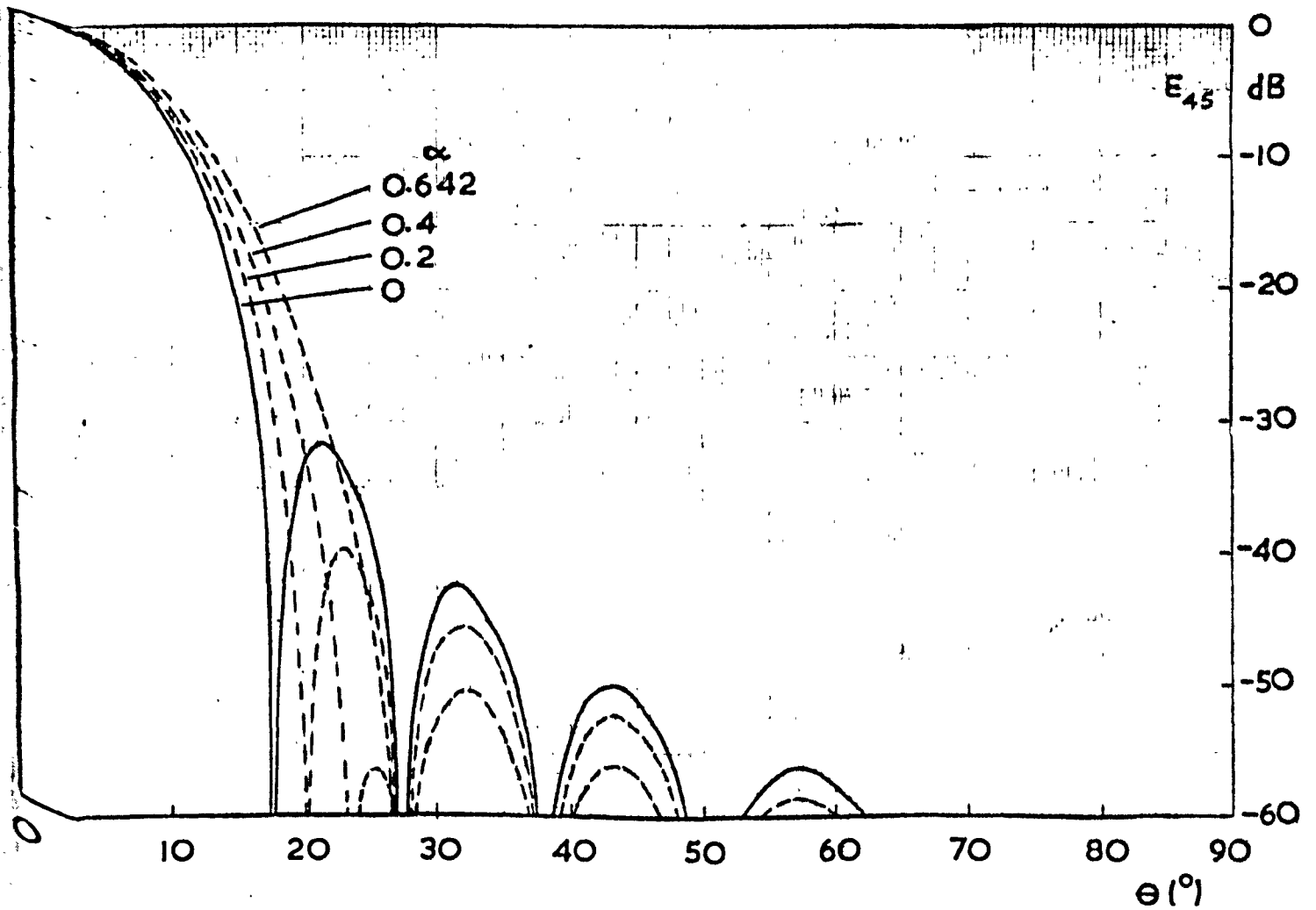

Fig. 6.3 (c) 45°- Plane Sum Channel Feed Radiation Patterns $a' = 2.29\lambda_0$

illumination law so as to broaden the main lobe of the corresponding radiation pattern and reduce the sidelobe level, without affecting the E-plane law and radiation pattern. The use of both LSE_{12} and H_{30} modes in addition to the H_{10} therefore allows the sum-channel beamwidth to be varied while maintaining equal E and H-plane reflector illumination tapers, and in this way simultaneous optimisation of sum and difference performance can be achieved. However, it is not in general possible with the simple feed configuration of figure 6.1 to generate both LSE_{12} and H_{30} modes with the desired amplitudes, and to arrange for them to have the required phases relative to the H_{10} mode in the aperture. Moreover, the aperture illumination distribution of a feed using all three modes changes more rapidly with frequency than that of one using two modes, owing to the strong frequency dependence of the differential phase shift between H_{10} and H_{30} modes. The three-mode feed therefore has a more limited bandwidth than the two-mode feed. For these reasons it was decided to eliminate the H_{30} mode by arranging for it to be cut off in the uniform waveguide, which requires $a/\lambda_0 < 0.75$.

The use of the LSE_{12} mode alone in addition to the H_{10} for the sum channel can lead to a very satisfactory compromise between sum and difference performances, as will be shown in Section 6.4.

6.3.2 Azimuth Difference Channel

With azimuth difference excitation, the lowest-order propagating mode that can exist in the feed aperture is the H_{20}, whose transverse electric field distribution, shown in figure 6.4 (a), may be written as:

$$E_{x'} = 0 \ , \ E_{y'} = 2A'_{20} \sin \frac{\pi x'}{a'} \qquad 6.8$$

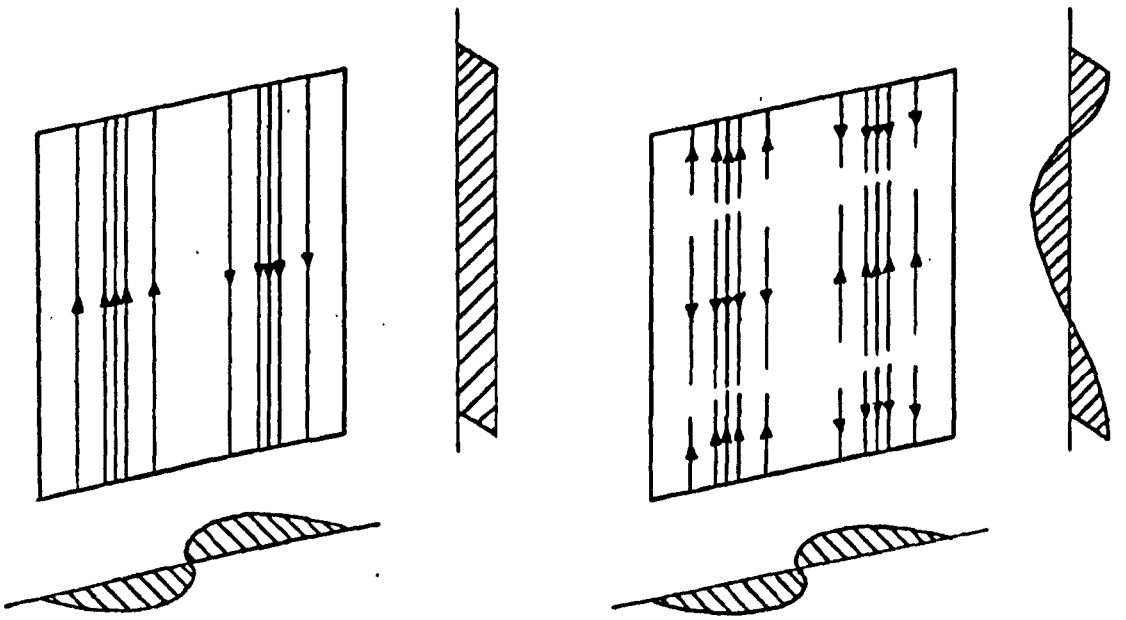

(a) H_{20} (b) EH_{22}

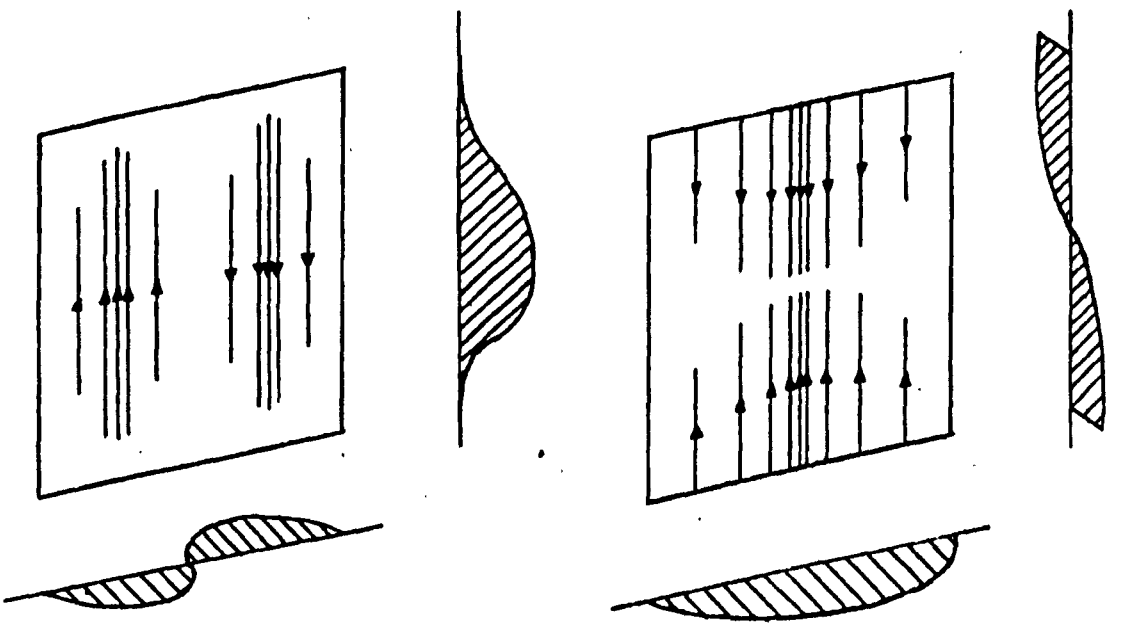

(c) H_{20} & EH_{22} (d) EH_{11}

Fig6.4 Feed Aperture Electric Field Distributions for Difference Channel Modes

The resulting far-field radiation pattern has no E-plane component, the H-plane pattern being given by:

$$E_\theta = 0 \ ,$$
$$E_\phi = -2\, A'_{20}\, \frac{k_o a'^2}{\rho}\, (\cos\theta + \bar{\beta}'_{20})\, \frac{\sin(k_o a' \sin\theta)}{(k_o a' \sin\theta)^2 - \pi^2}\, e^{-jk_o\rho} \qquad 6.9$$

This pattern (fig.6.5 (a)), which is antisymmetric about the axis of the feed, has a reasonably low sidelobe level ($<$-19dB) as a result of the sinusoidal taper of the H-plane illumination law, which is also responsible for the wide main lobes.

If the H_{30} mode is to be suppressed in the sum-channel case, the only modes which can be used to modify the above pattern are the H_{22} and E_{22}. These can, as a first approximation, be considered to form the LSE_{22} (EH_{22}) hybrid, which has the following transverse electric field in the feed aperture:

$$E_{x'} = 0, \quad E_{y'} = 2(A'_{22} + B'_{22}) \sin\frac{\pi x'}{a'} \cos\frac{\pi y'}{a'} \qquad 6.10$$

in which $A'_{22} = B'_{22}$.

The radiation pattern of this mode has no principal-plane component, and the effect of combining the H_{20} and LSE_{22} modes in the feed aperture is most clearly seen by examining the 45°-plane radiation pattern (fig.6.5 (b)). The two modes are assumed to be in antiphase in the aperture, thus giving rise to the illumination distribution of figure 6.4 (c). Their amplitude ratio is denoted by α', where:

$$\alpha' = \left|\frac{A'_{22}+B'_{22}}{A'_{20}}\right| = 2\left|\frac{A'_{22}}{A'_{20}}\right| = 2\left|\frac{B'_{22}}{A'_{20}}\right| \qquad 6.11$$

Thus, if it is assumed that $\bar{\beta}'_{20} = \bar{\beta}'_{22} = 1$, in which case the 45°-plane pattern has equal θ and ϕ components, the expression for

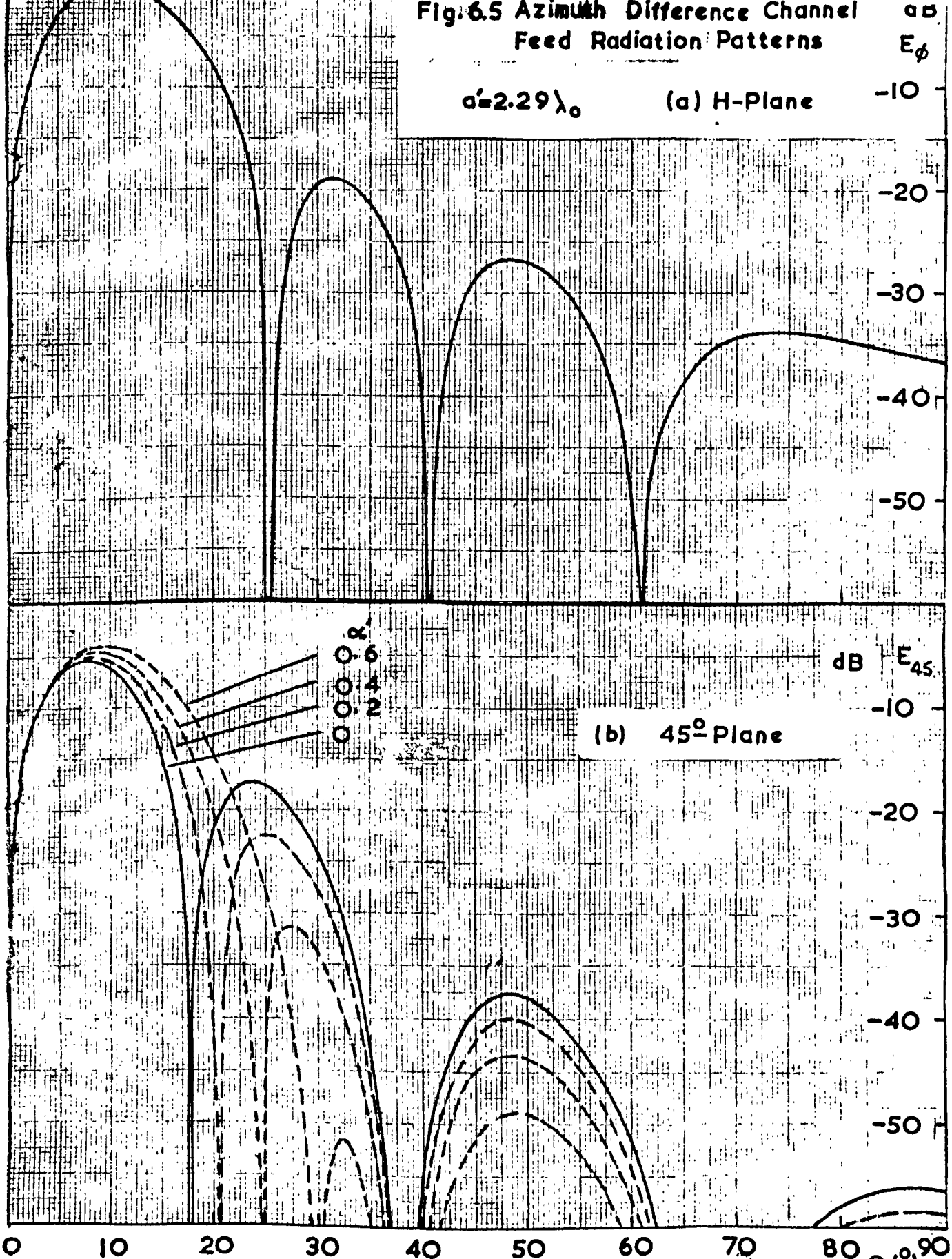
Fig. 6.5 Azimuth Difference Channel Feed Radiation Patterns
a'=2.29λ0
(a) H-Plane
dB
Eφ
-10
-20
-30
-40
-50
α'
0.6
0.4
0.2
0
dB
E45
(b) 45° Plane
-10
-20
-30
-40
-50
0
10
20
30
40
50
60
70
80
90
θ(°)

$E_{45}(=\sqrt{2}E_\theta = \sqrt{2}E_\phi)$ is:

$$E_{45} = -\sqrt{2}\, A'_{20} \frac{k_o^2 a'^3}{\rho} \sin\theta(1+\cos\theta) \frac{\sin^2(t)}{t^2 - \pi^2} \left\{ \frac{1}{t^2} - \frac{\alpha'}{t^2 - \pi^2} \right\} e^{-jk_o\rho} \qquad 6.12$$

in which $t = (k_o a' \sin\theta)/\sqrt{2}$

It has been shown by Hannan [33] that one of the most important difference-channel characteristics, namely the gain in the direction of the secondary radiation pattern's main lobe peaks, is optimised when the reflector illumination due to the feed matches that which would be produced by a distant point source displaced from the principal axis by an amount which maximises the odd power in the reflector aperture. This illumination is a truncated sinusoid whose wavelength is constant at any cross-section of the aperture parallel to the displacement plane. If, as in the azimuth difference-channel case, displacement is in the ϕ =0 plane, the aperture distribution in any other plane containing the axis therefore has a wavelength $\Lambda_o/\cos\phi$, where Λ_o is the wavelength when ϕ=0. The peak amplitude of the distribution is independent of ϕ. Thus in the 45°-plane, the main lobes of the primary pattern should have the same amplitude as in the H-plane, and their widths should be greater by a factor of approximately $\sqrt{2}$. Examination of figures 6.5(a) and (b) shows that these conditions are not satisfied when the H_{20} mode alone is used, since the main lobes are narrower in the 45°-plane than in the H-plane, and their peak amplitudes are lower by about 5dB. However, it can be seen that the effect of increasing α' is to broaden the main lobes and increase their amplitude, at the same time reducing the level of sidelobes. Thus the use of both H_{20} and LSE_{22} modes can give a better azimuth difference reflector illumination and lower spillover than the use of the H_{20} mode alone. As will be shown in Section 6.4, this can lead to a secondary pattern with much improved characteristics.

6.3.3 Elevation Difference Channel

The odd x and y dependences of modes excited at the step in this case, and the restriction that a/λ_o be less than 0.75, imply that the H_{11} and E_{11} modes are the only propagating ones in the feed aperture. As with other mode pairs, they are considered in the form of an LSE hybrid, with a transverse electric field in the aperture:

$$E_{x'} = 0$$

$$E_{y'} = (A'_{11}+B'_{11}) \sin\frac{\pi x'}{2a'} \cos\frac{\pi y'}{2a'} \qquad 6.13$$

$$\text{in which } A'_{11} = B'_{11}$$

This field, together with the E and H-plane illumination tapers, is shown in figure 6.4 (d). If it is assumed that $\bar{\beta}'_{11}=1$, there is no H-plane component of radiated field and the E-plane pattern (fig.6.6(a)) is:

$$E_\theta = -2(A'_{11}+B'_{11}) \frac{k_o^2 a'^3}{\pi^2 \rho} \sin\theta\,(1+\cos\theta) \frac{\cos(k_o a' \sin\theta)}{(k_o a' \sin\theta)^2 - \pi^2/4} e^{-jk_o\rho} \qquad 6.14$$

$$E_\phi = 0.$$

The narrow main lobes and high sidelobes in this plane are due to the discontinuous nature of the corresponding aperture field distribution.

In the 45°-plane, E_θ and E_ϕ are equal if $\bar{\beta}'_{11}$ is taken as unity, and the far-field radiation pattern in this plane (fig.6.6 (b)) is then given by:

$$E_{45} = \sqrt{2}\, A'_{11} \frac{k_o^2 a'^3}{2\rho} \sin\theta(1+\cos\theta) \left\{\frac{\cos(t)}{t^2 - \pi^2/4}\right\}^2 e^{-jk_o\rho} \qquad 6.15$$

$$\text{in which } t=(k_o a' \sin\theta)/\sqrt{2}$$

The level of the main lobe peaks in this plane is only 3dB below that in the E-plane, and the width of these lobes is somewhat greater than

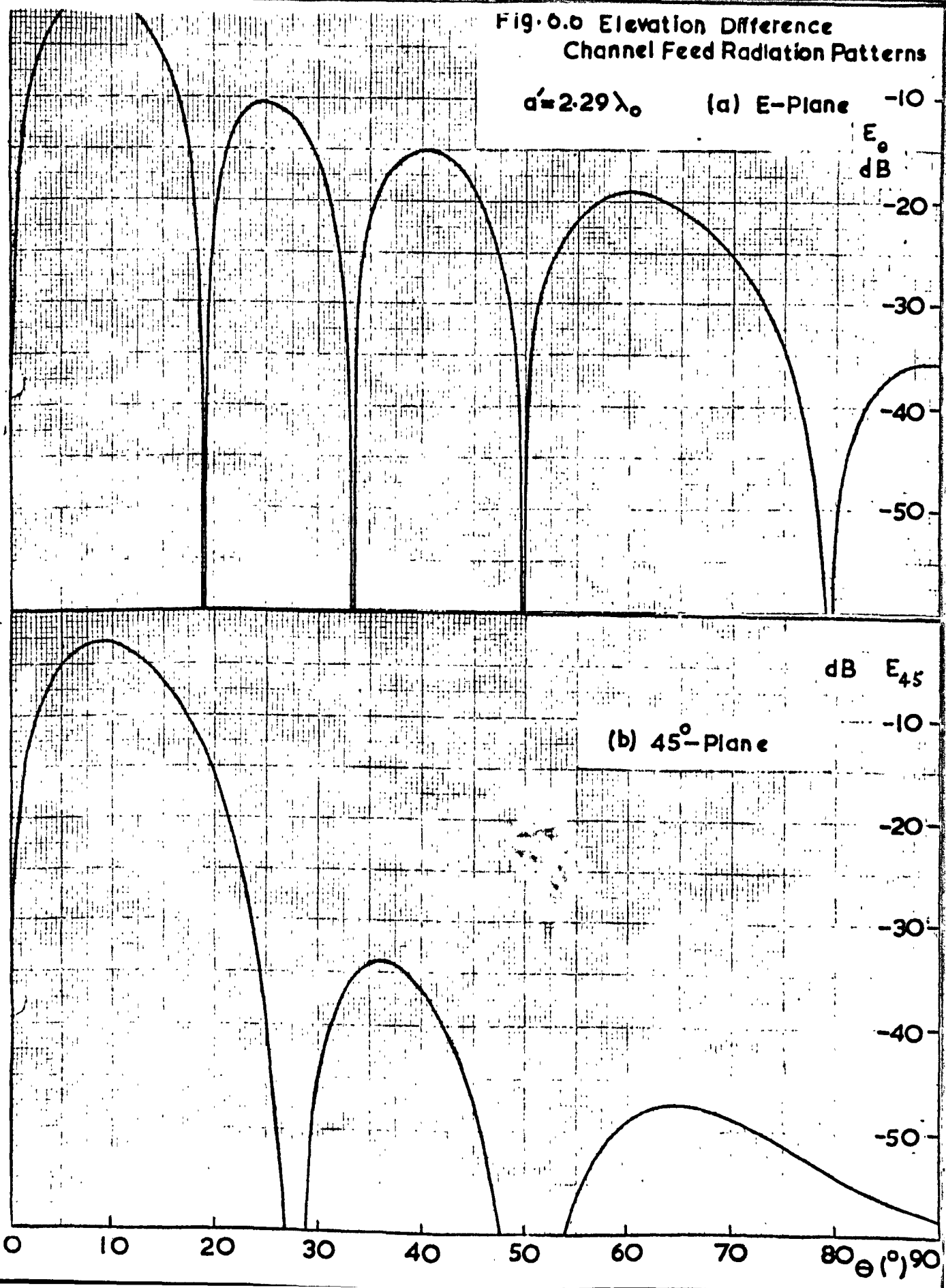
Fig·6.6 Elevation Difference
Channel Feed Radiation Patterns
a'=2.29λ₀
(a) E-Plane
E₀
dB
-10
-20
-30
-40
-50
dB E₄₅
(b) 45°-Plane
-10
-20
-30
-40
-50
0
10
20
30
40
50
60
70
80
θ (°) 90

in the E-plane. The sidelobe level in the 45°-plane is good (< -30dB)

The $LSE_{11}(EH_{11})$ radiation pattern can produce a reflector illumination that corresponds well with the theoretical maximum difference gain illumination described in Section 6.3.2, the only major disadvantage being the spillover loss caused by the high E-plane sidelobes. Since the main lobes are considerably narrower than in the case of the azimuth difference channel, sum and elevation difference performances can be optimised simultaneously more readily than sum and azimuth difference , a fact that will be more clearly seen when the secondary characteristics of the antenna system have been calculated.

6.4 Radiation Characteristics of a Paraboloidal Reflector Illuminated by a Multimode Feed.

6.4.1 A General Expression for the Far-Field of the Reflector

The following evaluation of the feed-reflector system's secondary characteristics is for a front-fed paraboloid, but it can also be applied with a good degree of accuracy to most Cassegrain systems. On the basis of geometric optics, such a system can be shown to be equivalent to a front-fed paraboloid whose diameter is equal to that of the Cassegrain main reflector, and whose focal length is such that the Cassegrain hyperboloid subreflector and the equivalent paraboloid subtend the same angle at the feed centre. The equivalence holds when the subreflector is large compared with λ_o (about $10\lambda_o$ minimum diameter), as is usually the case in practice. The following assumptions are made:

(i) The reflector has a sufficiently long focal length for it to lie entirely within the far-field of the feed.

(ii) The effect of blockage caused by the feed, support structure, or Cassegrain subreflector is negligible.

(iii) The theoretical phase-centre of the feed, i.e. the centre of the feed aperture, coincides with the focus of the reflector.

Fig. 6.7 shows the co-ordinate system used for expressing the primary and secondary radiation patterns.

The radiation from the feed, whose electric component may be written in the general form:

$$\underline{E}_i = E_0(\theta,\phi)\ \hat{\underline{e}}_i \frac{e}{\rho}^{-jk_o\rho} \qquad 6.16$$

where $\hat{\underline{e}}_i$ is a unit vector denoting polarization, is incident on the paraboloidal reflector whose boundary subtends an angle $\pm\theta_o$ at the focus. Since all rays from the focus of a paraboloid are reflected parallel to the axis, the field distribution in the "aperture plane" may, on the basis of geometric optics, be considered as the projection of the reflector field distribution onto this plane. The aperture plane field may therefore be written as:

$$\underline{E}_{ap} = E_0(\theta,\phi)\ \hat{\underline{e}}_{ap} \frac{e}{\rho}^{-jk_o\rho\,(1+\cos\theta)} \qquad 6.17$$

The unit polarization vector $\hat{\underline{e}}_{ap}$ can be shown to be related to $\hat{\underline{e}}_i$ in the following way: if, in the incident field,

$$E_0(\theta,\phi)\ \hat{\underline{e}}_i = E_\theta \hat{\underline{i}}_\theta + E_\phi \hat{\underline{i}}_\phi\ , \qquad 6.18$$

then, in the aperture plane field:

$$E_0(\theta,\phi)\ \hat{\underline{e}}_{ap} = -E_\theta \hat{\underline{i}}_r - E_\phi \hat{\underline{i}}_\phi\ . \qquad 6.19$$

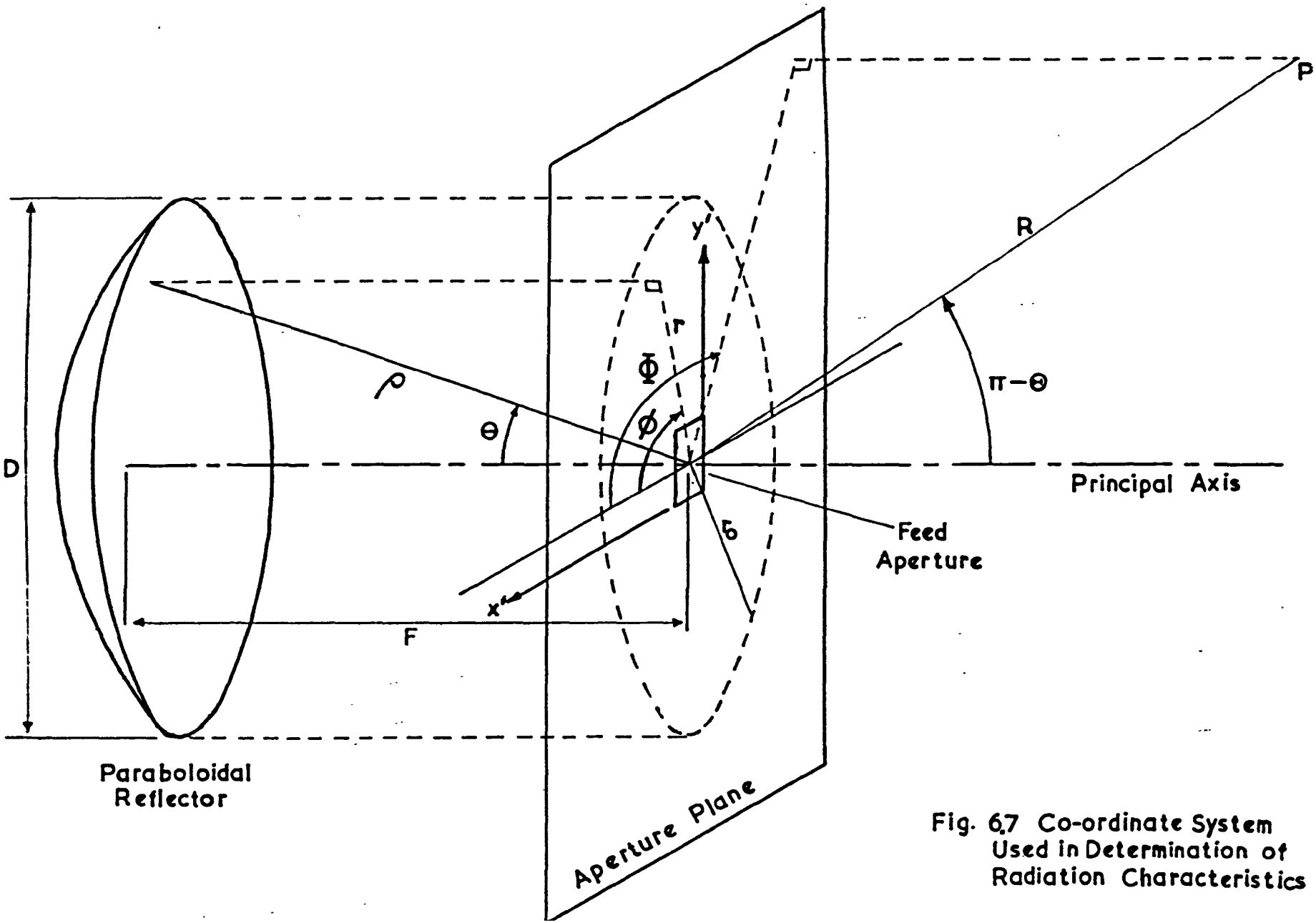

Fig. 6.7 Co-ordinate System Used in Determination of Radiation Characteristics

This result follows from consideration of the boundary conditions imposed by the perfectly conducting reflector surface.

By using the fundamental equation for a paraboloid surface:

$$\rho(1 + \cos\theta) = 2F \qquad 6.20$$

it is apparent from equation 6.17 that there is no phase variation over the aperture plane provided the phase of $E_0(\theta,\phi)$ is constant for all θ and ϕ.

The far-field for small values of Θ due to this aperture plane field distribution may be determined approximately by Fourier transformation, i.e.

$$\underline{E}(R,\Theta,\Phi) = j\frac{k_o}{2\pi}\frac{e}{R}e^{-jk_oR}\int_0^{r_o}\int_0^{2\pi}\underline{E}_{ap}\, e^{jk_or\sin\Theta\cos(\phi-\Phi)}\, r\, d\phi\, dr \qquad 6.21$$

It is clear from figure 6.7 that r, ρ and θ are related through the equation:

$$r = \rho\sin\theta = 2F\tan\frac{\theta}{2} \qquad 6.22$$

Thus,

$$dr = F\sec^2\frac{\theta}{2}\,d\theta = \rho\, d\theta \qquad 6.23$$

By substituting for $\underline{E}_{ap}$ using 6.17 and eliminating r and ρ using 6.22 and 6.23, 6.21 becomes:

$$\underline{E}(R,\Theta,\Phi) = j\frac{k_o}{2\pi}\frac{e}{R}e^{-jk_o(R+2F)}\int_0^{\theta_o}\int_0^{2\pi}2F\, E_0(\theta,\phi)\hat{\underline{e}}_{ap}\tan\frac{\theta}{2}\, e^{jk_o2F\tan\frac{\theta}{2}\sin\Theta\cos(\phi-\Phi)}\, d\phi\, d\theta \qquad 6.24$$

Note that the above expression is not exact, because of the geometric optics approximation and the restrictions implied in the

use of the Fourier transform. For practical reflectors many wavelengths in diameter, however, expression 6.24 is quite adequate, particularly if the fine structure of the secondary patterns is not of interest.

6.4.2 Efficiency Factors for Feed-Reflector System.

(i) Spillover Efficiency

Since only the power radiated by the feed within the cone $\theta \leqslant \theta_o$ is incident on the reflector, there is a loss of efficiency on transmission due to spillover energy radiated at angles greater than θ_o. On reception, radiation from directions for which $\theta > \theta_o$ is detected by the feed. This is usually in the form of noise, and contributes to the noise temperature of the system. Spillover efficiency is defined as that fraction of the power radiated by the feed which is incident on the reflector, and may be written as:

$$\eta_S = \frac{\frac{1}{2\eta_o}\int_0^{\theta_o}\int_0^{2\pi} |E_o(\theta,\phi)|^2 \sin\theta \, d\phi \, d\theta}{\frac{1}{2\eta_o}\int_0^{\pi}\int_0^{2\pi} |E_o(\theta,\phi)|^2 \sin\theta \, d\phi \, d\theta} \qquad 6.25$$

Since reflections of modes at the feed aperture are assumed negligible, the denominator of the above expression can alternatively be written as P_T, the sum of the powers associated with the propagating modes in the feed aperture. The expression is applicable to both sum and difference channels.

(ii) Cross-Polarization Efficiency

In a system designed for linear polarization, the secondary radiated field at a far point may be thought of as consisting of a

component polarized in the required direction, and a cross-polarized component. Provided that directions close to the principal axis are considered, each of these components is due solely to the component of field in the aperture plane with the same polarization. If the feed is polarized in the y - direction, the wanted component E_y in the aperture plane is given by:

$$E_y = E'_r \sin\phi + E'_\phi \cos\phi \qquad 6.26(a)$$

the cross-polarized component being:

$$E_x = E'_r \cos\phi - E'_\phi \sin\phi \qquad 6.26(b)$$

E_y and E_x may also be expressed in terms of the primary radiated field, using 6.19:

$$E_y = -E_\theta \sin\phi - E_\phi \cos\phi \qquad 6.27(a)$$

$$E_x = E_\phi \sin\phi - E_\theta \cos\phi \qquad 6.27(b)$$

The cross-polarization efficiency is defined as the ratio of the power in the aperture plane associated with the required polarization component to the total power in that plane.

It may also be expressed in terms of the field incident on the reflector, being the ratio of the incident power associated with E_y, given by 6.27(a), to the total incident power, i.e.

$$\eta_{CP} = \frac{\int_0^{\theta_o}\int_0^{2\pi} |E_y(\theta,\phi)|^2 \sin\theta \, d\phi \, d\theta}{\int_0^{\theta_o}\int_0^{2\pi} |E_0(\theta,\phi)|^2 \sin\theta \, d\phi \, d\theta} \qquad 6.28$$

Here again, the expression can be applied to both sum and difference channels.

6.4.3. Gain Factors.

In any assessment of antenna performance, an important factor to consider is the gain of the antenna, in some specified direction, relative to a given reference source. In the case of a circular aperture, it can be shown that the on-axis gain is maximised when the aperture is uniformly illuminated, and such an aperture is chosen as the reference source for the gain calculations in this section. The "gain factor" of a given paraboloid is then defined as the ratio of the power per unit solid angle in the specified direction associated with the "wanted" polarization component to that which would exist on the axis if the aperture were uniformly illuminated with no spillover.

Consideration of equation 6.17 shows that in the primary pattern giving rise to the "ideal" illumination, E_0 is proportional to ρ, and may be written as

$$E_0 = A\rho, \quad |\theta| \leqslant \theta_o, \quad E_0 = 0, |\theta| > \theta_o \qquad 6.29$$

where A is a constant. The polarization is such as to eliminate the cross-polarized component. Equation 6.24 for the secondary far-field gives, after substitution for ρ, the following result for the on-axis power in the "ideal" case:

$$P_0(0,0) = A^2 B \left| \int_0^{2\pi} \int_0^{\theta_o} 2F^2 \tan\frac{\theta}{2} \sec^2\frac{\theta}{2}\, d\theta\, d\phi \right|^2 \qquad 6.30$$

B is also a constant. Since the power incident on the reflector in the ideal case must equal the total power P_T radiated by the feed in the actual case, A may be found from:

$$\frac{A^2}{2\eta_o} \int_0^{2\pi} \int_0^{\theta_o} 2F^2 \tan\frac{\theta}{2} \sec^2\frac{\theta}{2}\, d\theta\, d\phi = P_T \qquad 6.31$$

Equation 6.24 gives the power per unit solid angle associated with E_y in the direction (Θ,Φ) due to the actual illumination as:

$$P(\Theta,\Phi)=B\left|2F\int_0^{2\pi}\int_0^{\theta_o} E_y(\theta,\phi)\tan\frac{\theta}{2}\, e^{jk_o 2F\tan\frac{\theta}{2}\sin\Theta\cos(\phi-\Phi)}\, d\theta\, d\phi\right|^2 \qquad 6.32$$

By eliminating A from 6.30 using 6.31, and recognizing that the integral in these expressions has the value $4\pi F^2\tan^2\frac{\theta_o}{2}$, the following expression for the gain factor can be obtained:

$$G(\Theta,\Phi)=\frac{P(\Theta,\Phi)}{P_o(0,0)}=\frac{\left|\int_0^{2\pi}\int_0^{\theta_o} E_y(\theta,\phi)\tan\frac{\theta}{2}\, e^{jk_o 2F\tan\frac{\theta}{2}\sin\Theta\cos(\phi-\Phi)}\, d\theta\, d\phi\right|^2}{2P_T\eta_o\pi\tan^2\frac{\theta_o}{2}} \qquad 6.33$$

(i) Sum Channel Gain Factor

For the sum channel, peak gain occurs in the direction along the principal axis, i.e. $\Phi=0$, $\Theta=\pi$, the gain factor then being:

$$G_\Sigma=\frac{\left|\int_0^{2\pi}\int_0^{\theta_o} E_{y\Sigma}(\theta,\phi)\tan\frac{\theta}{2}\, d\theta\, d\phi\right|^2}{2P_{T\Sigma}\eta_o\pi\tan^2\frac{\theta_o}{2}} \qquad 6.34$$

This gain factor may also be viewed as the product of three efficiencies:

$$G_\Sigma=\eta_S \times \eta_{CP} \times \eta_I \qquad 6.35$$

where η_I is termed the "illumination efficiency" and is a measure of the degree to which the aperture plane illumination matches the ideal uniform distribution.

Figure 6.8 shows how the sum gain factor varies with the parameter $X=2\pi\frac{D}{F}\frac{a'}{\lambda_o}$, for various values of α, which expresses the ratio of the modes LSE_{12} and H_{10} in the feed aperture. The curves were calculated using a digital computer, the integral in expression 6.34 being evaluated by Simpson's Rule. Although the calculation was

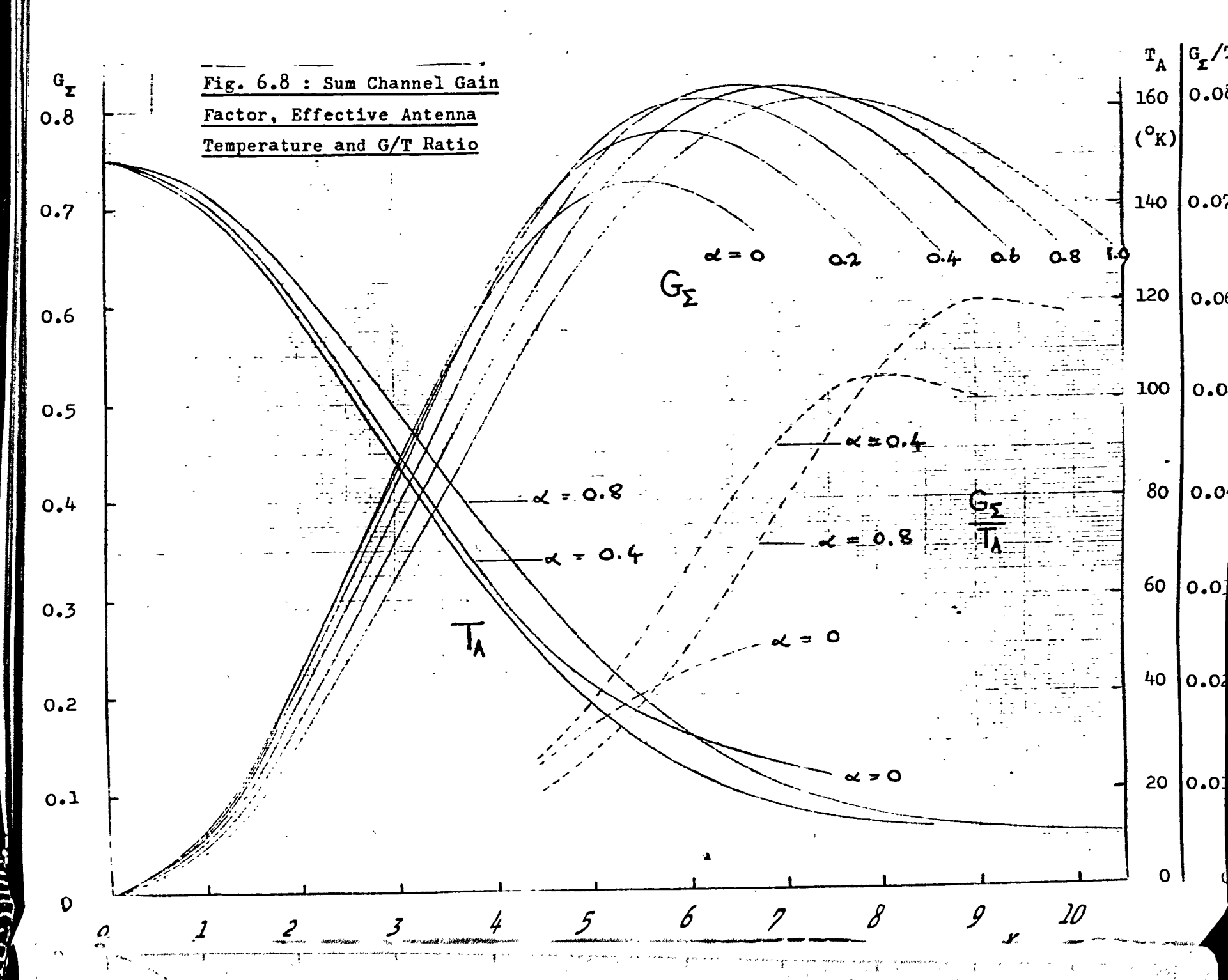
Fig. 6.8 : Sum Channel Gain Factor, Effective Antenna Temperature and G/T Ratio
G_Σ
T_A
G_Σ/T
(°K)
G_Σ
$\alpha = 0$ 0.2 0.4 0.6 0.8 1.0
$\alpha = 0.8$
$\alpha = 0.4$
T_A
$\frac{G_\Sigma}{T_A}$
$\alpha = 0.4$
$\alpha = 0.8$
$\alpha = 0$
$\alpha = 0$
0 0.1 0.2 0.3 0.4 0.5 0.6 0.7 0.8
0 20 40 60 80 100 120 140 160
0 1 2 3 4 5 6 7 8 9 10
y

performed for $a' = 2.29\lambda_o$, the use of the parameter X as co-ordinate enables the variation of gain factor with θ_o to be determined for other feed aperture widths, provided these are sufficiently large for the H_{10} and LSE_{12} propagation coefficients not to deviate appreciably from that of free space.

It can be seen from the sum-channel primary patterns shown in figure 6.3 that, for a given feed aperture, the secondary aperture illumination becomes more tapered as θ_o increases, causing a decrease in η_I. However, the amount of radiated power intercepted by the reflector increases with θ_o and so, in consequence does η_S. The maximum gain factor corresponds to the best compromise between these two efficiencies. The feed aperture field due to the superimposed H_{10} and LSE_{12} modes is linearly polarized, and in the corresponding radiation pattern the cross-polarized component given by 6.27(b) is eliminated when the aperture width is large. Thus η_{CP} is very nearly 100% in the cases considered.

As would be expected from the discussion of section 6.31, the maximum gain factor increases with α. Also, for a given a'/λ_o, the value of θ_o for which maximum gain occurs increases with α, a fact which will be shown to have an important bearing on the simultaneous optimisation of sum and difference performance.

(ii) Difference Channel Gain Factors.

The values of Θ corresponding to the main lobe peaks of the secondary difference patterns cannot easily be determined mathematically, and for this reason it was decided to plot gain as a function

of Θ and then determine the peak gain factor and corresponding value of Θ by inspection.

Peak gain occurs in the plane $\Phi = 0$ for the azimuth difference channel, and in the plane $\Phi = \frac{\pi}{2}$ for the elevation difference channel. In both cases it is found that the real part of the integral vanishes, giving:

$$G_{\Delta AZ}(\Theta, 0) = \frac{\left| \int_0^{2\pi} \int_0^{\theta_o} E_{y\Delta AZ}(\theta,\phi) \tan\frac{\theta}{2} \sin(2Fk_o \tan\frac{\theta}{2} \sin\Theta\cos\phi)\, d\theta\, d\phi \right|^2}{2\eta_o P_{T\Delta AZ} \pi \tan^2\frac{\theta_o}{2}} \qquad 6.36$$

$$G_{\Delta EL}(\Theta, \tfrac{\pi}{2}) = \frac{\left| \int_0^{2\pi} \int_0^{\theta_o} E_{y\Delta EL}(\theta,\phi) \tan\frac{\theta}{2} \sin(2Fk_o \tan\frac{\theta}{2} \sin\Theta\sin\phi)\, d\theta\, d\phi \right|^2}{2\eta_o P_{T\Delta EL} \pi \tan^2\frac{\theta_o}{2}} \qquad 6.37$$

Figure 6.9 shows how the peak azimuth and elevation difference gain factors vary with the parameter X. In the case of the azimuth difference channel, curves are plotted for various values of α', the ratio of LSE_{22} to H_{20} in the feed aperture. Here again, the maximum values represent the best compromise between spillover and secondary aperture illumination. As mentioned in section 6.3.2, the aperture illumination leading to the maximum possible difference gain factor takes the form of a truncated sinusoid whose amplitude and wavelength are constant in any plane parallel to that in which peak gain is required to occur, and Kinsey [34] has shown that the required wavelength for a circular aperture is 1.223 times the aperture diameter. The corresponding gain factor at the difference peak is 0.566.

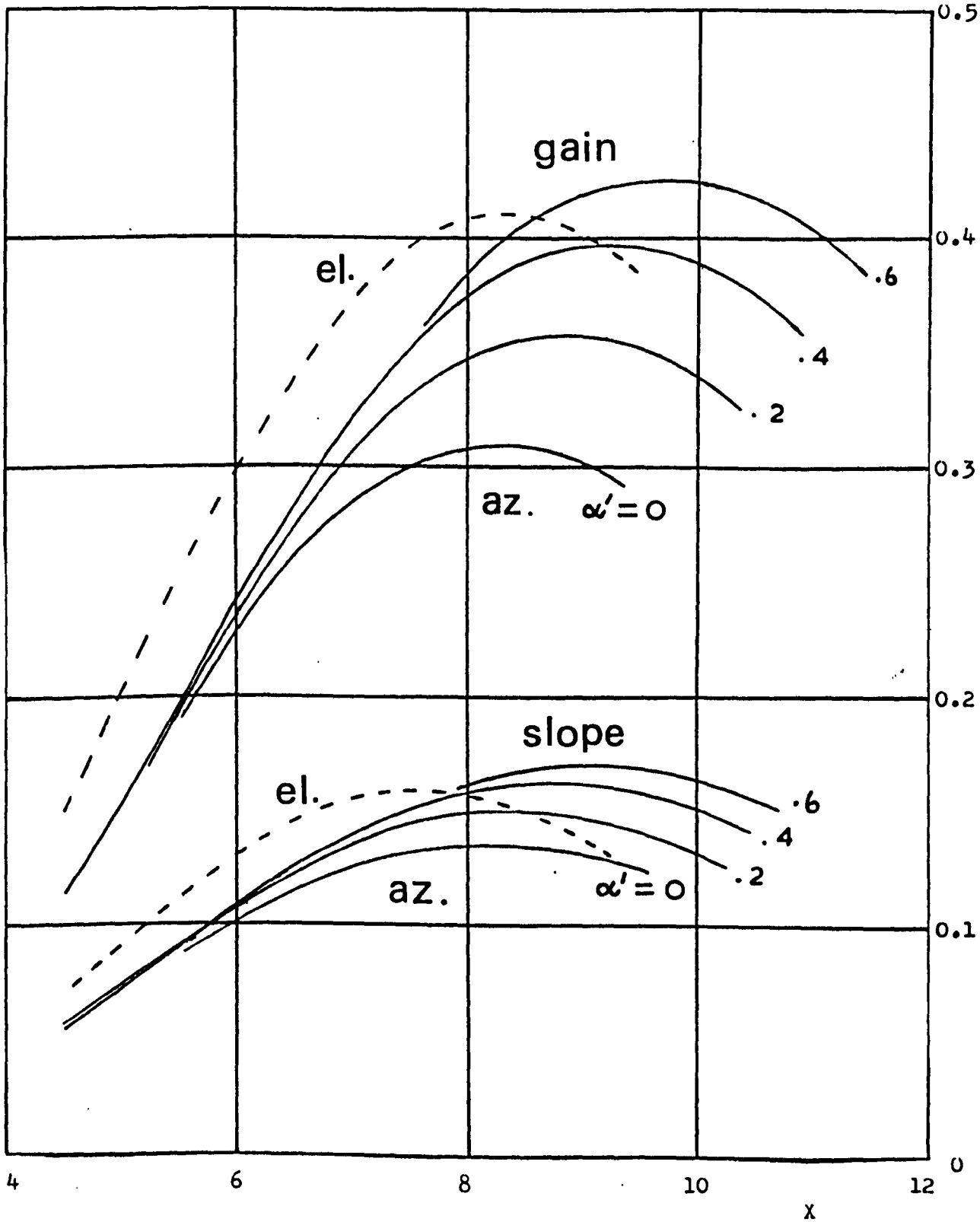

Fig. 6.9 Difference Channel

Gain and Slope Factors

6.4.4. Difference Channel Slope Factor.

When dealing with the tracking ability of a monopulse antenna, an important consideration is its sensitivity to small changes in the direction of the received signal, which depends to a large extent on the slope of the secondary difference radiation pattern measured at the principal axis. A "slope factor" is therefore introduced, being defined as:

$$S = \left\{ \frac{\partial (G_{\Delta}^{\frac{1}{2}})}{\partial u} \right\}^{2}_{u=0} \qquad 6.38$$

where $u = (\pi D \sin\theta)/\lambda_0$.

Slope factors for both difference channels are included in figure 6.9, and were determined graphically, although it is possible to obtain a good approximation to the slope factor by calculating the gain factor corresponding to u=1, the secondary pattern being almost linear in this region.

The aperture illumination corresponding to the maximum possible slope factor has been shown by Kirkpatrick [35] to have a linear, odd distribution. The value of the slope factor in this case is 0.25. The primary difference patterns described in sections 6.3.2 and 6.3.3 are, however, such that this ideal illumination cannot be approached without excessive spillover. It is not surprising, therefore, that the slope factors in figure 6.9 fall well short of the maximum possible value.

6.4.5. Discussion.

Now that performance figures for the complete system of feed and reflector have been determined, it is possible to see precisely the effect of the addition of the higher-order modes LSE_{12} and LSE_{22}. Figures 6.8 and 6.9 show that in the case $\alpha=0$, corresponding to the use of the H_{10} mode alone in the sum-channel case, the maximum gain factor occurs when X=5.6, whereas maximum difference-channel gain and slope factors are all obtained when X is in the region of 8. Thus if the dimensions of the system are chosen for maximum sum-channel gain, difference-channel performance is poor, and vice-versa. However, the introduction of the LSE_{12} mode not only increases the maximum sum gain factor by as much as 14%, but also causes it to occur at larger values of X. In fact, if a value of α in the region of unity is chosen, sum and difference gain factors are almost maximised simultaneously. Notice that the value $\alpha=0.642$ which was shown in section 6.3.1 to produce an almost circularly symmetric reflector illumination is also nearly optimum for the sum gain factor.

It is seen in figure 6.9 that the elevation difference gain and slope factors, due to the LSE_{11} mode, are considerably better than those of the azimuth difference channel when the H_{20} mode alone is used (i.e. $\alpha'=0$). The reasons for this were outlined in section 6.3.3. When the system is used with circular polarization, it is particularly important that the elevation and azimuth gain and slope factors should be similar, otherwise the feed responds differently to each of the two equivalent linearly polarized components of the signal received from a source displaced in either principal plane,

and the resulting waves excited in the four small guides then have elliptical rather than circular polarization. The use of the LSE_{22} mode can be seen to improve significantly the azimuth difference gain and slope factors, but unfortunately it causes the peak values to occur at even larger values of X. The improvement at any given value of X can still be considerable, however. When α' is in the region of 0.5, the azimuth and elevation difference performance factors have similar values when X=8, the point at which the elevation difference gain and slope factors are both near their respective maxima.

Although maximum sum-channel gain is desirable when the antenna is used for transmission, it is often the ratio of signal to noise which must be maximised for reception. When the paraboloid is front-fed it is possible, assuming losses other than those due to spillover to be negligible, to make an estimate of the effective antenna temperature T_A in terms of the spillover efficiency η_S. The elevation of the antenna is assumed to be such that half the spillover pattern picks up noise radiated by the earth, while the other half, and the entire secondary pattern, pick up noise from the sky. By taking the noise temperature of the earth as 290°K, and that of the sky as 10°K, it is found that:

$$T_A = (150 - 140\,\eta_S)^\circ K \qquad 6.39$$

Graphs showing the variation of T_A with X, for various values of α, are included in figure 6.8, as are also some graphs of G/T_A, which is proportional to the signal-to-noise ratio of the antenna. The peak

values of this factor occur at larger values of X than those of the gain factor, so that a smaller value of α is required if tracking ability is to be optimised simultaneously with signal-to-noise ratio rather than gain.

In a Cassegrain system, power spilled over past the subreflector "sees" only the cold sky, so that T_A is much less than in the front-fed case. Ideally, in fact, it would be independent of η_s and equal to the sky temperature, in which case the optimum G/T_A for the system would occur when the sum-channel gain factor was a maximum.

6.5. Design of the Mode-Converter.

6.5.1 Method of Analysis for Single-Step Converter.

With reference to the discontinuity cross-section shown in figure 6.1, it is clear that there are three parameters which can be varied to control the excitation of propagating modes, while preserving the four-fold symmetry of the junction. They are:

(i) The width b of the small waveguides relative to the free-space wavelength λ_o. Since overmoding of these waveguides is undesirable, the allowed range of variation is that in which only the H_{10} and H_{01} modes can propagate, i.e.

$$\frac{1}{2} < \frac{b}{\lambda_o} < \frac{1}{\sqrt{2}} \qquad 6.40$$

(ii) The width 2a of the large waveguide, relative to λ_o. This factor determines whether the modes excited by the step are propagating or evanescent.

(iii) The diagonal displacement of the small waveguides towards the centre of the step, denoted by c/a. The range for this para-

meter is:

$$b/(2a) \leqslant c/a \leqslant (2a-b)/(2a) \qquad 6.41$$

It would be possible to obtain solutions to the discontinuity problem using the method described in section 3.7 involving the partitioned matrix formulation, but in this particular case the symmetry of both the junction itself and the excitation can be used to simplify the analysis. The transverse modal fields in the large waveguide have the following forms:

H_{MN} mode

$$E_x = -A_{MN}\, N \cos\frac{M\pi x}{2a} \sin\frac{N\pi y}{2a}$$

$$E_y = A_{MN}\, M \sin\frac{M\pi x}{2a} \cos\frac{N\pi y}{2a} \qquad 6.42$$

$$H_x = j\frac{\Gamma_{MN}}{\omega\mu_o} E_y \qquad H_y = -j\frac{\Gamma_{MN}}{\omega\mu_o} E_x$$

E_{MN} mode

$$E_x = B_{MN}\, M \cos\frac{M\pi x}{2a} \sin\frac{N\pi y}{2a}$$

$$E_y = B_{MN}\, N \sin\frac{M\pi x}{2a} \cos\frac{N\pi y}{2a} \qquad 6.43$$

$$H_x = -j\frac{\omega\varepsilon_o}{\Gamma_{MN}} E_y \qquad H_y = j\frac{\omega\varepsilon_o}{\Gamma_{MN}} E_x$$

The co-ordinate system is that shown in figure 6.1. In the above expressions:

$$\Gamma_{MN} = \sqrt{\left(\frac{M^2+N^2}{4a^2}\pi^2 - k_o^2\right)} \qquad 6.44$$

It can be seen from 6.42 and 6.43 that if M is even, E_y vanishes in the plane x=a, corresponding to the existence of an electric wall in

that plane. Similarly, if N is even, E_x vanishes when y=a and an electric wall can be considered to exist there also. If M is odd, H_y vanishes at x=a, as does H_x at y=a when N is odd. A magnetic wall can therefore be inserted in the appropriate plane without disturbing the fields. As shown in table 6.1, M and N are each either even or odd for all modes corresponding to a given monopulse channel. Thus a wall of the appropriate type may be considered to exist in each of the planes x=a and y=a for that particular excitation. It is then possible to analyse the discontinuity by considering only one quarter of the structure, i.e. a junction between two square waveguides, the larger of which has two walls which can be either electric or magnetic. Figure 6.10 shows the simple junctions equivalent to the four excitations of table 6.1. Each junction can be treated using the method of section 3.1, the relevant matrix equation being 3.4. The evaluation of the elements of [R] and [S] is given in the Appendix.

Restrictions on the modes taken into account in the solution were imposed by matching the highest-order spatial frequencies separately in both x and y directions. In many of the configurations considered, b/2a was of the order of 1/3. The highest x dependence was 3 in the small guide and 9 in the large guide, the corresponding highest y- dependences being 2 and 6. Thus 14 modes were taken into account in the small guide and between 20 and 22 in the large guide, depending on the channel in question.

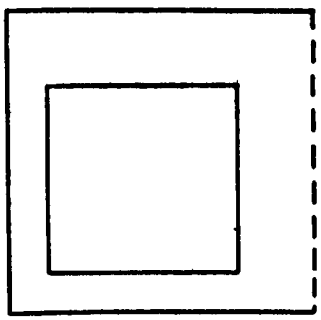

Sum

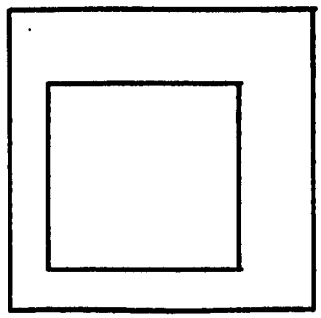

Azimuth Difference

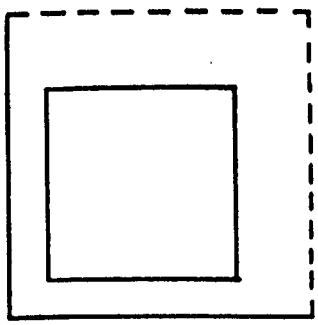

Elevation Difference

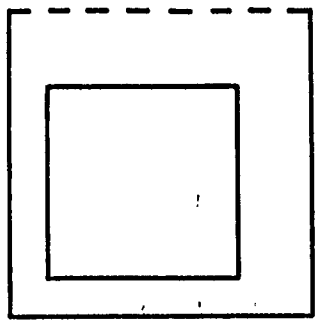

Double Difference

Fig. 6.10 Equivalent Single-Waveguide Junctions for Monopulse Feed Step Discontinuity

——— Electric Wall

- - - - Magnetic Wall

6.5.2 Computed Results.

The first parameter whose variation was considered was the diagonal displacement of the input waveguides. In order to obtain a fairly large range for this variation, the waveguide sizes were chosen so that $a=0.77\lambda_0$, $b=0.7a$, in which case the H_{30} mode can propagate in the large guide. 6.41 then gives the range of c/a as 0.35 to 0.65. Figures 6.11(a), (b) and (c) show the proportions in which the incident power is divided among the various transmitted and reflected propagating modes, as functions of c/a, while figures 6.12 (a), (b) and (c) give the phases of these modes relative to that of the H_{10} mode incident in number 1 input waveguide. All three monopulse excitations are considered.

In the sum-channel case (figs. 6.11(a) and 6.12(a)), it can be seen that the H_{12} and E_{12} modes are most strongly excited when c/a=0.35 or c/a=0.65, whereas, when c/a=0.5, they are completely suppressed owing to the symmetry of the equivalent junction. A reversal of the phase of these modes occurs as c/a passes through this point. The need for them to be excited strongly relative to the H_{10} mode for a satisfactory multimode radiation pattern suggests the choice of either the corner position (c/a=0.35) or the centre position (c/a=0.65), which also give small relative phase angles between the two modes. In the former case, less than 1% of the incident power is reflected, compared with 13% in the latter. However, if the dimensions are reduced so that the H_{30} mode can no longer propagate, computation shows that the amount of power reflected is similar in the two cases, and is typically about 5%. As there seems to be

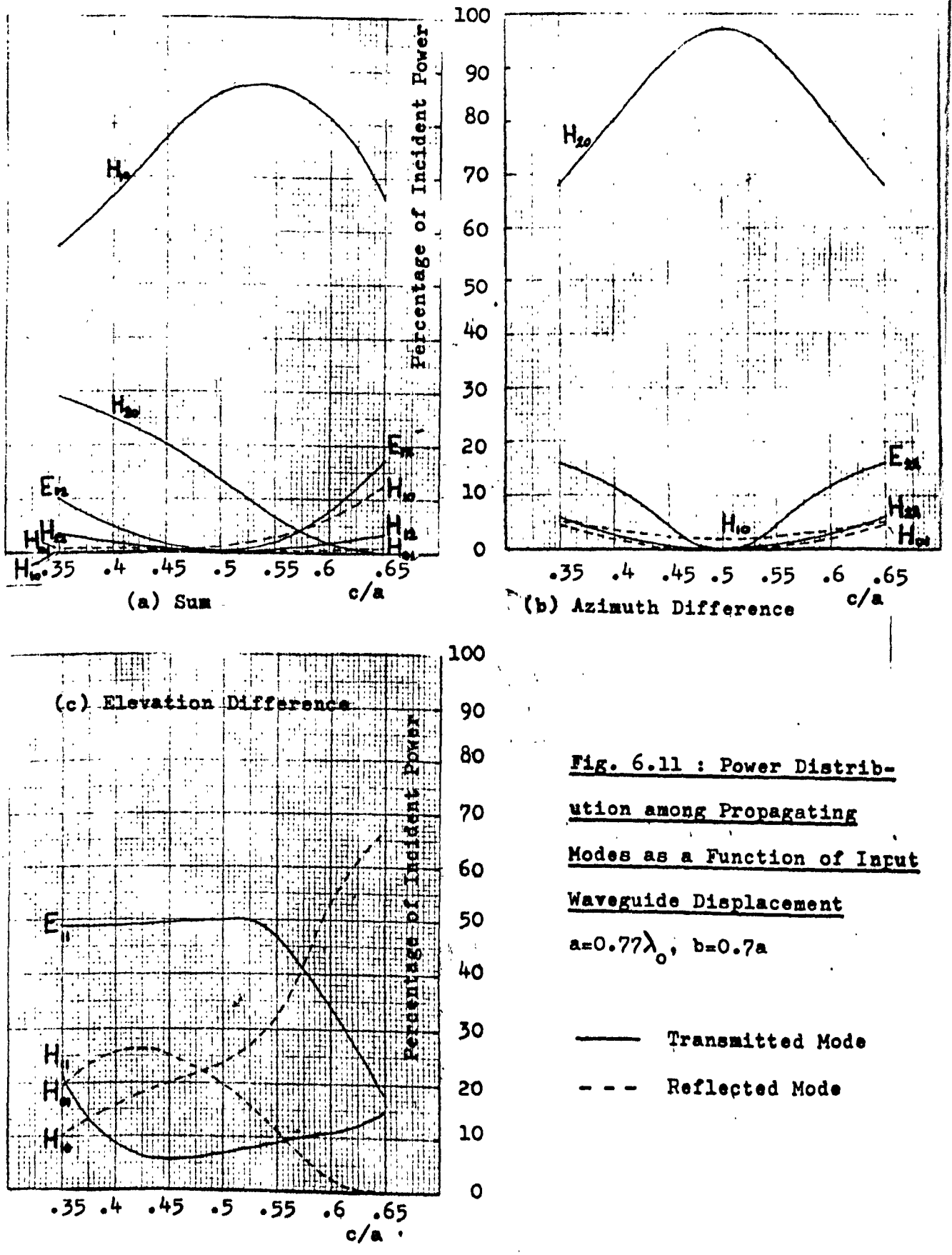

Fig. 6.11 : Power Distribution among Propagating Modes as a Function of Input Waveguide Displacement

$a=0.77\lambda_o$, $b=0.7a$

——— Transmitted Mode

- - - Reflected Mode

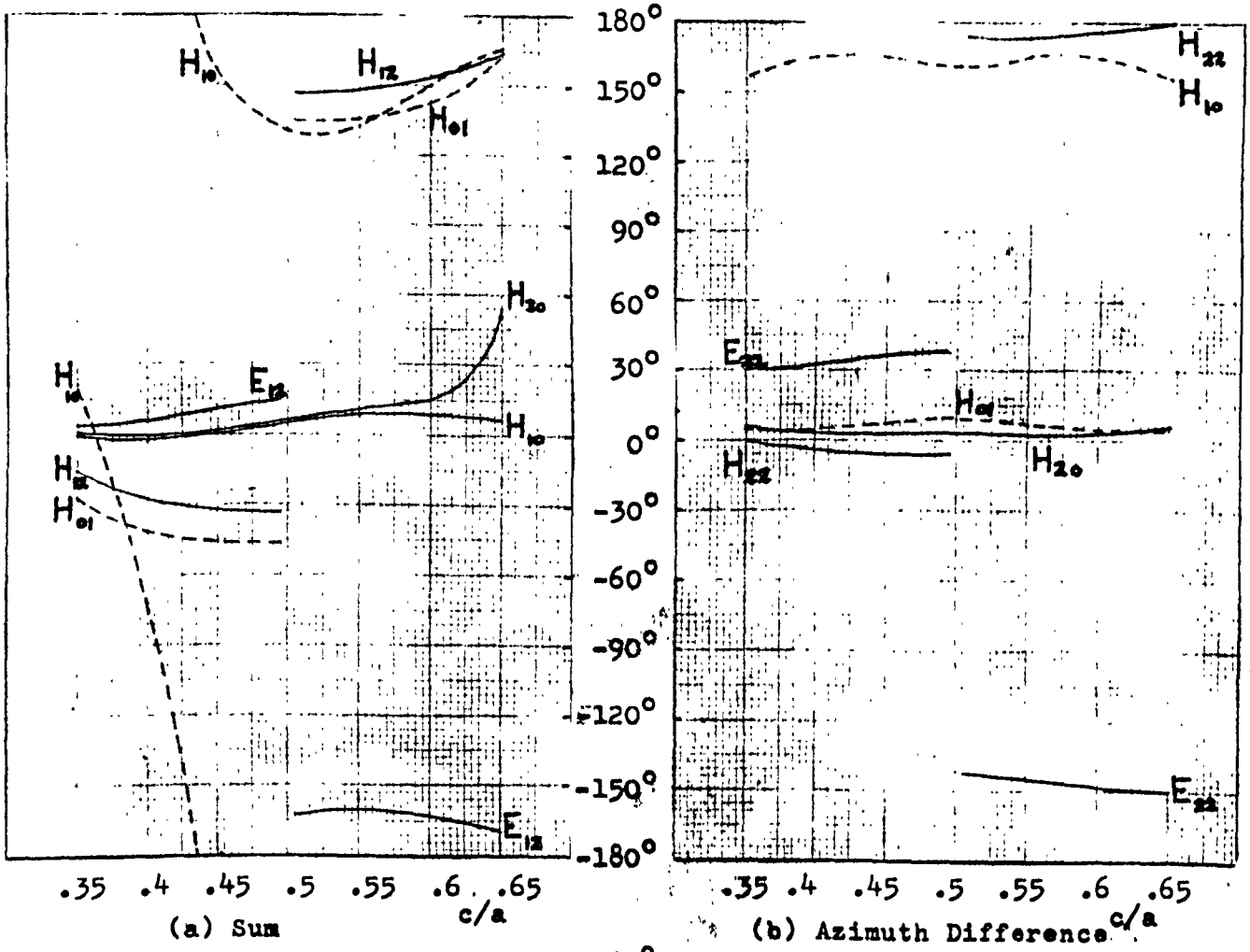

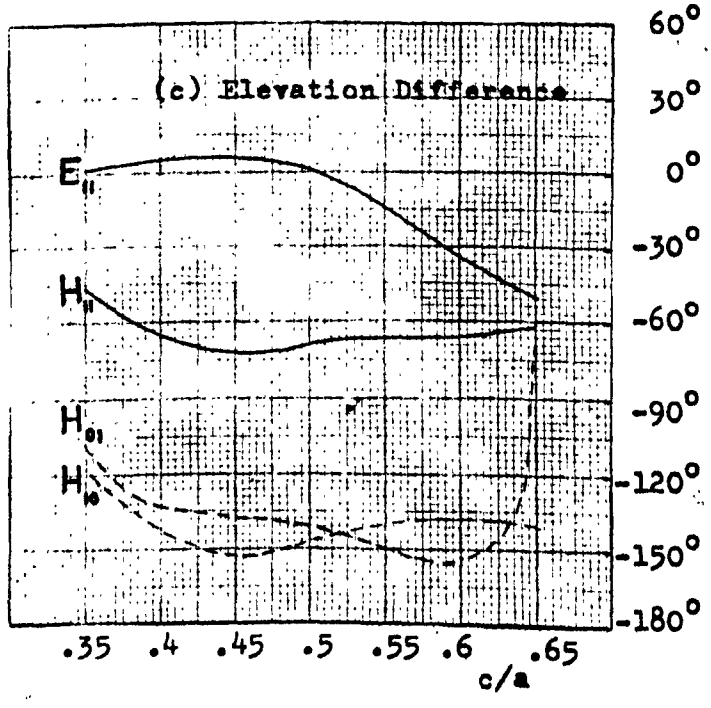

Fig. 6.12 : Phases of Excitation of Propagating Modes as Functions of Input W/G Displacement

$a=0.77\lambda_o$, $b=0.7a$

——— Transmitted Mode

- - - Reflected Mode

little to choose between the corner and centre positions from the sum-channel point of view, the choice will depend on the behaviour of the discontinuity with difference-channel excitation.

The equivalent output waveguide for the azimuth difference channel, shown in figure 6.10(b), has four electric walls, so that a junction with input guide displacement c is identical to one in which the displacement is a-c. Thus the curves showing the distribution of power among the propagating modes (fig. 6.11(b)) are symmetrical about the value c/a=0.5. By analogy with the 1,2 modes in the sum-channel case, the H_{22} and E_{22} modes are not excited when c/a=0.5, the point at which they undergo a phase reversal as the input waveguide displacement is varied (see fig. 6.12(b)). Here again, the positions c/a=0.35 and c/a=0.65 give rise to the minimum relative phase angle for the pair of modes (about 30°). About 10% of the incident power is reflected in these cases.

In figures 6.11(c) and 6.12(c) the curves corresponding to the elevation difference channel are given. It can be seen that the mismatch at the discontinuity is much more serious than in the other two cases, particularly if the four input guides are grouped together at the centre of the step. About 29% of the incident power is reflected when c/a=0.35, as opposed to 67% when c/a=0.65, which suggests that the corner position should be chosen for best elevation difference matching. In this case the H_{11} and E_{11} modes are excited with a relative phase of about 50°, which, although a high figure, cannot be improved without increasing c/a to a point at which an excessive amount of power is reflected.

Having chosen the corner position c=b/2 as that which gives best all-round performance, there are two further parameters the effect of whose variation needs to be determined, namely the waveguide widths b and 2a. The range for b is given by 6.40, whereas that for a is:

$$\sqrt{5}\lambda_o/4 < a < 3\lambda_o/4 \qquad 6.44$$

This is the condition for the H_{30} mode to be cut off, but for the H_{12} and E_{12} to be propagating. The curves in figures 6.13, 6.14 and 6.15 show amplitude and phase variations with b/λ_o of propagating modes excited at the step when a/λ_o takes values from 0.64 to 0.74, in steps of 0.02. When a/λ_o is 0.72 or 0.74, the H_{22} and E_{22} modes, which are excited in the azimuth difference case, are above cut-off in the large waveguide.

With sum-channel excitation, figures 6.13(a) and (b) show that for the H_{12} and E_{12} modes to be strongly excited relative to the H_{10} mode, as required for a satisfactory multimode radiation pattern, b/λ_o should be kept small, while a/λ_o should be as large as possible. Note that these higher modes are suppressed when a=b, because of the symmetry of the equivalent simple discontinuity. Despite the increasing higher-mode excitation near input guide cut-off, operation in this region is undesirable because of the high attenuation which occurs in practice. Also, figure 6.13(c) shows that reflected power in the form of the H_{10} mode increases rapidly as cut-off is approached. A choice of $b/\lambda_o = 0.6$ avoids these difficulties, giving a total reflected power which does not exceed 6% of the input power. At this point the phase angle between the H_{12} and E_{12} modes is about 33° for all the values of a/λ_o considered (see fig. 6.13(d)).

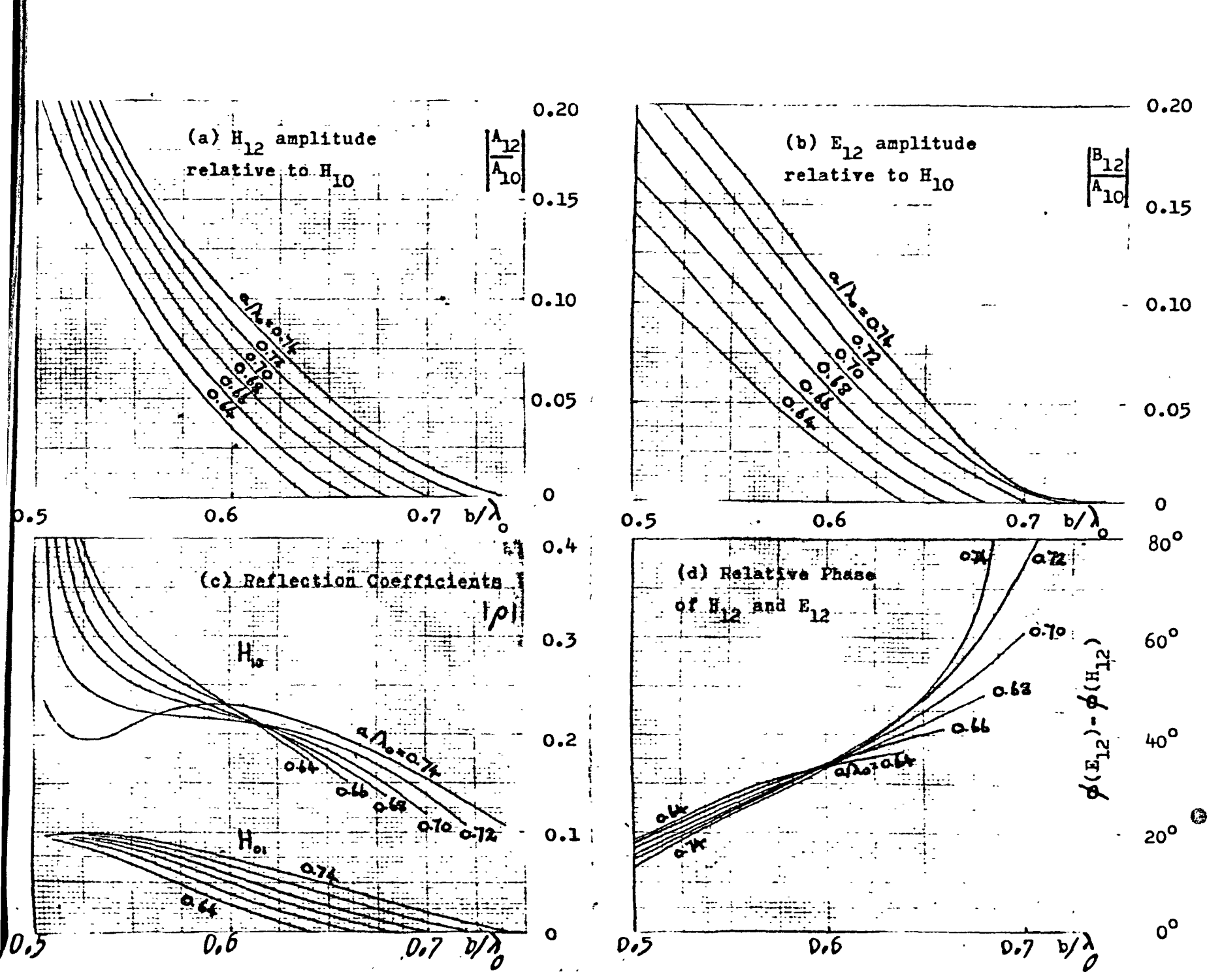
(a) H_{12} amplitude relative to H_{10}
$\left|\frac{A_{12}}{A_{10}}\right|$
a/λ_0=0.74
0.72
0.70
0.68
0.66
0.64
0.20
0.15
0.10
0.05
0
0.5
0.6
0.7
b/λ_0
(b) E_{12} amplitude relative to H_{10}
$\left|\frac{B_{12}}{A_{10}}\right|$
a/λ_0=0.74
0.72
0.70
0.68
0.66
0.64
0.20
0.15
0.10
0.05
0
0.5
0.6
0.7
b/λ_0
(c) Reflection Coefficients $|\rho|$
H_{10}
a/λ_0=0.74
0.72
0.70
0.68
0.66
0.64
H_{01}
0.74
0.64
0.4
0.3
0.2
0.1
0
0.5
0.6
0.7
b/λ_0
(d) Relative Phase of H_{12} and E_{12}
0.74
0.72
0.70
0.68
0.66
a/λ_0=0.64
0.64
0.74
$\phi(E_{12})-\phi(H_{12})$
80°
60°
40°
20°
0°
0.5
0.6
0.7
b/λ_0

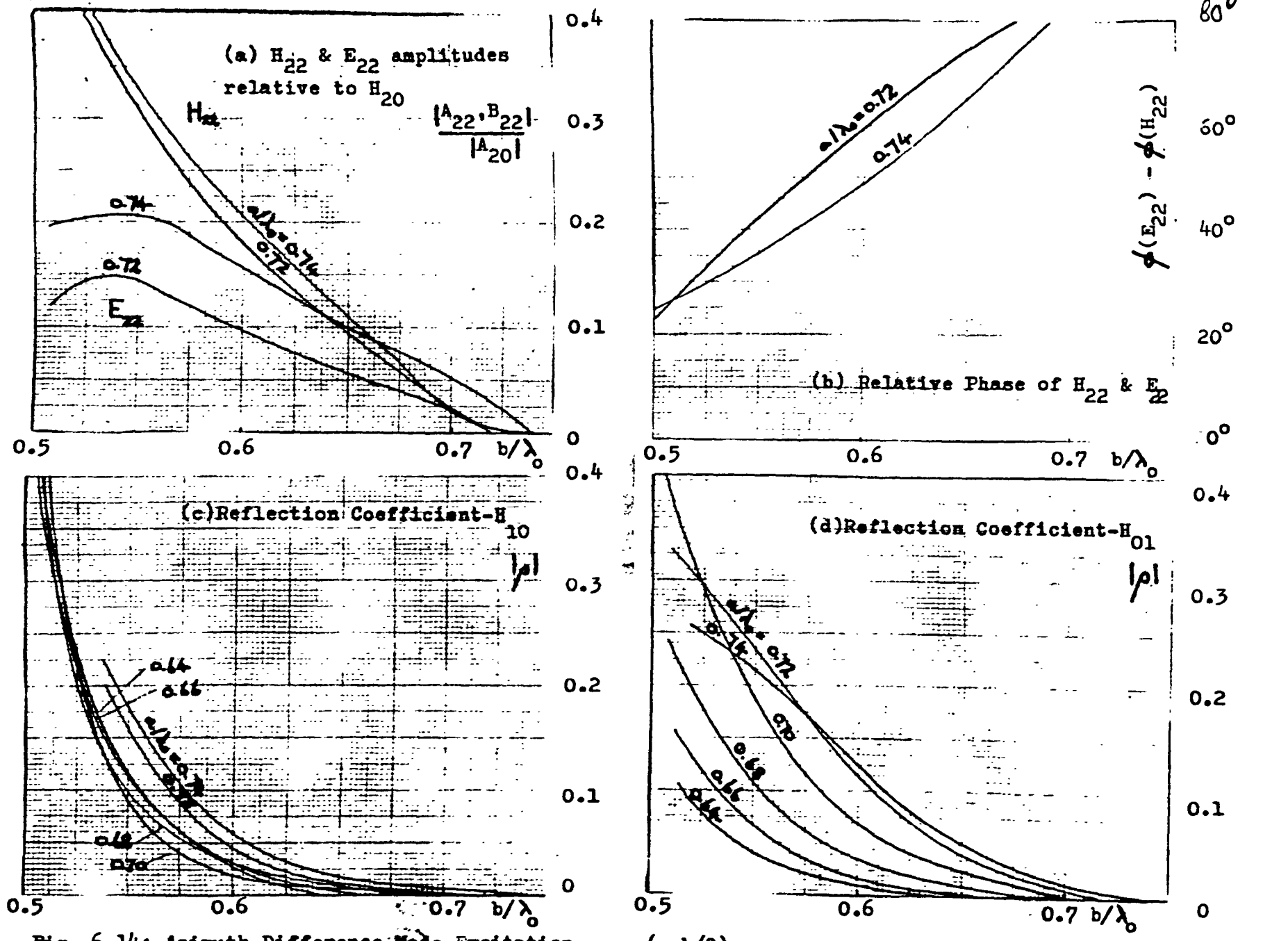

Fig. 6.14: Azimuth Difference Mode Excitation

(c=b/2)

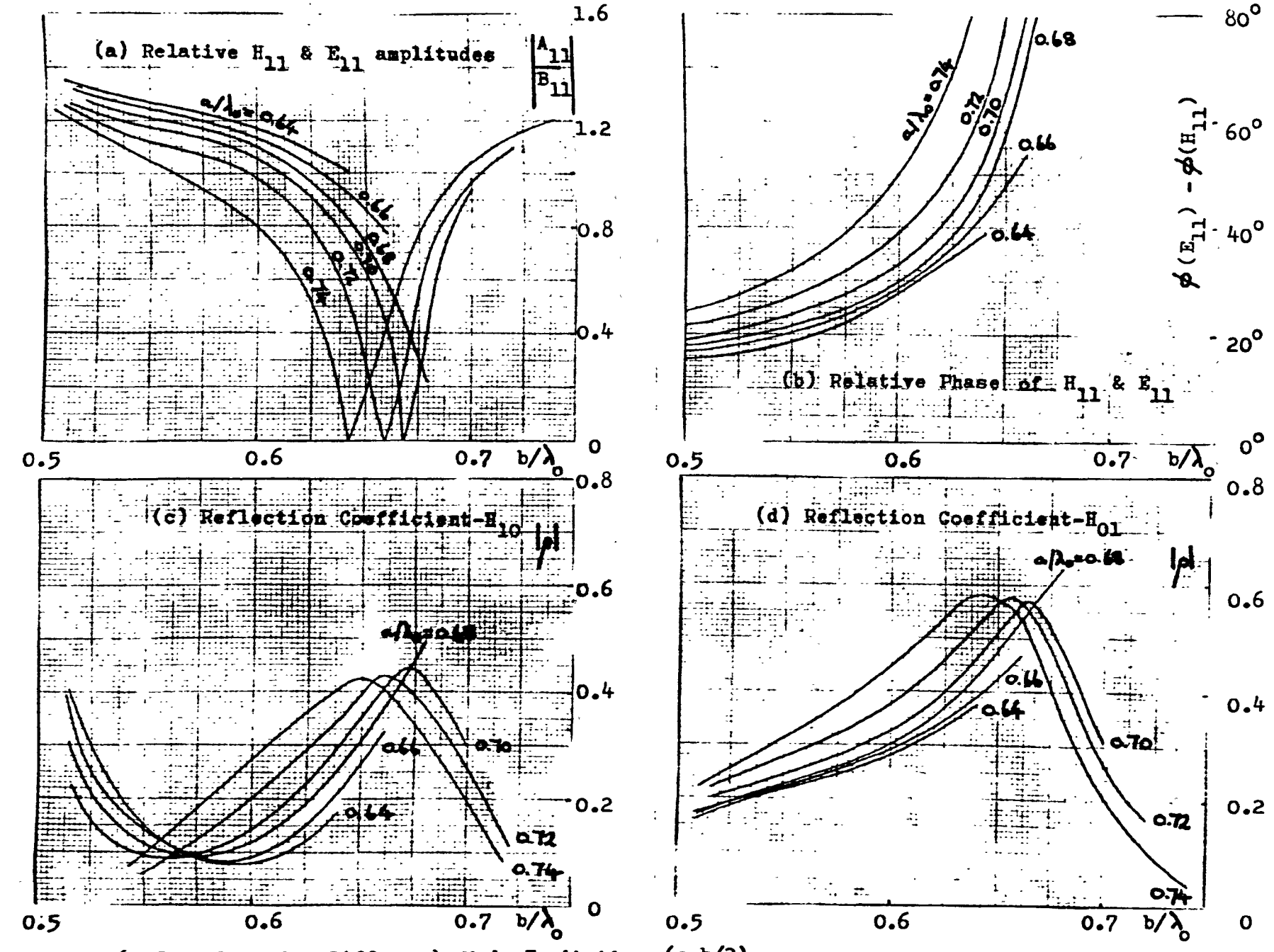

Fig. 6.15 : Elevation Difference Mode Excitation (c=b/2)

In the azimuth difference case, it can be seen in figure 6.14 (a) that the curves showing the H_{22} mode excitation are similar to those for the H_{12} mode in the sum-channel case, whereas those for the E_{22} mode have peaks in the region $b/\lambda_o \approx 0.53$. The H_{20} mode alone satisfies the matching conditions when a=b, so both normal and cross-polarized reflection coefficients are zero at this point (see figs. 6.14(c) and (d)). The reflection coefficients increase smoothly as b/λ_o decreases, but here again the mismatch is not serious unless the input waveguides are operating close to cut-off. In fact, when $b/\lambda_o = 0.6$, the proportion of input power reflected is only about 2% in the worst case. The relative phase angle of the H_{22} and E_{22} modes, whose variation is shown in figure 6.14(b) increases rapidly with b/λ_o, the value for $b/\lambda_o = 0.6$ being between 50^o and 60^o.

The dependence upon a/λ_o and b/λ_o of the H_{11} and E_{11} elevation difference modes is shown in figure 6.15(a) and (b). Figure 6.15(a) shows that the amplitude of the H_{11} mode decreases initially relative to that of the E_{11} as b/λ_o is increased from cut-off, and that for $a/\lambda_o \geq 0.70$ a point is reached at which the H_{11} mode is not excited at all. After this its level increases again towards a value similar to that near input guide cut-off. The points of H_{11} mode suppression are also those at which the curves showing the amplitudes of the reflected H_{10} and H_{10} modes have peaks (see figs. 6.15(c) and (d)). These regions should be avoided for good monopulse operation, since the H_{11} and E_{11} modes must be launched with similar amplitudes if the aperture field is to approximate the LSE_{11} hybrid mode. As with the other channels, a choice of b/λ_o in the region of 0.6 seems to be

optimum, as this gives reasonably low reflection coefficients and is not too close to input guide cut-off, while avoiding the region of H_{11} suppression. In contrast to the sum channel, however, a/λ_o should here be as low as possible, since, for $b/\lambda_o=0.6$, the value $a/\lambda_o=0.64$ gives the lowest reflected power (about 8½%) and smallest relative phase angle (28°) between the H_{11} and E_{11} modes (see fig. 6.15(b)).

It appears, then, that choosing b/λ_o as 0.6 gives a satisfactory compromise between the requirements for good matching and strong higher-mode excitation for all channels. The choice of a/λ_o is less straight-forward, however, since good H_{12} and E_{12} generation for the sum channel is incompatible with satisfactory elevation-difference matching. This will be more thoroughly investigated in section 6.6.4, where secondary characteristics corresponding to different values of a/λ_o are evaluated.

6.5.3. An Alternative Mode-Converter Design Using Two Step Discontinuities.

With the mode-converting step described above, the maximum value of $|\alpha|$ that can be realised when $b/\lambda_o=0.6$ is about 0.35, which, as can be seen from figures 6.8 and 6.9, is insufficient for simultaneous optimisation of sum and difference gain factors. It is therefore worth considering how the H_{12} and E_{12} modes might be more strongly generated without reducing b/λ_o. Clearly, their excitation increases with a/λ_o for either the corner (c=b/2) or centre (c=a-b/2) location of the small guides, but the magnitude of this parameter cannot exceed 0.75, otherwise unwanted propagating modes are generated. The

restriction can be removed, however, if the step is followed by a transition involving a further step or taper to a guide in which only the required modes can propagate. A configuration using a second step is shown in figure 6.16, and can be solved by the method of section 3.8, (boundary enlargement at first discontinuity, reduction at second), recognizing that, as with the single step converter, only one quarter of the structure needs to be considered because of symmetry. Two walls of the equivalent intermediate and output waveguides can be either electric or magnetic, depending on the channel to which the excitation corresponds, the choice of wall type being as for the single step (fig. 6.10). The division of power among propagating modes in the input and output guides when $b=0.6\lambda_o$, $a=0.77\lambda_o$ and $d=0.7\lambda_o$ has been calculated as a function of intermediate section length l' for the cases c=b/2 (fig. 6.18) and c=a-b/2 (fig. 6.17). The calculation took into account 14 modes in each input waveguide and between 20 and 22 in both intermediate and output guides. As mentioned in section 3.8, the results were not considered reliable for values of l' in excess of about $2\lambda_o$, as power was not then shown to be conserved exactly.

From the sum-channel point of view the c=a-b/2 configuration (fig. 6.17(a)) is attractive, since reflected power is below 7% for l'/a less than 2.0, and generation of the 1,2 modes when l'/a is around 1.875 is strong enough for α to approach 0.6. Unfortunately this value of l'/a gives a bad azimuth-difference mismatch (fig. 6.17(b)), and better all-round performance would be achieved with l'/a around 1.14 when α can reach about 0.45. As with the single

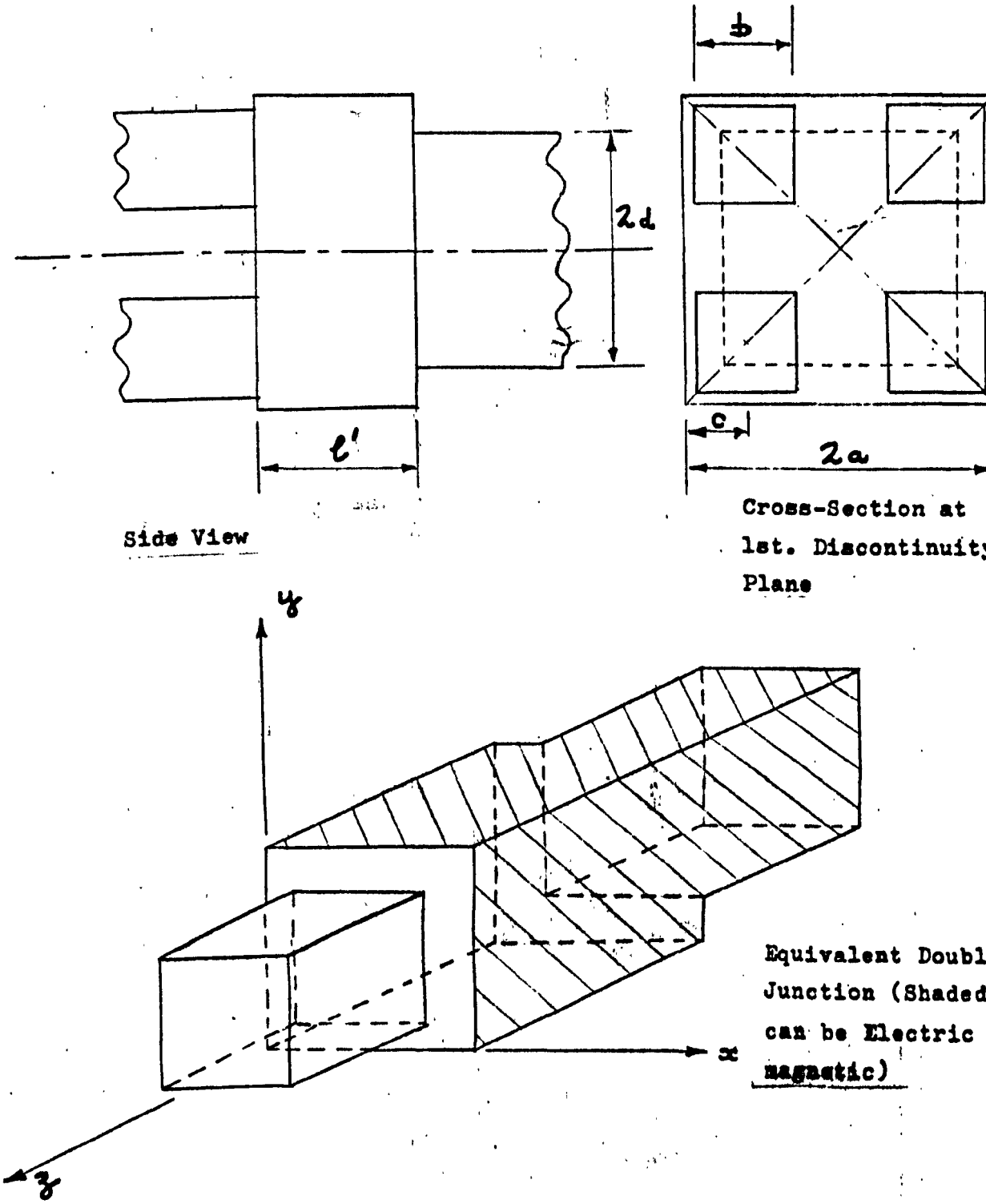

Fig. 6.16 : Double Step Monopulse Exciter

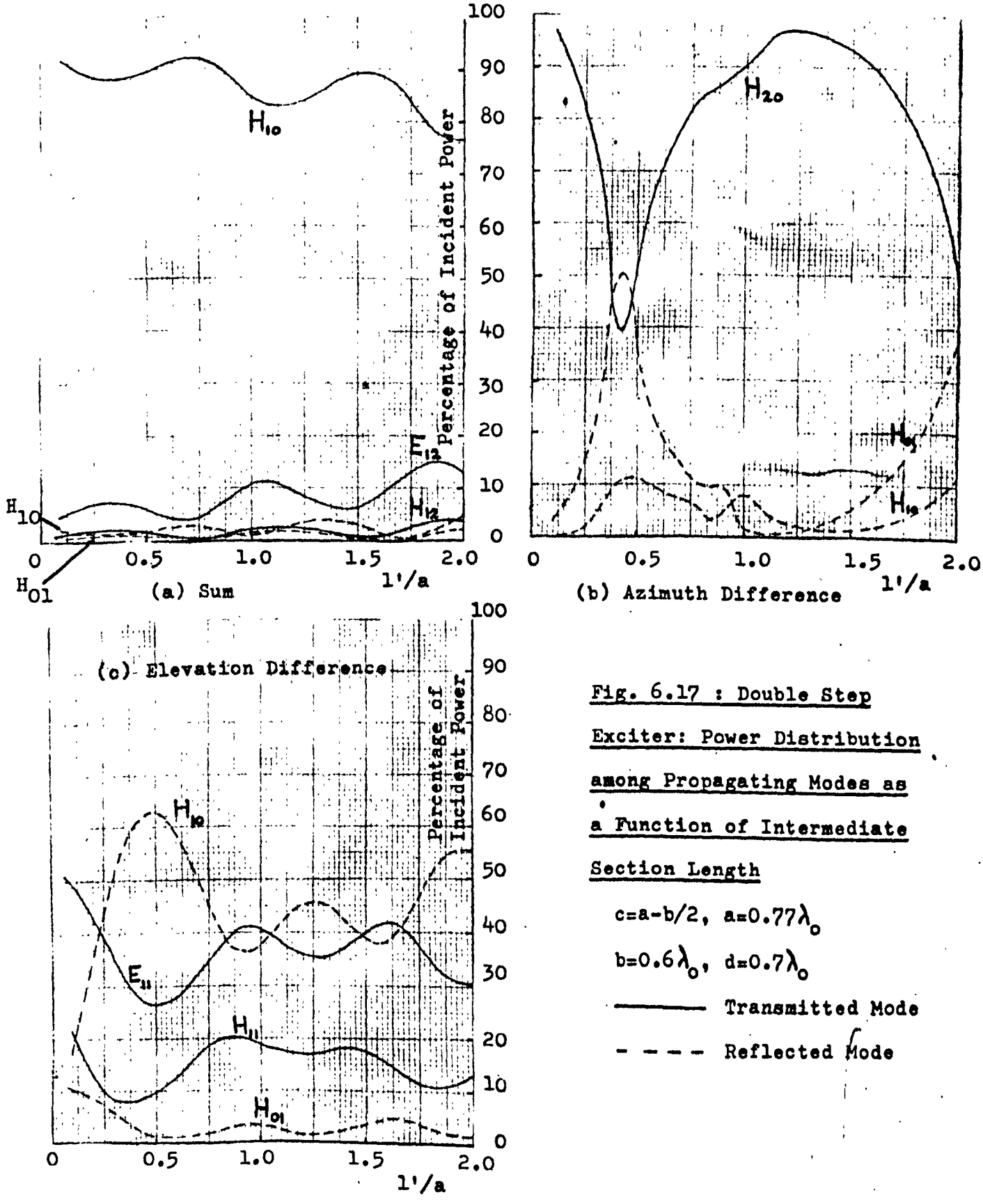

Fig. 6.17 : Double Step Exciter: Power Distribution among Propagating Modes as a Function of Intermediate Section Length

$c=a-b/2$, $a=0.77\lambda_o$

$b=0.6\lambda_o$, $d=0.7\lambda_o$

——— Transmitted Mode

- - - - Reflected Mode

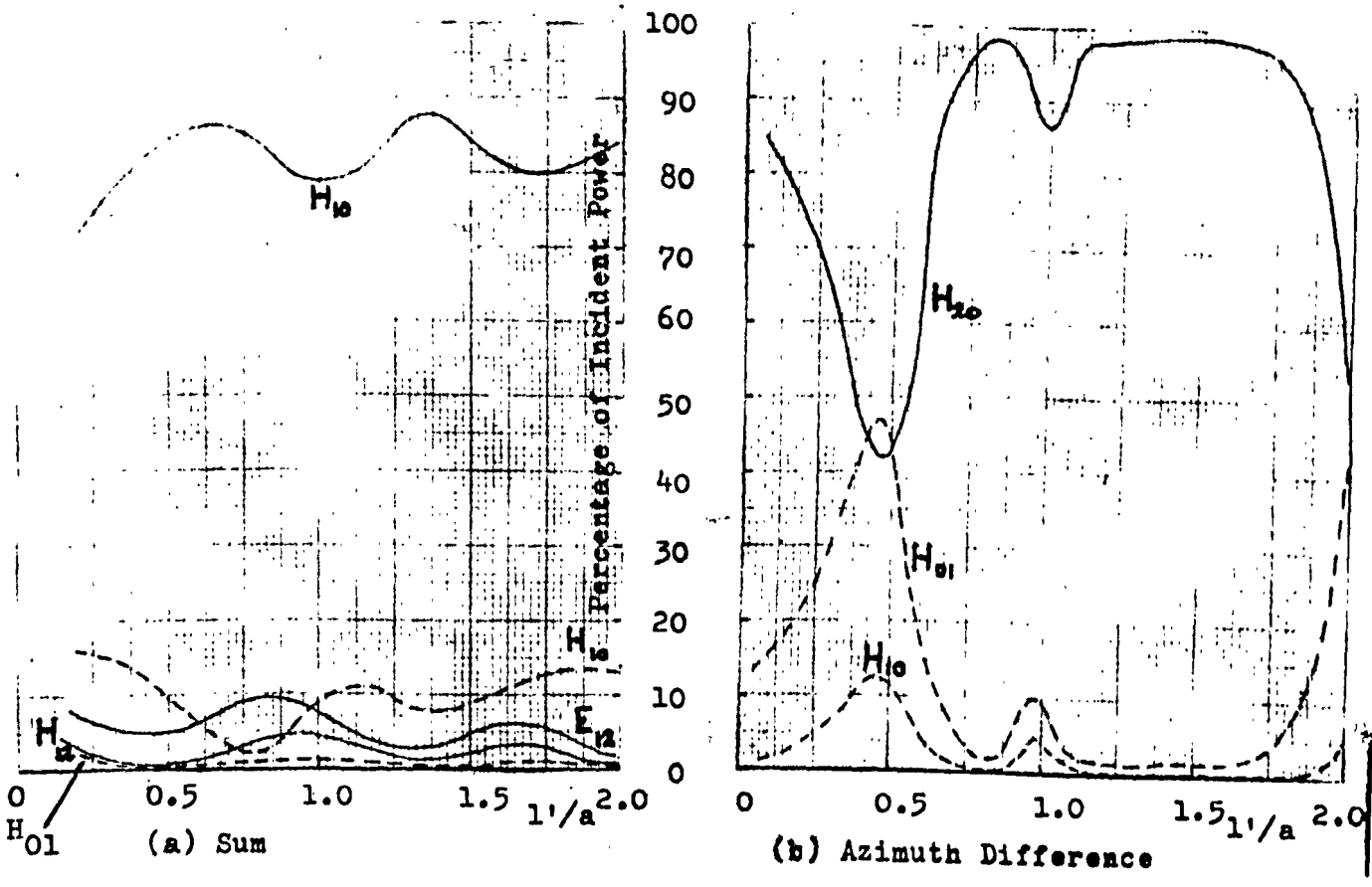

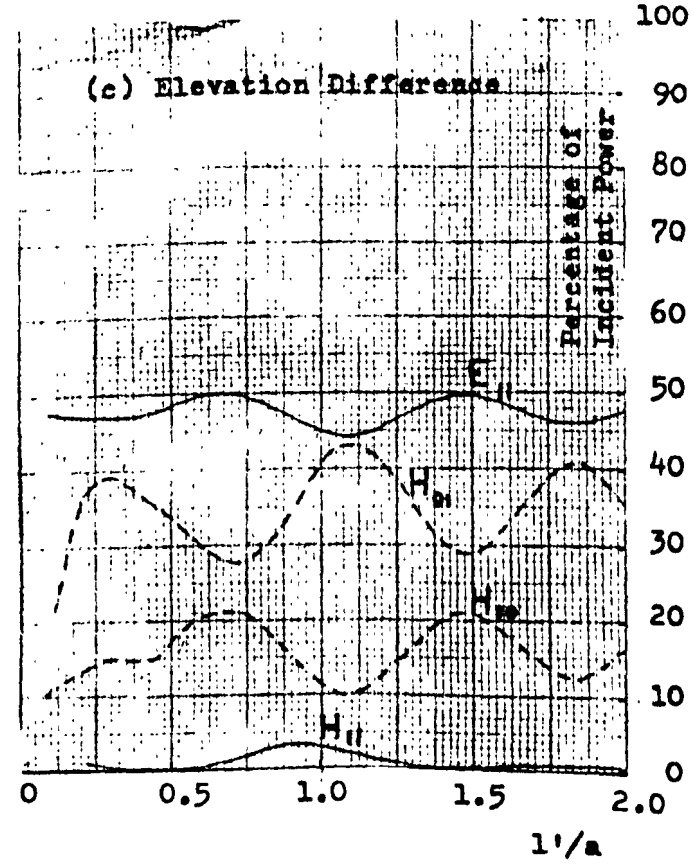

Fig. 6.18 : Double Step Exciter: Power Distribution among Propagating Modes as a Function of Intermediate Section Length

$c=b/2$, $a=0.77\lambda_o$

$b=0.6\lambda_o$, $d=0.7\lambda_o$

——— Transmitted Mode

– – – – Reflected Mode

step, reflected power for the elevation difference channel (fig. 6.17 (a)) is very high, generally more than 40%.

The c=b/2 configuration gives a generally higher level of sum-channel reflected power (fig. 6.18(a)) than when c=a-b/2, except when l'/a is around 0.75, where it is down to only 3%, and where the excitation of the 1,2 modes is greatest. Values of α of approximately 0.5 can be achieved in this region. The greatest drawback with this choice of c is that excitation of the H_{11} elevation difference mode is very weak compared with that of the E_{11} mode (fig. 6.18 (c)), giving a radiation pattern with a very strong cross-polarized component.

Further improvements in all-round performance might be achieved by increasing a, and sum-channel mode conversion for $a=0.95\lambda_o$ has been investigated. Although high values of α are possible, the modal amplitudes fluctuate very rapidly with l' and λ_o. This emphasises the main drawback of double-step exciters: their dependence on multiple reflections of propagating modes imposes serious bandwidth limitations. For this reason a practical feed design based on a double-step exciter will not be considered here. However, it is suggested that such a design might form the subject of future work on multimode feeds for single-frequency operation.

6.6 Complete Feed Designs Using the Single-Step Exciter, with Corresponding Secondary Characteristics.

6.6.1. Determination of the Amplitudes and Phases of Propagating Modes in the Feed Aperture.

In section 6.5.1, the determination of the amplitudes and

phases of propagating modes in the uniform section at the discontinuity plane z=0 was described. Since these modes generally propagate with different velocities in the uniform section, and horn flare, their relative phases change during passage from step to aperture. The relative amplitudes of their transverse field components are also affected, because of the requirement, mentioned in section 6.2, for the power associated with any propagating mode to remain constant. This requirement allows the calculation of the modal amplitudes at the aperture in terms of those at the step. It is found that:

$$\frac{|A'_{MN}|}{|A_{MN}|} = \frac{a}{a'}\sqrt{\frac{\beta_{MN}}{\beta'_{MN}}} \quad , \quad \frac{|B'_{MN}|}{|B_{MN}|} = \frac{a}{a'}\sqrt{\frac{\beta'_{MN}}{\beta_{MN}}} \qquad 6.45$$

The phase angle χ_u of a propagating mode in the plane of transition from uniform to flared waveguide is given by:

$$\chi_u = \chi_o - \beta_{MN} l \qquad 6.46$$

where χ_o is the phase in the plane z=0.

Using the "quasi-uniform" approximation, the phase change that a propagating mode undergoes in the flared guide may be determined by treating each elemental length δZ (see fig. 6.1) of the flare as a section of uniform waveguide, calculating the phase shift across this element, and summing the effects of all such elements along the length of the flare. The propagation coefficient in a plane with coordinate Z is given by:

$$\beta_{MN}(Z) = \sqrt{(k_o^2 - (M^2 + N^2)(\frac{\pi}{2x})^2)} \qquad 6.47$$

where $x = Z\tan\varphi$. The phase-shift $\delta\chi$ across the element δZ is:

$$\delta\chi = -\beta_{MN}(Z)\,\delta Z,$$

and the total phase-shift in the flare is therefore

$$\chi_f = -\int_{Z_1}^{Z_2} \beta_{MN}(Z)\, dZ \qquad 6.48$$

By making the substitution $dZ = \cot\zeta\, dx$ and using 6.47, the integral is evaluated to give:

$$\chi_f = -\cot\zeta \left\{ (a'^2 k_o^2 - v^2)^{1/2} - (a^2 k_o^2 - v^2)^{1/2} - v\cos^{-1}\frac{v}{k_o a'} + v\cos^{-1}\frac{v}{k_o a} \right\} \qquad 6.49$$

where $v = \frac{\pi}{2}\sqrt{(M^2 + N^2)}$

The above method of determining phase-shift in the flare is not exact, since it depends on the assumption that transverse field components at any cross-section of the flare can be expressed in terms of the normal modes for a square waveguide of the same cross-section, there being no transfer of energy between modes during their propagation along the flare. Thus the quasi-uniform method is only applicable when ζ is sufficiently small for the modal wavefronts to have negligible curvature.

A rigorous analysis of the field structure within the flare requires a solution of Maxwell's equations subject to the boundary conditions imposed by the pyramidal structure. Such a solution is difficult to obtain, since the surfaces defining the walls of the flare cannot be expressed as functions of only one co-ordinate of a spherical co-ordinate system centred at the apex of the pyramid, as would be the case with a conical horn. However, Keeping [18] states that the modes would have radial field variations depending on the Hankel functions $h'_n(k_o Z)$ of orders $n = \frac{\pi}{2\zeta}\sqrt{(M^2+N^2)} - 1/2$ and $n = \frac{\pi}{2\zeta}\sqrt{(M^2+N^2)} - 3/2$. The arguments of such functions are not well

tabulated, and Keeping therefore uses approximate expressions applicable when $k_o z > n$. His expression for the higher-order function is found to be identical to 6.49, and the contribution from the lower-function is stated to be negligible. Calculated phase-shifts are therefore exactly the same as those which would be obtained using the quasi-uniform method.

6.6.2 Phasing Requirements for the Three Channels

(i) Sum Channel Phasing Requirement

It was shown in section 6.3.1. that the hybrid LSE_{12} mode needs to be in antiphase to the H_{10} mode in the feed aperture if the desired multimode illumination is to be produced. However, the computations of section 6.5 show that a pure LSE_{12} mode cannot be excited in practice, so it is necessary to find the relative phases of the modes H_{10}, H_{12} and E_{12} in the aperture which give the best radiation pattern, bearing in mind that the relative phase of the H_{12} and E_{12} modes is fixed by the design of the step.

In the ideal case of section 6.3.1, there is a unique phase-centre located at the centre of the feed aperture, but in practice, when the H_{12} and E_{12} modes are not in phase, the position of the phase-centre varies with ϕ (see co-ordinate system, fig. 6.7): only in the H-plane, where the 1,2 modes do not contribute to the radiation pattern, is the phase-centre always located at the aperture centre. Phase errors in the resulting reflector illumination can be minimised by adjusting the relative phase of the H_{10} mode and the 1,2 pair so that the E and H-plane phase-centres are coincident. If, in the E-

plane pattern expression given by 6.6, α is now defined as the complex quantity $(A'_{12} + 2B'_{12})/A'_{10}$, comparison with the H-plane pattern expression 6.2(a) shows that the imaginary part of α must vanish for phase-centre coincidence. If ψ_o is the phase angle by which the E_{12} mode leads the H_{12}, then the required angle ψ by which the H_{12} leads H_{10} in the aperture is, to satisfy the above condition:

$$\psi = \tan^{-1}\left\{ - \frac{2|B'_{12}|\sin\psi_o}{|A'_{12}| + 2|B'_{12}|\cos\psi_o} \right\} \qquad 6.50$$

Table 6.2 gives the values of ψ corresponding to mode-converter solutions for the case $b/\lambda_o = 0.6$, where a/λ_o takes values from 0.64 to 0.74 in steps of 0.02, together with the required phase-shift between the H_{10} mode and 1,2 pair from step to aperture. a' was taken as $2.29\lambda_o$, but the results are quite accurate for larger values of a' since $\bar{\beta}'_{10}$ and $\bar{\beta}'_{12}$ are both approximately equal to 1 in such apertures.

(ii) Azimuth Difference Channel Phasing Requirement.

As the H_{22} and E_{22} modes do not give rise to an E-plane component of radiated field, H-plane and 45°-plane phase-centres are made to coincide for the azimuth difference channel. α' in the expression for the normally polarized 45°-plane component (eqn. 6.12) is now the complex quantity $(A'_{22} + B'_{22})/A'_{20}$, and its imaginary part must vanish for phase-centre coincidence with the H-plane pattern given by 6.9. This occurs when

$$\psi' = \tan^{-1}\left\{ - \frac{|B'_{22}|\sin\psi'_o}{|A'_{22}| + |B'_{22}|\cos\psi'_o} \right\} , \qquad 6.51$$

$\frac{a}{\lambda_o}$	$\left\|\frac{A_{12}}{A_{10}}\right\|$	$\left\|\frac{B_{12}}{A_{10}}\right\|$	ψ_o	Phase of H_{12} relative to H_{10} at step	$\left\|\frac{A'_{12}}{A'_{10}}\right\|$	$\left\|\frac{B'_{12}}{A'_{10}}\right\|$	ψ	Required phase-shift between H_{10} and 1,2 pair
0.64	0.0355	0.0266	33.53°	-35.27°	0.0261	0.0389	154.71°	189.98°
0.66	0.0496	0.0414	33.97°	-34.17°	0.0380	0.0578	154.24°	188.41°
0.68	0.0630	0.0572	33.98°	-32.98°	0.0499	0.0772	154.13°	187.11°
0.70	0.0760	0.0740	33.80°	-31.78°	0.0617	0.0970	154.17°	185.95°
0.72	0.0885	0.0913	33.43°	-30.80°	0.0734	0.1166	154.39°	185.19°
0.74	0.0999	0.1084	33.22°	-30.02°	0.0844	0.1355	154.49°	184.51°

TABLE 6.2

$\frac{a}{\lambda_o}$	$\left\|\frac{A_{22}}{A_{20}}\right\|$	$\left\|\frac{B_{22}}{A_{20}}\right\|$	ψ'_o	H_{22} phase rel. H_{20} at step	$\left\|\frac{A'_{22}}{A'_{20}}\right\|$	$\left\|\frac{B'_{22}}{A'_{20}}\right\|$	ψ'	Req. p.s. between H_{20} and 2,2 pair
0.72	0.1799	0.0984	59.02°	-3.75°	0.0934	0.2573	135.68°	139.43°
0.74	0.2062	0.1573	49.01°	-8.04°	0.1321	0.3249	144.61°	152.65°

TABLE 6.3

$\frac{a}{\lambda_o}$	$\left\|\frac{B_{11}}{A_{11}}\right\|$	ψ''_o	H_{11} phase rel. H_{20} at step	$\left\|\frac{B'_{11}}{A'_{11}}\right\|$	ψ''	Req. p.s. between H_{20} & 1,1 pair
0.64	0.8588	28.07°	-16.47°	1.0179	14.16°	357.69°
0.66	0.8789	28.70°	-17.24°	1.0285	14.56°	357.32°
0.68	0.9062	30.24°	-19.27°	1.0481	15.48°	356.21°
0.70	0.9494	33.30°	-22.52°	1.0869	17.36°	354.84°
0.72	1.0299	38.90°	-30.14°	1.1680	21.02°	351.96°
0.74	1.2507	49.79°	-42.92°	1.4087	29.40°	346.48°

TABLE 6.4

a/λ_o	ζ, n=0	ζ, n=1	ζ, n=2
0.64	17.02°	6.06°	3.64°
0.66	16.29°	5.73°	3.43°
0.68	15.59°	5.45°	3.21°
0.70	15.01°	5.22°	3.15°

TABLE 6.5

a/λ_o	$1/\lambda_o$	ζ^o	Flare length
0.72	2.533	4.35°	$20.66\lambda_o$
0.74	4.658	6.09°	$14.53\lambda_o$

TABLE 6.6

ψ' being the angle by which the H_{22} phase leads that of the H_{20} at the aperture, and ψ'_o that by which E_{22} leads H_{22}. Table 6.3 gives values of ψ' and corresponding relative phase-shifts for a/λ_o=0.74 and 0.72, the other dimensions being as for the sum-channel case. Notice that if $|A'_{22}|$ and $|B'_{22}|$ are not equal, a cross-polarized component will also exist in the 45°-plane.

(iii) Difference-Channel Phasing for Circular Polarization.

A distant circularly polarized source displaced from the principal axis of the antenna in either the E or the H-plane produces in the feed aperture two orthogonal linearly polarized field distributions, differing in phase by 90°. One of these distributions consists of the "azimuth difference" modes H_{20}, H_{22}, E_{22} etc., whereas the other consists of the "elevation difference" modes H_{11}, E_{11} etc. Owing to the differences in phase velocity of these modes, and the different matching conditions at the step, the H_{10} and H_{01} modes excited in each small waveguide will not have a 90° phase difference unless the relative phase-shifts between modes in the horn are correctly controlled, and if circular polarization is achieved by including a circular polarizer in each small guide there may be a serious degradation of tracking performance. If the feed is thought of as transmitting the difference patterns, the phasing requirement is that the H-plane phase-centre under linearly polarized azimuth difference excitation should coincide with the E-plane phase-centre under elevation difference excitation. This occurs when the H_{20} mode has a phase leading that of the H_{11} mode in the aperture by ψ'', where

$$\psi'' = \tan^{-1}\left\{\frac{|B'_{11}|\sin\psi''_o}{|A'_{11}| + |B'_{11}|\cos\psi''_o}\right\} \qquad 6.52$$

ψ_o'' being the angle by which the E_{11} phase leads that of the H_{11} mode. The results of the phase-shift calculation for this case are given in table 6.4, the dimensions being as in sub-section (i), above.

6.6.3 Choice of Horn Dimensions to Satisfy Phasing Requirements

It was hoped that by suitably choosing l and ζ, it would be possible to satisfy phasing requirements 6.50 and 6.52 simultaneously, but calculation has shown that, in all cases of interest, the differential phase-shift per unit length between the H_{10} and 1,2 modes is almost exactly twice that between the 1,1 and H_{20} modes, both in the uniform section and in the flare. Since the required differential phase-shift between the H_{10} and 1,2 modes is approximately $(2n+1)\pi$ radians, and that between the 1,1 and H_{20} modes approximately $(2m+2)\pi$ radians, where n and m are any positive integers, it is therefore not possible to satisfy both requirements simultaneously unless the horn is extremely long. This would make any inaccuracies in the phase-shift calculation very significant, and would severely limit the bandwidth owing to the rapid change with frequency of the relative phases of modes in the aperture.

The difference-channel circular polarization phasing requirement may alternatively be satisfied by modifying the comparator circuitry so that an additional phase-shift between the horizontally and vertically polarized components of the difference channel signals is introduced to compensate for the phase error caused by the horn. A drawback is that the circuitry now needs to be considerably more complex than before. For example, eight hybrid-Tees are required instead of

the previous four.

For some satellite-tracking applications, the polarization of the incident wave is linear, but randomly orientated, and a circularly polarized feed is used to give a signal level independent of this orientation. Such a wave can be viewed as a combination of equal-amplitude left and right-hand circularly polarized components, only one of which contributes to the signal at the feed output. As the effect of a 180° phase-error between tracking modes at the step is merely to reverse the sense of each component, the tracking signal levels are not affected in this case.

Under circumstanes such as those mentioned above, where phasing requirement 6.52 is not applicable, the choice of 1 and ζ depends only on the sum-channel phasing requirement when $a<\lambda_o/\sqrt{2}$. Since only one of these parameters needs to be adjusted to give correct phasing, it is possible in this case to put 1 equal to zero, so that the flare commences at the step discontinuity. The flare angle can then be determined using expression 6.49 and the values of differential phase-shift between the H_{10} mode and the 1,2 pair given in table 6.2, to which may be added an integral number n of complete phase rotations. The larger the value of n, the more restricted is the bandwidth of the feed, whereas if n is too small the flare angle may be so large that the quasi-uniform approximation can no longer be applied. Table 6.5 gives the values of ζ for the cases a/λ_o=0.64, 0.66, 0.68 and 0.70, when n=0,1 and 2. a' is taken as $2.29\lambda_o$. The values of ζ for n=1 appear to be the best compromise between the small flare angle and broad bandwidth requirements.

When $a \geqslant \lambda_o/\sqrt{2}$, the sum and azimuth difference phasing requirements can be simultaneously satisfied by suitably choosing l and ζ. The required differential phase-shift between sum-channel propagating modes is as given in table 6.2, plus n complete phase rotations, whereas that for the azimuth difference channel is as given by table 6.3, to which m phase rotations may be added. Here again, bandwidth and small flare angle requirements must be borne in mind when selecting m and n, and suitable values for the cases a/λ_o=0.74 or 0.72 were found to be m=3, n=2 when a' was equal to $2.29\lambda_o$. The corresponding feed dimensions are given in table 6.6.

6.6.4. Secondary Characteristics.

The gain and slope factors of the sum and difference secondary patterns when the modal amplitudes and phases in the feed aperture are as given in tables 6.2 to 6.4 may be determined from the expressions in sections 6.43 and 6.44. Since the component E_y of the primary pattern is now a complex function of θ and ϕ, separate integrations are performed for the real and imaginary parts. In figures 6.19 to 6.21, the variation with $X(=2\pi\frac{D}{F}\frac{a'}{\lambda_o})$ of the gain and slope factors corresponding to the six previously considered values of a/λ_o is shown. Both the case in which the input waveguides are equipped with perfect matching devices, and that where reflected power is absorbed by a load are considered.

The use of the parameter X as co-ordinate enables the graphs to be used with fair accuracy for any feed aperture large enough for the modes to have propagation coefficients approaching that of free space.

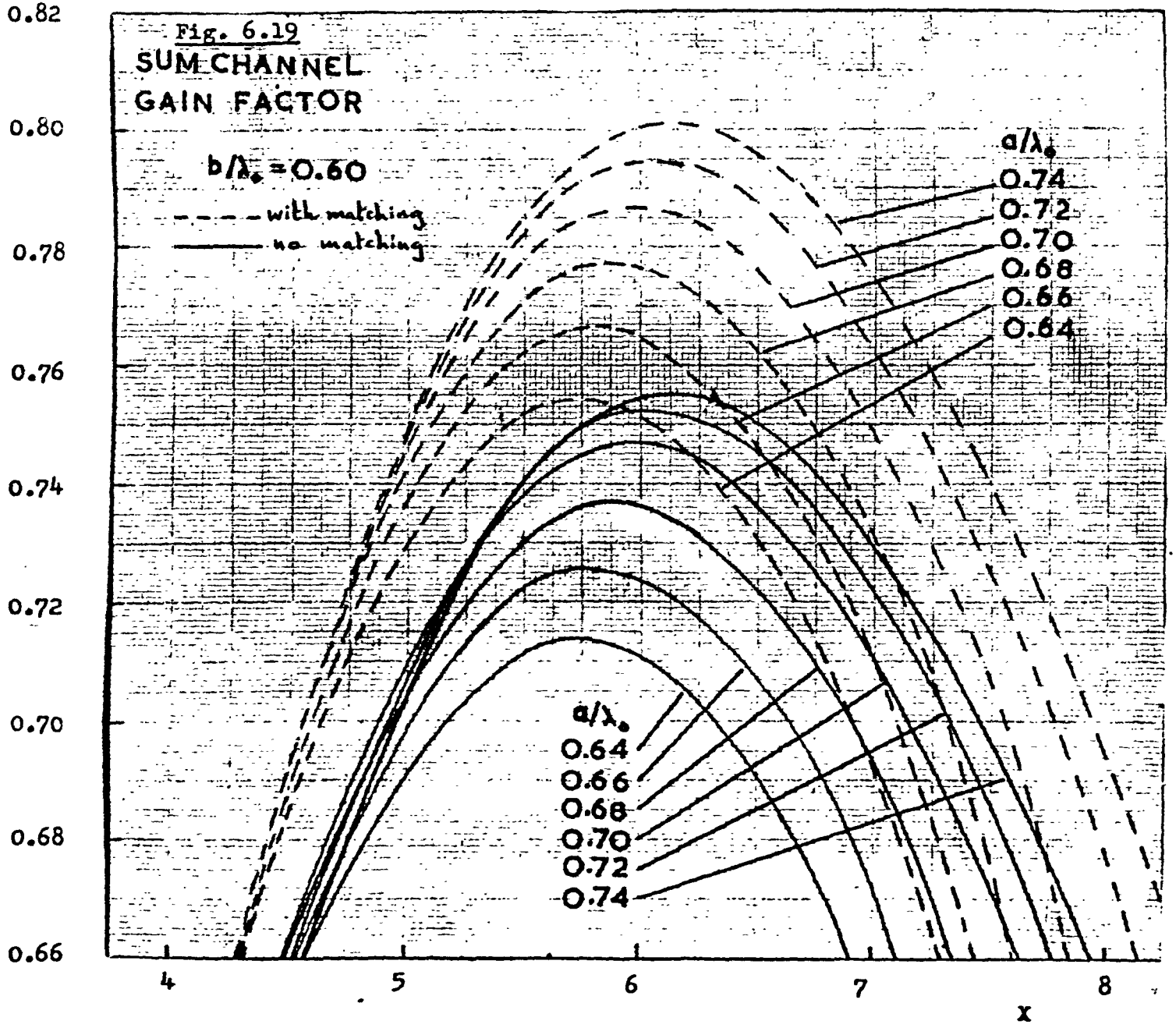
Fig. 6.19
SUM CHANNEL
GAIN FACTOR
G_Σ
$b/\lambda_0 = 0.60$
with matching
no matching
a/λ_0
0.74
0.72
0.70
0.68
0.66
0.64
a/λ_0
0.64
0.66
0.68
0.70
0.72
0.74
0.82
0.80
0.78
0.76
0.74
0.72
0.70
0.68
0.66
4
5
6
7
8
x

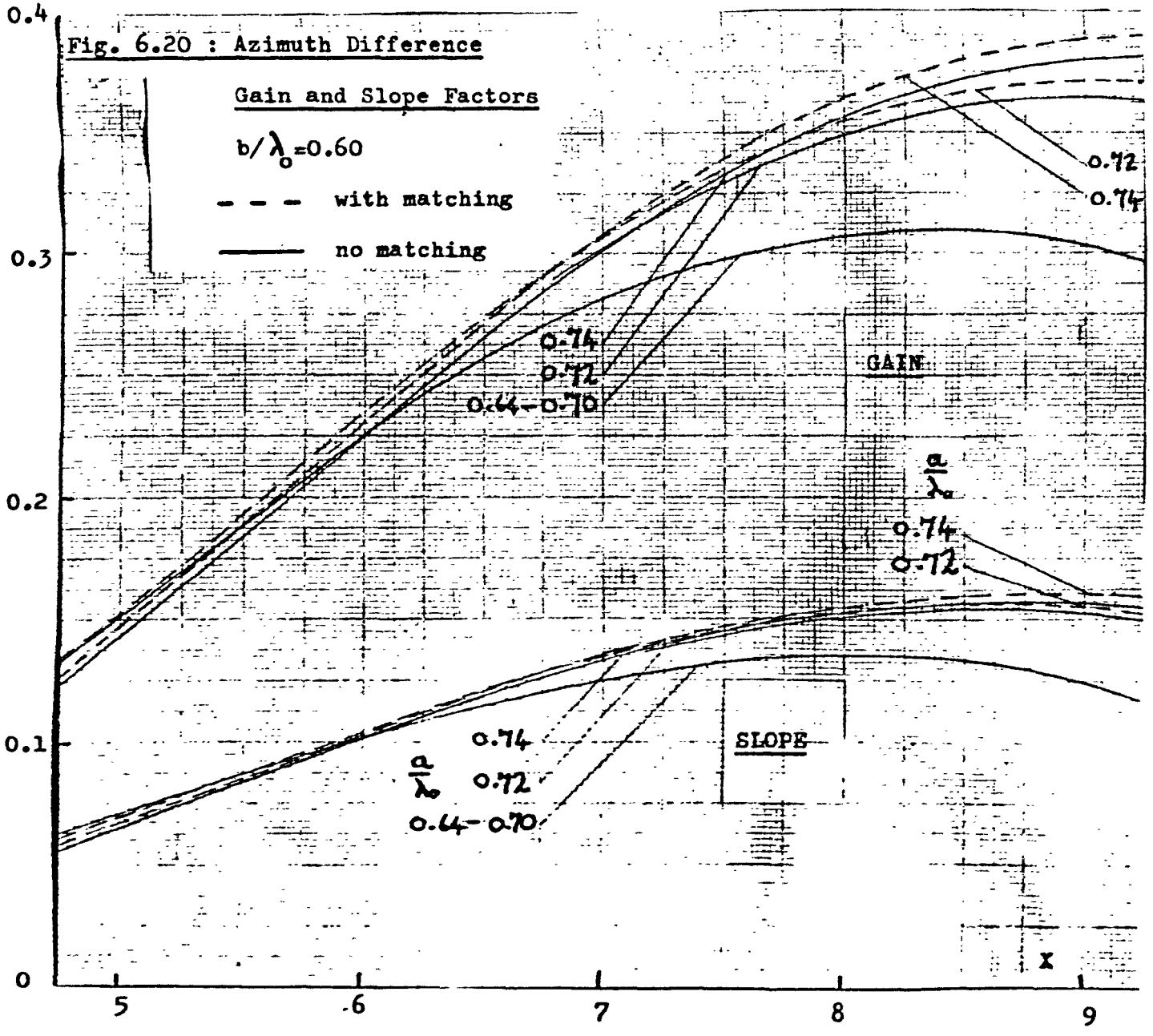
Fig. 6.20 : Azimuth Difference
Gain and Slope Factors
b/λ₀=0.60
with matching
no matching
0.72
0.74
GAIN
0.74
0.72
0.64-0.70
a/λ₀
0.74
0.72
SLOPE
0.74
a/λ₀ 0.72
0.64-0.70
0.4
0.3
0.2
0.1
0
5
6
7
8
9
X

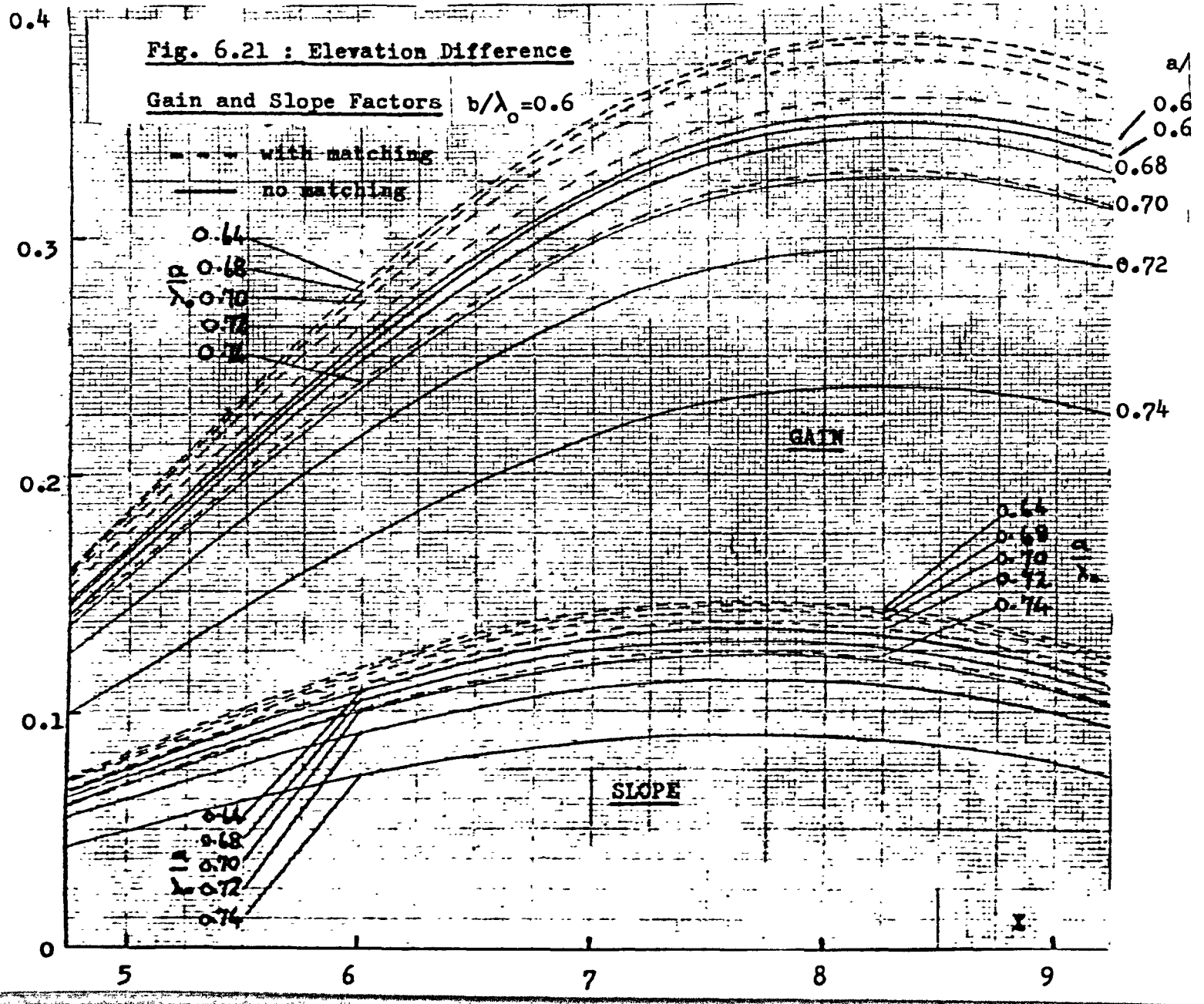
Fig. 6.21 : Elevation Difference
Gain and Slope Factors b/λo=0.6
with matching
no matching
a/λo
0.64
0.68
0.70
0.72
0.74
GAIN
SLOPE
0.4
0.3
0.2
0.1
0
5
6
7
8
9
X

The increase with a/λ_o of the 1,2 to H_{10} mode amplitude ratio for the sum channel, which was shown in section 6.5.2, can be seen from figure 6.19 to be associated with an increase in gain factor. With correct matching, this can reach 0.801 when $a=0.74\lambda_o$ but if no matching is provided there is a reduction in gain of about 5½% in all cases considered.

For azimuth difference operation (figure 6.20) the effect of the mismatch at the step is negligible when only the H_{20} mode propagates, and is only very slight when the H_{22} and E_{22} modes are also above cut-off. The use of these modes can be seen to produce an appreciable improvement in gain factor. For example, when $a=0.74\lambda_o$, the maximum gain factor is 0.39, as opposed to 0.31 when a is less than $\lambda_o/\sqrt{2}$: an increase of about 25%. There is a corresponding increase in the slope factor, which can reach 0.16 when $a=0.74\lambda_o$, the maximum value when a is less than $\lambda_o/\sqrt{2}$ being about 0.14. In no case does the cross-polarization efficiency for this channel fall below 98.5%.

The elevation difference gain and slope factors can be seen from figure 6.21 to decrease as a/λ_o increases. Reference to table 6.4 shows that this is due to increases in the relative phase angle between the H_{11} and E_{11} modes, and in the deviation of the amplitude ratio of these modes from unity. Associated with this deviation is a decrease in cross-polarization efficiency, which falls from 94% when $a=0.64\lambda_o$ to 80% when $a=0.74\lambda_o$, and also an increase in primary H-plane radiation, which is only completely suppressed when the illumination is a pure LSE_{11} mode. This radiation has an adverse effect on tracking performance when circular polarization is used, since a

signal from a source displaced in one of the principal planes gives rise to outputs in both difference channels. The antenna then comes into alignment with the source via a spiral rather than a direct path. If no matching is provided, the elevation difference gain and slope factors are further reduced because of the increase in reflected power which occurs as a/λ_o is increased. With correct matching, however, the gain factor can attain 0.385 when $a=0.64\lambda_o$, a value comparable with the maximum azimuth difference gain factor. The best possible slope factor is 0.145, somewhat lower than that in the azimuth difference case.

As the values of a/λ_o for best sum and azimuth difference performance also gives the poorest elevation difference performance, and vice versa, a compromise must be made if both sum gain and tracking ability are of equal importance. For example, when $a=0.70\lambda_o$ azimuth and elevation difference gain and slope factors are similar in the unmatched case, but this is achieved by accepting a 2% reduction in peak gain factor compared with the $a=0.74\lambda_o$ configuration.

Comparison of figures 6.19, 6.20 and 6.21 confirms that the H_{12} and E_{12} modes cannot be excited sufficiently strongly to bring about simultaneous optimization of sum and difference gain and slope factors. The value of $|\alpha|$ in the case $a=0.74\lambda_o$ is about 0.35, compared with the value of 1.0 mentioned in section 6.4.5 as being required for simultaneous optimisation. However, it was also shown that, for a front-fed paraboloid, difference slope and sum gain-temperature ratio are maximised simultaneously at a lower value of $|\alpha|$, and figure 6.22 shows that when $a=0.74\lambda_o$ $|\alpha|$ is large enough for

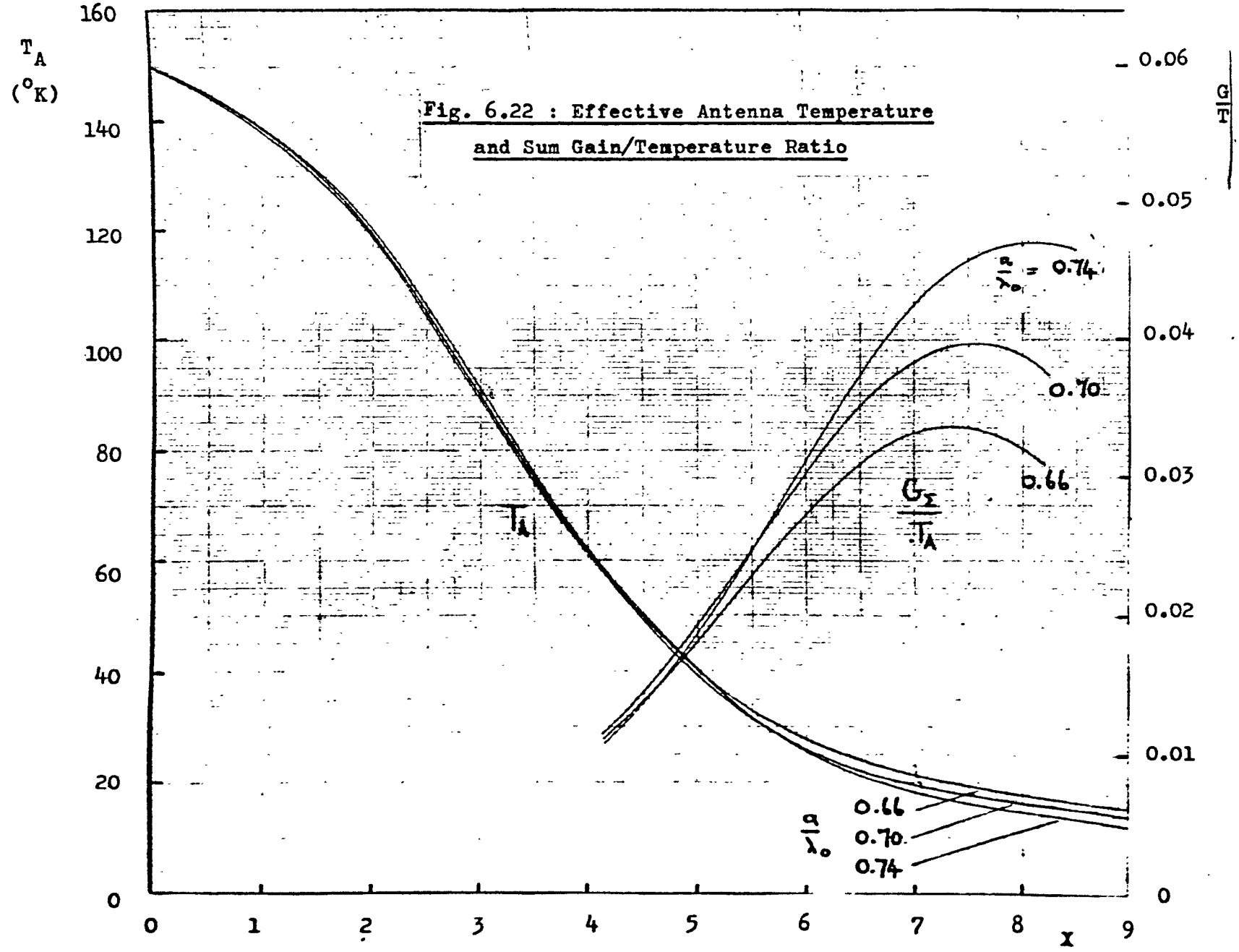

Fig. 6.22 : Effective Antenna Temperature and Sum Gain/Temperature Ratio

this to occur. Difference slopes and G/T_A all have peaks in the region of X=8 for this case.

The relative merits of multimode feeds for which a/λ_o equals 0.74, 0.70 and 0.66 and of a conventional feed consisting of a cluster of four square single-mode horns are compared in table 6.7. The feeds are assumed correctly matched for all channels. Because of the greatly improved feed aperture illumination, the sum-channel gain factor using a multimode feed can exceed that for the four-horn cluster by between 35% and 40%. In many cases there is also a significant increase in difference slope, and in no case is the slope

Feed	Sum Gain Factor		Δ_{AZ} Slope Factor		Δ_{EL} Slope Factor		G_Σ/T_A	
	Peak value	Corresp. X	Peak value	Corresp. X	Peak value	Corresp. X	Peak value	Corresp. X
Multimode: $a=.74\lambda_o$	0.801	6.15	0.161	8.9	0.125	7.7	0.047	8.1
Multimode: $a=.70\lambda_o$	0.786	6.00	0.138	8.1	0.142	7.7	0.040	7.6
Multimode: $a=.66\lambda_o$	0.767	5.85	0.138	8.1	0.145	7.7	0.034	7.3
4-Horn Cluster	0.570	4.30	0.141	6.7	0.122	6.3	0.010	4.9

TABLE 6.7

obtained with a multimode feed appreciably less than that for the four-horn cluster. Furthermore, the value of X for maximum difference

slope is between 30% and 35% greater than that for maximum sum gain with a multimode feed, as against 50% in the case of the four-horn cluster: thus sum gain and difference slope are more nearly simultaneously optimised when multimode feeds are used. The most striking improvement, however, is in the G_Σ/T_A ratio for a front-fed paraboloid which is greater in the multimode case by a factor of as much as 4.7. In a receiving system which, apart from the antenna, is noise-free, this represents an increase in signal - to - noise ratio of 6.7dB, but in a practical system with receiver and lead-in noise the increase would not be so great.

Using geometric optics, the results displayed in figures 6.19 - 6.21 can be applied to a Cassegrain system by considering the equivalent front-fed paraboloid. As mentioned in section 6.4.1, diffraction effects at the subreflector are usually ignored when its diameter exceeds about $10\lambda_o$. However, as a program for evaluating such effects was available, it was decided to have the main reflector sum -channel illumination and spillover efficiencies calculated for the $a=0.74\lambda_o$, $a'=2.29\lambda_o$ feed, used at 7.3GHz, in a Cassegrain antenna having a 40' diameter main dish of F/D ratio 0.3. A subreflector of eccentricity 1.295 is required under these circumstances. Two configurations were considered; that in which the feed was located at the apex of the dish, requiring a subreflector of diameter 59.6" for maximum sum gain, and that corresponding to the minimum blockage condition, with the feed centre positioned 79.8" in front of the apex and a subreflector 26.6" in diameter. The method used in the analysis was that of Rusch [36]. In the former case, main reflector spillover effic-

iency was calculated as 99.3%, and in the latter case as 99.0%. The calculated illumination efficiencies were 90.1% and 88.9% respectively, as opposed to 89.4% using the equivalent front-fed paraboloid method. These results show that, at least for the sum channel, the effect of diffraction at the subreflector is small and that it is justifiable to neglect it. For the difference channels the effect would probably be more serious because of the higher fields at the subreflector edge, but an analysis of this case was not possible because of the asymmetric nature of the primary patterns.

6.6.5 Frequency Dependence of Sum-Channel Gain.

As it is usual for satellite communication antennas to use different frequencies for transmission and reception, sum-channel bandwidth is an important consideration in their design. Figure 6.23 shows the variation of sum-channel gain factor with frequency for antennas using unmatched multimode feeds in which $a=0.66\lambda_o$, $0.70\lambda_o$ and $0.74\lambda_o$ at the design frequency, the other feed dimensions being as given in tables 6.5 and 6.6. The F/D ratio is taken as that for maximum sum gain factor at the design frequency.

The primary beamwidth, which depends largely on the electrical size of the feed aperture, is chosen to give the best compromise between illumination and spillover at the design frequency. Any change in beamwidth caused by frequency deviation therefore reduces the gain factor. Also, the frequency-dependence of propagation coefficients causes the relative phases of modes in the feed aperture to change with frequency, leading to an increase in primary sidelobes and in the asymmetry of the reflector illumination. This effect is

Fig. 6.23 : Frequency Dependence of Sum Gain Factor

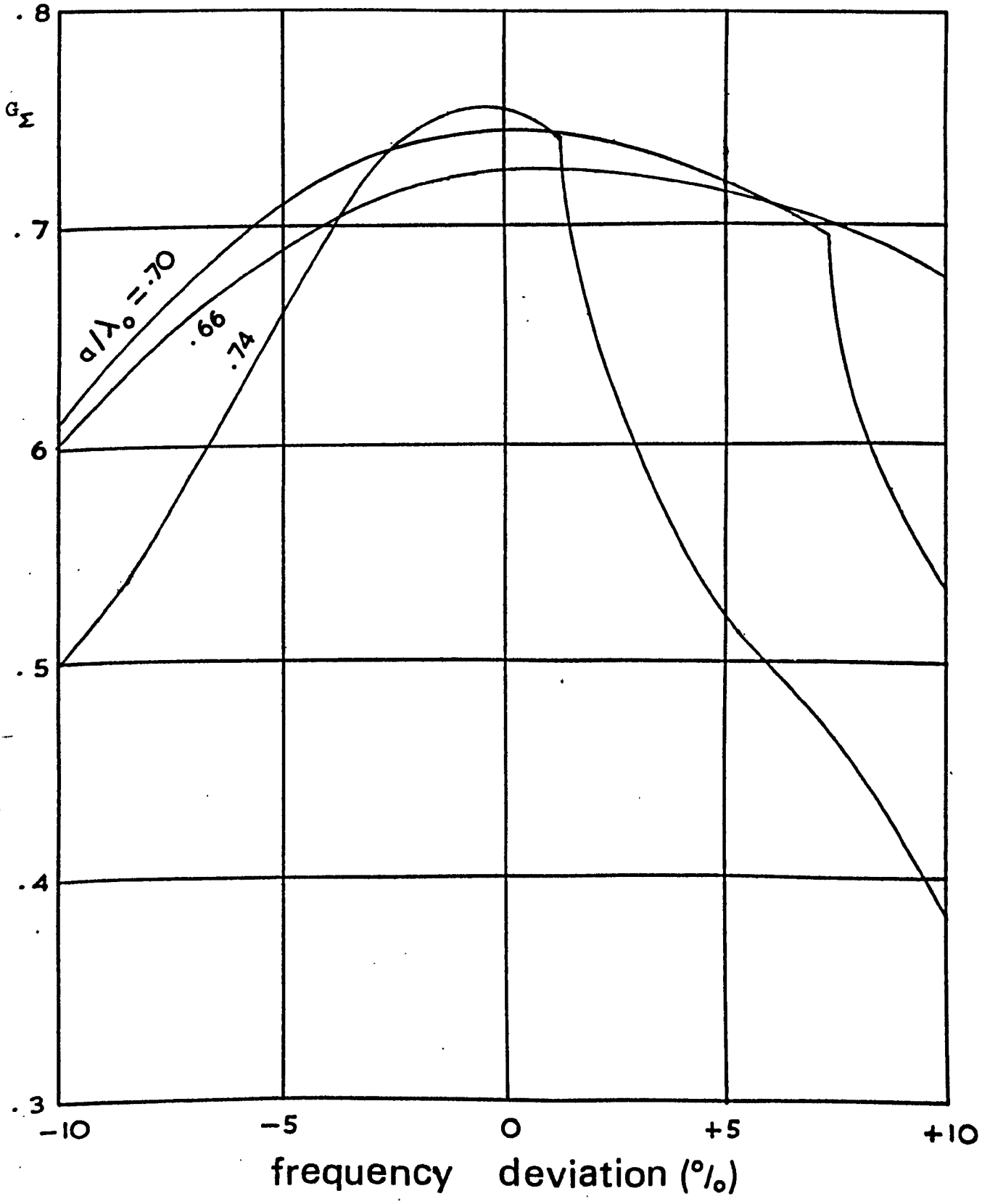

particularly noticeable with the $a=0.74\lambda_o$ feed, where a 10% frequency reduction causes the relative phase of the H_{10} and 1,2 modes in the aperture to change by almost 180°. The lengthening of the feed caused by the introduction of the uniform section makes the phases particularly frequency-sensitive in this case.

Another factor affecting the antenna bandwidth is the introduction of the H_{30} mode, which begins to propagate when $\lambda_o=4a/3$. The presence of this mode is detrimental to the gain factor, since, depending on its phase, it either broadens the H-plane primary beamwidth, causing excessive spillover, or tapers it so as to give a poor reflector illumination and high H-plane sidelobes.

The gain of the antenna relative to an isotropic source does not vary with frequency in quite the same way as the gain factor, since the gain of the reference source in the latter case (a uniformly illuminated aperture) varies as the square of the frequency. Thus the antenna gain may increase slightly with frequency over a small range, even though the gain factor is reduced.

For military satellite communications, typical transmission and reception frequencies are 8.0 and 7.3GHz. respectively. If the antenna is designed for maximum gain at the reception frequency, the relative gain at the transmission frequency is as given in the following table:

TABLE 6.8

a/λ_o at 7.3 GHz	Gain at 8.0 GHz relative to that at 7.3 GHz
0.74	-2.01dB
0.70	-0.55dB
0.66	+0.52dB

It can be seen that by using the $a=0.66\lambda_o$ feed a slight increase in gain can, in fact, be achieved at the transmission frequency. This advantage is offset, however, by a loss in gain at the reception frequency when compared with an antenna using the $a=0.74\lambda_o$ feed.

APPENDIX TO CHAPTER VI. EVALUATION OF MATRIX ELEMENTS FOR SOLUTION OF THE SINGLE-STEP MONOPULSE EXCITER

Field Expressions for number 1 small W/G

H_{mn} mode:

$$E_x = - a_{mn}\, n \cos \frac{m\pi}{b}(x-c+\frac{b}{2}) \sin \frac{n\pi}{b}(y-c+\frac{b}{2})$$

$$E_y = a_{mn}\, m \sin \frac{m\pi}{b}(x-c+\frac{b}{2}) \cos \frac{n\pi}{b}(y-c+\frac{b}{2})$$

$$H_x = j \frac{\gamma_{mn}}{\omega\mu_o} E_y \qquad H_y = -j \frac{\gamma_{mn}}{\omega\mu_o} E_x$$

E_{mn} mode:

$$E_x = b_{mn}\, m \cos \frac{m\pi}{b}(x-c+\frac{b}{2}) \sin \frac{n\pi}{b}(y-c+\frac{b}{2})$$

$$E_y = b_{mn}\, n \sin \frac{m\pi}{b}(x-c+\frac{b}{2}) \cos \frac{n\pi}{b}(y-c+\frac{b}{2})$$

$$H_x = -j \frac{\omega\varepsilon_o}{\gamma_{mn}} E_y \qquad H_y = j \frac{\omega\varepsilon_o}{\gamma_{mn}} E_x$$

In these expressions, $\gamma_{mn} = \sqrt{(\frac{m^2+n^2}{b^2}\pi^2 - k_o^2)}$

Field expressions for the modes in the large waveguide are given by 6.42 and 6.43.

Expressions for the Elements of [R] and [S]

1. i refers to H_{MN} mode in large w/g, j to H_{mn} mode in small w/g.

$$R_{ij} = \frac{2\varepsilon_{NO}}{a^2} \frac{nNI_1I_2 + mMI_3I_4}{N^2 + M^2} \qquad S_{ji} = \frac{\varepsilon_{nO}\varepsilon_{mO}}{b^2} \frac{\Gamma_{MN}}{\gamma_{mn}} \frac{nNI_1I_2 + mMI_3I_4}{n^2 + m^2}$$

2. i refers to E_{MN} mode in large w/g, j to H_{mn} mode in small w/g.

$$R_{ij} = \frac{4}{a^2} \frac{mNI_3I_4 - nMI_1I_2}{N^2 + M^2} \qquad S_{ji} = -\frac{\varepsilon_{nO}\varepsilon_{mO}}{b^2} \frac{k_o^2}{\gamma_{mn}\Gamma_{MN}} \frac{mNI_3I_4 - nMI_1I_2}{n^2 + m^2}$$

3. i refers to E_{MN} mode in large w/g, j to E_{mn} mode in small w/g.

$$R_{ij} = \frac{4}{a^2} \frac{mMI_1I_2 + nNI_3I_4}{N^2 + M^2} \qquad S_{ji} = \frac{4}{b^2} \frac{\gamma_{mn}}{\Gamma_{MN}} \frac{mMI_1I_2 + nNI_3I_4}{n^2 + m^2}$$

4. i refers to H_{MN} mode in large w/g, j to E_{mn} mode in small w/g.

$$R_{ij} = S_{ji} = 0.$$

Integrals $I_1 - I_4$ are defined as follows:

$$I_1 = \int_{c-b/2}^{c+b/2} \cos\frac{M\pi x}{2a} \cos\frac{m\pi}{b}(x-c+\tfrac{b}{2})dx \qquad I_2 = \int_{c-b/2}^{c+b/2} \sin\frac{N\pi y}{2a} \sin\frac{n\pi}{b}(y-c+\tfrac{b}{2})dy$$

$$I_3 = \int_{c-b/2}^{c+b/2} \sin\frac{M\pi x}{2a} \sin\frac{m\pi}{b}(x-c+\tfrac{b}{2})dx \qquad I_4 = \int_{c-b/2}^{c+b/2} \cos\frac{N\pi y}{2a} \cos\frac{n\pi}{b}(y-c+\tfrac{b}{2})dy$$

General case $M/2a \neq m/b$

m even: $I_1 = \frac{M}{a\pi} \frac{\cos \frac{M\pi c}{2a} \sin \frac{M\pi b}{4a}}{(M/2a)^2-(m/b)^2}$ $\quad I_3 = \frac{2m}{b\pi} \frac{\cos \frac{M\pi c}{2a} \sin \frac{M\pi b}{4a}}{(M/2a)^2-(m/b)^2}$

m odd: $I_1 = -\frac{M}{a\pi} \frac{\sin \frac{M\pi c}{2a} \cos \frac{M\pi b}{4a}}{(M/2a)^2-(m/b)^2}$ $\quad I_3 = -\frac{2m}{b\pi} \frac{\sin \frac{M\pi c}{2a} \cos \frac{M\pi b}{4a}}{(M/2a)^2-(m/b)^2}$

Special case $M/2a = m/b$

$$I_1 = I_3 = \frac{b}{2} \cos m\pi\left(\frac{c}{b} - \frac{1}{2}\right)$$

General case $N/2a \neq n/b$

n even: $I_2 = \frac{2n}{b\pi} \frac{\cos \frac{N\pi c}{2a} \sin \frac{N\pi b}{4a}}{(N/2a)^2-(n/b)^2}$ $\quad I_4 = \frac{N}{a\pi} \frac{\cos \frac{N\pi c}{2a} \sin \frac{N\pi b}{4a}}{(N/2a)^2-(n/b)^2}$

n odd: $I_2 = -\frac{2n}{b\pi} \frac{\sin \frac{N\pi c}{2a} \cos \frac{N\pi b}{4a}}{(N/2a)^2-(n/b)^2}$ $\quad I_4 = -\frac{N}{a\pi} \frac{\sin \frac{N\pi}{2a} \cos \frac{N\pi b}{4a}}{(N/2a)^2-(n/b)^2}$

Special case $N/2a = n/b$

$$I_2 = I_4 = \frac{b}{\varepsilon_{n0}} \cos n\pi\left(\frac{c}{b} - \frac{1}{2}\right)$$

CHAPTER VII. EXPERIMENTAL STUDY OF THE MULTIMODE MONOPULSE FEED.

7.1. Introduction.

The extent to which the theoretical predictions of the previous chapter could be experimentally verified was limited by the availability of suitable equipment. In particular, it was not possible to gain access to a reflector system in order to measure secondary characteristics, so that experimental work had to be confined to measurement of the feed radiation patterns.

The $a=0.74\lambda_o$ configuration was selected for the experimental feed, as the effect of higher-order propagating modes on the sum and azimuth-difference patterns is most pronounced in this case. Discrepancies between measured and theoretical sidelobe structures and cross-polarized energy levels were expected to enable errors in the predicted relative amplitudes and phases of modes in the aperture to be determined. It was also hoped that the effects of factors neglected in the theory, such as the excitation of unwanted propagating modes in the flare and the sphericity of the aperture wavefront could be deduced from the radiation patterns.

As microwave circuit components for X-band were readily available, a design frequency of 9.5GHz was chosen.

7.2 Construction of the Feed and Comparator.

The basic dimensions of the feed are as given in table 6.6, with λ_o equal to 1.244". The structure of the experimental feed is shown in figure 7.1, and in the photographs of figure 7.2, there being a

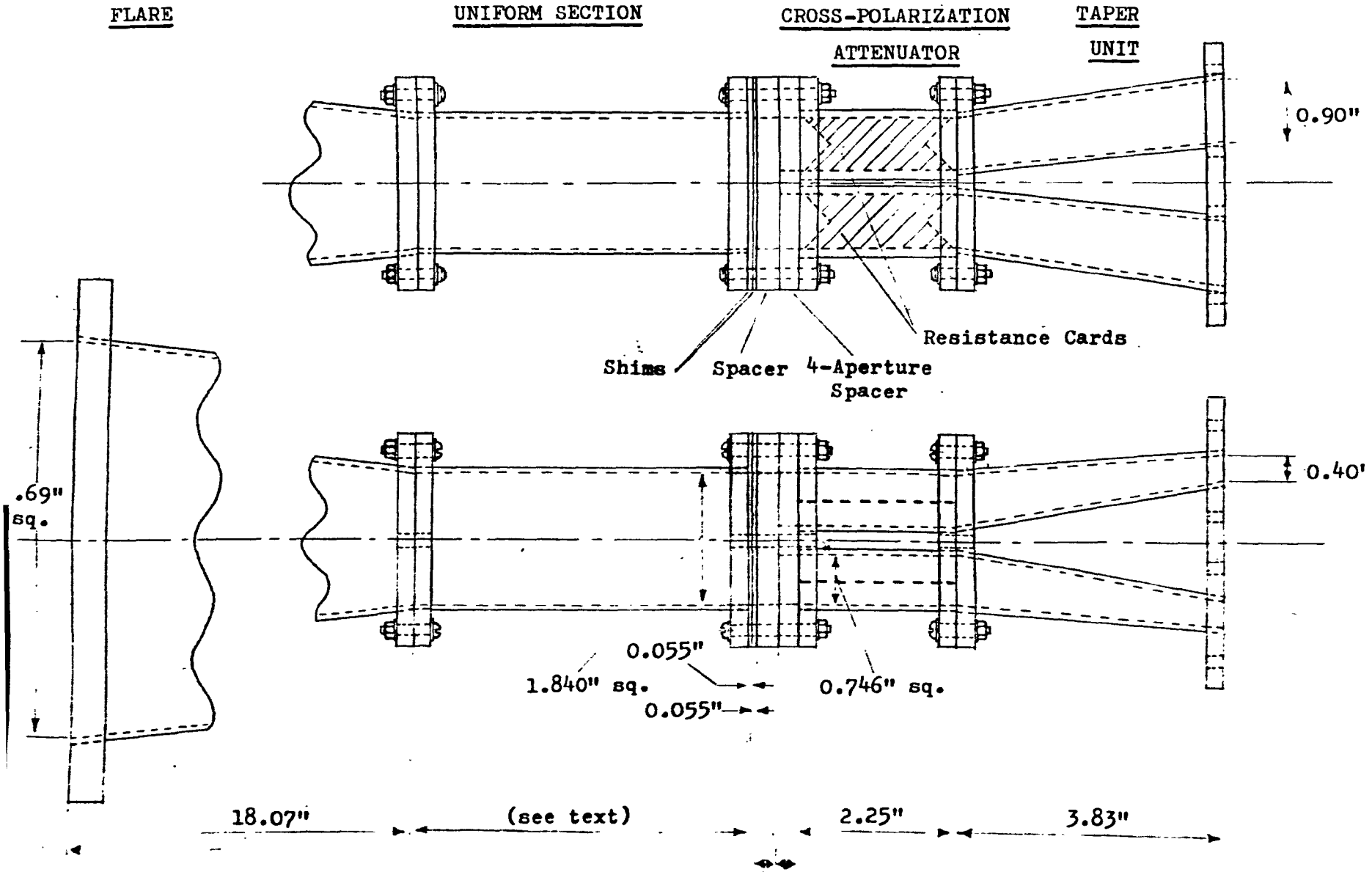

Fig. 7.1 : Experimental Monopulse Feed Horn

Fig. 7.2(a):Multimode Feed Components (Horn Flare, Basic Uniform Section, Cross-Polarization Attenuator, Input Taper Unit, Spacers and Shims)

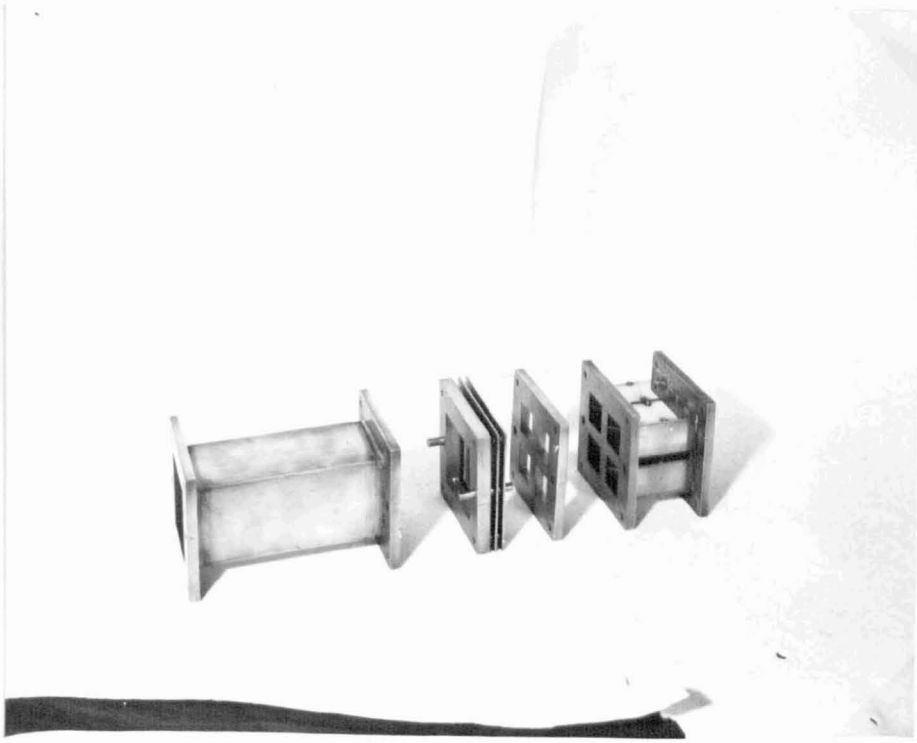

Fig. 7.2(b): Mode Converter Sub-Assembly

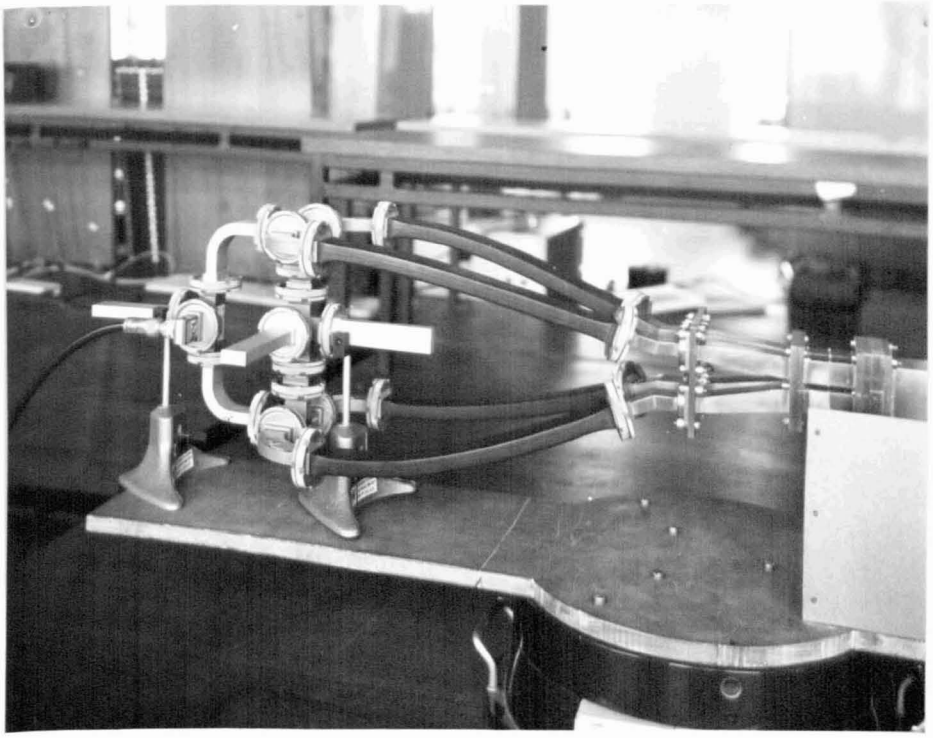

Fig. 7.2(c): Monopulse Comparator Network

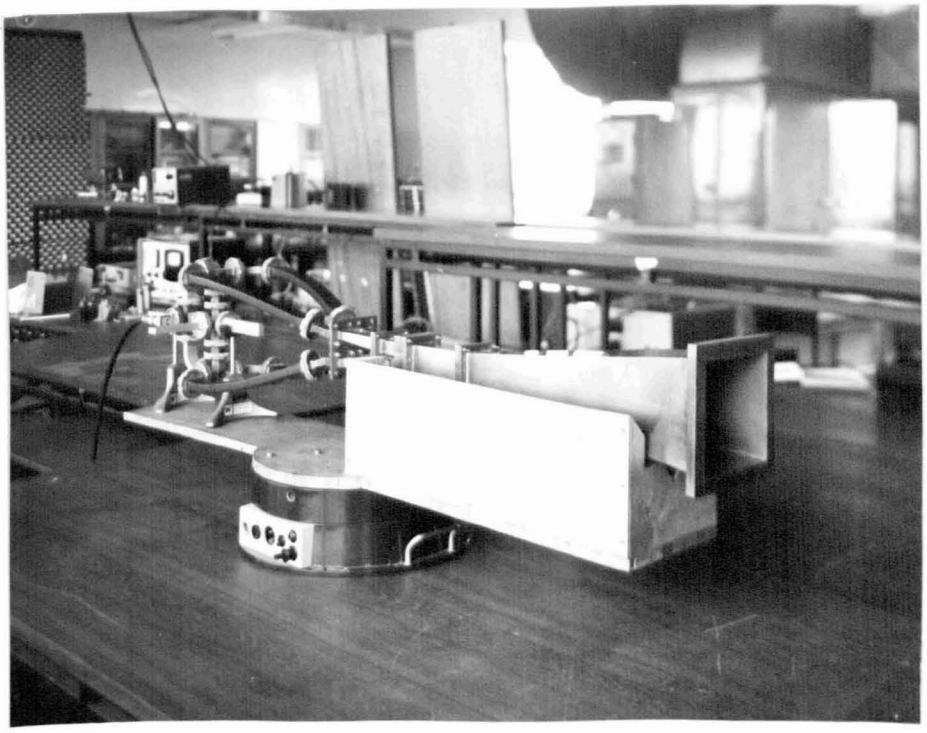

Fig. 7.2(d): Complete Feed and Comparator Assembly, with Support Structure and Turntable

number of separate component parts which are illustrated in figure 7.2(a). The flare and uniform section were made from 0.055" brass sheet. For structural rigidity, a ¼" flange was fitted to each end of the uniform section and to the narrow end of the flare, and a ½" flange to the end forming the radiating aperture. Originally, a uniform section having the calculated length of 5.79" was used, but some modification was later necessary so as to adjust the relative phases of modes in the aperture. The reasons for this will be explained in section 7.4. Figures 7.1 and 7.2 show the final version, with a basic uniform section length of 4.78", extendable to 5.34" by the addition of a 0.34" spacer and up to four 0.055" shims. The uniform section is followed by a ¼" spacer having four 0.746" square apertures, whose outer edges align with the inner surfaces of the uniform section walls, the junction of these components forming the mode-converting step.

To allow standard no. 16 waveguide to be used for input to the horn, a taper unit was constructed, having four symmetrically arranged waveguides tapering linearly from 0.746" x 0.746" to 0.9" x 0.4" internal dimensions. To ensure rigidity, a single ¼" brass flange was fitted at each end of the unit, that at the end nearest the mode-converter having its four square apertures arranged to match exactly those in the four aperture spacer. The other flange was made sufficiently large, and drilled in such a way, that no. 16 waveguides terminated in standard square flanges could be bolted on directly. As with the experimental box-horn (chapter 5), the length of the tapers was determined using the formulae given by Johnson [30],

which show that the V.S.W.R. for a correctly terminated taper depends only on the internal dimensions at the terminal planes, and the perpendicular distance between the planes. For the above dimensions, V.S.W.R. minima occur when this distance is a multiple of 0.957", and a value of 3.83" was found convenient. The theoretical V.S.W.R. for this taper is 1.010, so close to unity that the effect of the taper should be negligible.

For elevation difference operation, fairly high levels of power reflected from the mode-converter in the form of the cross-polarized H_{01} mode were expected. As this mode is below cut-off in no.16 waveguide at 9.5GHz, reflection back towards the junction can occur within the tapers, causing discrepancies between theoretical and actual mode generation at the step. It was therefore decided to eliminate the cross-polarized energy by interposing between taper and four-aperture spacer short lengths of square waveguide fitted with centrally positioned horizontal strips of resistive card, which theoretically do not affect H_{10} propagation, but cause the H_{01} mode to be highly attenuated. Propagation characteristics for such waveguides have been determined by Marcuvitz [4], and these indicate that, using 400Ω/□ resistive card, the attenuation of the H_{01} mode for the dimensions in question will be about 26dB. The cards were "fishtailed" to minimise reflections from the ends of the attenuator. Figure 7.2(b) shows the assembly of the cross-polarization attenuator with the mode-convertor components.

To ensure correct alignment of the various units, 3/16" diameter brass dowels were fitted at the junctions between flare and uniform

section and attenuator and taper, and at the mode-converter junction.

The monopulse comparator network is shown in figure 7.2(c), and schematically in figure 7.3. It consists basically of four hybrid Tees, T_1-T_4, interconnected in such a way that an input to the H or E arm of either T_1 or T_2 produces, at the ends of the through arms of T_3 and T_4, one of the four phase combinations given in table 6.1. In practice T_3 and T_4 were connected to the taper unit via H-plane bends, 12" lengths of flexible waveguide and short, angled, lengths of waveguide, the latter providing the required change from circular to square flanges and reducing the distortion of the flexible guides. Input to the network was from 50Ω coaxial cable via a coax. / waveguide transformer, unused input ports being terminated in matched loads.

7.3 The Antenna Test Range.

The experimental set-up used for radiation pattern measurements, shown in figure 7.4, is based on that described by Green [37]. The feed was used as the transmitting antenna, and, together with the comparator circuitry, was mounted on a turntable using a wooden support structure (see fig. 7.2(d)). The cradle for the horn itself had mounting positions for H, E and 45° plane pattern measurement. The transmitted signal was amplitude-modulated with a 1kHz square wave.

A superheterodyne receiving system was used because of its high selectivity and consequent good signal-to-noise performance. The

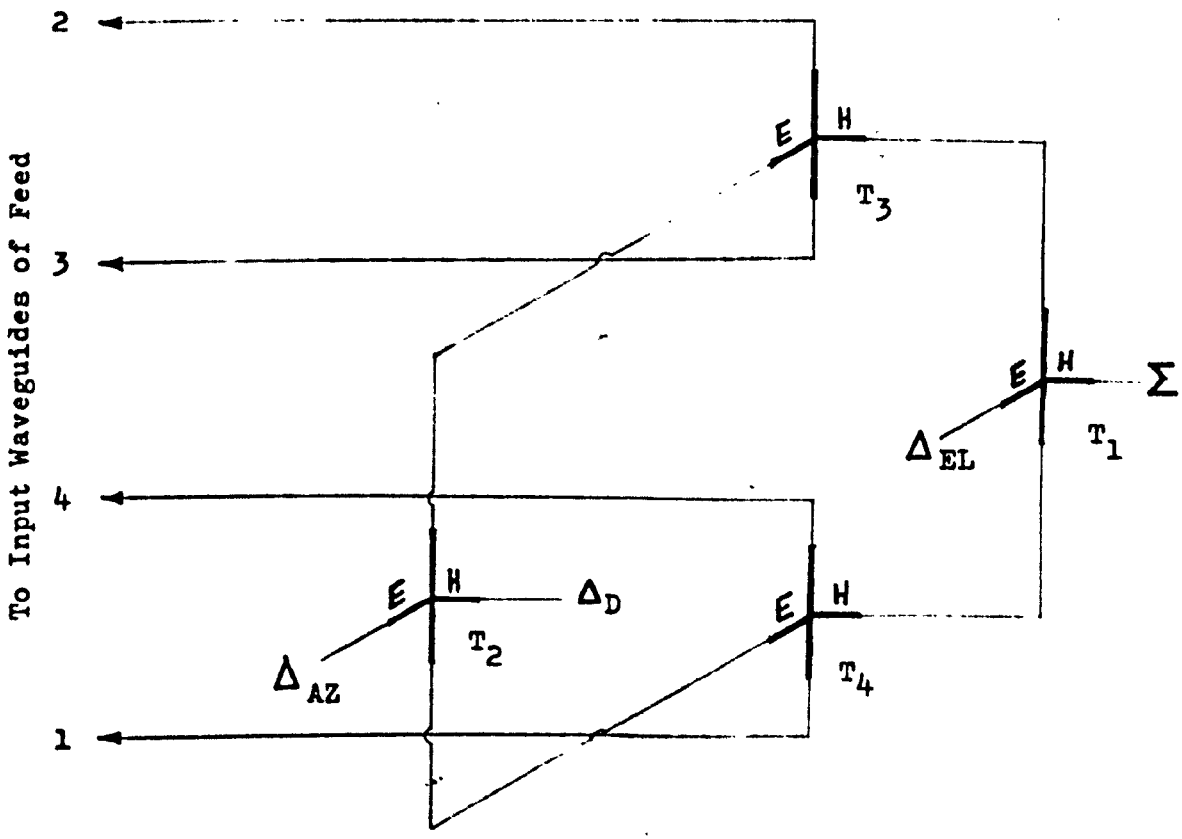

Fig. 7.3 : Basic Comparator Network

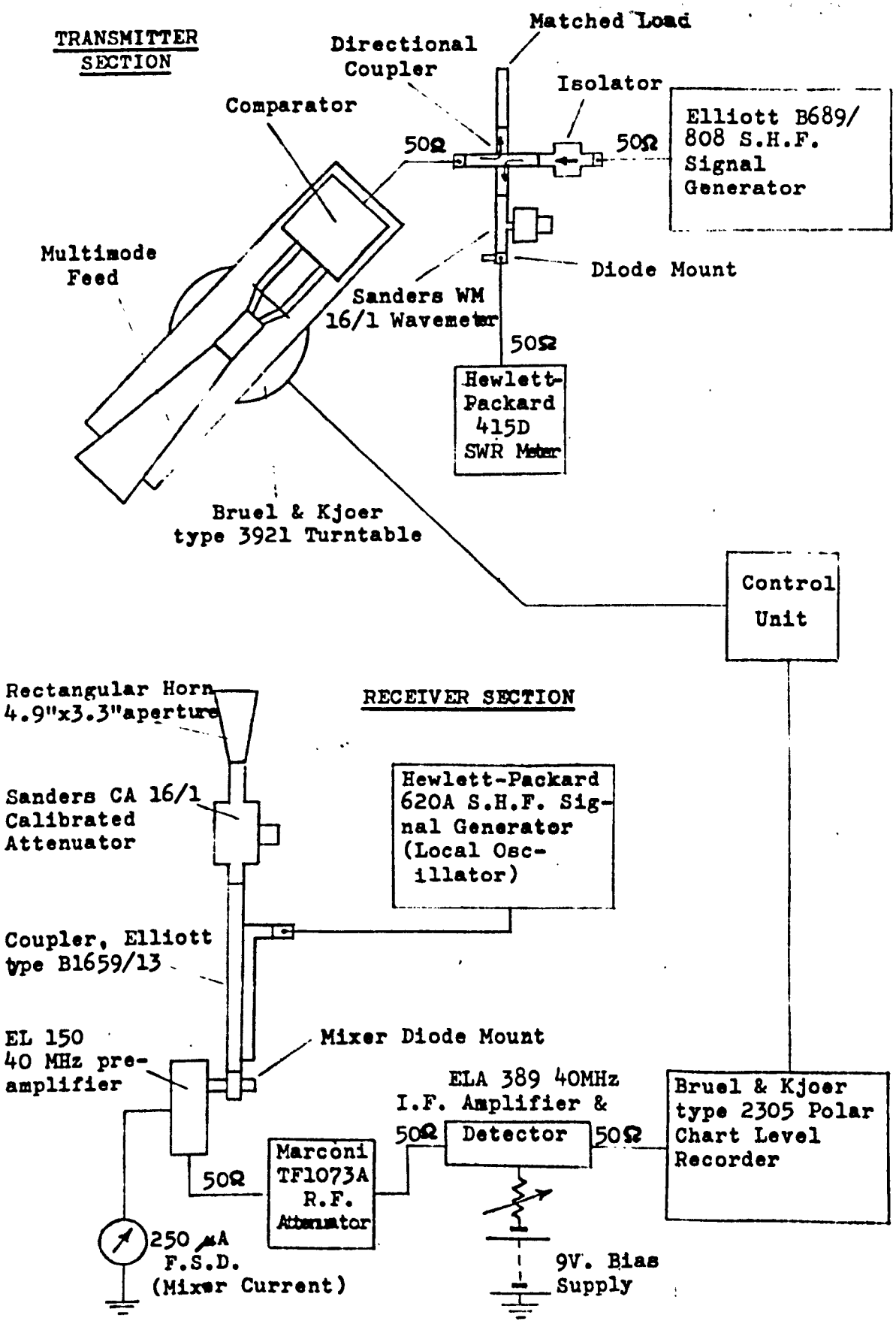

Fig. 7.4:Set-up for Radiation Pattern Measurement

diode mixer was followed by a 40 MHz I.F. amplifier chain terminating in a diode detector from which the audio signal was fed to a polar-chart level recorder. As it was not possible to obtain a linear response from the detector over the large range of signal strength required (about 32dB), calibrating points were plotted at 4dB intervals on each chart, a calibrated attenuator following the receiver horn being used for this purpose. The recorder chart was set to rotate in synchronism with the turntable, a complete rotation occuring in about 80 seconds. A control unit allowed remote operation of the turntable and recorder, and enabled the turntable to be reversed, for rapid re-setting to a required position. Reference 37 should be consulted for full details of this unit.

The separation of transmitting and receiving horns was about 12', compared with 4'4" as given by $2\frac{(2a')^2}{\lambda_0}$, the minimum separation for the predominance of the far-field pattern. The peak signal-to-noise ratio for sum-channel patterns with the 12' separation was at least 35dB, high enough for detailed measurements of sidelobes structures to be made.

As the experiments were performed in a laboratory, reflections from walls, floor, ceiling and nearby objects were possible causes of inaccuracy. To minimise such reflections, transmitting and receiving antennas were mounted at a height of about 5', approximately equidistant from floor and ceiling, and the whole set-up was kept to the centre of the room. A microwave absorbent screen measuring 6' x 6' was available, and this was placed in front of possible sources of reflection, but as no detectable change in measured

patterns occurred it was concluded that the reflections were too weak to be significant.

Ideally, the feed should have been rotated about an axis in the plane of the radiating aperture, but this was not possible because of the need to distribute correctly the load on the turntable. This meant that θ, the angular displacement of the receiving horn, measured at the feed aperture centre, was in general slightly larger than θ', that indicated by the recorder. Furthermore, the horn separation increased as the feed rotated away from the $\theta'=0$ axis, causing a reduction in received signal strength which could reach about 2dB for 90° rotation. However, these effects could be accurately calculated, and were taken into account when preparing theoretical patterns for comparison purposes.

The measured signal level was also affected by the receiving horn's radiation pattern, since the angle of the feed aperture centre, as seen from the receiving horn, varied with θ' up to a maximum of about 11° for θ' equal to 90°. Because of this it was found essential to align the horn correctly, with its axis in the $\theta'=0$ plane, otherwise asymmetries in the recorded patterns resulted. The dimensions of the horn aperture were such that H and E plane patterns were similar, and the reduction in signal strength in these planes for increasing θ' was calculated assuming the aperture field distribution to be that of the H_{10} rectangular waveguide mode. The results are shown in figure 7.5, together with curves of error due to varying horn separation and estimated total error. These curves should be consulted when comparing theoretical and measured patterns, since the errors are significant even for small values of θ'.

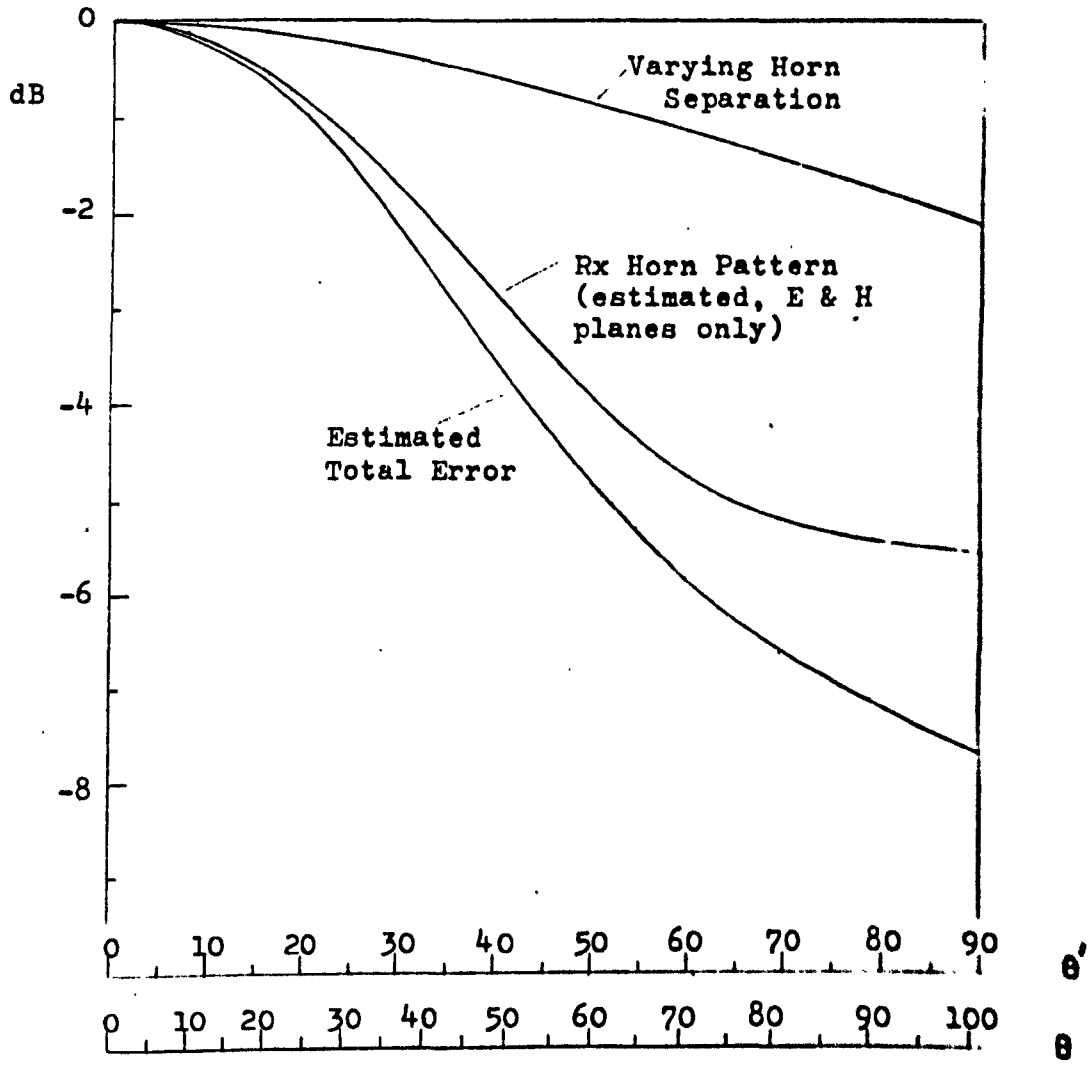

Fig. 7.5 : Errors in Measured Signal Strength for Practical Test Set-up

7.4 Theoretical and Experimental Patterns Compared.

In figures 7.6 - 7.14, measured radiation patterns for all three monopulse channels are shown, together with corresponding theoretical patterns calculated from the results of chapter 6. The latter were obtained by summing patterns, as given by Silver [29], for individual modes having in most cases the relative amplitudes and phases at the aperture given by tables 6.2 - 6.4. The theoretical patterns were modified to show signal strength as a function of measured angle θ' rather than actual angle θ, and were corrected to account for varying horn separation. Corrections for receiving horn main lobe taper were not made, however, as its effect was only approximately known.

7.4.1 Sum Channel.

For the sum channel, H, E and 45° plane patterns are of interest, and these are shown in figures 7.6, 7.7 and 7.8 respectively, for operation at 9.5 GHz.

As pointed out in chapter 6, the H-plane pattern should be that of the H_{10} mode alone for $a<0.75\lambda_o$, but the measured pattern (fig. 7.6(a)) shows evidence of over-moding since the level of the first sidelobes, corrected for reception pattern taper, is about -19½dB, compared with -23½ dB in theory, and the first nulls are not clearly defined. These effects are thought to be due to the presence of the H_{30} mode, which is only just below cut-off at the mode-converter when $a=0.74\lambda_o$ and may therefore still have a significant amplitude at the point where the flare becomes wide enough to support it. In the E-plane, on the other hand, multi-moding is intentionally intro-

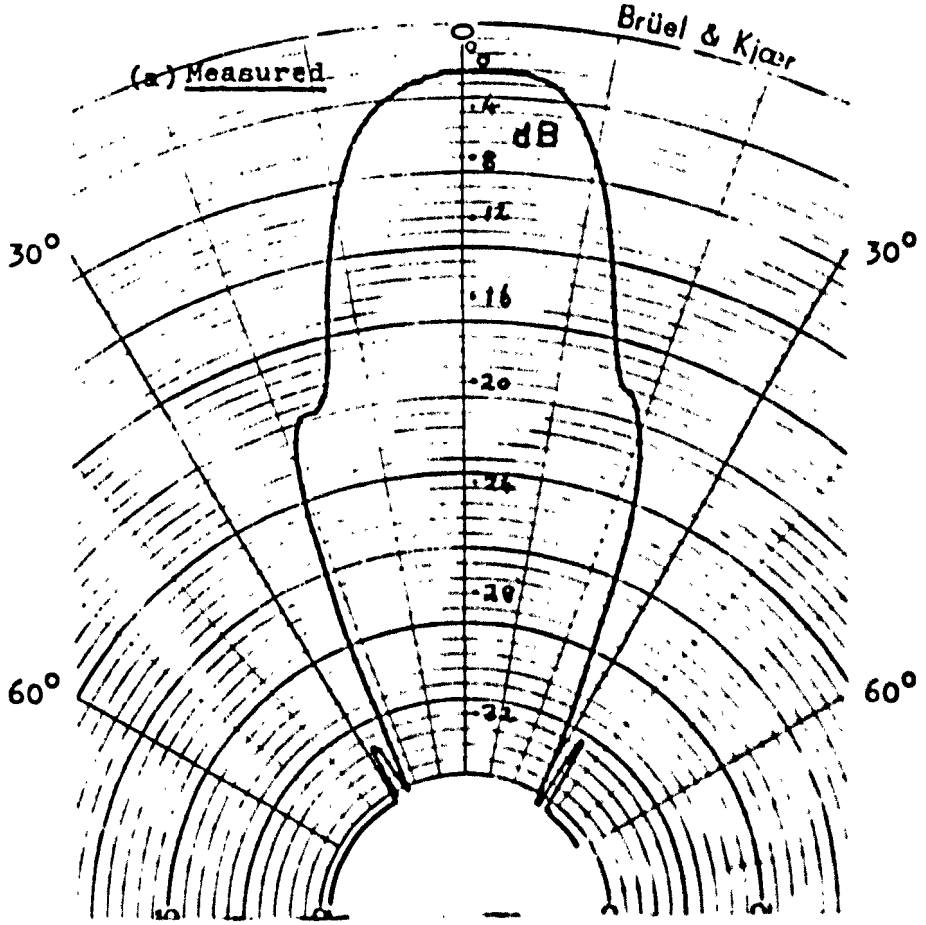

Fig. 7.6 :Sum-Channel Primary Patternn - H-Plane, 9.5GHz

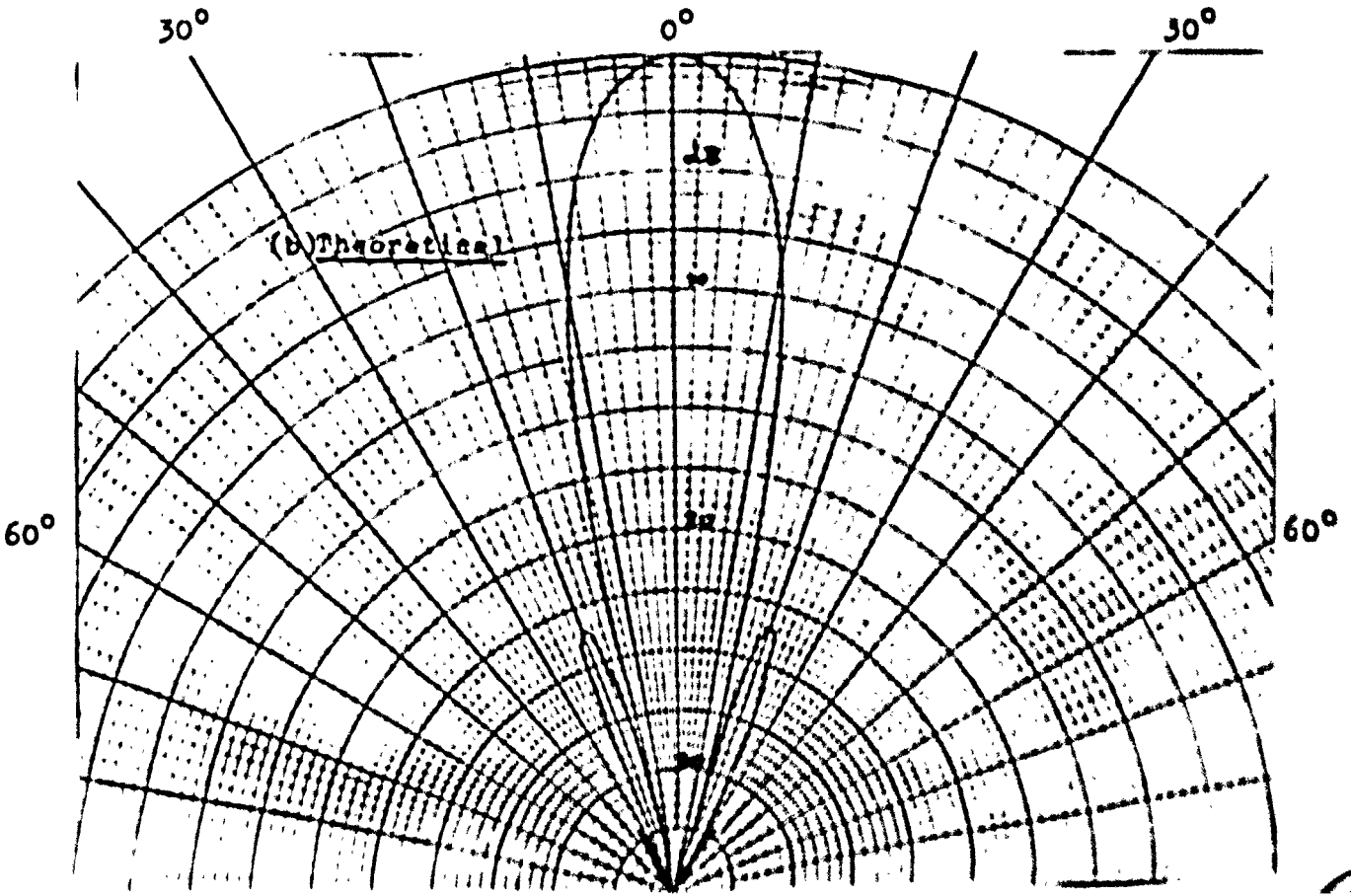

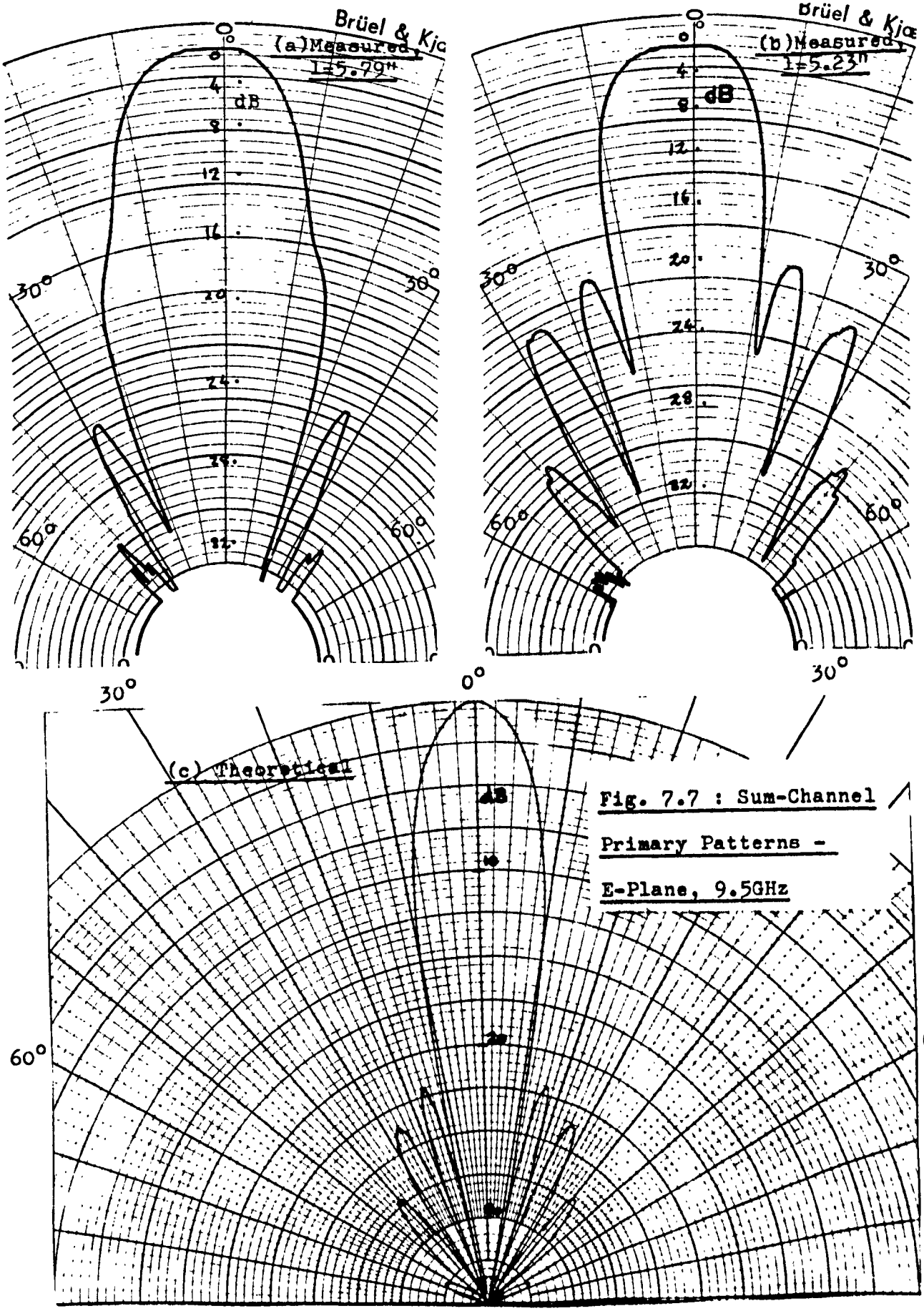

Fig. 7.7 : Sum-Channel Primary Patterns - E-Plane, 9.5GHz

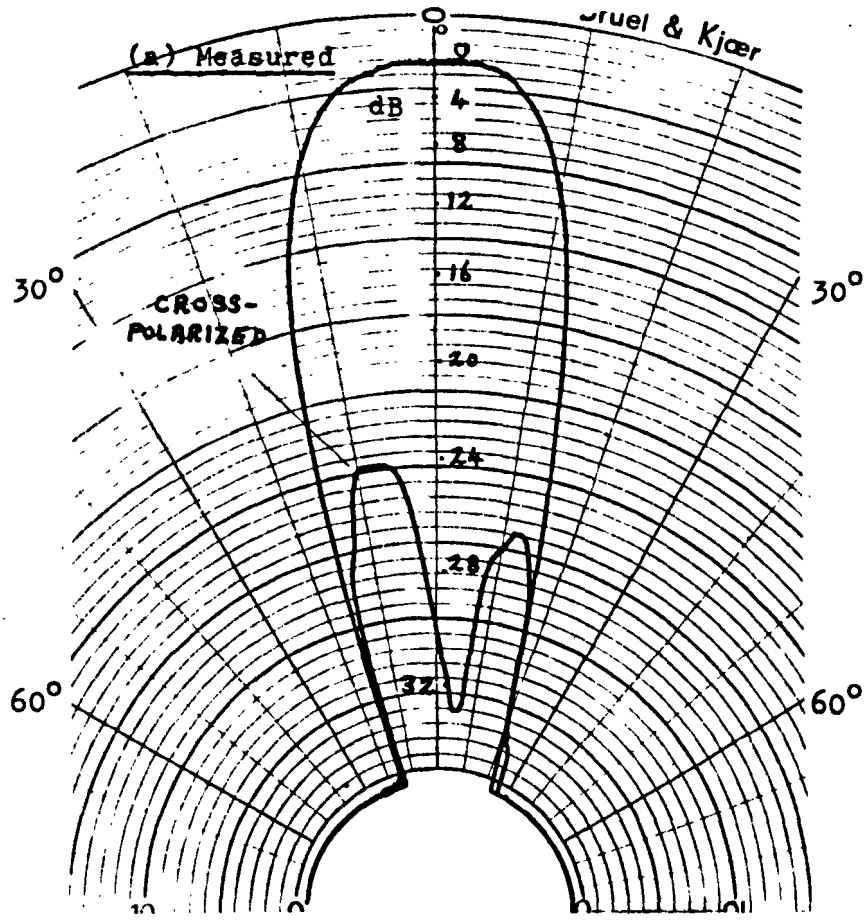

Fig. 7.8 : Sum-Channel Primary Patterns - 45°-Plane, 9.5GHz

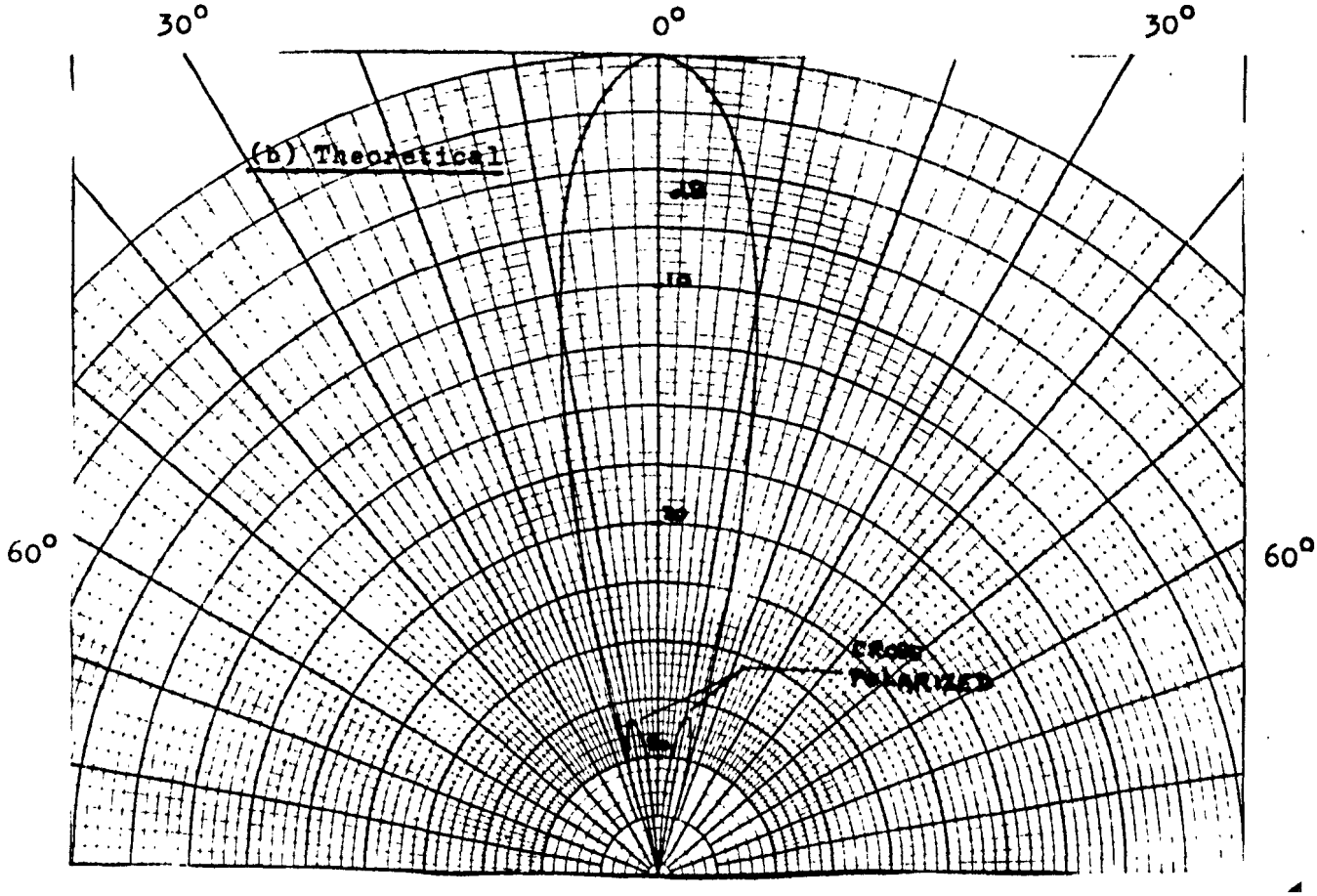

duced, and its effect can be seen in figure 7.7. The measured pattern obtained with a uniform section having the calculated length of 5.79" (fig. 7.7(a)) shows there to be a significant error in the relative phase of H_{10} and LSE_{12} modes at the aperture, causing the first sidelobes to appear as "shoulders" on the main lobe. However, after some experimentation with different values of uniform section length l, the pattern shown in figure 7.7(b) was obtained for l=5.23", with distinct first nulls indicating near-perfect phasing. With this value of l, the measured levels of the first three sidelobes, corrected for reception pattern taper, are approximately -19½, -21 and -26dB compared with -22, -23½ and -27dB as calculated, showing that the amplitude of the LSE_{12} hybrid relative to that of the H_{10} mode at the aperture is slightly less than predicted, although the improvement over the single-mode E-plane pattern is still very considerable. It can be seen that the theoretical and measured angles of nulls and sidelobes are in excellent agreement.

The phase error with the original uniform section is thought to be largely due to shortcomings in the "quasi-uniform" method for calculating phase-shifts in the flare. The amount of reduction in l required shows this error to have been about 46°, of the same order of magnitude as that which Nagelberg [24] showed would result if the quasi-uniform method were used to calculate phase-shift between H_{11} and E_{11} modes in a conical horn of similar flare-angle. It seems, then, that accurate evaluation of the Hankel Function arguments is necessary for a satisfactory phase-shift calculation.

The theoretical and experimental patterns for the normally-

polarized component in the 45° plane (fig. 7.8) agree well in respect of mainlobe beamwidth and the absence of sidelobes above -35dB. The measured cross-polarized pattern shows evidence of spurious H_{11} and E_{11} mode generation due to errors in the phasing of the four input waveguides, but when this is allowed for the agreement with theory is satisfactory.

Principal-plane patterns were also measured at 10.41 GHz, this being equivalent to the 8.0GHz transmission frequency for a 7.3GHz feed design. As can be seen in figures 7.9 and 7.10, agreement with theory is good, differences in sidelobe levels being in most cases attributable to reception pattern taper. The narrow main lobe and high sidelobes at this frequency emphasise the narrow bandwidth of the $a=0.74\lambda_o$ feed, which was predicted in figure 6.23. The phases, relative to the H_{10} mode, of the H_{30} mode, which affects the H-plane pattern (fig. 7.9), and the H_{12} and E_{12} modes, which affect the E-plane pattern (fig. 7.10), are here such as to cause a reduction in beamwidth and an increase in sidelobe level, the opposite of what is required for good illumination of the dish.

7.4.2 Azimuth Difference Channel

In this case none of the modes involved radiates a field component in the E-plane, so only H-plane (figure 7.11) and 45°-plane (figure 7.12) patterns are considered.

In the H-plane, where theoretically only the H_{20} mode contributes, measured angles of sidelobes agree well with theory, as does the level of the second sidelobes, but there is evidence of a higher-

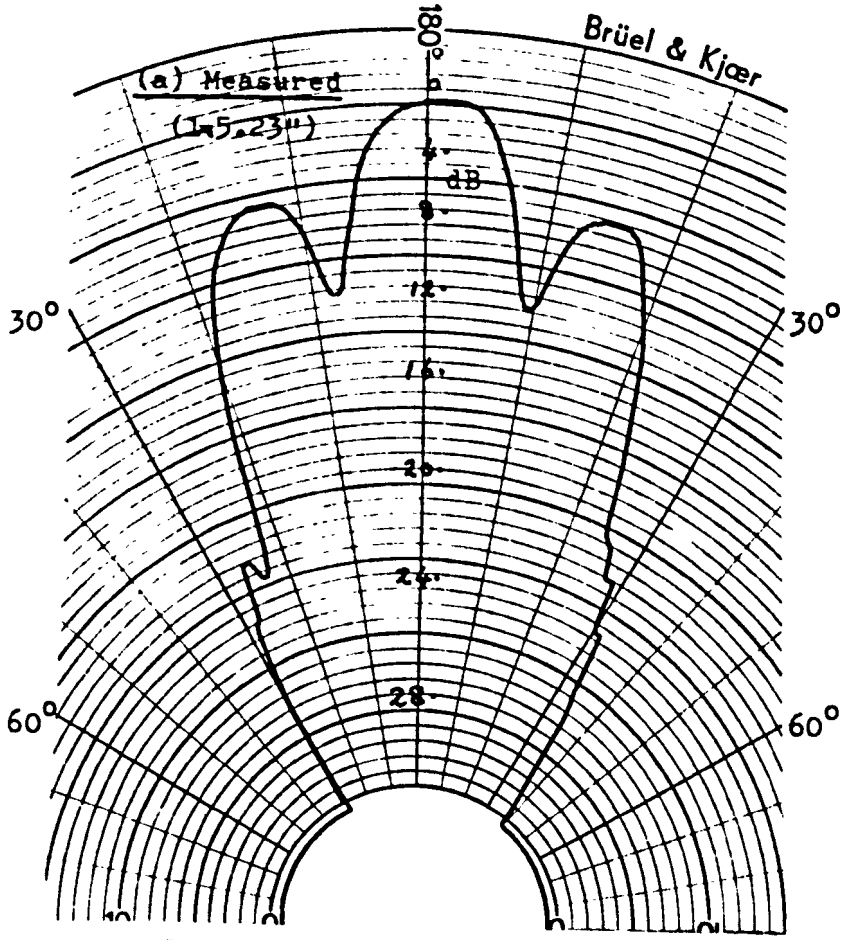

Fig. 7.9: Sum-Channel Primary Patterns - H-Plane, 10.41 GHz

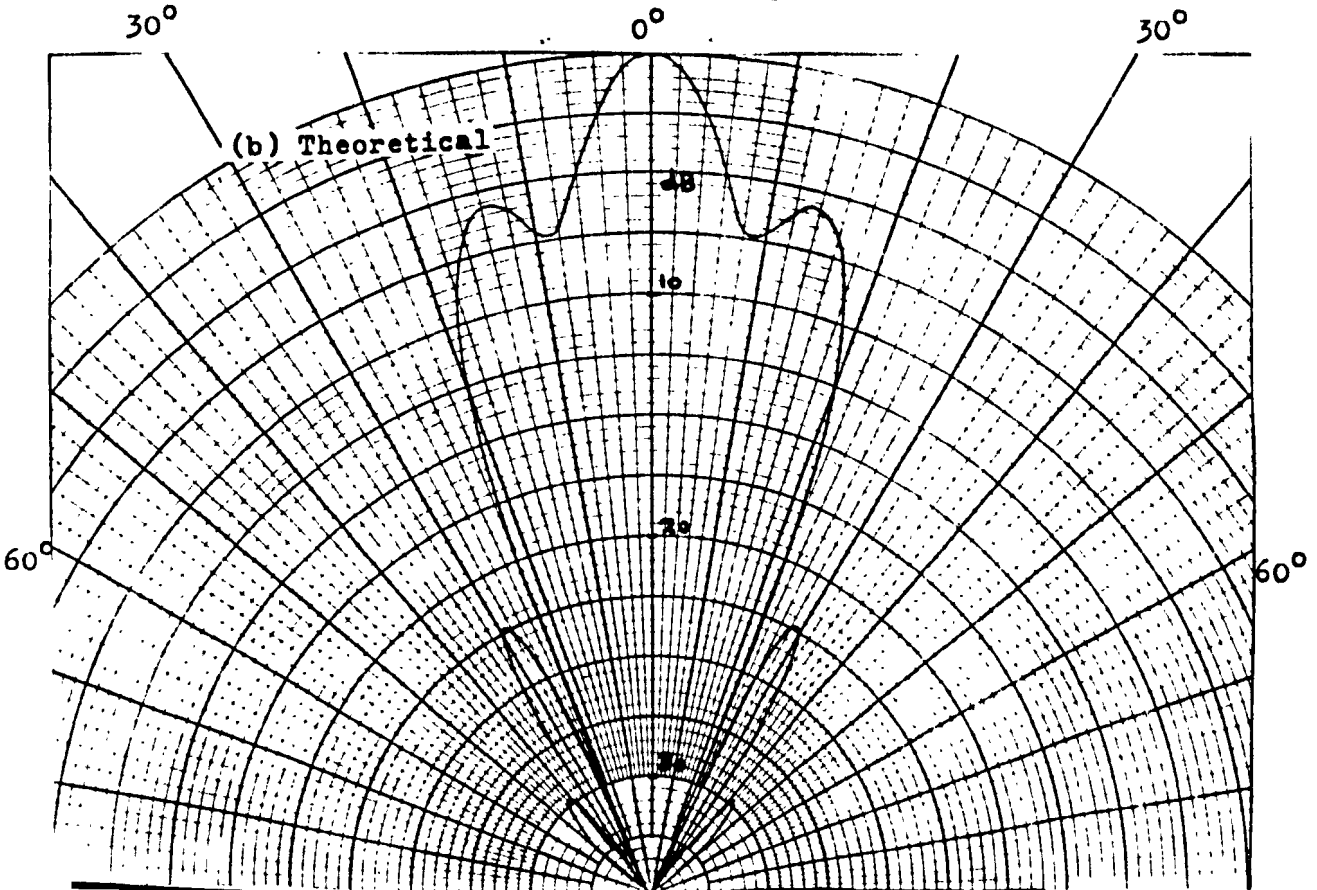

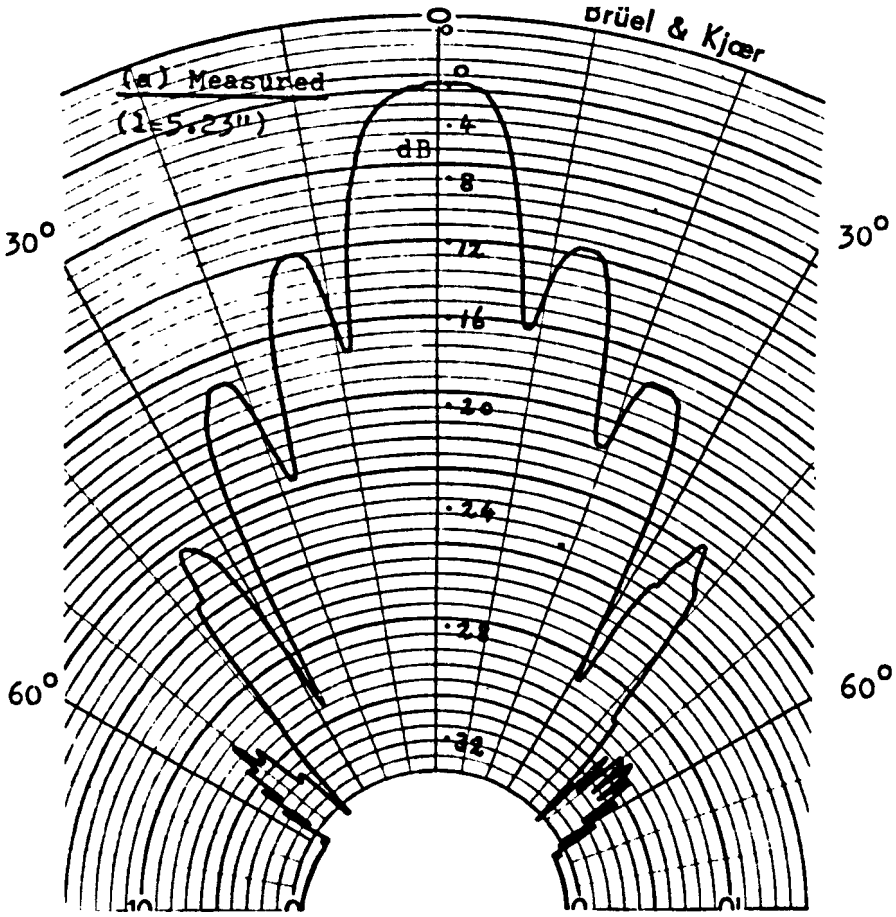

Fig. 7.10: Sum-Channel Primary Patterns - E-Plane, 10.41 GHz

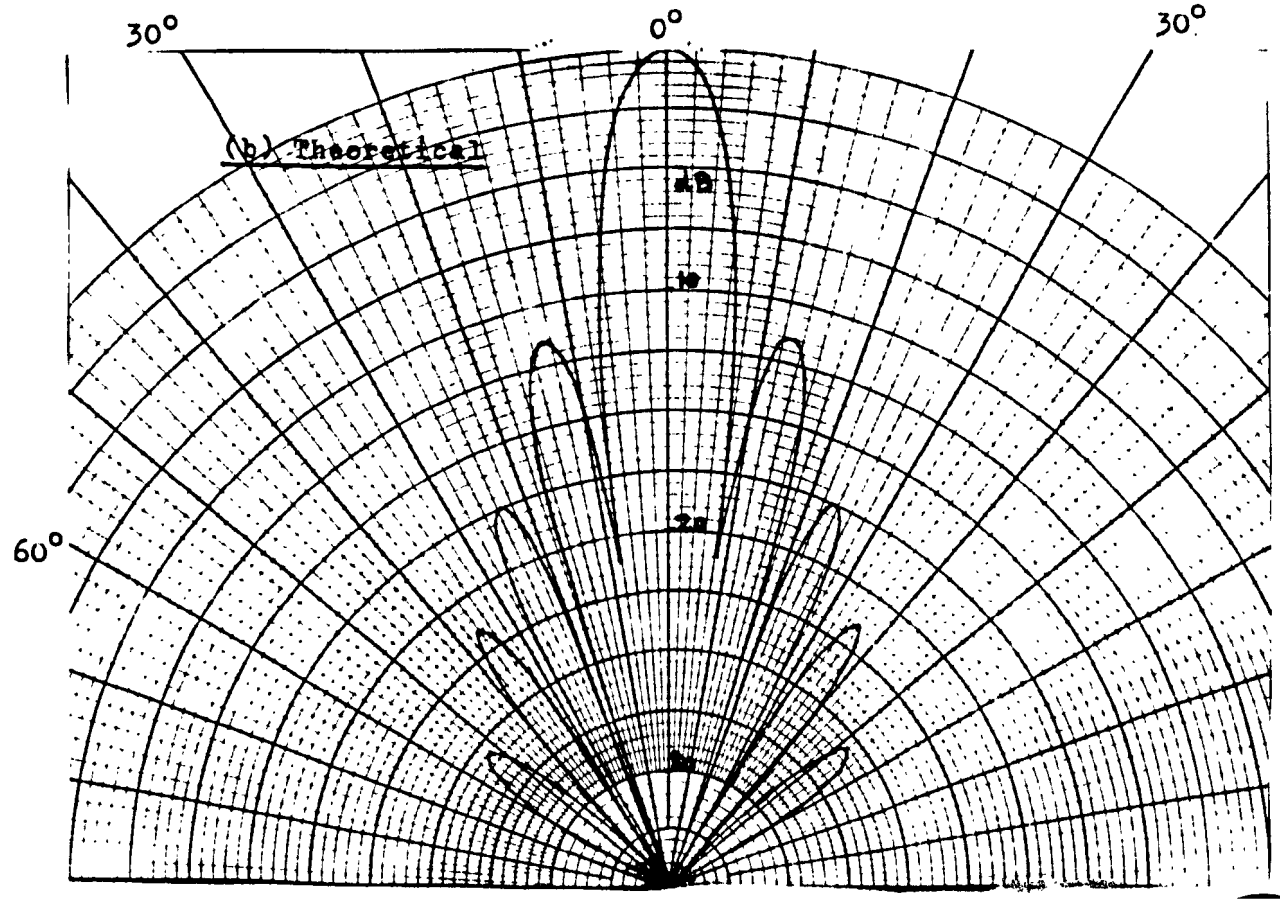

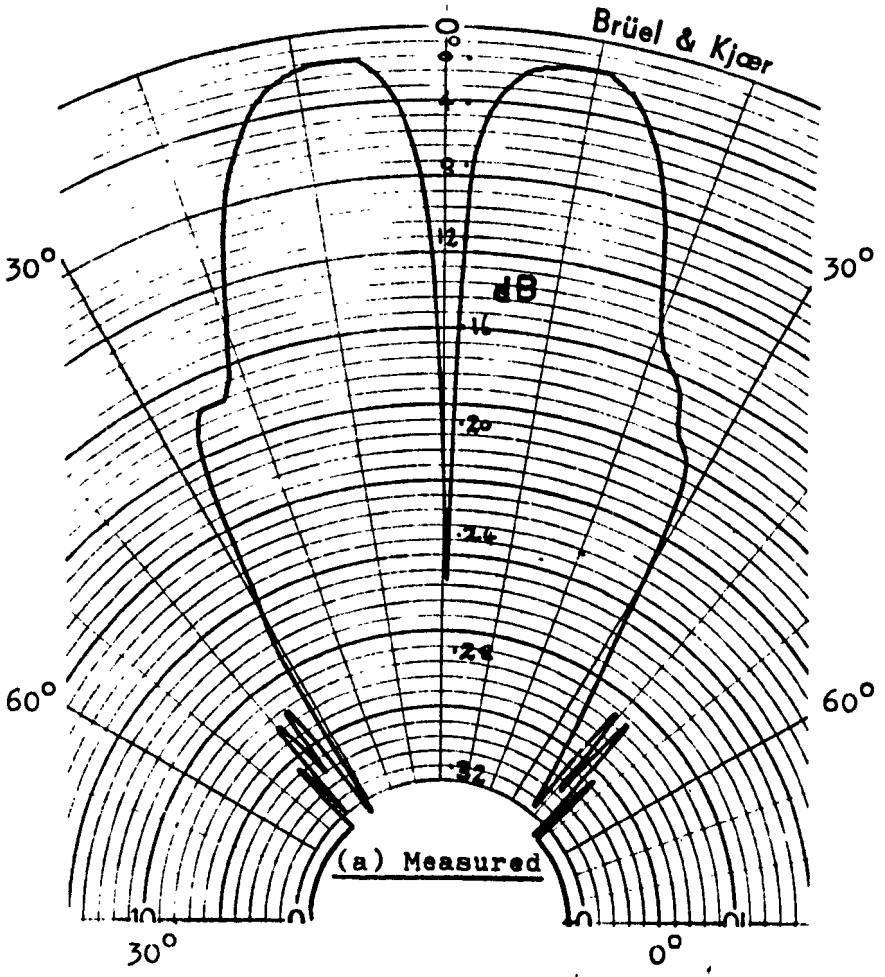

Fig. 7.11: Azimuth Difference Primary Patterns - H-Plane, 9.5 GHz

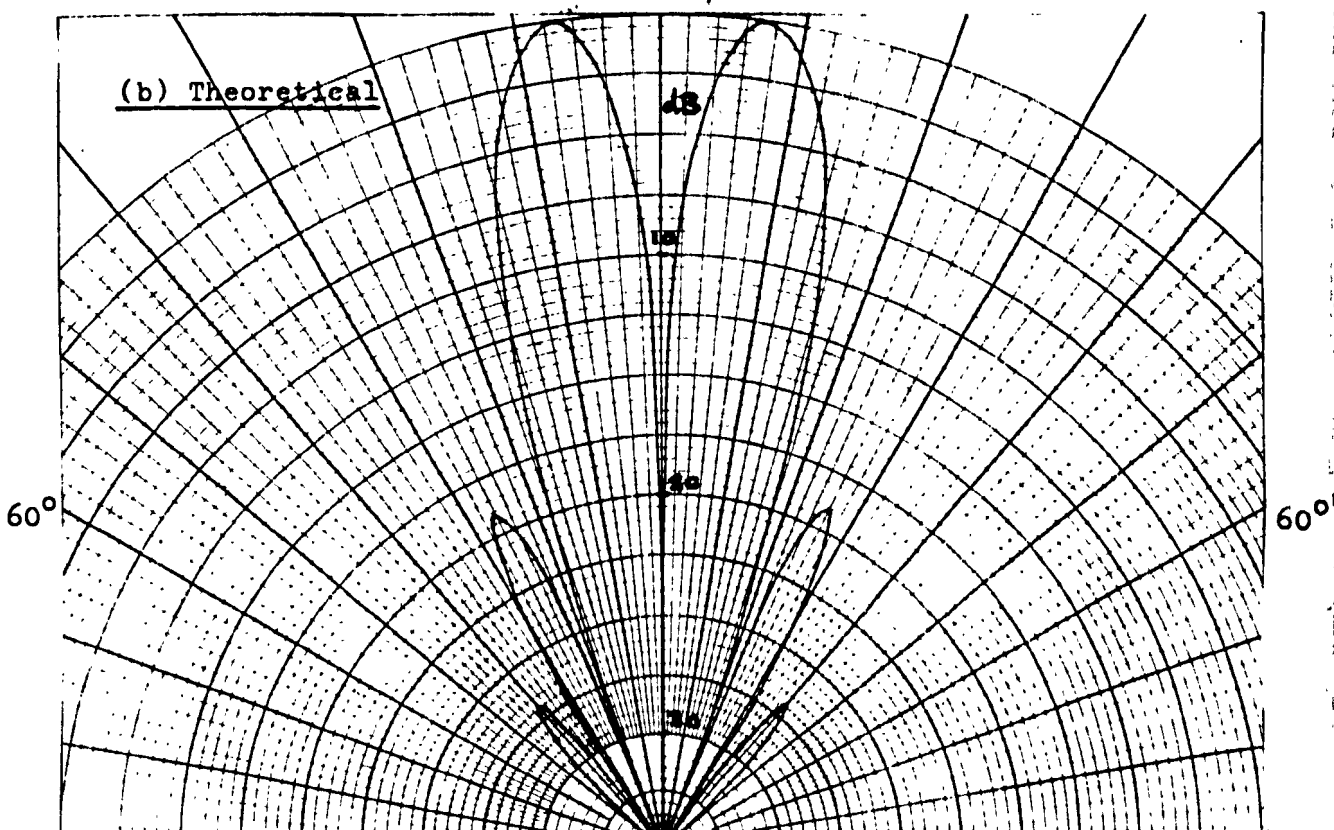

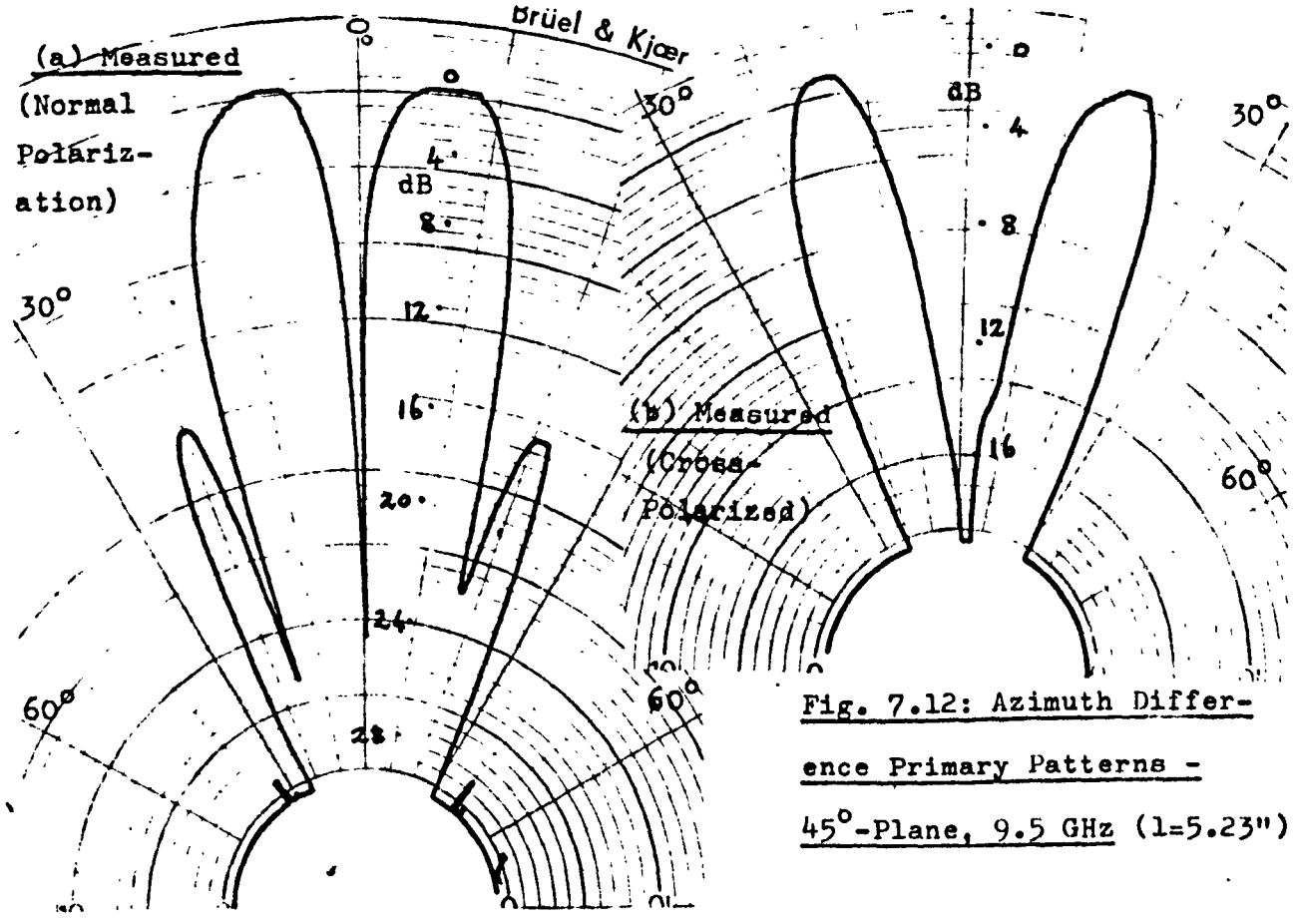

Fig. 7.12: Azimuth Difference Primary Patterns - 45°-Plane, 9.5 GHz (l=5.23")

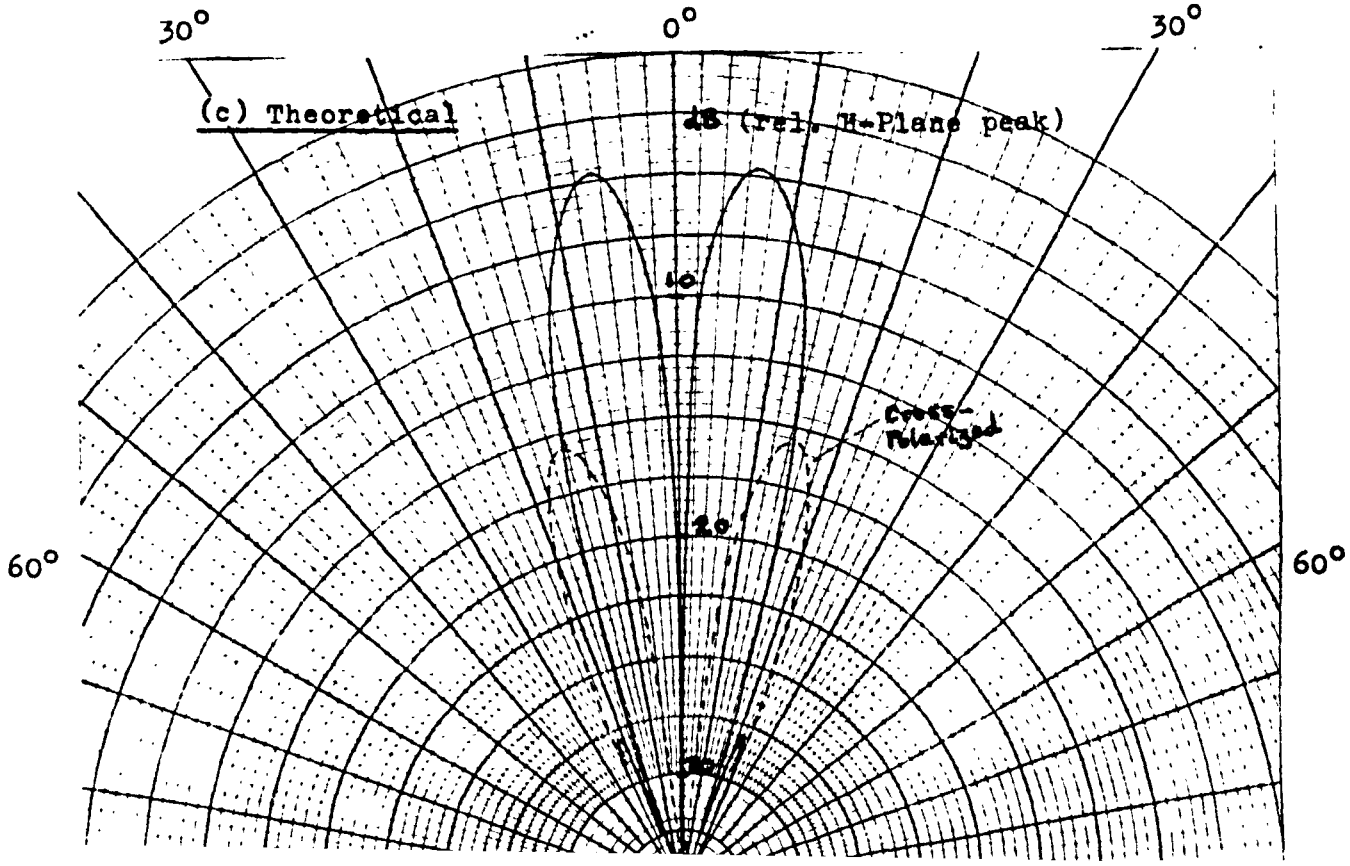

order mode, probably the H_{40}, causing "filling-in" of the first nulls and an increase of about 3dB in the first sidelobe level. The on-axis null is clearly defined, its finite depth being due to spurious sum mode excitation caused by input waveguide phase errors, and the limited response of the recorder pen.

In the 45°-plane the effect of the additional H_{22} and E_{22} modes can be examined. As with the sum channel, the use of the original uniform section did not produce the expected sidelobe structure, but the reduction to 5.23" leads to better agreement with theory, although the measured sidelobe level for the normally-polarized component (fig. 7.12(a)) exceeds the theoretical level by about 7dB, indicating that phasing errors may still be present.

Measurements of the peak 45°-plane normally-polarized energy level relative to the H-plane peak were made, and a value of -5.9 $\pm$0.3dB was obtained, although the accuracy of this is doubtful as the time required to change from 45°-plane to H-plane measurement was sufficient for significant variations in radiated power and receiver gain to occur. The theoretical level is -4.8dB.

The 45°-plane cross polarized pattern (fig. 7.12(b)) should be due entirely to the H_{22} and E_{22} modes, and its level therefore provides a check on their amplitudes relative to one another, and to the H_{20} mode in the aperture. The shape of this pattern clearly agrees well with theory and its measured level of -9.75 $\pm$0.42dB relative to the peak normally-polarized level compares favourably with the predicted value of -10.9dB.

7.4.3 Elevation Difference Channel.

It can be seen in figure 7.13 that there are no major discrepancies between measured and theoretical E-plane patterns for this channel. Angles of nulls and sidelobes are as predicted, and after correction for reception pattern taper, the sidelobe levels agree to within about 2dB. Here again the on-axis null is clearly shown, but other nulls are not as deep as expected, an effect which is also evident in some of the patterns for other channels, and which is probably due to a phase variation across the aperture caused by the sphericity of the wavefront.

Agreement between theory and experiment in the 45°-plane (fig. 7.14) is also good, and the predicted peak level of -2.8dB relative to the E -plane peak is confirmed experimentally.

The level of cross-polarized radiation in the H-plane shows the deviation from unity of the relative amplitudes of H_{11} and E_{11} modes in the aperture. The measured level was -6.5±1.0dB relative to the normally-polarized E-plane pattern, which is in satisfactory agreement with the calculated value of -5.72dB. With the cross-polarization attenuator removed, the relative level was only -2dB, showing the importance of this unit for meaningful measurements.

7.5 Problems of V.S.W.R. Measurement.

It was hoped that calculated values of input V.S.W.R. for the multimode feed could be verified experimentally, but reflections from comparator components were found to be of the same order of magnitude as those from the mode converter, making measurements at the compara-

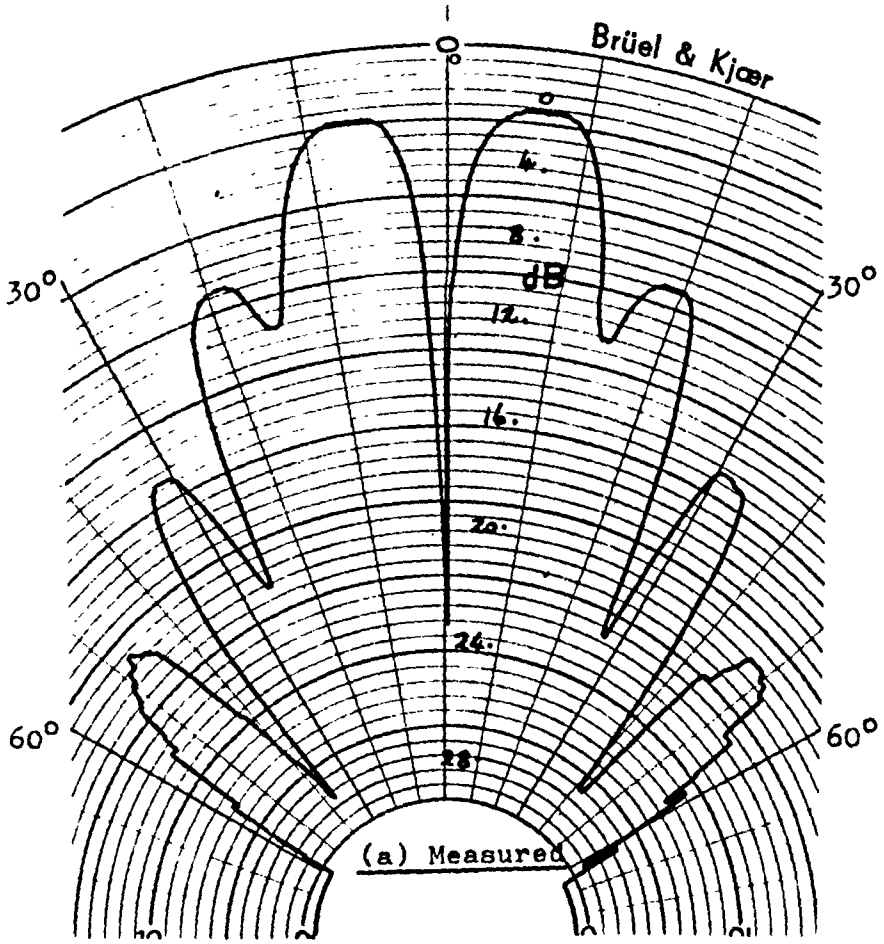

Fig. 7.13: Elevation Difference Primary Patterns - E-Plane, 9.5 GHz

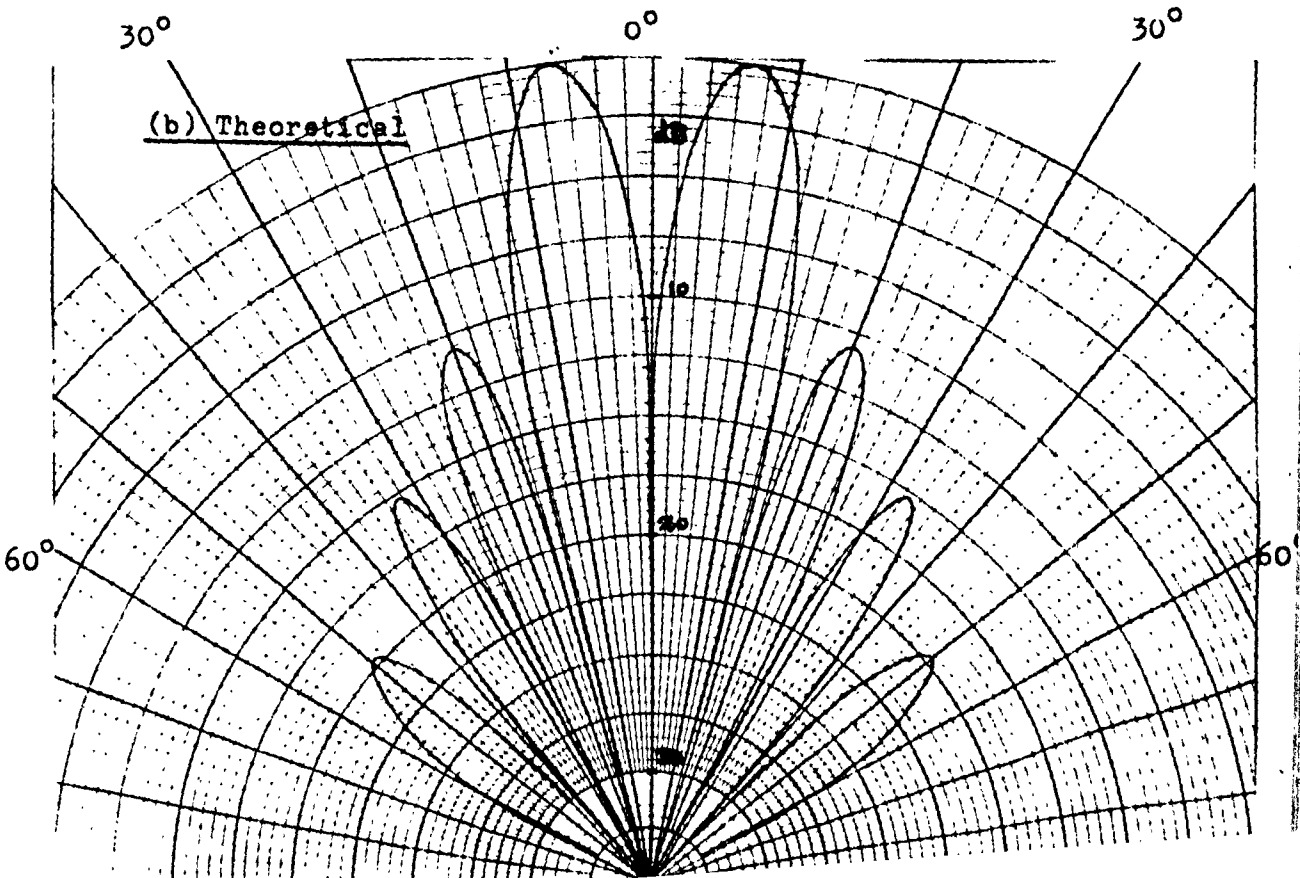

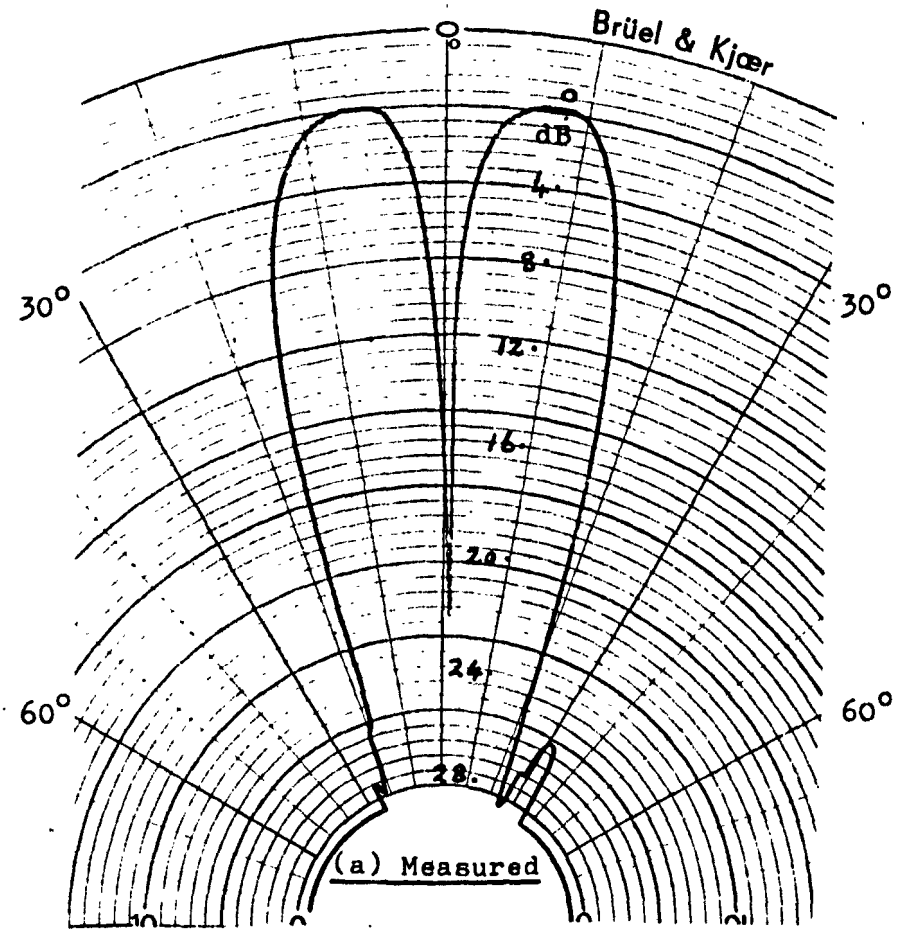

Fig. 7.14: Elevation Difference Primary Patterns - 45°-Plane, 9.5 GHz

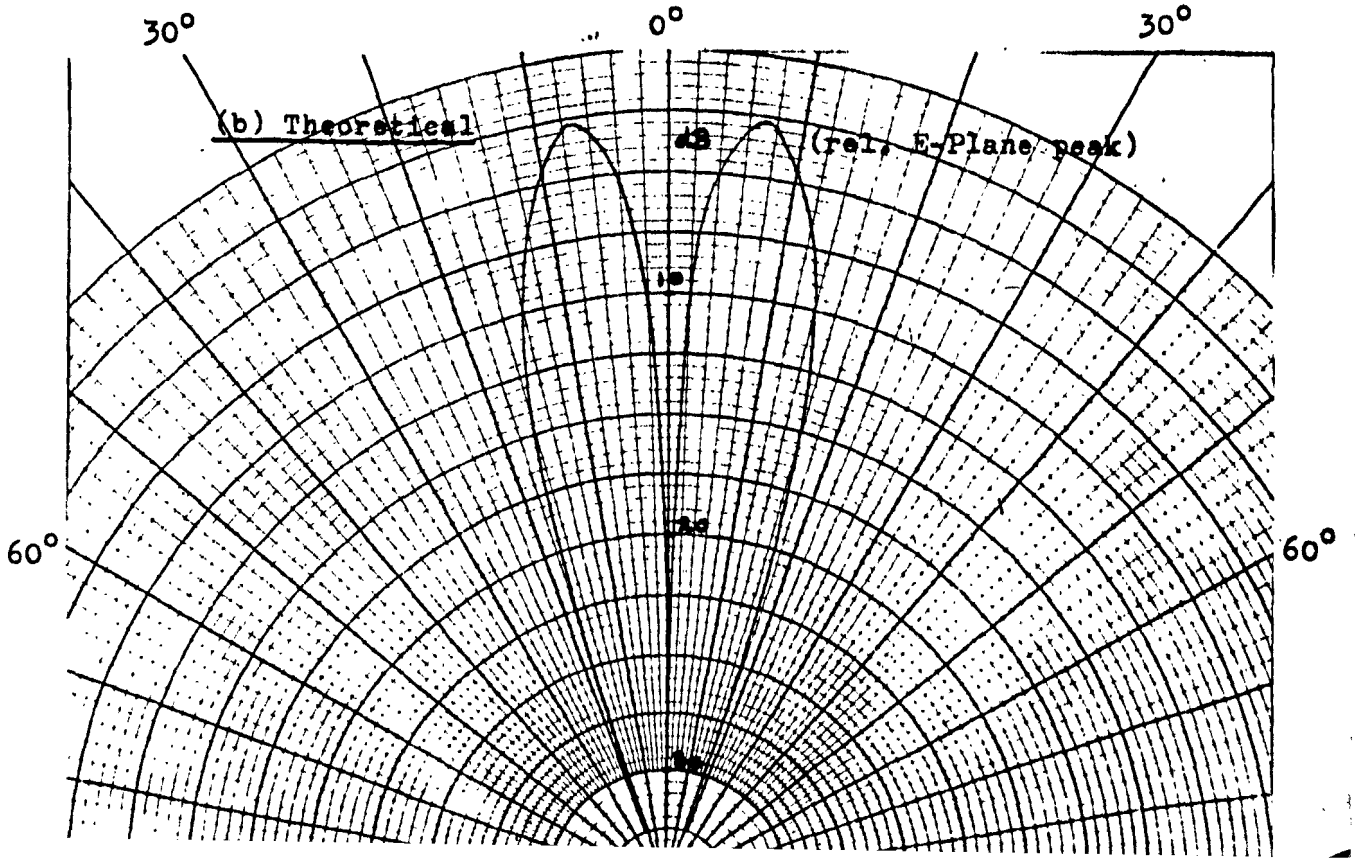

tor input ports meaningless. Measurement of V.S.W.R. in one of the four input waveguides was not attempted because of the difficulty of providing compensation in the other three guides for the presence of the slotted line, so as to preserve the phase balance.

7.6 Comparison with the Modified SCAT Feed.

As mentioned in the introduction, the research into multimode feed design was instigated by the results of modifications to the SCAT feed [19], basically a cluster of four quite sharply flared square horns intended for use at 7.275 GHz. It was found that by adding a 4½" parallel-sided extension to each horn a significantly greater sum-channel efficiency was obtained than with the theoretical uniform x double-cosine aperture distribution. The improvement is thought to be due to the excitation of higher modes, particularly the H_{30}, at the junction between flare and extension, the length of the latter being such as to phase H_{30} and H_{10} modes at the aperture to create a more nearly uniform H-plane distribution.

Measured primary patterns for the modified SCAT feed were available, and principal features of these are summarized in table 7.1, together with corresponding results for the $a=0.74\lambda_o$ multimode feed.

Channel	Property	SCAT feed	Multimode Feed
Σ	H-Plane /E-Plane 10dB beamwidth ratio	1.07	1.20
	Peak H-Plane Sidelobe level	-7dB	-19½dB
	Peak E-Plane Sidelobe level	-10½dB	-19½dB
Δ AZ	H-Plane/Average Σ 10dB beamwidth ratio	2.14	1.87
	Peak H-Plane Sidelobe level	-16dB	-16½dB
Δ EL	E-Plane/Average Σ 10dB beamwidth ratio	1.96	1.40
	Peak E-Plane Sidelobe level	-4½dB	-9dB

TABLE 7.1

It is clear that the more nearly optimum aperture distributions of the multimode feed lead to superior radiation characteristics. In all cases the sidelobe level is lower than with the SCAT feed, for the sum channel by at least 9dB. Moreover, the ratios of difference to sum channel beamwidth are smaller with the multimode feed, showing that simultaneous optimisation of the three channels can be more nearly achieved. One slight advantage of the modified SCAT feed, however, is that the sum-channel main lobe is almost circularly symmetric.

Although no figures are available, it is likely that the modified SCAT feed has a considerably greater bandwidth and lower input mismatch than the multimode feed, and this may make it preferable for some applications.

7.7 Discussion.

After correction of phasing errors the theoretical and experimental patterns presented in this chapter agree sufficiently well to confirm the accuracy of the multimode feed mode-converter solution. Such discrepancies as there are seem to be largely due to mode-conversion at the junction between flare and uniform section, to the generation of unwanted higher modes in the flare and to the spherical aperture wavefront, but the combined effect of these factors is clearly too minor to affect the secondary characteristics significantly. Moreover, the measured levels of cross-polarized energy, particularly for the elevation difference channel, confirm the assumption that the power associated with individual H_{mn} and E_{mn} modes during passage through the horn remains constant, rather than that associated with the equivalent LSE_{mn} and cross-polarized LSE_{nm} modes.

In conclusion, it is felt that the experimental results show the design technique of chapter 6 to be adequate except in the prediction of horn length for correct phasing, a more rigorous solution for the field structure in a pyramidal horn being required for satisfactory accuracy.

CHAPTER VIII GENERAL CONCLUSIONS AND SUGGESTIONS FOR FUTURE WORK

8.1 On the Computational Method for Solving Waveguide Discontinuity Problems

It has been shown that the computational method can be applied to a wide range of both transverse and longitudinal discontinuities, and its accuracy has been confirmed by comparing results with those obtained by other methods in some special cases. The most important innovation has been in the computational treatment of discontinuities involving thin diaphragms, although a considerable amount still remains to be done in this field. For example, although the "breakpoint" technique for selecting optimum ratios of modes and aperture functions has been found satisfactory for certain geometries, a general method has yet to be developed. As suggested in section 2.5, a study of the effect of these ratios on the degree to which the edge condition is satisfied may be the best approach to this problem. Future work should also include the analysis of irises whose aperture geometries differ from those of the waveguide cross-section, since this would enable a general method for calculating the mode/aperture-function ratio to be tested. Such irises might include ones with apertures of irregular shape, where the choice of aperture functions is not straightforward.

A longitudinal discontinuity problem requiring further consideration is that of the partially dielectric-filled rectangular waveguide containing thin conducting strips, dispersion characteristics for which should be calculated using the method presented in chapter 4.

A computer program has been written at Queen Mary College, London, for this purpose, but this is not operational at the time of writing. Another longitudinal discontinuity worth considering is mentioned in section 4.1, namely a radiating slot in a thin-walled circular waveguide, results for which could be compared with Clarricoats and Slinn's values for the thick-walled case [12].

8.2 On the Design of Multimode Horns and Satellite Communication Antennas.

The research described in chapters 5,6 and 7 has shown that the version of the computational method applicable to step discontinuities is a powerful tool in the design of multimode antennas, permitting accurate calculation of modal amplitudes and phases at mode-converting junctions. For the monopulse feed, however, the method for referring such amplitudes and phases to the aperture is less satisfactory, and it is here that the existing design technique has most need of improvement. Accurate evaluation of the Hankel Function arguments, mentioned in section 6.6.1, should allow the phases of modes in the horn aperture to be adequately predicted, but an entirely satisfactory treatment would require a closed-form solution to Maxwell's equations for the pyramidal horn. The difficulties caused by the awkward boundary conditions could to some extent be overcome by considering the quasi-pyramidal structure bounded by the planes $\phi = \pm \phi_0$ and the conical surfaces $\theta = \frac{\pi}{2} \pm \theta_0$, which is not significantly different from an actual pyramid for small flare angles.

The structure of the monopulse feed treated in this thesis was

never regarded as the optimum, and there are several modifications which might be made to improve performance. In particular, increasing the excitation of the LSE_{12} mode relative to the H_{10} would lead to higher sum gain and greater compatibility of sum and difference primary beamwidths. The double-step exciter has been suggested in this connection, and the preliminary results of section 6.5.3 have shown that this merits further investigation. Another possibility which does not involve such severe bandwidth restrictions is to reduce the size of the input waveguides, and thus increase the step area, by loading them with dielectric or with a symmetric arrangement of longitudinal ridges. The fitting of such ridges in the horn itself might also be useful as this could alter the guide wavelengths in such a way that sum and circularly-polarized difference-channel phasing requirements could be simultaneously satisfied.

The primary main lobe taper sets an upper limit to the secondary sum-channel gain factor obtainable with the type of feed-reflector system treated in this thesis, and it is worth considering how this limitation can be overcome. A synthesis technique in which the focal-plane field distributions resulting from the incidence of plane waves on the main reflector are approximately matched by series of waveguide modes in the feed aperture is one possibility, but the problems of exciting more than two modes per channel with the required amplitudes and phases over a useful band-width are considerable. A better method is to modify the main and sub-reflector profiles so as to increase the illumination efficiency for a given feed pattern without creating phase errors, in the manner described

by Williams [38]. Computation has shown that a sum-channel illumination efficiency of 97.6% could be obtained if the $a=0.74\lambda_o$ multimode feed were used in such a system. However, the effect of such modifications on the difference-channel characteristics is not known, and could be detrimental.

The main drawback of the multimode monopulse feed for many applications is its very limited bandwidth, but recent work on the design of Scalar Feeds indicates how this might be overcome. Scalar Feeds have horn flares fitted with transverse corrugations of such a depth that electric and magnetic field boundary conditions at a wall are similar, so that modes of the balanced hybrid type can propagate. Such modes have similar principal-plane field distributions, and in a Scalar horn of square cross-section the dominant EH_{11} mode produces an aperture distribution resembling that due to an ideal H_{10}/LSE_{12} combination in the multimode horn, but the need to phase two modes is eliminated and the bandwidth is consequently much greater. Early work on Scalar Feeds, for example that of Simmons and Kay [39], was concerned with corrugated conical horns, which have subsequently been theoretically analysed by Clarricoats and Saha [40] and Clarricoats [41] for narrow and wide-angle cases respectively. However, Bryant [42] has recently determined the nature of modes, including those which could be used for tracking, in corrugated square waveguide and this shows that the design of a broadband monopulse feed similar in structure to the multi-mode feed, but with a corrugated flare, should be a practical proposition. The throat discontinuity would be amenable to solution by the computational method, although there would

probably be little flexibility in its design because of the need to prevent excitation of higher modes and surface waves.

A satellite communication antenna using a Scalar monopulse feed to illuminate a Williams-modified reflector system should combine excellent sum-channel spillover and illumination efficiencies with broad bandwidth (at least 30%) and adequate tracking ability. It is therefore suggested that future work should be concerned with the design of such an antenna.

REFERENCES

1. R.E. Collin: "Field Theory of Guided Waves" (McGraw-Hill 1960), Chapter 10
2. R.E. Collin: op. cit., Chapter 8
3. L. Lewin: "Advanced Theory of Waveguides" (Iliffe, 1951)
4. N. Marcuvitz: "Waveguide Handbook", M.I.T. Radiation Lab. Series, no. 10 (McGraw-Hill 1951)
5. K.R. Slinn: "The Excitation and Some Applications of Backward Waves in Dielectric-Loaded Waveguides", Ph.D. Thesis, Leeds University, 1966, Chapter 6.
6. P.J.B. Clarricoats and K.R. Slinn: "Numerical Solution of Waveguide Discontinuity Problems", proc. I.E.E. 114 (7), 1967, p.878
7. A.Wexler: "Solution of Waveguide Discontinuities by Modal Analysis", Trans. I.E.E.E. MTT-15 (9), 1967, p.508.
8. W.J. Cole, E.R. Nagelberg and C.M. Nagel: "Iterative Solution of Waveguide Discontinuity Problems", Bell Syst. Tech.J. 46 (3), 1967, p.649.
9. P.H. Masterman, P.J.B. Clarricoats and C.D. Hannaford: "Computer Method of Solving Waveguide-Iris Problems", Electronics Letters 5 (2), 1969, p.23
10. J.B. Davies and C.A. Muilwyk: "Numerical Solution of Uniform Hollow Waveguides with Boundaries of Arbitrary Shape", Proc. I.E.E. 113 (2), 1966, p.277
11. P.L. Arlett, A.K. Bahrani and O.C. Zienkiewicz: "Application of Finite Elements to the Solution of Helmholtz's Equation", Proc. I.E.E. 115 (12), 1968, p.1762.
12. P.J.B. Clarricoats and K.R. Slinn: "Computer Method of Determining the Propagation Coefficient of Slotted Waveguides", Electronics Letters 3 (5), 1967, p.191.
13. S. Silver: "Microwave Antenna Theory and Design", M.I.T. Radiation Lab. Series, no. 12 (McGraw-Hill 1949) p.377
14. P.D. Potter: "A New Horn Antenna with Suppressed Sidelobes and Equal Beamwidths", Microwave Journal, 6 (6), 1963, p.71.
15. P.W. Hannan: "Optimum Feeds for All Three Modes of a Monopulse Antenna", Trans. I.R.E. AP-9, 1961, p.444
16. L.J. Ricardi and L. Niro: "Design of a 12-Horn Monopulse Feed", I.R.E. International Convention Record, Pt.1, 1961, p.93.
17. S.W. Drabowitch: "Theorie et Applications des Antennes Multimodes", Revue Technique C.F.T.H. (37), 1962, also "Multimode Antennas", Microwave Journal 9 (1), 1966, p.41

18. K.J. Keeping: "Design and Construction of a Multimode Circularly Polarized Monopulse Tracking Feed for High-Power Application in a Cassegrain Reflector System", I.E.E.E. International Convention Record, (5), 1965, p.101

19. D. Harris: "The Electrical Design and Performance of a 40' Cassegrain Aerial", I.E.E. Conference Publication no. 21 on Design and Construction of Large Steerable Aerials, p.324

20. R. Mittra: "Relative Convergence of the Solution of a Doubly Infinite Set of Equations", J. Res. Nat. Bur. Stand. 67D (2), 1963, p.245

21. R.E. Collin and J. Brown: "Calculation of the Equivalent Circuit of an Axially Unsymmetric Waveguide Junction", Proc. I.E.E. 103C, 1956, p.121

22. L. Felsen: Private Communication

23. E.R. Nagelberg and J. Shefer: "Mode Conversion in Circular Waveguides", Bell Syst. Tech. J., September 1965, p.1321.

24. E.R. Nagelberg: Bell Telephone Labs. internal memo. on the design of dual mode conical horns for communication antennas, 1966 (unpublished).

25. L.O. Goldstone and A.A. Oliner: "Leaky Wave Antennas I: Rectangular Waveguides", I.R.E. Trans. AP-7, 1959, p.307

26. L.O. Goldstone and A.A. Oliner: "Leaky Wave Antennas II: Circular Waveguides", I.R.E. Trans. AP-9, 1961, p.280

27. S. Ahmed: Discussions with author at Leeds University.

28. R.S. Elliott: "Two-Mode Waveguide for Equal Mode Velocities", Trans. I.E.E.E. MTT-16 (5), 1968, p.282

29. S. Silver: op. cit., p.342

30. R.C. Johnson: "Linear Tapers in Rectangular Waveguide", Trans. I.R.E. MTT-7, 1959, p.374

31. P.A. Jensen: "A Low-Noise Multimode Cassegrain Monopulse Feed with Polarization Diversity", NEREM Record, 1963, p.94

32. V.V. Galindo and C.Y. Pon: "Control and Optimization of a Multimode Square Feed for Sum and Difference Patterns", NEREM Record, 1963, p.96

33. P.W. Hannan: "Maximum Gain in Monopulse Difference Mode", Trans. I.R.E. AP-9, 1961, p.314

34. R.R. Kinsey: "Monopulse Difference Slope and Gain Standards", Trans. I.R.E. AP-10, 1962, p.343

35. G.M. Kirkpatrick: "Aperture Illuminations for Radar Angle-of-Arrival Measurements", I.R.E. Trans. on Aeronautical and Navigational Electronics, September 1953, p.20.

36. W.V.T. Rusch: "Scattering from a Hyperboloid Reflector in a Cassegrain Feed System", Trans. I.E.E.E. AP-11, 1963, p.414

37. P.E. Green: "Inhomogeneous Waveguide Travelling Wave Antennas", Ph.D. Thesis, Leeds University, 1966

38. W.F. Williams: "High Efficiency Antenna Reflector", Microwave Journal, 8 (7), 1965, p.79

39. A.J. Simmons and A.F. Kay: "The Scalar Feed- A High Performance Feed for Large Paraboloid Reflectors", I.E.E. Conference Publication no. 21 on Design and Construction of Large Steerable Aerials, p.213

40. P.J.B. Clarricoats and P.K. Saha, "Theoretical Analysis of Cylindrical Hybrid Modes in a Corrugated Horn", Electronics Letters 5 (9), 1969, p.187

41. P.J.B. Clarricoats: "Analysis of Spherical Hybrid Modes in a Corrugated Conical Horn", Electronics Letters, 5 (9) 1969, p.189

42. G.H. Bryant: "Propagation in Corrugated Waveguides", Proc. I.E.E. 116 (2), 1969, p.203.